Impact of charging mechanisms

on the reliability of RF MEMS devices

Piotr Czarnecki

In collaboration with

imec vzw

November 2010

KATHOLIEKE UNIVERSITEIT LEUVEN
FACULTEIT INGENIEURSWETENSCHAPPEN
DEPARTEMENT ELEKTROTECHNIEK
AFDELING ESAT - DIVISIE MICAS
Kasteelpark Arenberg 10, B-3001 Leuven, Belgie

Impact of charging mechanisms

on the reliability of RF MEMS devices

Piotr Czarnecki

Jury:
Prof. Yves Willems, president

Prof. Robert Puers, promoter
Prof. Chris Van Hoof, promoter
Prof. Robert P. Mertens
Prof. Martine Wevers
Prof. Ingrid De Wolf
Prof. George Papaioannou
Prof. Laurent Francis
Dr. Harrie A.C. Tilmans

Dissertation presented in partial
fulfillment of the requirements for
the degree of Doctor
in Engineering

In collaboration with

imec vzw

November 2010

Moim Mamusi, Tatusiowi i siostrze Ewelinie

Acknowledgments

Finally. I am now in the point where I can say "It is over". It was a long, very interesting and challenging journey; a journey to the world of MEMS reliability. After six years spent on mainly destroying work of other people, I feel that I have just stepped into that world. I am hoping to have a possibility to explore it more in the future.

My inborn device-breaking ability and natural "what's inside" curiosity often employed during the studies would be worth nothing without help of many people that I would like acknowledge now.

First, I would like to thank my parents and my sister for supporting the decision about starting my Ph.D. studies. I could not do that without them.

I would like thank my promoter Prof. Robert Puers for accepting me as a student, for his help and support.

Extra special thanks must go to Prof. Ingrid De Wolf for guidance, help and support, providing freedom and bearing all the crazy ideas, removing obstacles and tolerating mistakes and failures.

I would like to acknowledge the jury members: Prof. Chris Van Hoof, Prof. Robert Mertens, Prof. Martine Wevers, Prof. George Papaioannou and Prof. Laurent Francis. I particularly would like to thank Harrie A.C. Tilmans for help and support.

Special thanks go to W. Merlijn van Spengen for introducing me to the MEMS reliability world.

I want to thank Xavier Rottenberg, Phillip Ekkels and Paresh Limaye for help, many fruitful discussions, inspiration and accompaniment during the voyages through the hills and valleys and abyss and shallows of the world of science.

I cannot forget to acknowledge the former and present members of the REMO team: Robert Modlinski, Stanislaw Kalicinski, Veerle Simons, Myriam Van De Peer, Petar Ratchev, Liu Caroline Chen, Frederic Duflos, Jeroen De Coster, Olalla

Abstract

The growth of MEMS (micro electro-mechanical systems) technology, initiated by Nathanson et al. in 1967 with the presentation of the first micro electro-mechanical device (the resonant gate transistor), let many ideas come into existence. Among more or less fascinating concepts a capacitive RF MEMS switch has been introduced by Goldsmith et al. in 1996.

The capacitive RF MEMS switch is a device manufactured using MEMS technology that can switch (route) RF signals. Very promising expected properties of the device, such as high linearity, low loss, low power consumption, low mass and dimensions and low production costs make the capacitive RF MEMS switch a competitive alternative to solid-state RF switches. The advantages of the technology were appreciated by many researchers. The reported variety of applications and forms of the switch illustrated the potential of the capacitive RF MEMS switch.

However, the commercialization of these devices is hindered by poor reliability. The lifetime of the capacitive switches is drastically limited by a number of failure mechanisms, from which charge trapping is recognized as the most severe one. In 2001 Goldsmith et al. proposed using tailored biasing schemes as a remedy for charge trapping. This method can rise the lifetime by a limited factor but it does not solve the problem. Several additional ideas improving the lifetime have been proposed but they mainly try to circumvent the problem without understanding the causes of the failure.

The focus of the work presented in this document is on the physics and reliability of the RF MEMS devices. As a representative the electrostatically driven capacitive RF MEMS switch is chosen. The main goal is a better understanding of the physics of failure. The obtained observations and conclusions are expected to help designers and technologists develop a reliable capacitive RF MEMS switch.

The goal of the first experiments was to verify whether the failure mechanism of the available devices was similar to the one described in literature. The obtained results pointed to Poole-Frenkel mechanism as a possible failure mechanism. A verification of the remedy proposed by Goldsmith, bipolar actuation voltages, showed only a

slight improvement.

Besides that, an impact of the gas breakdown and/or electron emission on the lifetime of the switches was observed.

The results obtained in the first experiments were used in an FMEA (Failure Mode and Effect Analysis). As a result a number of possible failure mechanisms were listed in a FMEA study and the one with the highest priority, charging, was determined. It was chosen for a more detailed study.

Based on the experience gained during the first part, a number of dedicated test structures were fabricated and tested. The design consisted of not fully functional, yet, representative from the charging point of view, electrostatically driven switchable capacitors. The design assured the compatibility with the available and further improved testing equipment (ELT). Also dedicated test structures to study the impact of the environment were foreseen.

However, not all structures could be used due to processing issues. Still, a relatively large number of identical test structures allowed performing experiments under a large variety of testing conditions.

Further, a comparison of a few interposer dielectric candidates was done. A number of simplified wafers were fabricated and tested. The two best candidates, AlN1 and AlN2, were chosen for further investigation. In depth experiments were then performed on fully processed test structures using the two candidates.

The lifetime experiments performed using various magnitudes of the actuation voltage amplitude, and both positive and negative polarities showed a disagreement with the model based on the Poole-Frenkel conduction mechanism. The unusual behavior pointed to more than one charging mechanism present in the capacitive RF MEMS switches. The substrate charging was identified besides the interposer dielectric charging. The impact of the substrate was first studied with devices fabricated on two different types of substrate material: AF-45 glass and oxidized high-resistivity silicon. The different sensitivity of both materials to various environmental conditions is presented.

The next part is focused on the identification of different charging mechanisms. It is shown that the C-V characteristic measurements combined with different configurations of the actuation methods can give new insights into charging mechanisms.

Once the two charging mechanisms were observed, the study of each of them became easier. A number of different testing techniques including fabrication of special test structures (e.g. thicker interposer dielectric layer) allowed isolating particular mechanisms. The use of various actuation methods was supposed to allow locating the mechanisms. However, the observed results were different than the expected, yet, very consistent. It became very clear that the impact of the

substrate and substrate charging cannot be neglected.

The last experiments, consisting of testing devices with a modified HR-Si substrate, showed that the impact of the substrate and substrate charging is higher than anticipated. It definitely cannot be neglected. The C-V characteristic of the device can be modified in similar ways by both interposer dielectric and substrate charging. Therefore, both may be confused.

Using all this information, a proposal for a better capacitive RF-MEMS switch, from charging point of view, is made.

Samenvatting

Het ontstaan van MEMS technologie (micro elektro-mechanische systemen) dateert al van 1967, toen Nathanson et al. de eerste transistor met een mechanisch resonerende poort voorstelden. Sindsdien zijn er heel wat verschillende types MEMS componenten ontwikkeld, waaronder de MEMS schakelaar voor radio-frequenties (RF MEMS) van Goldsmith et al. uit 1996.

Een capacitieve RF MEMS schakelaar laat toe om het pad van signalen in RF circuits te configureren. In vergelijking met klassieke halfgeleidercomponenten, hebben MEMS schakelaars een aantal zeer aantrekkelijke eigenschappen, zoals bijvoorbeeld een uitstekende lineariteit, minimale verzwakking van het RF signaal, laag energieverbruik, kleine massa, beperkte afmetingen en lage productiekosten. Door dit sterke potentieel is er de afgelopen jaren heel wat onderzoek gedaan naar RF MEMS schakelaars, met als resultaat een heel aantal verschillende RF MEMS componenten voor uiteenlopende toepassingen.

Van een echte commerciële doorbraak is het echter nog geen sprake, voornamelijk omdat de levensduur van capacitieve RF MEMS schakelaars beperkt wordt door een aantal falingsmechanismen. Oplading wordt algemeen aanvaard als het meest fundamentele probleem voor deze componenten. In 2001 stelden Goldsmith et al. een strategie voor om oplading tegen te gaan door gebruik te maken van gewijzigde stuurspanningen. Deze methode slaagt er weliswaar in om de levensduur in beperkte mate te verlengen, maar is geen fundamentele oplossing van het probleem. Daarnaast werden nog een aantal andere technieken voorgesteld, maar ook zij proberen het probleem van oplading uit de weg te gaan, eerder dan het op te lossen.

Het voorliggend werk spitst zich dan ook toe op het bestuderen van de fysische mechanismen die werkzaam zijn in RF MEMS componenten, en hoe zij de levensduur beïnvloeden. Doorheen het werk wordt de capacitieve RF MEMS schakelaar als representatief onderdeel van de hele familie 'RF MEMS componenten' gebruikt. Het vooropgestelde doel is om een beter inzicht te verkrijgen in de voornaamste falingsmechanismen. De experimentele vaststellingen en besluiten

kunnen als leidraad dienen voor ontwerpers en technologen bij het ontwikkelen van nieuwe, betrouwbaardere RF MEMS schakelaars.

In eerste instantie werd op experimentele wijze en aan de hand van reeds bestaande RF MEMS componenten nagegaan of de vastgestelde falingsmechanismen wel degelijk dezelfde zijn als eerder al in de literatuur beschreven werd. Met name werd in de bestaande literatuur steeds gewezen op het optreden van Poole-Frenkel emissie. De door Goldsmith voorgestelde techniek, nl. het gebruiken van bipolaire stuurspanningen, resulteerde slechts in een beperkte toename van de levensduur.

Daarnaast werd ook de impact van elektrische doorslag in het omgevende gas enerzijds, en van electronenemissie anderzijds, bekeken.

Op basis van de resultaten uit de eerste experimenten werd een falingsanalyse (FMEA, falings-mode en effect analyse) gemaakt. Uit alle falingsmechanismen die in deze analyse bekeken werden, kwam oplading naar voor als het mechanisme met de hoogste prioriteit. Om die reden werd oplading gekozen als onderwerp voor deze studie.

Bovendien werd een aantal specifieke teststructuren ontworpen en gefabriceerd. Hierbij was het niet de bedoeling om structuren met een volledige RF funktionaliteit te ontwerpen, maar wel om componenten te maken die op vlak van elektrostatische oplading representatief zijn voor elektrostatisch geschakelde capaciteiten in het algemeen. Daarnaast werden ook structuren ontworpen om de invloed van omgevingsfaktoren te onderzoeken. Omdat de technologie waarmee deze componenten vervaardigd worden nog niet volledig op punt staat, konden niet al deze structuren in de praktijk gebruikt worden. Niettemin konden heel wat testen gedaan worden onder verschillende atmosferische condities op een groot aantal identieke structuren. Voor het testen werd de bestaande instrumentatie (ELT) verder verfijnd.

Om verschillende dielectrica met elkaar te kunnen vergelijken, werd een aantal wafers gemaakt met een vereenvoudigde procestechnologie en verschillende dielectrica. De twee meestbelovende materialen werden op basis van dit experiment geselecteerd voor verdere tests; hiervoor werden opnieuw structuren vervaardigd met de volledige procestechnologie.

De resultaten van levensduurtesten die hierop werden uitgevoerd met verschillende amplitudes van de stuurspanning en met positieve en negatieve polariteit, zijn in strijd met het Poole-Frenkel geleidingsmechanisme. Het geobserveerde gedrag kan enkel verklaard worden door aan te nemen dat meer dan één opladingsmechanisme actief is in capacitieve MEMS componenten. Meer specifiek wijzen de resultaten op oplading van het substraat, naast oplading van het dielectricum. Dat het substraat wel degelijk invloed heeft op de gevoeligheid voor oplading in verschillende atmosferische condities, werd aangetoond door teststructuren te vervaardigen op twee verschillende substraten, nl. op AF-45 glas en op geoxideerd hoog-resistief

silicium.

In het volgende deel wordt dieper ingegaan op het identificeren van verschillende mechanismen die aanleiding geven tot oplading. De voorgestelde strategie om C-V curves op te meten, gecombineerd met verschillende methodes voor het aanleggen van de stuurspanning, leverde nieuwe inzichten op met betrekking tot de opladingsmechanismen.

Het experimenteel observeren van twee mechanismen, nl. oplading van het dielectricum enerzijds en van het substraat anderzijds, was een belangrijke stap. Door speciale teststructuren te ontwerpen (bijvoorbeeld met een dikker dielectricum), konden beide effecten apart bestudeerd worden. Het gebruik van verschillende methodes voor het aanleggen van de actuatiespanning toonde duidelijk aan dat oplading van het substraat een zeer significante rol speelt; de mate waarin dit het geval is, bleek ook afhankelijk te zijn van het type substraat.

Tenslotte werden structuren gemaakt op aangepaste HR-Si substraten. Opnieuw bleek de rol van oplading in het substraat erg belangrijk te zijn. Bovendien wordt de C-V curve van teststructuren op een gelijkaardige manier beïnvloed door oplading in het substraat en in het dielectricum. Hierdoor worden beide opladingsmechanismen soms met elkaar verward.

Op basis van al de verzamelde gegevens wordt tenslotte een voorstel gedaan voor een verbeterde RF-MEMS schakelaar waarin oplading en de effecten ervan worden geminimaliseerd.

Glossary

AC	alternating current
AFM	Atomic Force Microscopy
a.u.	arbitrary unit
CMOS	Complementary Metal-Oxide-Silicon
CPW	Co-Planar Waveguide
CTE	coefficient of thermal expansion
C-V	capacitance vs. voltage
DAQ	data acquisition
DC	direct current
DUT	device under test
EFM	Electrostatic Force Microscopy
ELT	Electronic LifeTime
EOL	end-of-life
FMEA	Failure Mode and Effect Analysis
HR-Si	high-resistivity silicon
I-V	current vs. voltage
LDV	Laser Doppler Vibrometer
LT	lifetime
MEMS	Micro ElectroMechanical System
MOS	Metal-Oxide-Silicon
MIM	metal-insulator-metal
PC	personal computer
PECVD	plasma enhanced chemical vapor deposition
PCM	process check module
RF	radio frequency
SAM	self-assembled monolayer
VCO	voltage controlled oscillator

A	active area
C	capacitance
C_{switch}	capacitance of the switch
C_{up}, C_{down}	up- and down-state capacitance
C_{on}, C_{thon}	measured and theoretical capacitance in the on state, respectively
C_a, C_d	capacitance of an air capacitance, capacitance of a capacitor with dielectric
ΔC	capacitance difference, change
d	distance
E	electric field
E_{ch}, E_{act}	electric field generated by charge, electric field generated by actuation voltage
E	Young's modulus
EOLx%, EOLxV	end-of-life criteria
F_{el}, $F_{el}{}'$	electrostatic force, with and without charge
F_{el}^{A}, F_{el}^{B}	electrostatic force in A and B parts of the switch
F_{mech}	mechanical restoring force
f, Δf	frequency, frequency change
g	gap, initial distance between the beam and bottom electrode
J	current density
k, k', k''	spring constant, spring constant components
k	Boltzman's constant
L	inductance
L_b	beam length
L_{etch}	lateral etch length
L_{hole}	etch hole size
L_{metal}	size of the metal part
n	number of stressing-idling cycles
p	pressure
Q	charge
Q_{act}	charge to actuate the switch
$Q_{trapped}$	trapped charge

Q_{diel}	charge trapped (placed) in the interposer dielectric
Q_{sub}	charge trapped (placed) in the substrate
R	resistance
t	beam thickness
t	time
t_{on}, t_{off}	time to switch on and off
t_{CV}	C-V measurements time
T	temperature
U	voltage
U_{act}	actuation voltage
U_{ch}	equivalent voltage generated by trapped charge
U_{out}	ELT output voltage signal
U_{HF}	high frequency voltage
U_{opt}	optimal actuation voltage
U_{pad}	actuation voltage applied to the bottom actuation pad
U_{beam}	actuation voltage applied to the beam
U_{diel}	resultant voltage across the interposer dielectric
U_{sub}	resultant voltage across the substrate
U_{CV}	amplitude of the voltage applied during a C-V measurement
V_{pi}, V_{pi}^{+}, V_{pi}^{-}	pull-in voltage, positive and negative pull-in voltages
$V_{pi}{}'$, $V_{pi}+'$, $V_{pi}^{-}{}'$	pull-in, positive and negative pull-in after stressing
ΔV_{pi}, ΔV_{pi}^{+}, ΔV_{pi}^{-}	change of the pull-in, positive and negative
V_c, $V_c{}'$	center voltage of the C-V characteristic, before and after stressing
V_s	voltage shift of the C-V characteristic
V_{br}	breakdown voltage
w_b	beam width
w_s	width of the bottom electrode
w_g	slot width

W_{pi}	pull-in window
ΔW_{pi}	change of the pull-in window
$\Delta_w V_{pi}^+$, $\Delta_w V_{pi}^-$	change of the pull-in voltage (positive and negative) due to C-V narrowing
$\Delta_s V_{pi}^+$, $\Delta_s V_{pi}^-$	change of the pull-in voltage (positive and negative) due to C-V narrowing
β	Weibull distribution shape parameter, a.k.a. the Weibull slope
ε , ε_r	vacuum permittivity, relative permittivity
η	Weibull distribution scale parameter
ν	Poisson's ratio
ϕ_B	barrier height
σ	internal stress

Contents

List of Tables

Chapter 1

Introduction

This chapter introduces the content of this work to the reader. The motivation and the subject of the study: electrostatically driven capacitive shunt RF MEMS switch are presented first. The last part of this chapter presents a variety of articles published about other types of RF MEMS switches.

1.1 Motivation

The growth of MEMS (micro electro-mechanical systems) technology, initiated by Nathanson et al. in 1967 with the presentation of the first micro electro-mechanical device (the resonant gate transistor) [1], let many ideas come into existence. Among more or less fascinating concepts a capacitive RF MEMS switch has been introduced by Goldsmith et al. in 1996 [2]. The capacitive RF MEMS switch is a device manufactured using MEMS technology that can switch (route) RF signals (Fig. 1.1). The expected promising properties of the device, such as high linearity, low loss, low power consumption, low mass and dimensions and low production costs make the capacitive RF MEMS switch a competitive alternative to solid-state RF switches. The advantages of the technology were appreciated by many researchers. The reported variety of applications and forms of the switch illustrated the potential of the capacitive RF MEMS switch.

However, the commercialization of these devices is hindered by poor reliability. The lifetime of the capacitive switches is drastically limited by a number of failure mechanisms, from which charge trapping is recognized as the most severe one. In 2001 Goldsmith et al. proposed using tailored biasing schemes as a remedy for charge trapping [3]. This method can rise the lifetime by a limited factor but it does not solve the problem.

Several other ideas to improve the lifetime have been proposed but they mainly try to circumvent the problem without understanding the causes of the failure.

A literature survey performed in 2004 showed that there is a need for understanding the physics of the failure mechanisms in the capacitive RF MEMS switches. In about 30 articles presenting both capacitive and ohmic switches, less than 10% included (very limited) reliability data. In some of the articles, authors directly express a need for the reliability study.

The purpose of this work was to understand the physics of the charging in the capacitive RF MEMS switches as the key reliability issue. The study consisted of testing reliability of several types of devices provided in frames of different projects. One of the projects was focused on the study and the improvement of the reliability of the RF MEMS switches. The author had the opportunity to participate in the design of experiments and test structures.

Any experiment could not be performed without proper equipment. The lack of commercially available dedicated equipment forced the author to develop a measurement setup that could be used in the study. The improved ELT system embedded in the Suss MicroTec PAV150 environmental chamber proved to be a powerful tool allowing performing a large variety of experiments. The experiments performed under different conditions allow study of particular charging mechanisms.

The obtained results and conclusions are expected to help designers and technologists to develop a reliable capacitive RF MEMS switch.
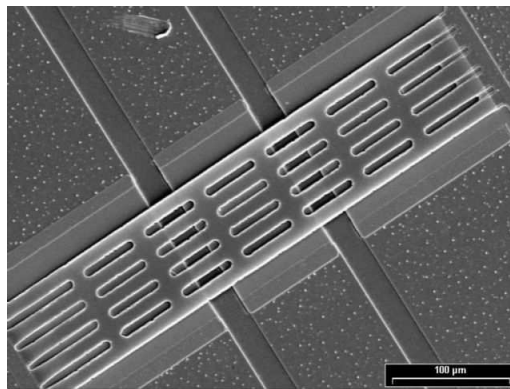
Figure 1.1: An example of a capacitive RF MEMS switch. IMEC courtesy.
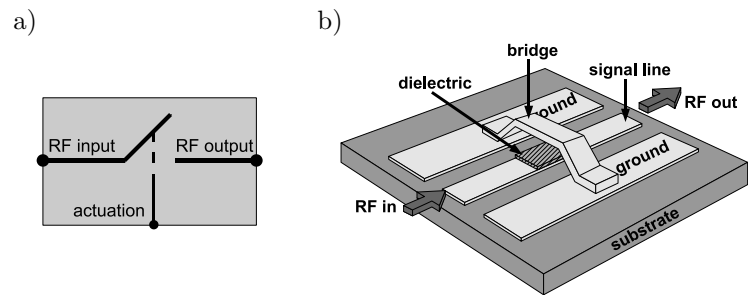
Figure 1.2: RF MEMS switch - the idea a) and an example of a clamped-clamped beam switch b).

1.2 Electrostatically driven capacitive shunt RF MEMS switch

1.2.1 The switch

The capacitive RF MEMS switch is a device, manufactured in MEMS technology, that can be used for switching (routing) radio-frequency (RF) signals (Figure 1.2a). The switching mechanism is based on changes of impedance of the device as a result of its variable capacitance. The capacitance changes thanks to displacements of the movable portion of the switch. Figure 1.2b shows one of the possible switch configurations: a capacitive shunt RF MEMS switch. A clamped-clamped beam (bridge), anchored in the ground pads, is suspended above the signal line of a coplanar waveguide (CPW). The movement of the beam causes changes of the capacitance of the switch. The dielectric layer, covering the signal line in the contact area, improves the RF properties of the switch and prevents short-circuiting.

The working principle of the capacitive shunt RF MEMS switch is schematically presented in Figure 1.3. The switch can stay in two stable states: ON (left column of Figure 1.3) and OFF (right column of Figure 1.3). The ON state allows an RF signal to pass (Figure 1.3a) and in the OFF state the signal is blocked (Figure 1.3b). The RF signal can pass through (Figure 1.3c) when the capacitance of the switch is low (Figure 1.3e). The RF signal is blocked (Figure 1.3d) when high capacitance occurs (Figure 1.3f). In that case, the impedance between the signal line and the ground is low. The switch exhibits low capacitance when the bridge is in the up (top) position (Figure 1.3g). High capacitance occurs when the beam is moved to the down (bottom) position (Figure 1.3h).
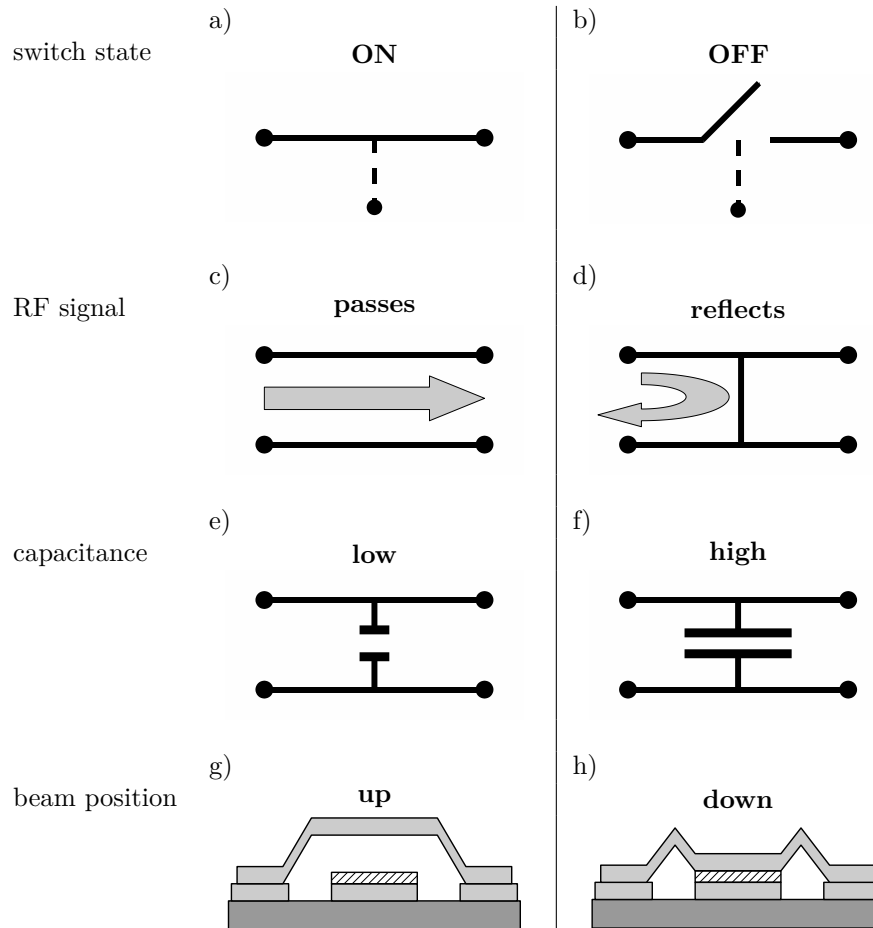
Figure 1.3: Working principle of the capacitive shunt RF MEMS switch: when the switch is ON a), the RF signal can pass through (c) the switch is exhibiting low capacitance (e) due to beam staying in the up position. The switch is OFF (b) - it blocks the RF signal (d) - when the capacitance of the switch is high (f). That takes places when the beam is in contact with the dielectric (down position, h).

1.2.2 The properties

An RF switch should fulfill several requirements:

- isolation (in off-state): the signal passing the switch in off-state should be as low as possible,

- insertion loss (in on-state): the loss of the signal passing the switch in on-state should be as low as possible,

- switching on and off time (t_{on} and t_{off}): the transition time between the states should be as short as possible,

- linearity: the signal should pass the switch without being distorted,

- power consumption: switching between the states should consume as low power as possible,

- size (dimensions, mass): a switch should be small and light,

- manufacturing costs: should be as low as possible.

The capacitive RF MEMS switches are expected to exhibit better RF properties than solid-state switches [4–7]. Lower insertion loss, higher isolation, extremely high linearity (immeasurable intermodulation products) and lower power consumption are presented as the main advantages of the MEMS over the solid-state technology. However, depending on the application different properties are classified as the most important. E.g. in aeronautics and space applications low mass, low dimensions and low power consumption are mostly appreciated [8–11]. High linearity, low insertion loss and high isolation are required in terrestrial millimeter-wave applications (radars, etc.) [12–14]. Low production costs are always welcome. Although the capacitive RF MEMS switches seem ideal devices they suffer some disadvantages: typically higher switching time and lower RF power handling. Nevertheless, there are many applications not affected by the mentioned disadvantages.

1.2.3 Electrostatic actuation

Switching, i.e. movement of the beam between the up and down positions, requires an actuation mechanism. There are several possibilities (see section 1.3.1) with the electrostatic actuation mechanism as one of the most common in MEMS. Low complexity and low power consumption fulfill MEMS needs. The presented electrostatically driven shunt capacitive RF MEMS switch employs a parallel-plate electrostatic actuator. A simplified model of the actuator is presented in Figure 1.4. It consists of two conductive electrodes: one mechanically fixed and one movable,
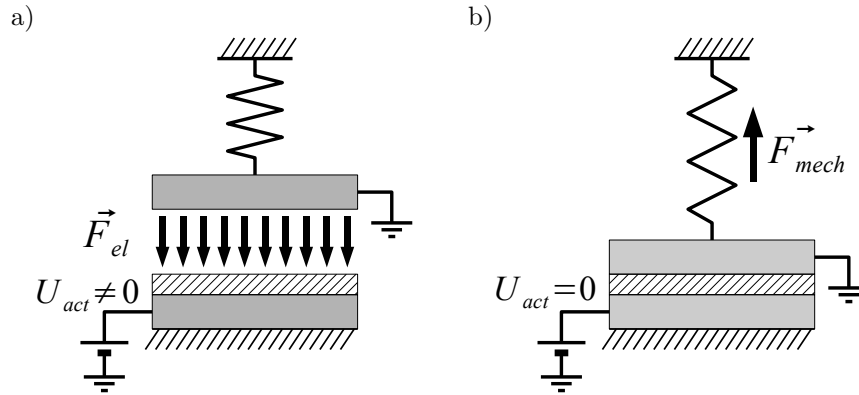
Figure 1.4: Electrostatic force attracts the movable beam to the fixed one a). Mechanical force brings the beam back to the up position when the electrostatic force disappears b).

suspended above the fixed one. One of the electrodes, usually the fixed one, can be covered with a layer of dielectric preventing short-circuits in case of contact occurrence. The bottom fixed electrode represents the signal line that is also the actuation electrode. The top movable electrode represents the beam of the switch.

The movement of the beam is an effect of two counteracting forces: the mechanical restoring force of the spring $\vec{F}_{mech}$ and the electrostatic $\vec{F}_{el}$. The electrostatic force causes movement of the beam from up do down position (Figure 1.4a). In the same time, the spring is strained, creating the restoring force that brings the beam back to up position when the electrostatic force disappears. (Figure 1.4b).

Basically, there are two methods to control the position of the beam: voltage and charge control. Depending on the control method, different characteristics of the actuator are obtained. The first one, the voltage control method, is the most common due to the ease of use. The second one, the charge control method, requires use of more complex biasing circuits. Though, its use can be beneficial.

Voltage control method

The displacement vs. applied actuation voltage relation can be found by equating the magnitudes of the two forces [4]:

$$\left\|\vec{F}_{mech}\right\| = \left\|\vec{F}_{el}\right\| \qquad (1.1)$$

The mechanical and electrostatic forces can be described as follows:

$$\left\|\vec{F}_{mech}\right\| = kx \qquad (1.2) \qquad \left\|\vec{F}_{el}\right\| = \varepsilon_0 \frac{AU_{act}^2}{2(g-x)^2} \qquad (1.3)$$

As a result, the displacement vs. actuation voltage relation is obtained.

$$\frac{2kx(g-x)^2}{\varepsilon_0 A} = U_{act}^2 \qquad (1.4)$$

where:
k - spring constant of the beam,
x - displacement of the beam from the initial position,
ε_0 - vacuum permittivity,
A - active (overlapping) area,
U_{act} - actuation voltage,
g - initial distance between the electrodes.

The displacement vs. actuation voltage curve is presented in Figure 1.5. The growing actuation voltage causes an increase of the electrostatic force. The beam is attracted towards the bottom electrode. In the same time the mechanical spring force grows as well. The mechanical force compensates the electrostatic force and the position of the beam is stable. However, the electrostatic force grows faster (x^2) than the F_{mech} (x). At a certain point the mechanical force cannot balance the electrostatic force anymore and the beam collapses. The instability point is at the displacement of $1/3$ of the initial gap.

Once the actuation voltage is high enough to move the beam to the $1/3$ point, the beam is pulled in towards the fixed electrode. The minimal voltage required to bring the beam to the $1/3$ point (pull-in point) is called the pull-in voltage (V_{pi}) and can be calculated using (1.5). Before that point, the position of the beam is stable and defined by the magnitude of the actuation voltage. Beyond that point, the beam is in the down position and stays there as long as the actuation voltage is higher than minimal actuation voltage necessary to keep the beam in the down position. This value is called the pull-out voltage (V_{po}) and can be calculated using (1.6).

$$V_{pi} = \sqrt{\frac{8kg^3}{27\varepsilon_0 A}} \qquad (1.5) \qquad V_{po} = \sqrt{\frac{2d^2 kg}{\varepsilon_0 \varepsilon_r A}} \qquad (1.6)$$
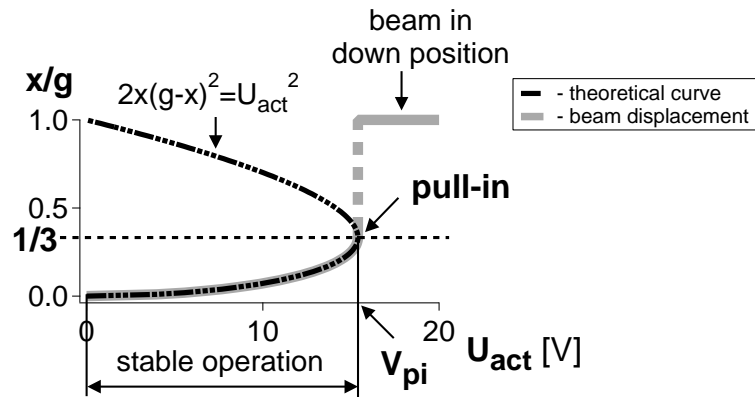
Figure 1.5: After traveling 1/3 of the distance between the up- and down-position, the mechanical force cannot compensate the electrostatic force anymore. The structure becomes unstable and the beam collapses - pull-in occurrs.

where:
d - dielectric layer thickness
ε_r - relative static permittivity of the dielectric layer, dielectric constant.

The influence of the dielectric layer (voltage drop) on the V_{pi} can be neglected as the capacitance of the air gap capacitor C_a is much lower than the capacitance of the dielectric capacitor C_d (Figure 1.6) (1.7-1.9).
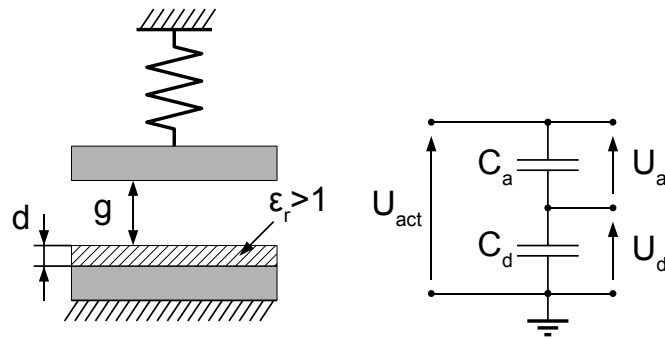
Figure 1.6: The voltage across the dielectric layer (U_d) is usually much lower than the voltage across the air gap (U_a). Hence it can be neglected.

$$\frac{U_d}{U_a} = \frac{C_a}{C_d} \qquad (1.7) \qquad\qquad \frac{C_a}{C_d} = \frac{\frac{\varepsilon_0 A}{g}}{\frac{\varepsilon_0 \varepsilon_r A}{d}} \qquad (1.8)$$

$$\frac{U_d}{U_a} = \frac{1}{\varepsilon_r}\frac{d}{g} \qquad (1.9)$$

E.g. for $g = 3\mu m$, $d = 200nm$ and $\varepsilon_r = 10$, $U_d/U_a=0.0067$. I.e. the voltage drop across the dielectric layer (U_d) is more than 100 times lower than the voltage across the air gap (U_a).

Charge control method

Replacing the U_{act} with (1.10) and (1.11) in (1.3), the relation between the displacement and the charge can be found (1.13). The presented $x = Q_{act}^2$ curve (Figure 1.7) shows that the displacement of the actuator is defined in any location between the up and down position.

$$U_{act} = \frac{Q_{act}}{C} \qquad (1.10) \qquad\qquad C = \varepsilon_0 \frac{A}{g - x} \qquad (1.11)$$

$$F_{el} = \varepsilon_0 \frac{A\left(\frac{\frac{Q_{act}}{A}}{\varepsilon_0 \frac{1}{g-x}}\right)^2}{2(g - x)^2} \qquad (1.12)$$

$$kx = \frac{Q_{act}^2}{2\varepsilon_0 A} \qquad (1.13)$$

where:
Q_{act} - actuation charge.

The main difference between the voltage and charge control methods is the different behavior of the actuator. The voltage control allows controlling the position of the beam in only 1/3 gap range. During actuation, charge can flow to the structure
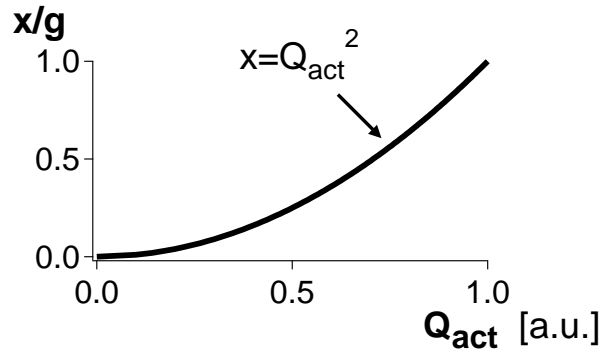
Figure 1.7: The beam displacement vs. actuation charge characteristic: the beam position is stable in the whole range.

without any limits as the voltage source can supply the necessary amount of charge. A drastic increase of the electrostatic force and pull-in is observed. The charge control method allows full control over the movable part of the actuator. The quantity of charge is allotted by the driving source preventing the pull-in occurrence. Any stable location of the beam (between the up and down position) can be obtained by controlling the quantity of the provided charge [15–18].

Several means of active controlling of the position of the movable part of the actuator are proposed based on this phenomenon:

- closed-loop control with optical or electrical displacement measurement [19–21],

- series capacitance feedback [22, 23],

- current drive [24].

1.2.4 C-V characteristic

As mentioned, the switching mechanism of the capacitive RF MEMS switch is based on changes of its impedance/admittance due to changes of its capacitance. Generally, the RF properties of an RF device are described using scattering parameters (S-parameters) [4, 25]. The S-parameters describe the distribution of incident and reflected power in an N-port radio-frequency (RF) device/system. Since the distribution of the RF power in the capacitive switch is related to the capacitance changes, it is possible to use the capacitance to describe the properties of the switch. The capacitance can be converted to impedance/admittance and further to S-parameters and vice versa.

The capacitance vs. voltage characteristic (C-V) is one of the basic characteristics of the capacitive RF MEMS switches. Its shape directly mirrors the shape of the displacement vs. actuation voltage curve presented in the previous section.

The (ideal) C-V characteristic is presented in Figure 1.8a. To measure such a curve a triangular actuation voltage is applied (Figure 1.8b).
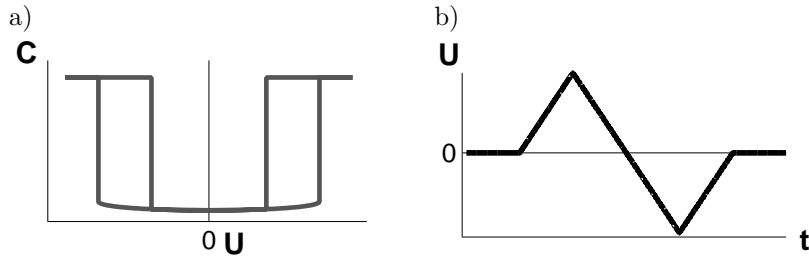
Figure 1.8: The ideal capacitance vs. voltage (C-V) characteristics of the capacitive RF MEMS switch a). To measure such a curve triangular actuation voltage is applied b).

With zero actuation voltage applied, the beam stays in the highest position, i.e. the distance between the electrodes is maximal. The switch exhibits the minimal capacitance (Figure 1.9a, point a). When the actuation voltage starts to increase (Figure 1.9b, section a-b), the electrostatic force causes displacement of the beam towards the fixed electrode. The capacitance increases. When the actuation voltage crosses the pull-in voltage, the beam collapses and a significant increase of capacitance is observed (Figure 1.9c, b-c transition). As the beam touches the surface of the dielectric, further increasing of the actuation voltage does not cause an increase of the capacitance in and ideal switch (Figure 1.9d, section c-d). The capacitance of the device reaches the maximum value (Figure 1.9d, point d). If now the actuation voltage is decreased (Figure 1.9e, section d-e), then the beam stays in the bottom position until the mechanical restoring force is higher than the electrostatic force (Figure 1.9e, point e). The pull-out occurs when the actuation voltage drops below the V_{po} (Figure 1.9f, e-f transition).

Further lowering of the actuation voltage decreases the switch capacitance back to the minimum capacitance point (Figure 1.9g, section f-a). The C-V characteristic is symmetric as the electrostatic force does not depend on the sign of the electric field (Figure 1.9h).

Exemplary C-V and S-V characteristics are compared in Figure 1.10. The curves can be used interchangeably.

The C-V characteristic allows finding several basic parameters of the switch (Figure 1.11):
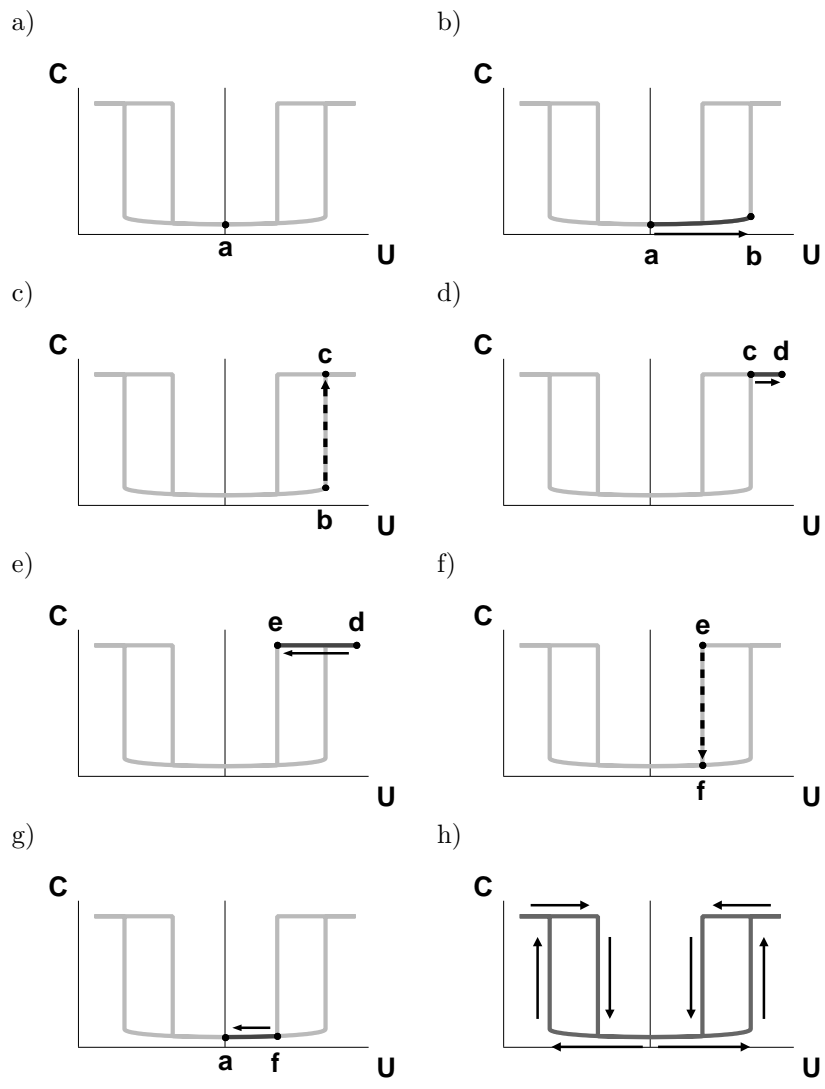
Figure 1.9: The C-V characteristic.
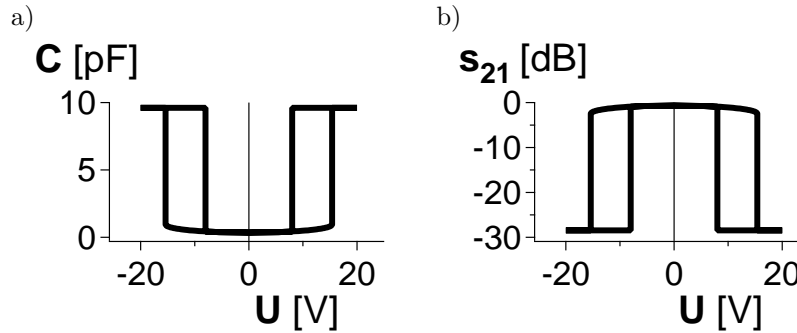
Figure 1.10: Exemplary C-V (a) and S-V (b) characteristics of a capacitive shunt RF MEMS switch. Low capacitance, in the non-actuated state ($U_{act} < V_{pi}$), results in high RF signal transmission (low loss). In the actuated state ($U_{act} > V_{pi}$) the switch exhibits high capacitance and low RF signal transmission (high isolation).

- both, positive and negative, pull-in (V_{pi}^{+} and V_{pi}^{-}) and pull-out (V_{po}^{+} and V_{po}^{-}) voltages,

- the minimal capacitance in the up-state ($U_{act} = 0$) - C_{up},

- the maximal capacitance in the down-state ($U_{act} > V_{pi}$) - C_{down}.

The C_{up} is determined by the overlapping area and the gap (Figure 1.12). The influence of the dielectric layer on the up-state capacitance can be neglected. The C_{down} depends on the active area A, the thickness d and permittivity ε_r of the dielectric and of the quality of the contact (roughness and/or planarity of the dielectric layer and the beam). The V_{pi} depends on the mechanical properties of the beam (k), the distance between the bottom (actuation) electrode and the beam (g) and overlapping area (A). The pull-out voltage depends on the shape and material properties of the beam and the thickness and the permittivity of the dielectric layer.

1.2.5 Standard operation

The standard operation of the switch involves a use of an actuation voltage. The properties of the actuation voltage (waveform shape, frequency, duty cycle etc.) are established by specifications of particular applications. The magnitude of the applied voltages should fit the V_{pi} and V_{po} parameters of the switch. To switch on the switch a voltage higher than the V_{pi} should be applied. Switching of the switch requires application of the voltage below the V_{po}. In practice 0V in off-state is applied. The resulting waveform is presented in Figure 1.13a. The rectangular shape actuation voltage is one of the simplest actuation waveforms.
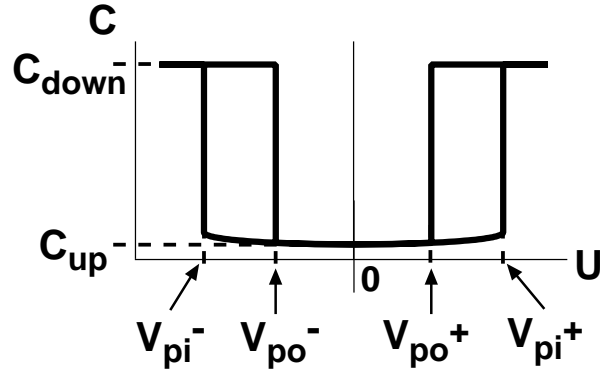
Figure 1.11: Basic parameters of the switch can be obtained from the C-V characteristic.
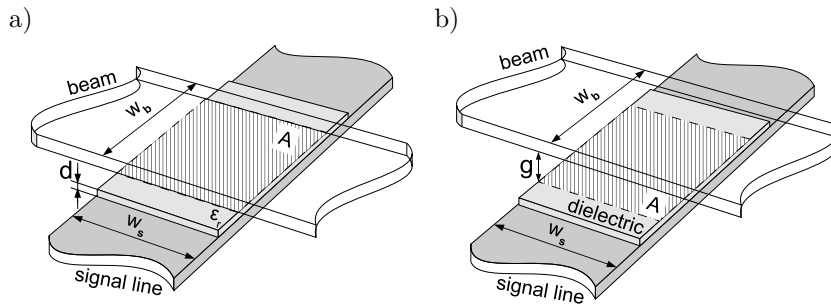
Figure 1.12: The down-state capacitance depends on the overlapping area A and the properties of the dielectric layer: thickness d and permittivity ε_r a). C_{up} depends on the distance g and overlapping area $A = w_s \cdot w_b$ (w_s - signal line width, w_b - beam width) b).

The response of the ideal switch on the applied square wave actuation voltage is presented in Figure 1.13b. High capacitance is exhibited (C_{down}) when a voltage higher than V_{pi} is applied. Low capacitance shows the off-state.

The C_{down} and C_{up} can be extracted from the $C(t)$ curve and plotted as functions of time or switching cycles (Figure 1.14). The graph is an example of a lifetime experiment result.

A similar graph can be plotted when S-parameters, instead of the capacitance, are measured.
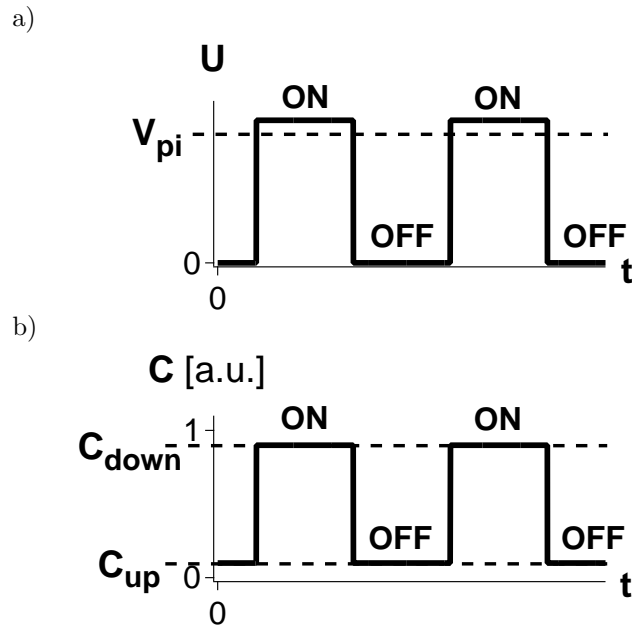
Figure 1.13: A basic actuation voltage waveform: the voltage is higher than the V_{pi} to switch on the switch and lower than the V_{po} (usually 0V) to switch it off a). The response of the switch (bottom) on such an applied actuation voltage (top) is observed as a capacitance vs. time $C(t)$ curve b).
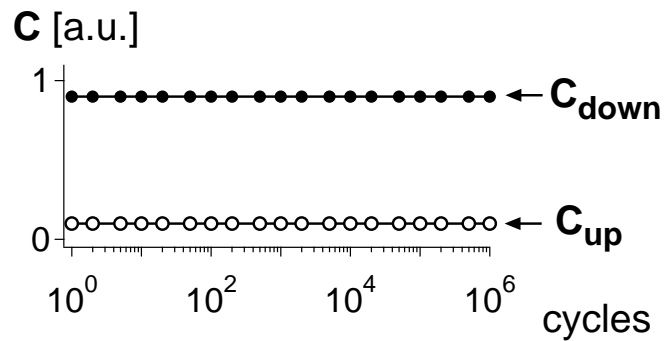
Figure 1.14: Extracted C_{up} and C_{down} plotted as functions of switching cycles are typical lifetime experiment results.

1.2.6 The role of the dielectric layer

The dielectric layer plays a double role in the capacititve RF MEMS switch. Besides improving the down-state capacitance it isolates the beam from the actuation electrode. When the actuation voltage is applied and the beam touches the dielectric layer the dielectric is treated with a relatively high electrostatic field. This fact causes the main reliability problem: charging of the dielectric. As the main topic of this work, the charging of the dielectric is discussed in more detail in section 2.4.

1.3 Other switches

1.3.1 Classification

The electrostatically driven capacitive switch described in section 1.2.1, is a member of the RF MEMS switch family presented in Figure 1.15. The RF MEMS switches can be categorized according to several criteria [4]:
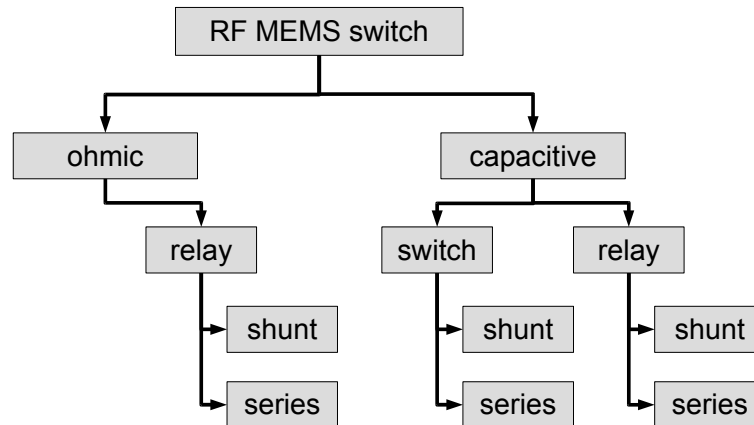
Figure 1.15: The RF MEMS switches family.

- contact type: ohmic and capacitive,

- circuit configuration: shunt and series,

- combination of RF and actuation signals: relays and switches,

- actuation mechanism: electrostatic, piezoelectric, thermal, etc.

As shown in Figure 1.15, not all the combinations are possible. E.g. ohmic type switches can be composed only as a relay. The ohmic contact of the beam and the bottom electrode would cause short-circuiting of the actuation signal. The capacitive shunt switch and the ohmic series relay are the most common.

Ohmic vs. capacitive

The difference between ohmic (also known as metal-metal contact) and capacitive switches is the switching mechanism (Figure 1.16). The ohmic switch employs a metal-metal contact to switch the signal. The switching mechanism of the capacitive switch is based on changes of capacitance. The ohmic switch can switch DC as well as AC. The capacitive switches work only with AC signals however they show better RF performance than the ohmic ones at higher frequencies.
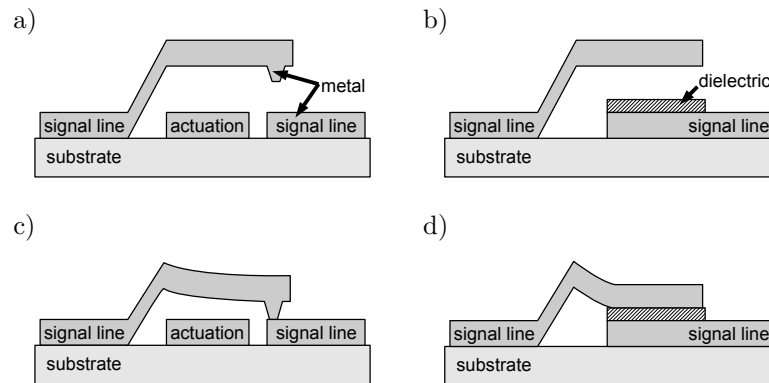
Figure 1.16: Ohmic (a: off-, c: on-state c) vs. capacitive (b: off-, d: on-state) series switches

Relay vs. switch

The difference between switches and relays is a consequence of different combination of the actuation and RF signals. The RF and actuation signals are electrically separated in the relay type of switches. In the switches, the actuation and RF signals are applied to the same port (Figure 1.17).

Shunt vs. series

The difference between series and shunt switches is presented in Figure 1.18. An actuated shunt switch causes short-circuiting of the signal that cannot pass further.
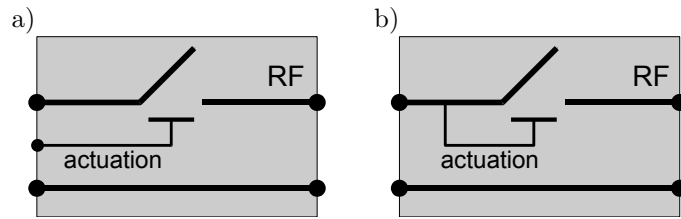
Figure 1.17: The difference between relays a) and switches b) is in application of the actuation signal.
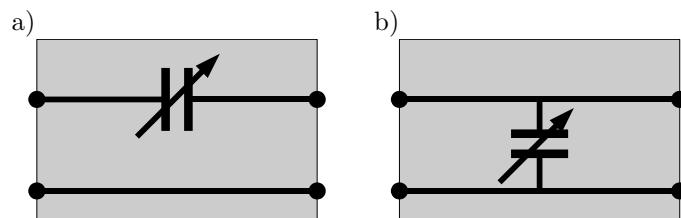
Figure 1.18: Shunt a) and series b) switches.

An actuated series switch creates a path for the RF signal. The most popular are capacitive shunt and series resistive switches.

Actuation mechanism

There are a number of different actuation mechanisms and their combinations that can be used in RF MEMS switches. Electrostatic actuation, described in section 1.2.3, is one of the most popular due to its low complexity and low power consumption. However, electrostatic actuation employed in the capacitive switches can cause reliability issues. On the other hand, e.g. ohmic switches, require a high actuation force in order to obtain low contact resistance. A high electrostatic force can be achieved by increasing the actuation voltage (additional DC/DC converters, higher power consumption, etc.) or increasing the size of the actuator. A thermal actuator is based on thermal expansion of materials. It can be based on expansion of one type of material (unimoprh) or two different materials (with different CTE) creating a bimorph-like structure. The thermal actuation allows achieving high actuation forces but it increases power consumption.

Piezoelectric actuators use the change of the shape of piezoelectric materials under an electric field. The piezoelectric actuators consume less power than the thermal actuators, allow achieving high force but are more complex than the electrostatic actuation.

In the literature (see section 1.3.3) several combinations of different actuation mechanisms are proposed in order to improve properties of the actuators. E.g. an electro-thermal actuator allows to obtain a high force and low power consumption at low actuation voltage.

1.3.2   Selected concepts

Ohmic switch

An ohmic switch (relay) is another possible MEMS device to switch RF signals. An example of such a device was presented by De Silva et al. in [26]. The device consists of an electrostatically driven beam that includes a metal contact at the tip (Figure 1.19). The metal contact connects two segments of a signal line when the beam is in down position. The switching mechanism is based on metal-to-metal contact thus the device can work with DC and low frequencies. The metal-to-metal contact switch can be realized only as a relay-type device. Otherwise the DC actuation voltage would be short-circuited leading to burning the device. The ohmic switches suffer from wear-out of the contact surface or caused by micro-welding, increasing RF loss in the switch. The micro-welding can lead to an immediate stiction: the switch does not open after removing the actuation voltage.
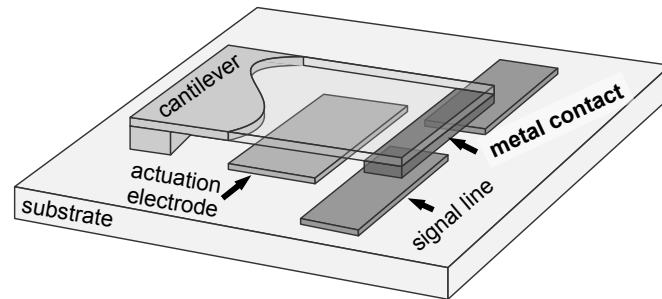
Figure 1.19: The ohmic RF MEMS switch from Motorola [26].

Boosted switch

A very interesting way of improving the RF performance of capacitive RF MEMS switches was presented by Rottenberg et al. in [27]. The performance of the capacitive switches depends on the down-state capacitance. The capacitance can be limited due to finite roughness and/or low planarity of the dielectric layer and the beam. The authors implemented an additional (electrically floating) metal layer deposited on the dielectric layer (Figure 1.20). The floating electrode creates

a fixed capacitor that can be switched on and off. The boosted switch exhibits a much higher down-state capacitance than the standard capacitive switch. The fixed capacitor is invisible for the RF signal when the beam is in the up-position.
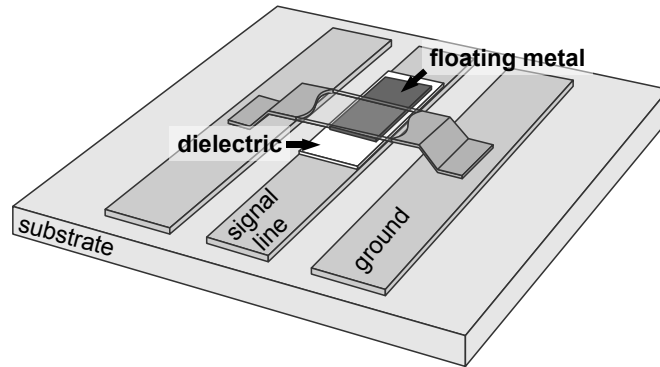
Figure 1.20: The RF MEMS boosted switch shows improved C_{up}/C_{down} ratio [27].

Electro-thermal actuation

One of the drawbacks of the electrostatic actuation is the need for high actuation voltages in order to create a sufficient electrostatic force to overcome the initial (large) gap. Moreover, ohmic switches need a relatively high force to obtain a low contact resistance. The use of high actuation voltages leads to more complex circuitry (additional power supplies, charge pumps, etc.).

A possible alternative is the employment of thermal actuators that can generate a higher force at a lower voltage. However, the power consumption of the thermal actuators is much higher than the electrostatic ones. A solution, proposed by Saias et al. in [13], combines electrostatic and thermal actuation mechanisms. Thermal actuation is used to move the beam from up- to down-state (Figure 1.21). An electrostatic force keeps the beam in the bottom position but the required actuation voltage is lower than in case of pure electrostatic actuation. High power consumption, needed to actuate the switch thermally, is necessary for only a short time, therefore the overall power consumption remains low.

A similar idea is presented by Driesen et. al in [29]

Low complexity switch

Another interesting concept of an electrostatically driven capacitive switch was presented by Siegel et al. in [28]. The switch consists of a cantilever fabricated on
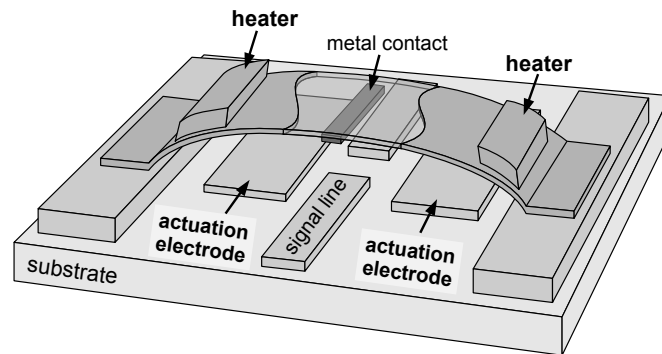
Figure 1.21: The thermo-electrically actuated RF MEMS switch [13].

top of an oxidized high resistivity silicon wafer (Figure 1.22). The grounded silicon wafer forms the actuation electrode. An actuation voltage applied to the cantilever creates an electrostatic force that attracts the cantilever to the surface of the silicon oxide. The increased capacitance between the cantilever and the fixed portion of the signal line allows the RF signal to pass. To improve the RF performance of the switch, an implantation of silicon was performed at the position of the tip of the beam. The tip lands on the implanted region and the RF signal can pass from the beam to the fixed part of the signal line. The implantation reduces the resistivity of the silicon in the contact area. The main advantage of the switch, emphasized by the authors, is the simplicity of the fabrication.
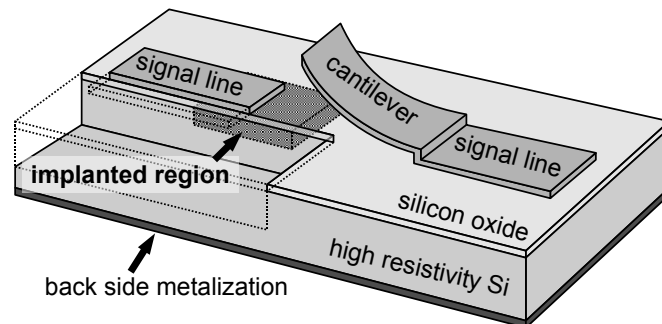
Figure 1.22: The low complexity RF MEMS switch [28].

1.3.3 Literature overview

A large number of publications has been released since the introduction of the first capacitive RF MEMS switch in 1996. The publications present different types

of switches and relays, different design and technology approaches. A number of papers present analysis of electrical, mechanical, thermal etc. performance of the devices. Also several papers deliberate about simulations and models of the switches. The presented list of publications should help in obtaining required information about different aspects of the RF MEMS switches. The overview does not include publications about dielectric charging and its influence on the reliability of the switches. That area is covered in the presented sections 2.4 and 2.5.

Overview:
[31], [39], [40], [51], [56], [59], [61], [99], [175], [180], [182], [203], [224], [228], [229], [236], [241–243], [248], [250], [253], [254], [260], [261], [263], [266], [269], [380], [280], [285].

Capacitive:
switches: [36], [38], [49], [53], [57], [76], [86], [90], [92], [107], [109], [110], [112], [113], [116], [117], [119], [123], [124], [126], [128],[132–135], [138–141], [143–145], [147], [172], [5], [188], [194], [196], [197], [199], [213], [239], [249–251], [257], [259], [262], [270], [276], [282].
relays: [115], [142],
dielectric-on-ground: [118].

Ohmic relays:
[32], [37], [74], [87], [94], [96], [114], [115], [120], [125], [131], [136], [137], [146], [167], [170], [173], [174], [177], [183], [184], [185], [187], [190], [192], [198], [215], [216–218], [220], [246], [255], [26], [11], [265], [272], [277], [284], [286].

Actuation mechanisms:
electrostatic: [5], [30], [32], [36], [38], [41–45], [48–50], [52–55], [57], [58], [64], [67], [68], [73], [75], [76], [78], [79], [86], [87], [90], [92], [94], [100–104], [106–124],[126], [128], [132], [133–147], [167], [171], [172], [174], [177–179], [183–185], [188], [190], [194], [198], [201], [205], [213], [215], [217], [218], [220], [221], [232–234], [238], [239], [245], [249], [251], [255–257], [259], [26], [262], [11], [265], [270], [272], [276], [277], [279], [282–284], [287], [288],
thermal: [37], [246],
piezoelectric: [74], [77], [99], [125], [148], [219], [286], [292],
thermal/electrostatic: [96], [173], [187], [192],
electrostatic/piezoelectric: [250],
magnetic/electrostatic: [170].

Applications:
phase shifters: [90], [140], [144], [172], [184], [194], [259],
delay network: [216],
reconfigurable antennas: [55], [102], [150], [162], [210–212], [264], [275],
switches: [152], [160], [161],
radars: [12],
switchable frequency-selective surface: [200],
reconfigurable IC: [46], [193], [278],
in space: [11].

Simulations and models:

mechanical: [63], [67], [141], [207], [222],

electromechanical: [43], [76], [135], [232], [251], [271], [276], [283], [290],

electrical: [116],

RF: [92], [196].

Analysis:

RF: [93], [98], [151], [199], [204], [234], [279],

mechanical: [79], [82], [117], [149], [189], [209], [265],

dynamic properties: [111], [122], [287],

thermal: [44],

comparizon: [60],

electrical: [64], [281],

yield: [129],

qualification: [52],

radiation: [156],

packaging: [71], [88], [206].

Manufacturing:

processing: [32], [80], [86], [91], [112], [115], [145], [171], [183], [5], [208], [257], [268], [270],

materials: [41], [65], [126], [138], [143], [183], [208], [238],

packaging: [33], [34], [71], [83], [88], [89], [97], [127], [130], [176], [191], [206], [223], [225], [226], [240], [244], [247], [267], [273],

integration: [95], [227], [273].

Design:

[30], [115], [255].

Chapter 2

Reliability

This section is focused on the reliability issues in the capacitive RF MEMS switches.

First, the role of the reliability in the modern creation process is shown and the most important terms like: reliability, lifetime, failure mode, failure mechanism, etc. are explained. Next, the Failure Mechanism and Effect Analysis technique is brought in.

Further, a selection of articles about charging-related reliability problems in the switches is presented. Different types of models and obtained results are described. Charging-related failure modes observed in the capacitive RF MEMS switches are listed.

Finally, a list of publications on other types of failure modes and mechanisms that can occur in the capacitive RF MEMS switches is presented.

2.1   Reliability - philosophy

In the past, reliability was often considered only at the end of a creation process. Lifetime of fully functional devices was tested and corrective actions (feedback to design and/or processing) were taken only if a failure occurred (Figure 2.1).

Nowadays, the reliability is a part of the creation process as important as the design and processing (Figure 2.2). This approach can improve the creation process by saving time and lowering costs. The reliability problems should be deliberated every time a part of a design or processing is modified.

The reliability study begins with the Failure Mode and Effect Analysis (FMEA)
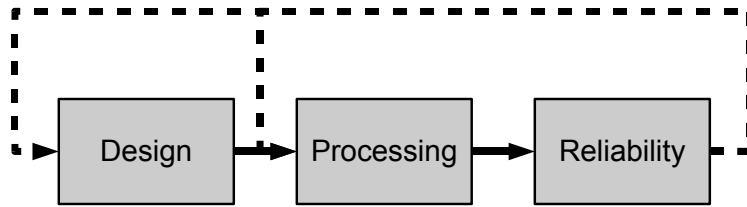
Figure 2.1: Typical place of the reliability.
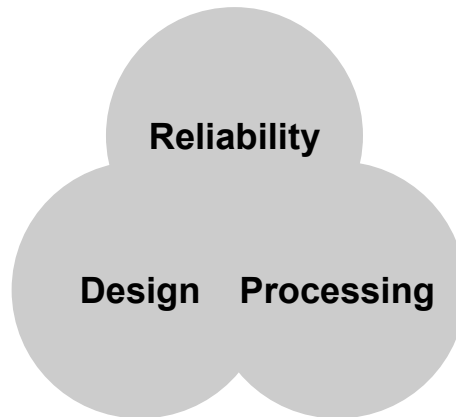
Figure 2.2: The reliability should be considered through the whole creation process.

(see section 2.3). The result of the FMEA is a list of failure modes, and related mechanisms, set in order of priority. Depending on the severity the failure modes and mechanisms can be further investigated.

A reliability study can be based on testing of simplified (not fully functional) tests structures representing individual reliability problems. Experiments, usually lifetime tests, performed under various stressing and/or environmental conditions allow isolating and emphasizing each failure mode and mechanism.

2.2 Reliability - definitions

2.2.1 Reliability

"Reliability is the ability of an item to perform a required function under stated conditions for a stated period of time." [293–296] (Figure 2.3).
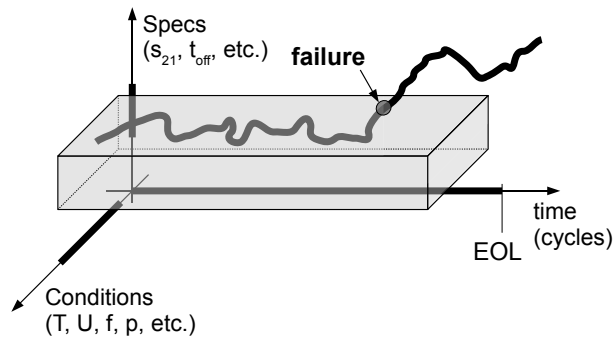
Figure 2.3: A device is reliable if it fulfills the requirements: Stays within the specs, under specified conditions, for a required time.

This definition points out three important elements: A required function, stated conditions and a stated period of time. The particular elements, corresponding to the capacitive RF MEMS switch, are further explained.

2.2.2   Required function, failure and failure mode

The function of a device can be described using several parameters. The definition of the function should specify allowed variations of the parameters.

The function of the capacitive RF MEMS switch is switching between two, on- and off-, states. The RF signal should not be impeded in the on-state and should not pass through in the off-state. The influence of the switch on the signal, in the on-state, is described with insertion loss and should be as low as possible. The ability of separating the ports of the switch, in the off-state, is called isolation and should be as high as possible. Another important parameter characterizing a switch is transition (switching) time between the states (t_{on} - time to switch on, t_{off} - time to switch off). A switch should change states as fast as possible. The range of frequencies can be specified as well.

The properties of the switch are application dependent and should be provided by designers. Exemplary specifications for a capacitive RF MEMS switch are listed below:

- bandwidth: 5 - 15 GHz,

- isolation (in off-state) not lower than $-30dB$,

- insertion loss (in on-state) not higher than $0.1dB$,

- switching time t_{on} and t_{off} not longer than $10\mu s$.

The isolation and insertion loss of the capacitive RF MEMS switch are direct resultants of the capacitance of the switch. Thus, the function of the device can be described by defining capacitance in the on- and off- states. E.g.:

- C_{up} not higher than 100fF,

- C_{down} not lower than 10pF.

A reliable switch should exhibit the specified C_{up} and C_{down} during the whole lifetime. Exceeding of the required specifications is a result of a failure and is defined as the failure mode (Figure 2.4). I.e. the failure mode is an indication of a failure.

Failure is an event, or a state of a device, when the requirements cannot be fulfilled.

2.2.3 Stated conditions, operating and test conditions

The "stated conditions" term refers to the operating conditions: biasing schemes and environmental conditions.

Electrostatically driven capacitive RF MEMS switches can be actuated using several types of biasing schemes ([4], pp. 189-190). The lifetime of a capacitive RF MEMS switch can vary depending on the type of employed actuation voltage. Therefore, the operating biasing scheme (waveform shape, amplitude, frequency etc.) should be specified.

A switch should be able to operate in a range of specified environmental conditions: composition of atmosphere, temperature, pressure, vibrations etc. The operating conditions are defined by the application of the device.

In order to facilitate the reliability study special conditions, called the test conditions, are used. The test conditions can purposely lead to early failures (accelerated testing). The combination of various parameters of biasing and/or different ambient allows emphasizing particular failure mechanisms.

2.2.4 Stated period of time, end-of-life and lifetime

The last part of the reliability definition refers to time. The moment the parameters of a device go out-of-specs is called end-of-life (EOL). The time from the beginning of stressing period to the end-of-life is defined as lifetime Figure 2.4). A device can be considered reliable, if it can perform the required function for a time not shorter than the specified lifetime. In case of switches, the lifetime can be also defined as a minimal number of switching cycles. Depending on the application, one or both requirements can be specified.
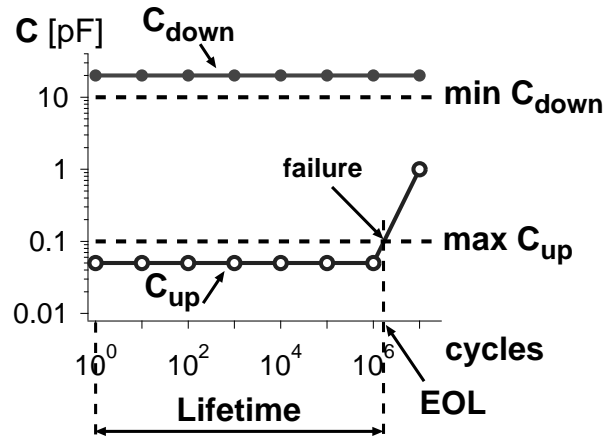
Figure 2.4: Lifetime is time (or number of cycles) from the beginning of an experiment until the end-of-life (EOL). The EOL is a moment, indicated by a failure mode, when a failure occurs.

2.2.5 End-of-life criteria

The "end-of-life criterion" (EOL criterion) term can be used when lifetime test results are discussed/reported. It describes artificial boundaries for device properties used as specs for reliability testing. A tested device which properties exceeded an EOL criterion can be still a functional device from the application specs point of view. Introduction of different EOL criteria can be useful in reliability study of the capacitive RF MEMS switches, e.g. accelerating lifetime experiments.

2.2.6 Failure defect, mechanism and cause

The origin of the failure mode (change in the properties) is the failure defect. For instance, stiction of the beam to the dielectric layer is a failure defect. A physical phenomenon behind the failure defect (e.g. dielectric charging) is called the failure mechanism. The failure cause (e.g. wrong material choice) can be a result of limited knowledge about failure mechanisms.

2.3   FMEA study

2.3.1   The idea

"Failure Mode and Effects Analysis (FMEA) is a procedure by which each potential failure mode in a system is analyzed to determine the results or effects thereof on the system and to classify each potential failure mode according to its severity. (...) The purpose of the FMEA is to study the results or effects of item failure on system operation and to classify each potential failure according to its severity." [297].

The FMEA study starts with creating a list of all possible failures and attributing to each item two numbers: severity (S) and occurrence (O). A more extended FMEA study defines also detectability (D) but it is more useful in case of mass production and it is not used in this work. The Severity (S) parameter describes how harmful the failure can be. Occurrence (O) determines how often the failure can occur.

Both severity and occurrence can be rated e.g. from 1 to 10. S=1 means that the failure mechanism does not cause any damage to the system, while S=10 means that the failure causes immediate end-of-life (Table 2.1). O=1 and O=10 indicate very low and very high chance of occurrence, respectively (Table 2.2). After ranking all the possible failure modes and mechanisms, the priority number PN=S·O should be calculated. The result is the list of failure modes and mechanisms with the most problematic on top [295, 298–300].

2.3.2   FMEA study of the capacitive RF MEMS switch

An FMEA study of the capacitive RF MEMS switch was performed in the frame of the ESA/ESTEC "ENDORFINS" project (contract no. 18613/05/NL/IA). The results are presented in Table 2.3.

The study was based on input of experts in different disciplines: MEMS processing, packaging, reliability, MEMS and RF designers and management. 18 failure modes and mechanisms are identified. Occurrence and Severity numbers are given to each failure mode and mechanism. The modes and mechanisms are listed in order of priority. The one from the top of the list is the dielectric charging.

Table 2.3: Results of the FMEA study on RF MEMS switches: $PN = O * S$, PN - priority number, O - occurence, S - severity.

No.	Potential Failure Mechanism	S	Failure Defect	Failure Mode	O	PN
1	Dielectric charging of the insulator of capacitive switches	8	Stiction to bottom electrode. Non-permanent (charges flow away when charging cause is taken away)	Drift in CV curves, drift in V_{pi} and V_{po}, dead device.	10	**80**
2	Micro-welding (ohmic switches and capacitive switches with contact metal on dielectric	9	Stiction	Dead devices, drift in contact resistance, anomalous switching behavior (temporary stiction)	7	**63**
3	T-induced elastic deformation of the bridge	7	Non-permanent deformation of the bridge (is restored when T-source is removed), possible stiction (to bottom electrode or top of cavity if packaged) if large deformation.	Shift of electrical parameters (V_{pi}, V_{po}, C, R), change of mechanical properties.	7	**49**
4	Plastic deformation of the bridge	7	Permanent deformation of the bridge, possible stiction (to bottom electrode or top of cavity if packaged) if large deformation	Shift of electrical parameters (V_{pi}, V_{po}, C, R), change of mechanical properties.	7	**49**
5	Structural short (electrical and non-electrical connections)	9	Particles, shorted metals, contamination, remains of sacrificial layer, stuck bridge.	Changes in electrical parameters, dead devices.	5	**45**
6	Capilary forces.	10	Stiction.	Dead devices.	4	**40**
7	Fusing	10	Opens, roughness increase.	Dead devices.	4	**40**
8	Fracture	10	Broken bridges and hinges.	Dead devices.	4	**10**
9	Dielectric breakdown of the insulator.	9	Dead device, possible stiction.	Shorts between bridge and actuation electrode.	4	**36**
10	Corrosion	7	Dendrites formation, oxidization, changes in color.	Degradation of electrical and mechanical properties, shorts.	5	**35**
11	Wear, friction, fretting corrosion.	8	Surface modifications, particles (debris), stiction.	Shorts, opens, shift of electrical parameters.	4	**32**
12	Creep	6	Deformation of the bridge in time.	Electrical and mechanical parameters shifts.	5	**30**

13	Equivalent DC voltage.	7	Self biasing, stiction.	Anomalous switching behavior, changes in electrical parameters.	4	**28**
14	Lorenz forces.	7	Self biasing, stiction.	Anomalous switching behavior, changes in electrical parameters.	4	**28**
15	Whisker formation.	7	Bumps in metal, holes in insulator on top of metal layers.	Anomalous down-state capacitance or contact resistance, possible increase of charging sensitivity.	4	**28**
16	Fatigue.	8	Broken bridges and hinges, cracks, micro-cracks, deformation of the bridge.	Electrical and mechanical properties shifts, dead devices.	3	**24**
17	Electromigration.	8	Cracks, opens, thickness changes (mass transpot) in metal lines.	Increase of resistance, opens, shorts.	2	**16**
18	Van der Waals force.	10	Stiction.	Dead devices.	1	**10**

2.4 Charging mechanisms

The failure mechanism at the top of the FMEA result list is the charging of the dielectric. The problem occurs in all devices working in normal conditions. It leads to a fast drift of the device out of specs and eventually to stiction of the device. In most cases the device can recover after removing electrical stress.

The "charging" term is commonly used to describe a series of several physical phenomena that affect quantity and/or distribution of charge in the capacitive switch dielectric layer.

The charging has been intensively studied by several research groups worldwide. The experimental results together with theoretical models have been presented in many publications.

In general, there are two types of models describing impact of the charge on the reliability of the switches. The first group is about the physics of the charging phenomena, i.e. how the charge emerges in the dielectric layer.

The second group tries to explain how location of the charges influences the behavior of the switch. The charge influences the C-V characteristic by V_{pi} and V_{po} modifications.

This section presents an overview of articles describing the first group of models. The models base on interpretation of experimental results obtained by several

groups working on the reliability of the capacitive RF MEMS switches. The papers about the second group of models can be found in the next section (2.5).

2.4.1 Dielectric in electric field

The source of the reliability problems comes from the working principle of the capacitive RF MEMS switch. When the switch is actuated and the beam touches the dielectric layer, the electric field across the dielectric is relatively high. As the thickness of the dielectric layer is usually in the order of hundreds of nm and the actuation voltages in order of tens of volts, the electric field across the dielectric layer can be in the order of $10^6 V/cm$.

When a piece of dielectric is placed in an electric field several effects can take place. First, even if the dielectric is an ideal material, the polarization of the dielectric (small movement of charges causes creation of dipoles) can occur [314, 315]. The dipoles can modify the resultant electrostatic force on the beam. Some of the dipoles can remain after the electric field removal. The polarized dielectric behaves like a voltage source generating an electric field. The electric field can create an electrostatic force causing an unwanted beam displacement.

Besides the polarization, dielectrics can trap charges. The traps in dielectrics (surface or bulk) can appear during processing of the dielectric itself (structure imperfections, impurities, etc.) or can be generated during succeeding processing steps (e.g. dielectric damages during plasma etching) [316, 317]. Charges can be trapped during traveling through the dielectric in the presence of electric field. The charge trapping is considered the dominant factor limiting the lifetime of the switches so far.

The next section present results of charging studies.

2.4.2 Charging model by Goldsmith

The first proposed explanation of a failure mechanism causing stiction of the capacitive RF MEMS switches is presented by Goldsmith et al. in [3]. The authors attribute the charge trapping to the Poole-Frenkel conduction mechanism. A mathematical model and its agreement with experimental data are presented.

The model assumes Poole-Frenkel conduction in the dielectric layer under high electric field conditions. Carriers can be injected into the dielectric and trapped. Depending on the thickness of the dielectric layer and the trap density, the carriers can escape from the dielectric by direct or indirect (hopping between traps) tunneling. The de-trapping time can last seconds or even days. Based on the equation describing the Poole-Frenkel mechanism (2.1) a lifetime vs. actuation

voltage model is proposed: Lifetime is exponentially related to the amplitude of the actuation voltage:

$$J \approx V e^{+2a\sqrt{V}/T - q\Phi_B/kT} \tag{2.1}$$

where:
J - current density,
V - applied voltage,
T - temperature in Kelvin,
Φ_B - the barrier height,
k - Boltzman's constant,
a - constant containing electron charge, dielectric permittivity and film thickness.

Thanks to that model accelerated reliability testing can be performed. First, the lifetime of the devices at higher actuation voltages has to be tested and then lifetime at operating actuation voltage can be extrapolated (Figure 2.5).
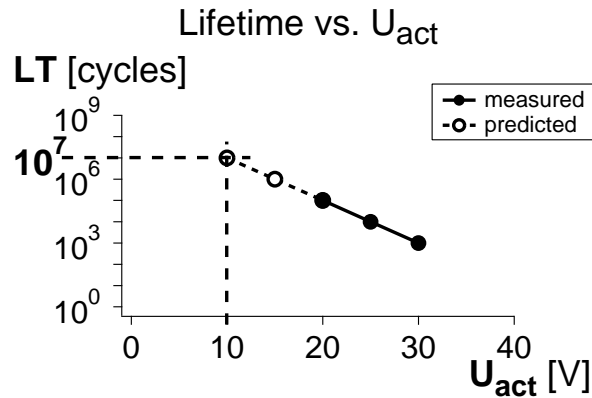
Figure 2.5: Accelerated lifetime testing of the capacitive RF MEMS is possible: first, the lifetime at higher actuation voltages has to be tested and then lifetime at lower U_{act} (e.g. operating conditions) can be extrapolated.

2.4.3 Charging model by van Spengen

A model to predict charging in the capacitive RF MEMS switches is presented by van Spengen et al. in [318]. The authors assume the Poole-Frenkel charging mechanism as the cause of the failure. First, the influence of a charge sheet on the pull-in voltage is deliberated (theoretical model). Then the influence of the amplitude of the actuation voltage on the lifetime is described. As charge

de-trapping can occur when no actuation voltage is applied, the influence of the actuation waveform duty cycles is taken into account. It is also shown that the lifetime of the switches does not depend on the frequency of the actuation waveform but on the total down time. The experimental data are compared with a model that allows predicting lifetime of the capacitive RF MEMS switches. The article confirms observations published by other research groups.

2.4.4 Charging model by Melle

The next article deliberating the physics of the charge trapping phenomena in the capacitive RF MEMS switches is presented by Melle et al. [319, 320]. It is shown that the lifetime of the capacitive RF MEMS switches is limited due to charging governed by the Poole-Frenkel conduction mechanism.

The authors introduce the SRAV (shift rate of the actuation voltages) parameter that describes change of the pull-in voltage in time as a function of actuation voltage.

However, the electric field across the dielectric can be modified by finite roughness of the dielectric and beam. As the contact quality influences the down-state capacitance as well, the C_{thon}/C_{on} (theoretical to measured down-state capacitance) ratio is used to calculate the effective electrical stress intensity.

The experimental data are further compared with theoretical models describing the Poole-Frenkel, Schottky and ohmic conduction mechanisms. The best agreement with the Poole-Frenkel mechanism is observed. This confirms that this type of conduction dominates the charge trapping in the investigated dielectrics.

Finally, it is shown that the presented model can be used in predicting lifetime of capacitive RF MEMS switches.

2.4.5 Charging model by Papaioannou

Most of the charging models assume the Poole-Frenkel conduction mechanism dominating the charge trapping in capacitive RF MEMS switches. A different approach is presented by Papaioannou et al. in [321–325]. The authors propose dipolar polarization of dielectric as an important dielectric charging mechanism influencing the lifetime of the capacitive RF MEMS switches.

It is shown that there is more than one charging mechanism present: free charge distribution, charge injection, dipole orientation, interfacial polarization etc. The dipolar polarization can be dominant in specific conditions.

Due to high asymmetry of the structure (different top and bottom metal-dielectric interfaces) some of the charging mechanisms depend on the polarity of the actuation voltage. Since the dipolar polarization is a dielectric intrinsic property, it is independent of the actuation voltage polarity.

Performing the experiments at different temperatures allows determining an activation energy of the mechanism. The observed activation energy was indeed the actuation voltage polarity independent. The dipolar polarization is dominant at higher temperatures.

The dipolar polarization is expected to be not influenced by the contact quality. However, the changes in the C-V characteristic (due to dielectric charging) are also observed if the actuation voltage applied is below the pull-in voltage. The observed C-V characteristic changes led to the conclusion that the dominant mechanism was the dipolar polarization.

Together with the experimental results theoretical models are introduced.

2.4.6 Charging model by Mardivirin

Another charging model, allowing lifetime prediction, is presented by Mardivirin et al. [326, 327]. The authors use the Curie-Von Schweidler "universal" law for dielectric relaxation to describe evolution of charge trapped in the switch. Observations of the trapped charge are based on the pull-down voltage (V_{pi}) measurements. The measurements are performed using a dielectric less structure. The only dielectric that can charge is the non-conductive substrate that is exposed to a relatively high electric field.

The proposed model takes the duty cycle of the actuation waveform into account as the duty cycle has a big influence on the changes of the pull-in voltage during stressing.

The presented experimental results show a good agreement of the model with the obtained results. The lifetime of structures tested with higher values of duty cycle is lower than when a low duty cycle actuation waveform is used. The model allows predicting lifetime at any duty cycle by testing a switch with DC actuation voltage (accelerated stressing) and recalculating it to required duty cycle waveform.

2.4.7 Charging model by Yuan

Results of a detailed study of the charge trapping mechanism in capacitive RF MEMS switches are presented by Yuan et al. in [328]. The authors use MIM (metal-insulator-metal) structures transient current measurements to obtain the properties of the used dielectric (SiO_2). Based on the results, theoretical models

of change of the pull-in voltage in time during stressing with unipolar actuation voltages are proposed. Good agreement of the presented models with experimental results is presented.

A similar technique is used to study temperature dependency of charging in the switches [329, 330]. MIM capacitors transient current at different temperatures are measured and properties of dielectrics are extracted. The obtained results are used to model the change of the pull-in voltage of MEMS structures.

2.4.8   Charging model by Peng

Peng et al. in [331] deliberate about differences between charge trapping through the top and bottom interfaces. The top (beam-dielectric) contact is different than the bottom (bottom metal-dielectric). The charging through the contact can occur at both positive and negative actuation voltages. However, the threshold voltages and the influence of the trapped charge on the pull-in voltage are different.

In [332] and [333], the authors show that positive and negative stressing cause similar dielectric charging (neglecting the sign). The bipolar actuation waveform should allow obtaining an infinite lifetime. Changes of the pull-in voltage caused by charge trapping during the positive part of the bipolar actuation waveform can be compensated during the negative part. Only small changes in positive and negative charge trapping make it difficult to find the correct balance. One of the mechanisms causes charge build-up and after some time the amount of trapped charge can cross the critical value and cause stiction. Empirical models are introduced. A good agreement of the models with experimental data is showed.

2.4.9   Charging model by Herfst

In [334], Herfst et al. show a square-root dependency of the pull-in voltage change in time. The authors compare experimental results with several models proposed by other researchers. The proposed, empirical, $\sqrt{t}$ model (t - time) fits the obtained results better than the other models.

A similar model is used to describe changes of MIM structures using the same type of dielectric (SiN). The authors conclude that the same phenomenon can be the cause of the lifetime limits of the presented switches.

2.4.10   Influence of environment

The influence of humidity on the reliability of electrostatic actuators is presented by Cabuz et al. in [335]. The authors observe degradation in electrostatic force when

the actuator is stressed in humid atmosphere. The force degradation is attributed to humidity enhanced surface charge trapping of the thin dielectric deposited on the electrodes. To avoid this effect a self assembled monolayer (SAM) coating is used making the surface of the dielectric hydrophobic. The SAM coated actuator shows a reliable long operation even in a high humidity atmosphere.

The influence of the environment on the reliability of the capacitive RF MEMS switches is shown by van Spengen in [336]. It is pointed out that packaging of the MEMS structures is needed not only to protect the devices against mechanical damages after processing.

Results of more detailed studies on the influence of the environment, mainly humidity, on the reliability of the capacitive RF MEMS switches can also be found in the literature. Authors show differences in the switches behavior dependent on the type of atmosphere: dry or humid air. Olszewski et al. show that narrowing or shift of the C-V characteristic in dry and humid air is observed, respectively [337]. Blondy et al. report humidity dependent increase or decrease of the pull-in voltage [338].

The observed changes are attributed to different charging mechanisms occurring under different environmental conditions.

2.4.11 Summary

According to the presented studies, the mechanism governing the change of the pull-in and pull-out voltages is mainly the Poole-Frenkel conduction. However, many models are empirical, not giving details on the physics of the charging mechanisms.

The presented models allow predicting lifetime of capacitive RF MEMS switches based on results of accelerated testing (higher actuation voltage, DC stressing etc.). However, other possible mechanisms are also involved: dipolar polarization and surface charging.

Influence of the environment (mainly humidity) is pointed out. The need for testing in a controlled environment to avoid unwanted influence of the environment is highlighted.

2.5 Effects of charging

This section presents effects of a charged (or polarized) dielectric on the reliability of the capacitive RF MEMS switches. Several models describing the influence of the charge on the C-V characteristic are shown.

2.5.1 The C-V characteristic as a charging gauge

Once the charge is trapped in the dielectric it can modify the electric field, and thus the electrostatic force. That results in changes of all the electrical parameters of the capacitive RF MEMS switch: V_{pi}^+, V_{pi}^-, V_{po}^+, V_{po}^-, C_{up} and C_{down}. The changes are directly reflected in the changes of the C-V curve shape.

In principle, the origin of the C-V characteristic modifications are the changes of the pull-in and pull-out voltages. However, observation of the C-V curve shape is a straightforward way of probing the charge in the switch. The changes of the state of the switch can be easily monitored before, during and after stressing with the C-V characteristic measurements. Besides the parameters of the switch, the C-V characteristic can be characterized with two more parameters: the position (voltage) of the center of the C-V characteristic (V_c) and the size of the pull-in window (width) of the C-V curve (W_{pi}) (Figure 2.6).
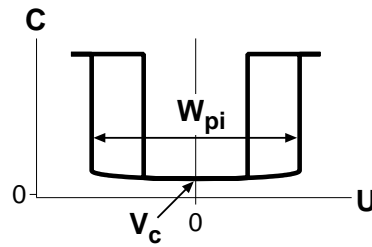
Figure 2.6: Definition of the V_c and W_{pi}.

The V_c is the voltage at which the minimal capacitance of the switch is obtained. Changes of the V_c are called the shift of the C-V characteristic (V_s). Changes of the W_{pi} are called the narrowing of the C-V characteristic (ΔW_{pi}) as mainly a decrease of the pull-in window size during stressing is observed. Similar parameters corresponding to the pull-out parameters can be defined.

Inspecting evolution of both, V_c and W_{pi} (V_s and ΔW_{pi}) can give valuable insights into charging by providing information about changes of the pull-in voltages as well as their mutual relations.

Often, the influence of the trapped charge on the shift and/or narrowing of the C-V characteristic is presented when results of reliability study are discussed.

2.5.2 Schematic representation of the C-V curve

In order to improve the readability of the graphs, a schematic representation of the C-V characteristic is introduced. Comparison of both, the theoretical and
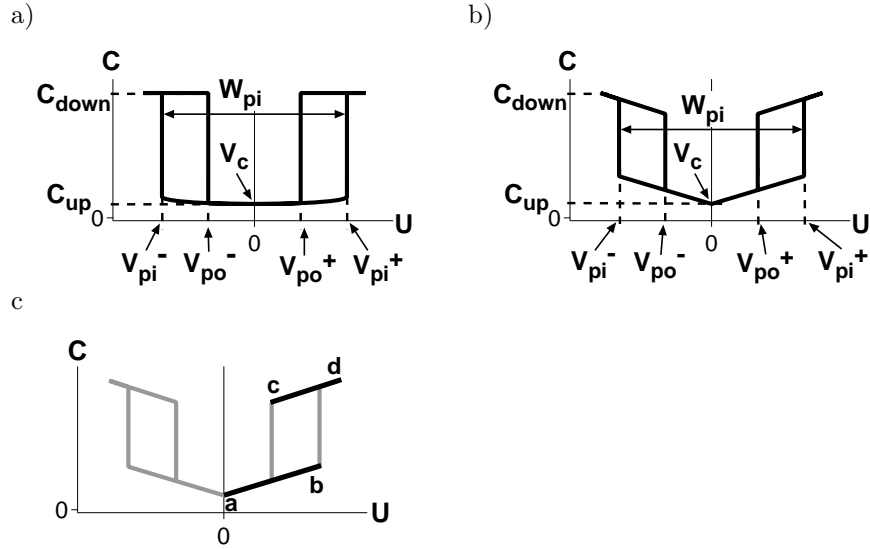
Figure 2.7: Theoretical C-V curve a) and schematic representation of the C-V curve b): the simplified curve contains all the important information about the actual C-V characteristic. The schematic C-V curve is further modified to emphasize effects observed in the measured C-V characteristic of the real devices c).

schematic C-V curves, is presented in Figure 2.7a and b.

The simplified curve contains all the points that can be determined from a real C-V characteristic: V_{pi}^+, V_{pi}^-, V_{po}^+, V_{po}^-, C_{up} and C_{down}. The V_c and W_{pi} are visible too. The simplified C-V characteristic is used to explain the influence of charging on the C-V characteristic. Results of simulations (analytical and FEM) that are performed for better understanding the physics of failure are presented using the schematic C-V curve as well.

The schematic C-V curve is further modified. The a-b section of the curve (Figure 2.7c) represents the non-linear, yet stable, operation in the up state (see 1.2.3). The non-linear part of the curve is replaced with a line to emphasize the position of the V_c.

The c-d part of the curve corresponds to the observed shape of the measured C-V characteristic of real devices. The increase of the capacitance in the down state is due to a non-ideal contact of the beam and the interposer dielectric. This is explained more in details in section (7.1).

2.5.3 C-V shift

The voltage shift of the C-V characteristic was first observed and described by Wibbeler et al. in [301].

Let the symbols F_{el}, V_{pi}^+, V_{pi}^-, V_c and W_{pi} be decorated with a prime in the charge-trapped cases. Not decorated symbols refer to the no-charge trapped cases. E.g. $V_{pi}^{+\prime}$ is used to describe the positive pull-in voltage of a structure with charge trapped and V_{pi}^- symbols is used to describe the negative pull-in voltage of a non-charged structure.

A case with the actuation voltage applied to the bottom electrode and grounded beam is considered (Figure 2.8).

The trapped charge creates a field component (E_{ch}) that can be added to or subtracted from the electric field generated by the actuation voltage (E_{act}). The positive polarity of the charge is considered. Depending on the polarity of the actuation voltage, the resultant electrostatic force (F_{el}') is lower (Figure 2.9a) or higher (Figure 2.9b) than the initial (F_{el}). I.e. to obtain the same magnitude of the electrostatic force at different polarities, different amplitudes of the actuation voltage have to be applied. Thus, the pull-in voltages change.
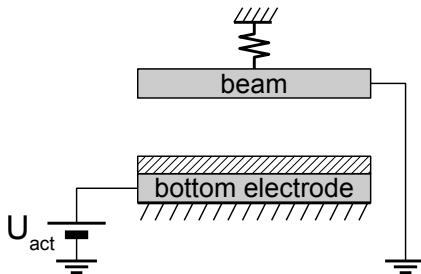
Figure 2.8: The effect of the charge on the C-V characteristic modifications depends on the biasing scheme. The case of the actuation voltage applied to the bottom electrode and grounded beam is considered.

The uniformly distributed charge acts like an additional DC voltage source connected in series with the actuation voltage source (Figure 2.10). The amplitude of the negative pull-in voltage is decreased and the amplitude of the positive pull-in voltage is increased (Figure 2.11a). The changes of the pull-in voltages are equal (2.2).

$$\Delta V_{pi}^+ = \Delta V_{pi}^- = \Delta V_{pi} \qquad (2.2)$$

a)

$U_{act} < 0$

E_{act} F_{el} E_{act} E_{ch} $F_{el}^{'}$

$Q = 0$ $Q = q^{\oplus}$

F_{el} $>$ F_{el}'

$|\,V_{pi}^{-}\,|$ $<$ $|\,V_{pi}^{-}\,|^{'}$

b)

$U_{act} > 0$

E_{act} F_{el} E_{act} E_{ch} $F_{el}^{'}$

$Q = 0$ $Q = q^{\oplus}$

F_{el} $<$ F_{el}'

$|\,V_{pi}^{+}\,|$ $>$ $|\,V_{pi}^{+}\,|^{'}$
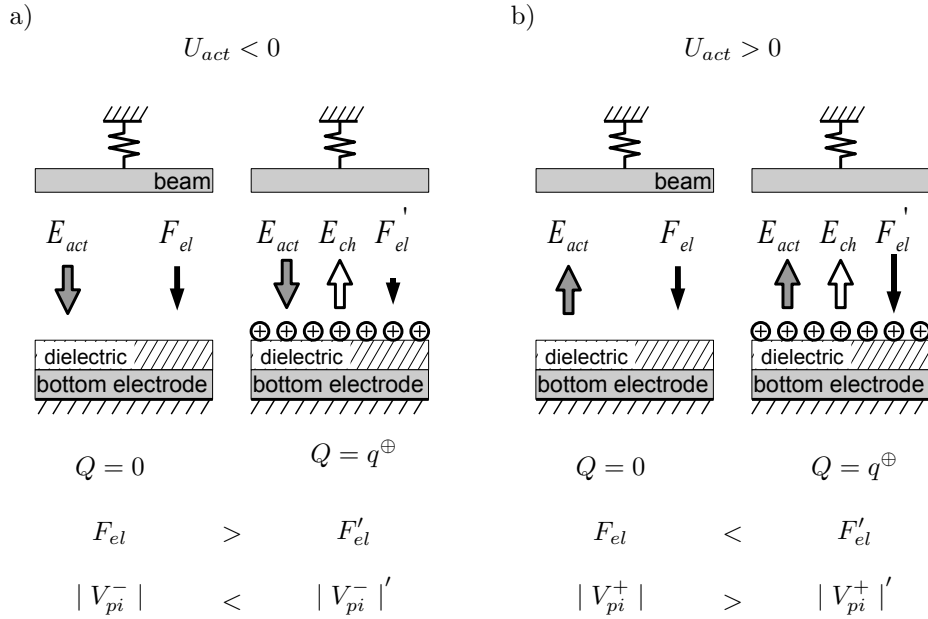
Figure 2.9: Negative actuation voltage applied to the bottom electrode, the beam grounded (a): the field created by the charge (E_{ch}) is subtracted from the electric field generated by the actuation voltage (E_{act}). The total electrostatic force (F_{el}') is lower than if no charge is trapped (F_{el}). Positive actuation voltage applied to the bottom electrode, the beam grounded (b): the field created by the charge (E_{ch}) is added to the electric field generated by the actuation voltage (E_{act}). The total electrostatic force (F_{el}') is higher than if no charge is trapped (F_{el}). The magnitude of the V_{pi}^{-} increases and the V_{pi}^{+} decreases.
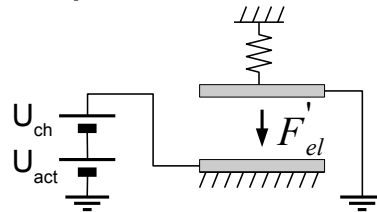
Figure 2.10: The trapped charge acts like a voltage source (U_{ch}) connected in series with the actuation voltage source (U_{act}).
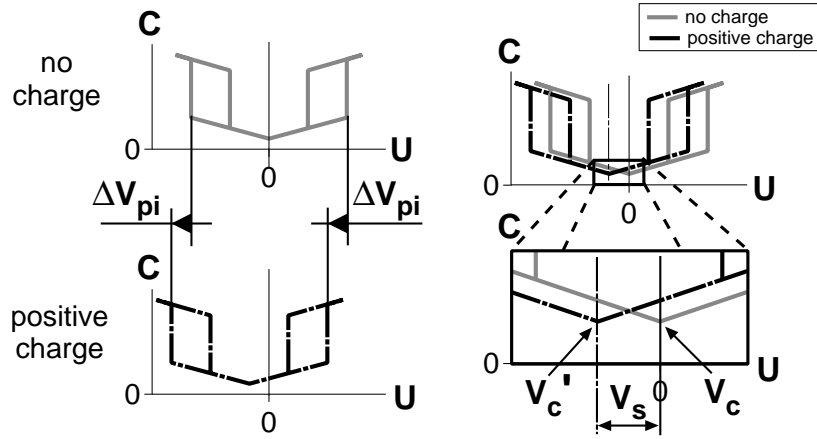
Figure 2.11: The positive and negative pull-in voltages are modified of the same value ΔV_{pi}^+ and ΔV_{pi}^-, respectively. As a result the whole C-V characteristic is shifted along the voltage axis of the V_s.

As the pull-out voltages are modified in a similar manner, the whole C-V curve is shifted along the voltage axis (Figure 2.11b).

The position of the V_c can be found from the C-V characteristic (2.3),

$$V_c = \frac{V_{pi}^+ + V_{pi}^-}{2} \tag{2.3}$$

and the change of the center voltage - the shift V_s - can be calculated using results of two C-V measurements (2.4 - 2.7).

$$V_c = \frac{V_{pi}^+ + V_{pi}^-}{2} \quad (2.4) \qquad V_c' = \frac{\left(V_{pi}^+ + \Delta V_{pi}\right) + \left(V_{pi}^- + \Delta V_{pi}\right)}{2} \quad (2.5)$$

$$V_s = V_c' - V_c \quad (2.6) \qquad\qquad V_s = \Delta V_{pi} \quad (2.7)$$

The pull-in window (W_{pi}) of the characteristic of the switch does not change as both of the pull-in voltages are modified with the same magnitude (2.8 - 2.11).

$$W_{pi} = V_{pi}^+ - V_{pi}^- \quad (2.8) \qquad W_{pi}' = \left(V_{pi}^+ + \Delta V_{pi}\right) - \left(V_{pi}^- + \Delta V_{pi}\right) \quad (2.9)$$

$$\Delta W_{pi} = W_{pi}' - W_{pi} \quad (2.10) \qquad\qquad \Delta W_{pi} = 0 \quad (2.11)$$

The V_s can be used to quantify the trapped charge. Models to calculate the

charge are proposed by Bochobza-Degani et al. [304], Rottenberg et al. [305], van Spengen et al. [318].

The charge can be trapped in the whole volume of the dielectric: in the bulk and on the surface. However, all the trapped charge can be represented with an equivalent surface charge ($Q_{trapped}$) that can be calculated using (2.12) [305].

$$Q_{trapped} = V_s \varepsilon_0 \varepsilon_r \frac{A}{d} \qquad (2.12)$$

An alternative method of the V_s measurement has been presented by Herfst et al. in [307]. Sweeping the actuation voltage below the V_{pi} allows locating the minimum capacitance of the switch. Since the minimal capacitance corresponds to the minimal electrostatic force, the voltage required to obtain the minimal capacitance is equal to the V_s. The advantage of the method is the use of relatively low actuation voltage and lack of the beam-dielectric contact during measurements. The trapped charge is modified less than in case of the full C-V characteristic measurement.

A similar technique for noncontact charge measurements has been presented by Reid et al. [308].

2.5.4 C-V narrowing

In the previous section, uniform charge distribution was assumed. In this case no change of the width of the C-V characteristic is expected ($\Delta W_{pi} = 0$).

However, an often experimentally observed effect of the trapped charge on the C-V characteristic is a change of the pull-in window W_{pi}. The effect is often called the C-V narrowing as mainly a decrease in the pull-in window size during stressing is observed. The narrowing of the C-V characteristic in presence of distributed charge is described by Rottenberg et al. in [305], [309].

First, the case with both (positive and negative) types of charges trapped in the dielectric is considered (Figure 2.12). The dielectric is divided in two equal parts: A (left) and B (right). Negative charge is placed in the part A ($Q^A = q^\ominus$) and positive charge is placed in the part B ($Q^B = q^\oplus$). The quantities are equal ($|Q^A| = |Q^B|$), i.e. the net charge Q is zero. The total electrostatic force F_{el} is a sum of the electrostatic force generated by the A (F_{el}^A) and B (F_{el}^B) parts of the switch (2.13, Figure 2.13).

$$F_{el} = F_{el}^A + F_{el}^B \qquad (2.13)$$

a)

$U_{act} < 0$

E_{act} E_{ch} $F_{el}^{A'}$ E_{act} E_{ch} $F_{el}^{B'}$

beam

dielectric

bottom electrode

$Q^A = q^\ominus$ $\qquad$ $Q^B = q^\oplus$

$F_{el}^{A'} > F_{el}^A$ $\qquad$ $F_{el}^{B'} = 0$

$F_{el}' > F_{el}$

$|V_{pi}^{-'}| < |V_{pi}^-|$

b)

$U_{act} > 0$

E_{act} E_{ch} $F_{el}^{A'}$ E_{act} E_{ch} $F_{el}^{B'}$

beam

dielectric

bottom electrode

$Q^A = q^\ominus$ $\qquad$ $Q^B = q^\oplus$

$F_{el}^{A'} = 0$ $\qquad$ $F_{el}^{B'} > F_{el}^B$

$F_{el}' > F_{el}$

$|V_{pi}^{+'}| < |V_{pi}^+|$
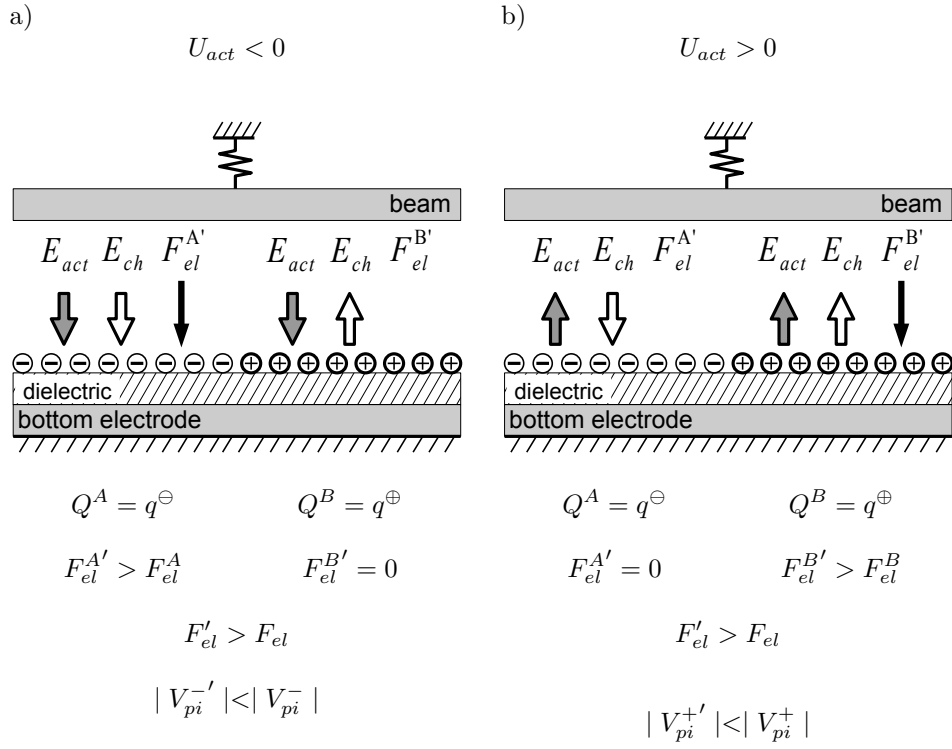
Figure 2.12: Influence of the trapped both types of charges on the V_{pi}^+ and V_{pi}^-.

$F_{el}^{A'}$ $\qquad$ $F_{el}^{B'}$ $\qquad$ F_{el}'

U_{ch}^- $\qquad$ U_{ch}^+

U_{act}
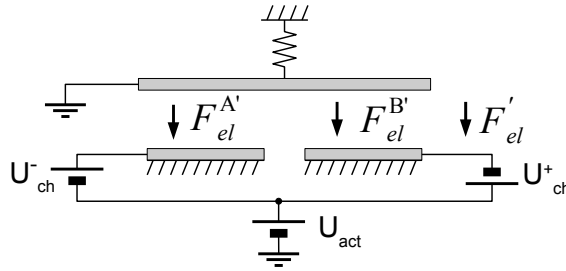
Figure 2.13: The resultant electrostatic force F_{el}' is a sum of two components. Both are influenced by the trapped charge.

If a negative actuation voltage is applied, then the negative charge increases the electrostatic force component, and the positive one decreases it. Due to the quadratic character of the electrostatic force, the increase of the force in one part is not compensated by the decrease in the other part. The magnitude of the electrostatic force depends on the mutual polarization of the electric field components generated by actuation voltage and the trapped charge. The E_{act} and E_{ch} vectors of opposite senses cause lower change of the resultant force than in case of vectors of the same sense (Figure 2.14). The total electrostatic force is higher than if no charge is trapped. The same situation is when a positive actuation voltage is applied. The electrostatic force increases when both, positive and negative actuation voltage are applied. Thus, the magnitude of both pull-in voltages (V_{pi}^{+} and V_{pi}^{-}) is lowered. The pull-in voltages are modified of the ΔV_{pi}^{+} and ΔV_{pi}^{-} components that are the same amplitude and opposite signs.

a)   b)
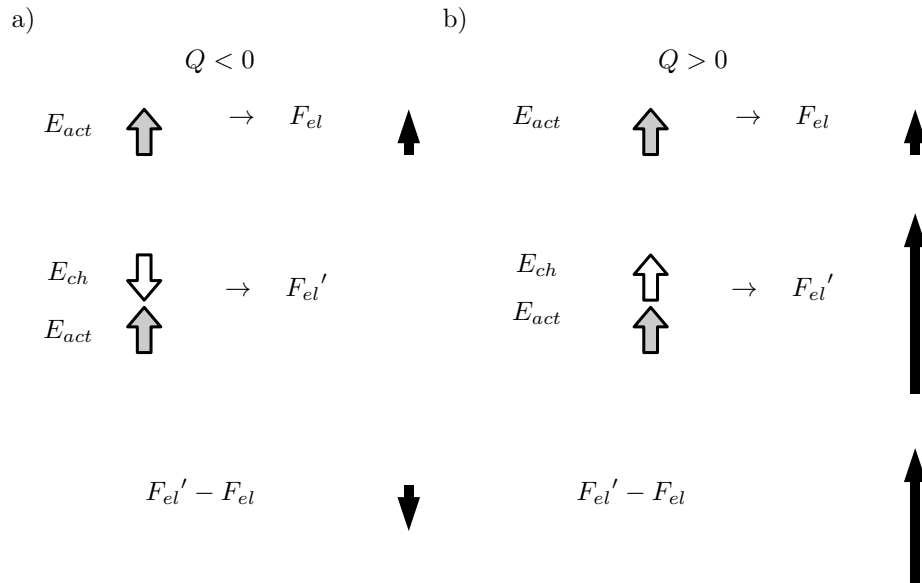
Figure 2.14: The electrostatic force magnitude depends on the mutual polarities of the actuation voltage and the trapped charge. If the E_{act} and E_{ch} vectors are of opposite sense, then the decrease of the resultant electrostatic force a) is lower than the increase of the force in case of the same sense vectors b).

That results in the C-V characteristic shape presented in Figure 2.15. The shift of the C-V characteristic is zero and the size of the pull-in window W_{pi} decreases (2.14-2.16).
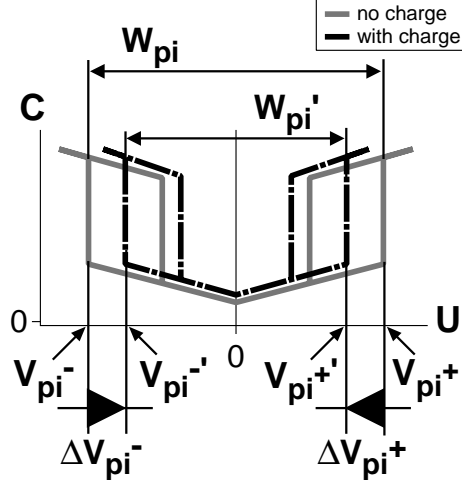
Figure 2.15: The change of the pull-in voltage results in change of the C-V shape with respect to the reference.

$$Q^A = -Q^B \tag{2.14}$$

$$\mid \Delta V_{pi}^- \mid = \mid \Delta V_{pi}^+ \mid = \Delta V_{pi} \tag{2.15}$$

$$V_s = V_c{'} - V_c \quad \rightarrow \quad V_s = 0 \tag{2.16}$$

$$\Delta W_{pi} = W_{pi}{'} - W_{pi} \quad \rightarrow \quad \Delta W_{pi} = -2 \cdot \Delta V_{pi} \tag{2.17}$$

2.5.5 Shift+narrowing

Both of the effects, the shift and narrowing of the C-V characteristic, can be observed at the same time when one type of charge is trapped in the dielectric and is non-uniformly distributed over the surface. The effect is described by Rottenberg et al. in [305]. Non-uniform charge distribution can be represented as charge trapped in only one part of the dielectric (Figure 2.16). In that case the resultant electrostatic force F_{el} is a sum of two components: F_{el}^A charge independent and F_{el}^B influenced by the trapped charge.

Depending on the polarity of the actuation voltage and the type of charge, the $F_{el}^{B'}$ is increased or decreased. Therefore, the resultant electrostatic force is modified.

The magnitude of the modifications depends on the mutual vector senses of the electric field components in the charged part of the actuator (E_{act}^+ and E_{ch}^+). E.g. the positive charge trapped causes a higher increase of the F_{el} when a positive

a) $U_{act} < 0$

E_{act} F_A E_{act} $E_{ch}^{\oplus}$ $F_B^{\oplus}$

beam

dielectric
bottom electrode

$Q^A = 0$ $\qquad$ $Q^B = q^{\oplus}$

$F_{el}^{A'} = F_{el}^A$ $\qquad$ $F_{el}^{B'} = 0$

$F_{el}' < F_{el}$

$\mid V_{pi}^{-'} \mid < \mid V_{pi}^{-} \mid$

b) $U_{act} > 0$

E_{act} F_A E_{act} $E_{ch}^{\oplus}$ $F_B^{\oplus}$

beam

dielectric
bottom electrode

$Q^A = 0$ $\qquad$ $Q^B = q^{\oplus}$

$F_{el}^{A'} = F_{el}^A$ $\qquad$ $F_{el}^{B'} > F_{el}^B$

$F_{el}' > F_{el}$

$\mid V_{pi}^{+'} \mid < \mid V_{pi}^{+} \mid$

$$\mid \Delta V_{pi}^{-} \mid \neq \mid \Delta V_{pi}^{+} \mid$$
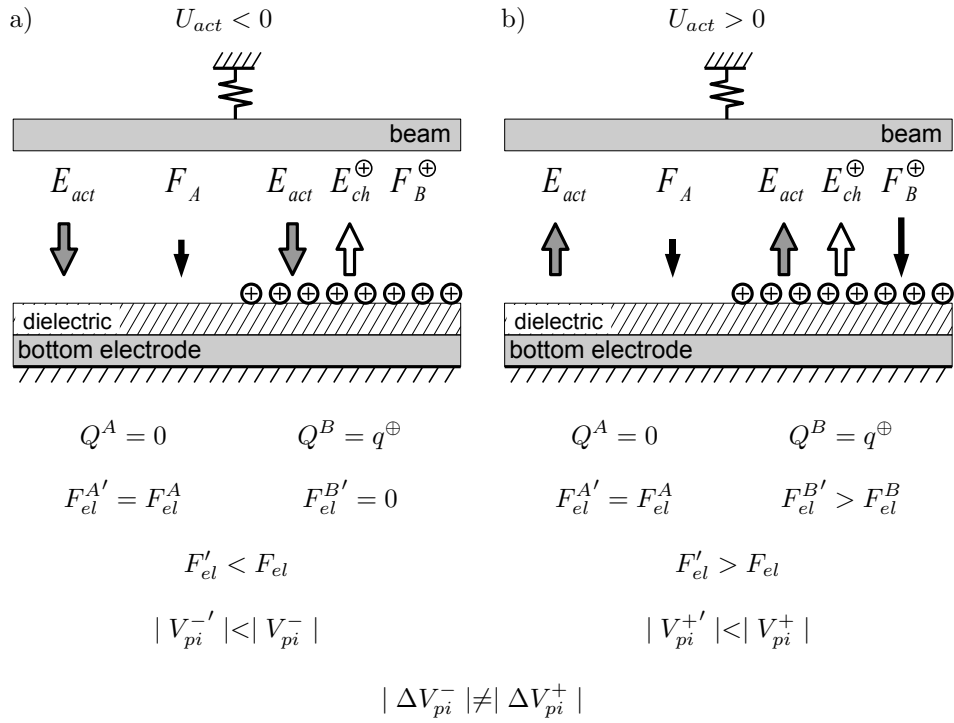
Figure 2.16: Non-uniform charge distribution causes different changes of the positive and negative pull-in voltages.

$\downarrow F_{el}^{A}{}'$ $\qquad$ $\downarrow F_{el}^{B}{}'$ $\downarrow F_{el}{}'$

U_{ch}^{+}

U_{act}
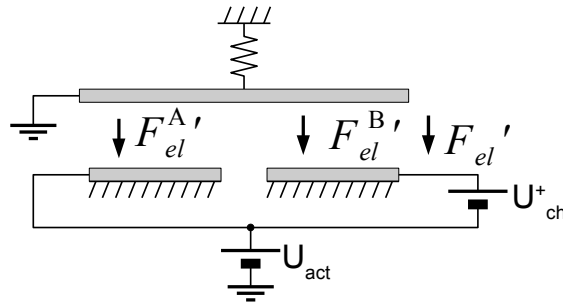
Figure 2.17: The total electrostatic force F_{el}' is a sum of two components: the charge trapped modified $F_{el}^{B'}$ and charge independent F_{el}^A.
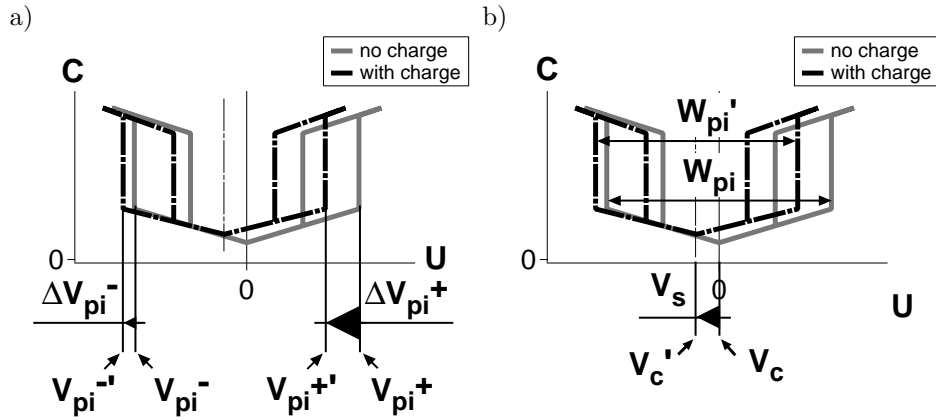
Figure 2.18: The positive and negative pull-in voltages are modified of ΔV_{pi}^+ and ΔV_{pi}^- that are not equal a) resulting in shift and narrowing of the C-V curve b).

actuation voltage is applied than a decrease of the force when a negative actuation voltage is applied. The changes of the electrostatic force cause different changes of the positive and negative pull-in voltages (Figure 2.18a).

The ΔV_{pi}^+ and ΔV_{pi}^- are not equal. They have the same sign though. The different changes of the pull-in voltages result in a shift and a modification of the pull-in window size of the C-V characteristic (Figure 2.18b). The V_s and ΔW_{pi} can be found from two C-V measurements, before and after charging.

2.5.6 Changes of the C_{up} and C_{down}

Two effects often accompanying the changes of the actuation parameters of the switch are changes of the C_{up} and C_{down}.

Changes of the C_{up}

The C_{up} capacitance is the capacitance of the switch without any actuation voltage applied. In a non-charged switch, the up-state capacitance is equal to the minimal capacitance that the switch can exhibit. However, the C_{up} can change due to charging.

The charge trapped in the dielectric creates an electrostatic force component F_{ch}. The force causes deflection of the beam from the original up position even if no actuation voltage is applied. That results in an increase of the C_{up}. The magnitude

of the C_{up} increase depends on the quantity of the trapped charge (Figure 2.19 and 2.20).

Once the critical value is reached (Q_{cr}) [304], the electrostatic force generated by the charge is high enough to keep the beam in the bottom position causing stiction of the beam to the dielectric [313]. This situation is reflected in C-V characteristic as presented in Figure 2.21. The pull-out voltage (positive or negative) reaches or crosses the zero voltage point.

Changes of the C_{down}

The C_{down} is defined as the capacitance exhibited by the switch when an actuation voltage of a magnitude higher than the V_{pi} is applied. The charge trapped in the dielectric can cause an increase of the pull-in voltage in a way that the V_{pi} is higher than the applied actuation voltage. In this case the beam is not pulled-in and the switch exhibits a capacitance lower than expected (Figure 2.22).

2.6   Charging-related failure modes

The failure mode is a measurable symptom of a failure. It is observed as a change of device's parameters and/or its characteristics. Usually, the capacitance of the switch is measured during stressing (testing). The C_{up} and C_{down} are determined and separately plotted as functions of switching cycles or time (Figure 2.23).

There are three main failure modes caused by charging of the dielectric in the capacitive RF MEMS switches:

- change of the C_{up},

- change of the C_{down},

- change of the t_{on} and/or t_{off}.

Changes of the C_{up}

The C_{up} is changed when the beam does not return to its initial position after the actuation voltage removal. A raise of the C_{up} is directly converted into decrease of the isolation of the switch in the off-state. Higher C_{up} indicates an additional electrostatic force component caused by charge trapping in the dielectric. Hence, it indicates that the critical amount of charge is trapped in the dielectric. Measurements of the up-state capacitance during switching are a non-invasive,

Table 2.1: Description of the ranking of the severity parameter of the FMEA analysis.

Ranking	Effect	Severity of effect
10	Catastrophic without warning	Produces an immediate and catastrophic death of the device
9	Catastrophic with warning	Fast drift out of specs, catastrophic death of the device
8	Very high	Slow drift out of specs, catastrophic death of the device. Fast drift out of specs, remediable after long time.
7	High	Slow drift out of specs, catastrophic. Fast drift out od specs, immediately remediable.
6	Moderate	Slow drift out of specs, remediable.
5	Low	Fast drift, remains in specs.
4	Very low	Slow drift, remains in specs.
3	Minor	The device has minor characteristics and behavior shifts. The device remains in specs.
2	Very minor	External appearance of the device changes (color for instance) but no changes in functionality.
1	None	No discernible effect.
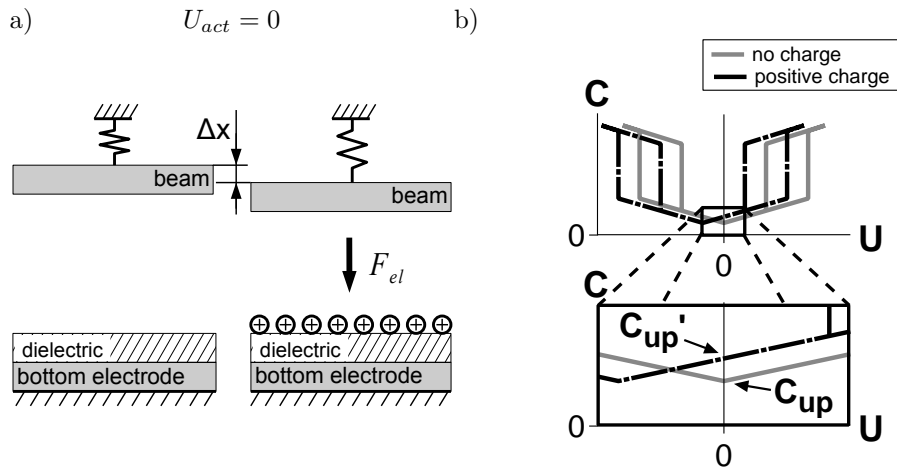
Figure 2.19: The trapped charge generates electrostatic force attracting the beam towards the bottom electrode with no actuation voltage applied a). The deflection Δx is directly observed as an increase of the C_{up} b).

Table 2.2: Description of the ranking of the occurrence parameter of the FMEA analysis.

Ranking	Probability	Likely Failure Rates
10	Very high: persistent failures	Occurs in all devices in normal use.
9	Very high: persistent failures	Occurs in all devices in special conditions.
8	High: frequent failures	Only in special devices in normal use.
7	High: frequent failures	Only in special devices, or package induced, occurs in special conditions.
6	Moderate: occasional failures	Proven failure mode.
5	Moderate: occasional failures	Proven failure mode: occurs in special conditions.
4	Moderate: occasional failures	Proven failure mode: occurs in special rare conditions.
3	Low: relatively few failures	Not proven failure mode.
2	Low: relatively few failures	Not proven failure mode, occurs in special conditions.
1	Remote: failure is unlikely	Less than/equal to 0.01 per thousand pieces.
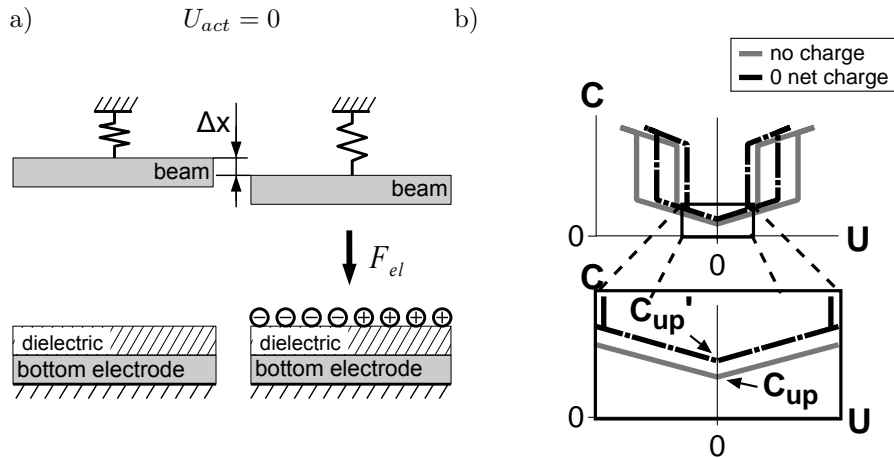
Figure 2.20: Trapping of both types of charges can cause increase of the C_{up} as well.

$$Q_{cr} \geq V_{po}\varepsilon_0\varepsilon_r\frac{A}{d} \qquad (2.18)$$
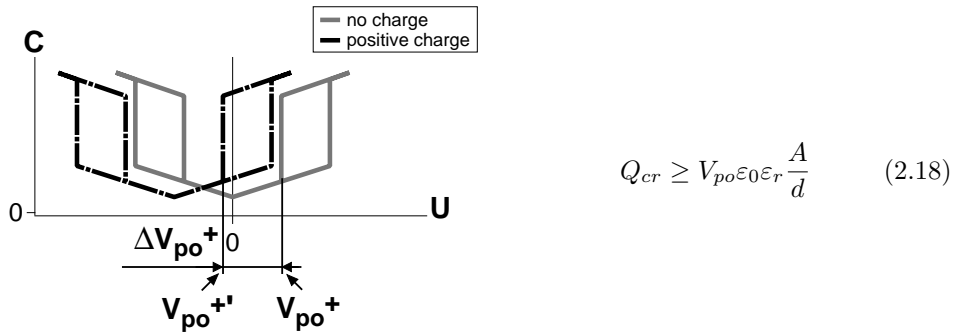
Figure 2.21: If more than the critical amount of charge is trapped in the dielectric, one of the pull-out voltages crosses the 0V point. The beam stays in the bottom position (high capacitance) after the actuation voltage removal.
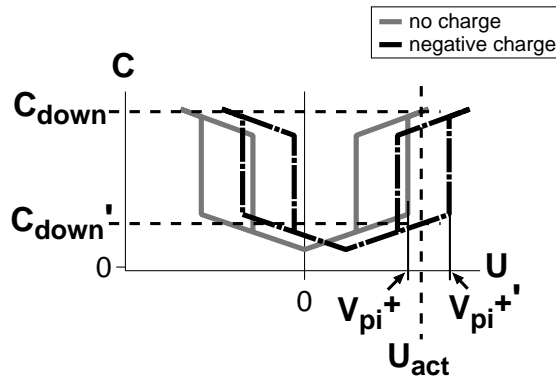
Figure 2.22: Decrease of the C_{down} due to the C-V shift.

natural way of monitoring the state of the switch (Figure 2.23a). However, the change of the C_{up} capacitance can be caused by different failure mechanisms. Therefore, it is not always possible to draw conclusions about the cause and mechanism of this failure mode.

Changes of the C_{down}

The C_{down} changes when the beam does not move from the up to down position when the actuation voltage is applied. If, during stressing, the pull-in voltage becomes higher than the actuation voltage, then the electrostatic force is not high enough to bring the beam to the down position. I.e. the pull-in does not occur and the switch exhibits a low capacitance. The decrease of the C_{down} is observed

a)

b)
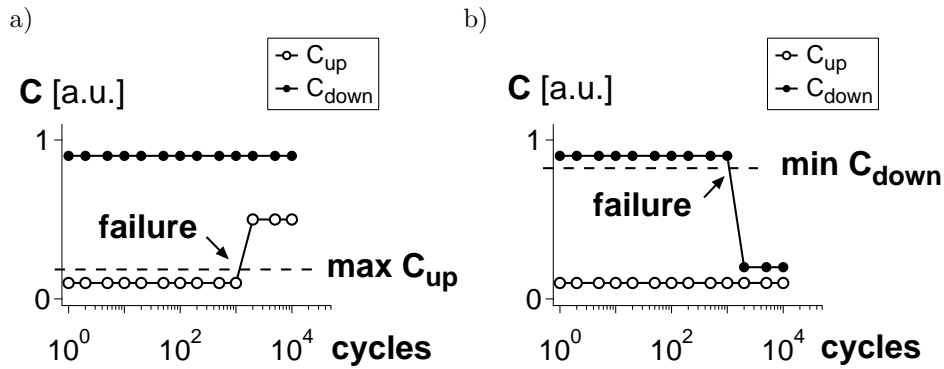
Figure 2.23: Too high C_{up} a) or too low C_{down} are indications of a failure.

a)

b)
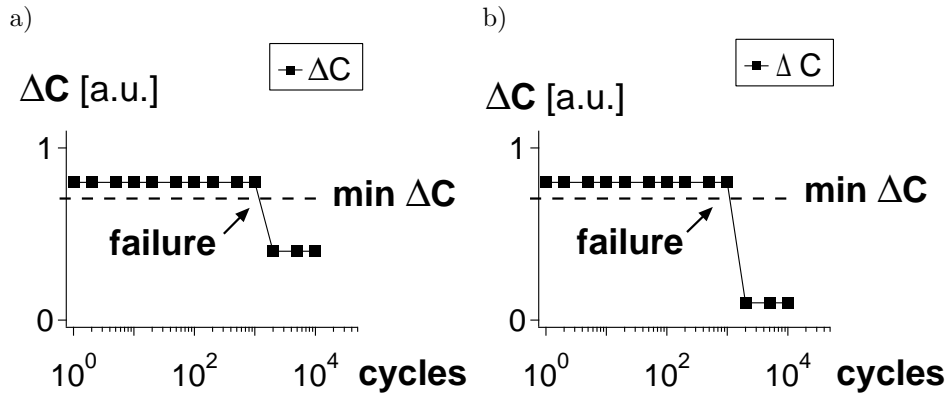
Figure 2.24: Change of the ΔC due to C_{up} increase a) and due to C_{down} decrease b). The ΔC observations allows failure detections.

as an increase of the insertion loss in the on-state. The change in the C_{down} is observed during device stressing as it is presented in Figure 2.23b. A not high enough capacitance exhibited by the switch in the down-state points to a failure.

Changes of the ΔC

The ΔC is another possible failure indicator. It is derived from the C_{up} and C_{down} measurements. The capacitance difference does not allow distinguishing whether the failure is due to the C_{up} increase or the C_{down} increase (Figure 2.24). However, it can be used as a simple failure indicator.
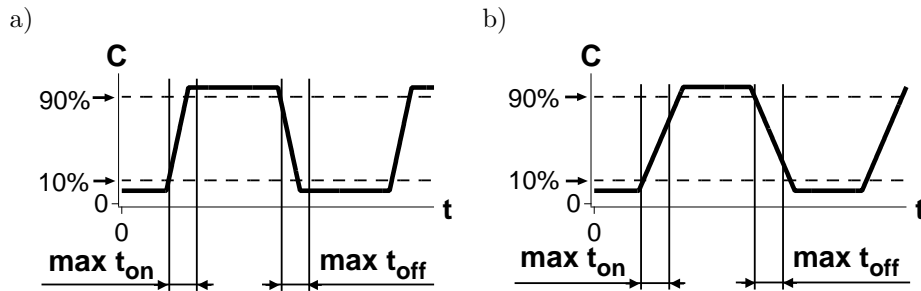
Figure 2.25: The switching times should stay below specified limits a). A failure can be considered when one or both of them are exceeded b).

Changes of t_{on} and t_{off}

Another type of failure mode is the change of switching t_{on} and/or t_{off} times. The switching on and off times of switches are finite and should stay below specified ranges (Figure 2.25a). Excessive increase of the t_{on} or t_{off} can be recognized as a failure (Figure 2.25b). The movement of the beam between up and down positions is not fast enough. Exceeding of the maximal transition time can be a problem in systems where the t_{on} and/or t_{off} are critical (e.g. GSM telecommunication). Change of the switch time can even be observed in a switch that fulfills the max C_{up} and min C_{down} requirements.

The charging mechanisms causes usually the increase in the switching off time. The additional electrostatic force decreases the restoring force that brings the beam to the up-position. Lower force accelerates the beam slower and the time to travel the distance increases. The t_{on} time is usually improved by the charging. The higher electrostatic force can accelerate the beam faster, reducing the travel time.

2.7 Other failure mechanisms

Charging is the main failure mechanism in capacitive RF MEMS switches and the focus of this work. However, the already presented list of possible failure mechanisms is much longer (2.3). An overview and discussion is given in [339]. More details can be found in the following articles:

More articles about charging:
[340], [313], [341], [342], [343], [344], [345], [346], [347], [348], [349], [350].

RF power related failures:

[351].

ESD:
[352], [353].

Dielectric breakdown voltage:
[354].

Stiction:
[355], [356], [357], [358].

Creep:
[359].

Materials:
[360].

Metal-contact degradation:
[361].

Temperature:
[370], [371], [372], [373].

Influence of shock and vibrations:
[366], [367].

Radiation effects:
[368], [369].

General information about reliability:
[374], [375], [376], [377], [378], [379], [380], [381].

Chapter 3

A look from the charging perspective

This section presents a look on the switch from the reliability point of view, related to charging in particular: the switch is considered as an electrostatically driven beam and the RF properties of the switch are neglected. A use of the beam as a charging sensor is proposed.

3.1 Charging perspective

As charging is a problem at the top of the FMEA list, a look on the switch from the charging perspective is presented. The mechanical, RF etc. properties and the influence on the reliability are not considered here.

Usually, the switch is presented as two parallel conductive electrodes with a dielectric layer deposited on top of one of them. The charge trapped in the dielectric modifies the electrostatic force actuating the beam by changing the electric field between the beam and the actuation electrode. In reality, the problem is more complex (Figure 3.1). The beam is actuated by the electrostatic force created by the electric field surrounding the beam. The electric field can be affected by any element of the switch. The beam can "feel" the substrate, the cap and the sealing ring. The environment inside the cavity should not be neglected as it is part of the system. The environment surrounding the beam inside the cavity (air, inert gas, vacuum etc.) should also be taken into account during the design process.

This work does not contain results of a study of the influence of the packaging on the lifetime. Only several basic experiments of the packaged structures were performed
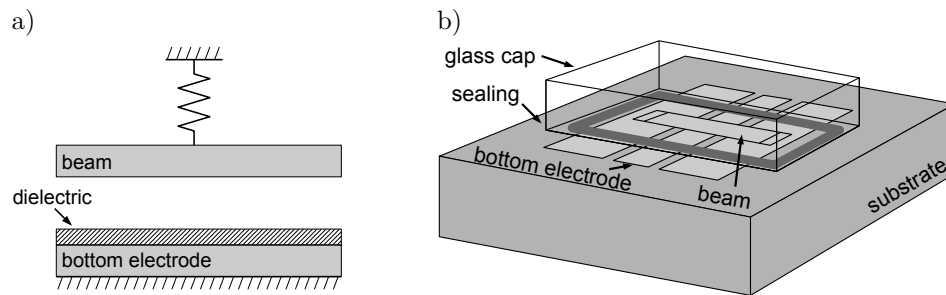
Figure 3.1: A comparizon of the parallel plate model of the switch a) and a model of a zero-level packaged structure b).

to check whether the switches survive the packaging process. Nevertheless, even without the package, the dielectric and the substrate material can create a high number of charging related reliability issues.

In principle, from the charging point of view, the capacitive RF MEMS switch can represent any electrostatically driven MEMS structure. The problems presented in this thesis can apply to most of the MEMS structures based on the electrostatic actuation mechanism.

3.2 The beam as a charge sensor

Several techniques to observe changes of the electric field on the surface of different materials are derived from the Kelvin probe technique proposed by Lord Kelvin in 1898 and implemented by Zisman in 1932. Originally, the Kelvin probe is a technique to measure the contact potential difference [382–386] (Figure 3.2a). However, the technique allows to measure much more.

After the introduction of the scanning tunneling and atomic force microscopes (STM and AFM) [387, 388], development of scanning probe microscopy (SPM) lead to an introduction of SPM implementations of the Kelvin probe [389–392] (Figure 3.2b). Scanning Kelvin probe microscopy, electrostatic force microscopy, scanning capacitance microscopy etc. are powerful tools in micro- and nanotechnology diagnostics [393, 394].

The techniques allow measurements of different factors influencing the surface potential of materials:

- work function and contact potential difference [390], [395], [386],

- charge trapping and detrapping [396], [399], [398], [397], [400],
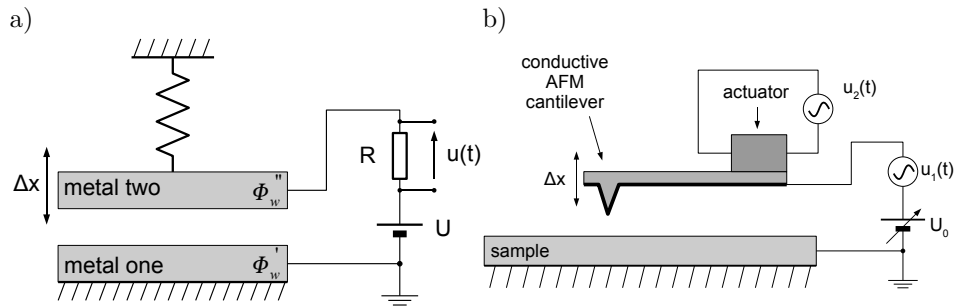
Figure 3.2: Kelvin probe is a very useful technique a). Implementation to the SPM family made a very interesting utensil in microtechnology.

- surface charge [402], [401],

- polarization behavior [403], [404],

- polarization space charge [405], [406],

- adsorption [407], [408],

- potentiometry, voltage distribution measurements [409], [410],

- variations in dielectric constant [389],

- doping profile [411, 412],

- defects [413],

- and more [414–417, 417, 418].

Scanning Kelvin probe microscopy has already been employed in the capacitive RF MEMS switch reliability study [400]. However, it is a destructive method. The beam of the switch has to be removed to give access to the area below the beam. The time between stressing and the potential distribution measurement is long enough to miss the fastest charging mechanisms.

The Kelvin-probe based techniques use an electrode suspended above a sample. This configuration brings to mind the capacitive RF MEMS switch. In that case, the beam of the switch can be used as a surface potential - thus a charge, measuring tool. The beam can be considered as the probe and the remaining elements, the substrate and the interposer dielectric, play the role of the sample.

The detection of the electric field is done by detecting the electrostatic force. The total electrostatic force to actuate the switch from its initial position is constant as long as the mechanical properties of the beam do not change. The difference between
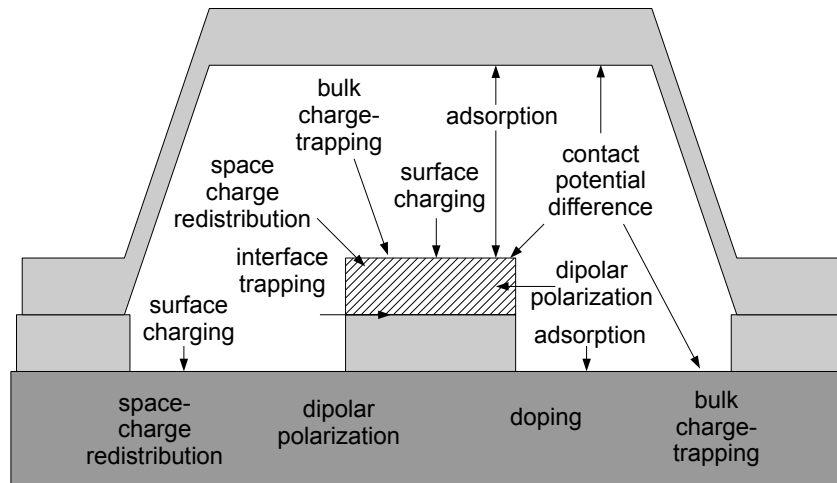
Figure 3.3: Possible factors influencing the reliability of capacitive RF MEMS switches.

the voltages necessary to actuate (V_{pi}) fresh and charged devices is proportional to the magnitude and distribution of the trapped charges. Combination of this information with the test conditions makes the study of the charging behavior of the capacitive RF MEMS switches possible.

The "probe" can give only limited information about the electric field below the beam. The electrostatic force actuating the beam is an average value that contains components created by the bottom electrode, the interposer dielectric and the substrate. However, it is still an interesting, fast, noninvasive and cheap way of testing the reliability of the capacitive RF MEMS switches.

The main drawback of the fact that the beam can sense all the mentioned factors, is that any of them can impact the reliability of the capacitive RF MEMS switches (Figure 3.3).

3.3   Solving the charging problems

The charging related reliability issues can be divided into two groups. The first group should study the influence of the beam on the charge. Several models have been presented. Still more work is necessary. The second group includes physical phenomena describing abilities of the material to charge and change the electric field during stressing. Also this group has already been studied but still not all the phenomena are fully understood and some of them are probably not revealed yet.

Improvement of the reliability of a switch can be based on dealing with the two groups of problems. The best way would be to avoid any charge trapping in the neighborhood of the beam. Sometimes this is not possible, e.g. the substrate must be nonconductive due to RF properties of the switch. If the charging cannot be avoided completely, then the beam should be designed as insensitive to the trapped charge as possible. Combining both aspects it is possible to improve the lifetime of the switch. However, to do this, complete knowledge about the physics governing the beam behavior is necessary.

3.4   The study

The lifetime can be influenced by several factors and their mutual relations (3.4). E.g. the lifetime depends on the amplitude of the actuation voltage but it can depend on the ambient atmosphere or the substrate material in the same time. The quality of the interposer dielectric has a direct impact on the lifetime. The beam-interposer dielectric contact may impact the reliability as well. As the beam can sense the electric field created or modified by the substrate, the impact of the substrate should be taken into account during the beam design.

A direct separation of different factors is sometimes impossible. E.g. a switch cannot work without the substrate. However, a proper combination of the test conditions allows emphasizing particular mechanisms. A use of dedicated test structures may help as well.

The experiments presented in the last part of this thesis aimed in distinguishing particular mechanisms. The results obtained during experiments performed under various combinations of the test conditions provided important information about the charging mechanisms. E.g. lifetime tests performed humid and dry atmosphere allowed observations of the impact of the substrate.
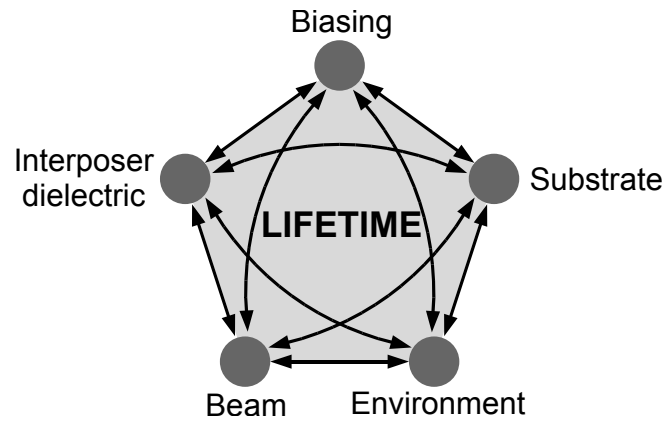
Figure 3.4: The lifetime of the capacitive RF MEMS switches is influenced by several factors and their mutual relations. E.g. the lifetime of the switches depends on the amplitude of the actuation voltage but it can be different depending on the type of substrate or ambient atmosphere.

Chapter 4

Test structures

Most of the experiments presented in this work were performed in the frame of several projects:

- MEMS2TUNE - *Development of a metal-based MEMS technology for realising tunable/switchable RF modules for wireless applications*, an European Commission FP5 project, IST-2000-28231,

- MIPA - *MEMS Based Integrated Phased Array Antennas*, an European Commission FP5 project, IST-2000-28276,

- RETINA - *Reliable, tuneable and inexpensive antennas by collective fabrication process*, an European Commission FP6 project, AERO1-2003-516121,

- ENDORFINS - *Enabling deployment of RF-MEMS technology in space telecommunication*, an ESA/ESTEC project, contract no. 18613/05/NL/IA.

The first three projects were focused on the RF properties of the RF MEMS devices and the reliability study was a small part. Generally, a (low) number of the switches were provided for lifetime experiments. The structures tested in the frame of these projects are briefly introduced in the first part of this section.

The focus of the ENDORFINS project was on the reliability of the RF MEMS switches. The author had the opportunity to participate in the design of the test structures dedicated to the reliability study. The fabrication and the design of the test structures are described in the last part of this section.

4.1 MEMS2TUNE switches

MEMS2TUNE switches are parallel-plate type of RF MEMS devices fabricated on a high-resistivity silicon substrate. The beam is made of an aluminum alloy. The interposer dielectric layer is made of PECVD silicon nitride. More details about the switches can be found in [419, 420].

a)   b)
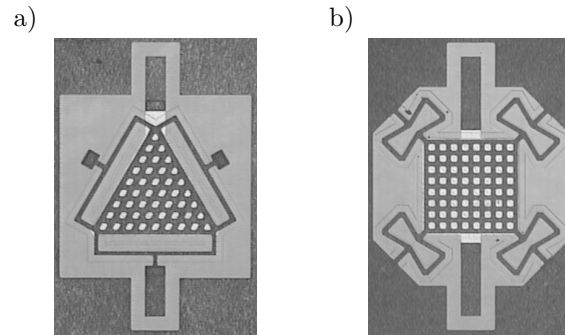
Figure 4.1: The MEMS2TUNE switches: capacitive series a) and capacitive shunt b).

4.2 MIPA switches

The MIPA switches used for reliability experiments (B- and D-type) are presented in Figure 4.2. The switch employs a modified clamped-clamped beam. The switches are fabricated on a high resistivity silicon substrate. The conductive parts of the switch (ground pads, signal line, beam) are made of an aluminum alloy (AlCu). The interposer dielectric layer is the PECVD Si_3N_4. More details about the switches can be found in [421–424].

4.3 RETINA MEMS switches

The RETINA structures were already introduced in section 1.3.2. The structures are based on the low complexity switch presented by Siegel et al. [28, 45]. A microphotograph of the switch is presented in Figure 4.3.

The RETINA structures use the substrate as the bottom actuation electrode. The actuation voltage is applied between the cantilever beam and the back side of the wafer (Figure 4.4a). The potential of the back side of the wafer is transferred to the

a) b)
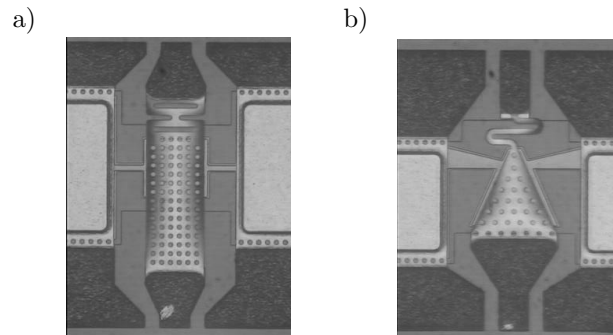
Figure 4.2: MIPA switches: B-type a) and D-type b).

Figure 4.3: RETINA switch microphotograph [28].

surface of the dielectric and the voltage across the air gap (U_{air}) is (approximately) equal the U_{act} (Figure 4.5). The voltage drop across the substrate can be neglected.

Once the cantilever is pulled-in, the tip of the beam lands on the implanted area. The implantation improves the capacitance between the beam and the signal line creating a low impedance path for the RF signal (Figure 4.4b). The low capacitance between the beam and the signal line in the up-state is observed as high isolation.

4.4 ENDORFINS test structures

4.4.1 The processing

There are many possible process flows but they are similar. Differences can be in the use of various depositing and etching techniques and materials.

The first step is depositing bottom metallization and patterning it (Figure 4.6a).
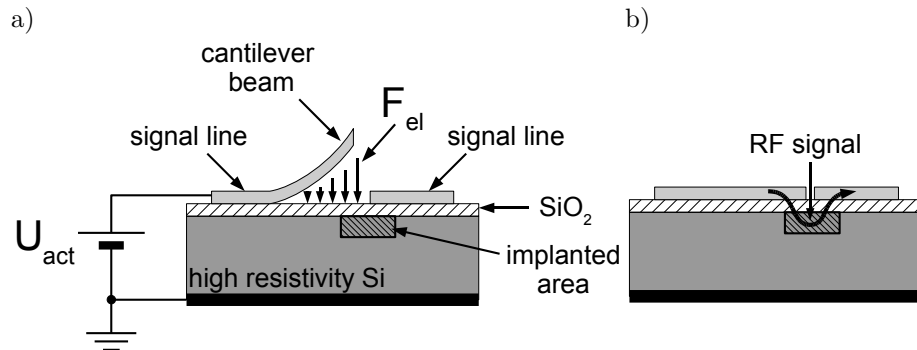
Figure 4.4: The idea of the RETINA switch a). The implanted area improves the capacitance in the down-state creating a low impedance path for the RF signal b).

$$C_{oxide} >> C_{air}$$

$$\downarrow$$
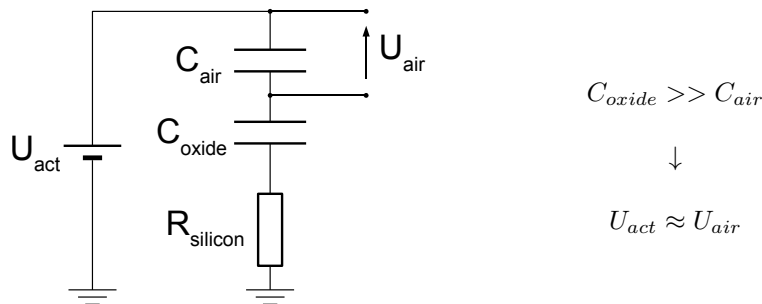
$$U_{act} \approx U_{air}$$

Figure 4.5: The potential from the backside of the substrate is transferred to the surface of the silicon oxide layer. The voltage generating the electrostatic force F_{el} is approximately equal to the actuation voltage U_{act}.

Then the interposer dielectric is deposited and patterned (Figure 4.6b). The third step is deposition and patterning of the sacrificial layer (Figure 4.6c). The fourth one is deposition the beam metallization and patterning it (Figure 4.6d). The fifth one is removing (etching) the sacrificial layer to release the beams (Figure 4.6e). The sixth one should be zero-level packaging of the devices.

The processing steps look simple. However, the large number of similar test structures, required for the reliability study, demands a high uniformity and a high repeatability of the particular processing steps.

cross-section   top view

a)

bottom
metal

substrate

b)

dielectric

c)

sacrificial
layer

d)

beam
metal

e)
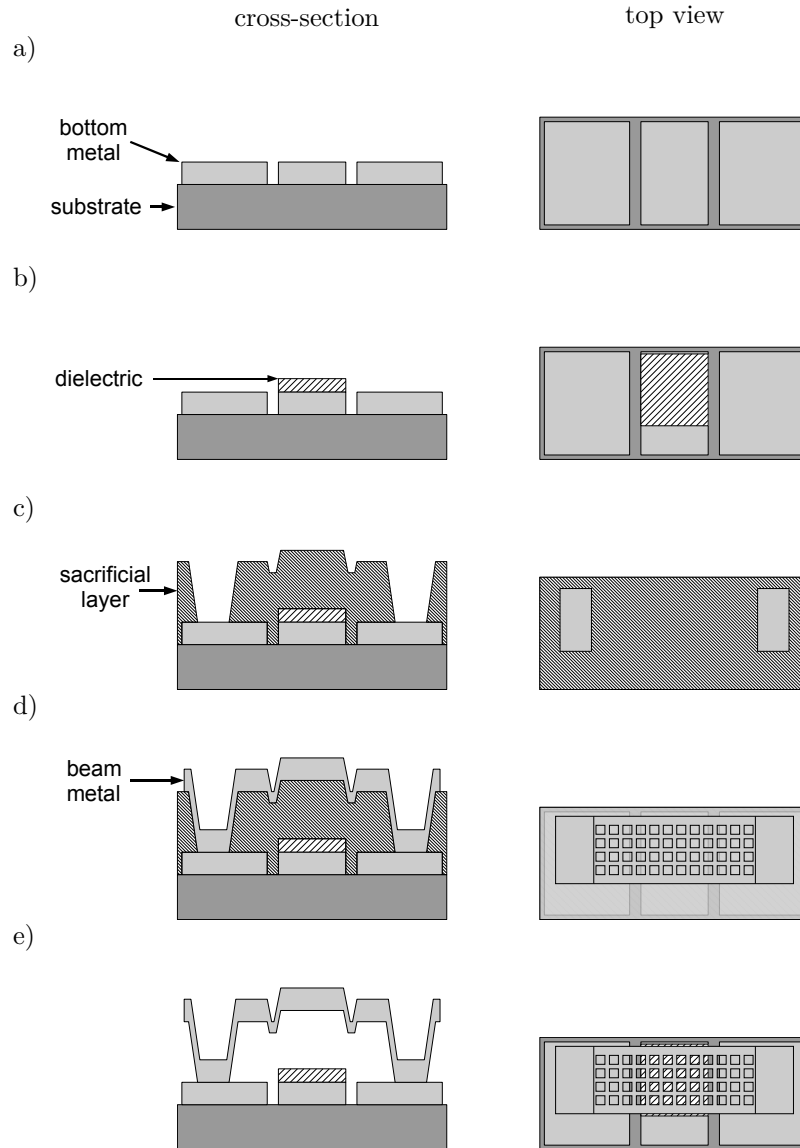
Figure 4.6: Process steps: bottom metal deposition and patterning (a), dielectric layer deposition and patterning (b), sacrificial layer deposition and patterning (c), beam metal deposition and patterning (d), sacrificial layer removal (e).

4.4.2 The dielectric

During the ENDORFINS project a number of dielectric materials as candidates for the interposer dielectric were tested in order to find the best performance. The set contained two different dielectrics: tantalum oxide and aluminum nitride. Both were processes with two recipes. That resulted in four dielectric materials to be investigated.

TaO1 and TaO2

The tantalum oxide dielectric was processed with two recipes. The first one (TaO1) was deposited using the reactive magnetron sputtering. The magnetron sputtering is a PVD (physical vapor deposition) process. The target material (Ta) is sputtered with Ar RF plasma. A mixture of oxygen and nitrogen is added to the chamber. The sputtered tantalum reacts with oxygen and TaO layer is deposited on the substrate. The nitrogen is added to improve the properties of the TaO.

The second tantalum oxide dielectric (TaO2) is fabricated using anodizing. First a layer of tantalum is sputtered with magnetron sputtering. Then the layer is anodized in a solution of citric acid. An anneal step after anodizing is applied.

AlN1 and AlN2

The AlN1 and AlN2 dielectrics were both aluminum nitride deposited using the pulsed DC reactive magnetron sputtering. However, a difference in the deposition parameters resulted in slightly different properties of the deposited materials. The AlN1 and AlN2 were deposited with 250kHz and 40kHz frequency of the pulses, respectively. The different frequency resulted in various crystallographic properties of the materials. The AlN1 exhibits a strong orientation along the c-axis and it shows piezoelectric properties. The AlN2 is expected to have a stronger orientation in the other crystal planes [425].

4.4.3 The design

As the focus of this work is on reliability, the design of the test structures was driven by several aspects. The required test structures do not have to be fully functional devices as long as they are representative from the reliability point of view, in particular to the charging effects. If the RF properties of the test structures are neglected, then movable electrostatically actuated beams with a dielectric layer between the electrodes are sufficient. The movement of the beam
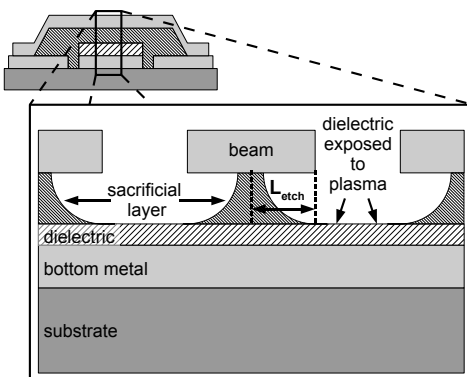
Figure 4.7: The sacrificial layer is etch via the holes in the beam. The L_{etch} part of the sacrificial material has to be removed to release the beam.

can be electrically detected by measurements of the capacitance between the fixed and movable electrodes.

The beam

A simple clamped-clamped strip-type beam was chosen.

The set of designed test structures should allow performing experiments on structures fabricated with various parameters of the processing steps: different levels of internal stress in the beam, various thicknesses of the beam and the sacrificial layer, different beam materials. Since they form the main factors influencing the actuation parameters, it is important to take into account during the design phase. It resulted in various lengths of the test structures that allowed actuating the beams with actuation voltages between 10 and 50V independently on the process steps parameters.

Previous studies revealed problems with obtaining a high uniformity of the test structures across a wafer. One of the main causes of the non-uniformity is the plasma attacking the dielectric during the sacrificial release step. The longer the release time, the more damaged the dielectric and higher charge trapping become. The sacrificial layer below the beam is etched from the lateral sides of the beam and through the etch holes. For full sacrificial removal, the L_{etch} part of the sacrificial layer has to be removed (Figure 4.7). If the distance varies across the wafer, then some structures are released sooner than other and the dielectric is unnecessarily exposed to the plasma. To avoid the unwanted extension of the release time, the etch length of all the structures is fixed.
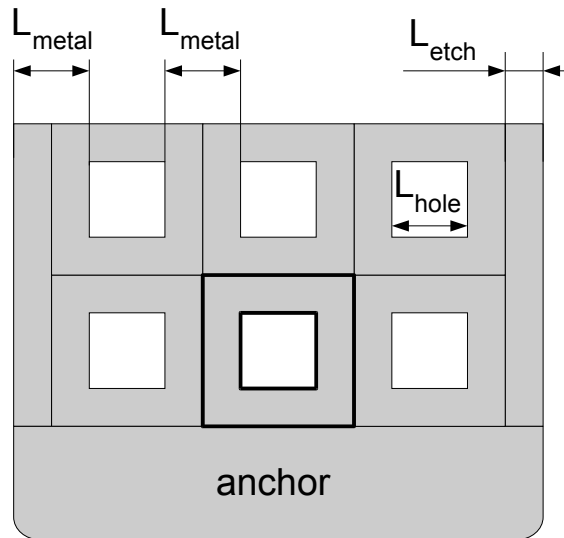
Figure 4.8: The beam consists of a number of modules of fixed metal part size. Additional metal stripes on the sides are added to fulfill the $L_{etch} = const$ requirement.
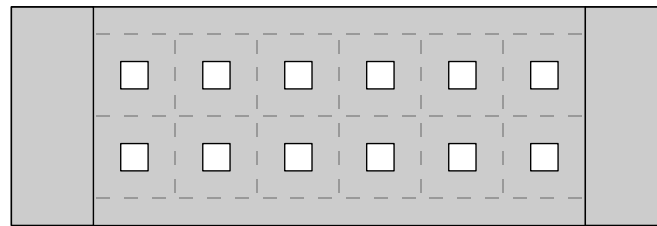
Figure 4.9: An example of a 2 modules wide and 6 modules long beam.

The constant L_{etch} and the need to cover a variety of processing parameters led to the choice of a modular design of the beam. The beam is constructed of a number of square-shaped modules (Figure 4.8). The module contains a square-shaped etch hole and metal portions around it. The width of the metal parts is fixed. The size of the etch hole can be modified. On both sides of the beam two stripes of metal are added to fulfill the constant L_{etch} requirement. Placing any number of the modules next to each other makes it possible to design test structures of any (discrete) length and width (Figure 4.9).
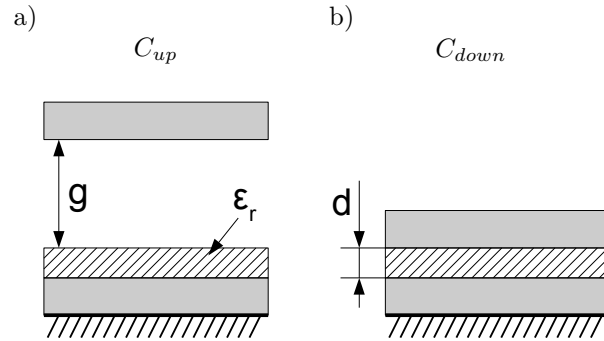
Figure 4.10: The C_{up}/C_{down} ratio is fixed by the technology: thickness d and the permittivity ε_r of the dielectric layer and the distance between the beam and the dielectric layer g.

The bottom electrodes

In order to find the dimensions of the beam and the bottom electrode, two main parameters, the V_{pi} and the C_{down}, should be specified. The C_{up}/C_{down} ratio is defined by the technology parameters: the distance between the beam and the bottom electrode and the thickness and the permittivity of the dielectric layer (4.1, Figure 4.10).

$$\frac{C_{up}}{C_{down}} = \frac{\frac{\varepsilon_0 A}{g}}{\frac{\varepsilon_0 \varepsilon_r A}{d}} = \frac{d}{g \varepsilon_r} \tag{4.1}$$

In the case of the clamped-clamped beam the C_{down} is defined by the overlapping area A between the beam, bottom electrode and dielectric. A is a product of w_b and w_s (4.2. The w_b and w_s are defined in Figure 4.11.

$$A = w_b w_s \tag{4.2}$$

The pull-in voltage of the switch depends on the actuation area and the spring constant of the beam (4.3). The spring constant k of the clamped-clamped beam actuated by a force applied to the central portion of the beam depends on several factors (Figure 4.12) [4]. The thickness t, material type (Young's modulus E, Poisson's ratio ν) and internal tensile stress σ are fixed by the technology.

The spring constant k is a sum of two components (4.4). k' describes the dependency of the spring constant on the distribution of the force alongside the beam (4.5) and k'' is an internal stress related component (4.6).
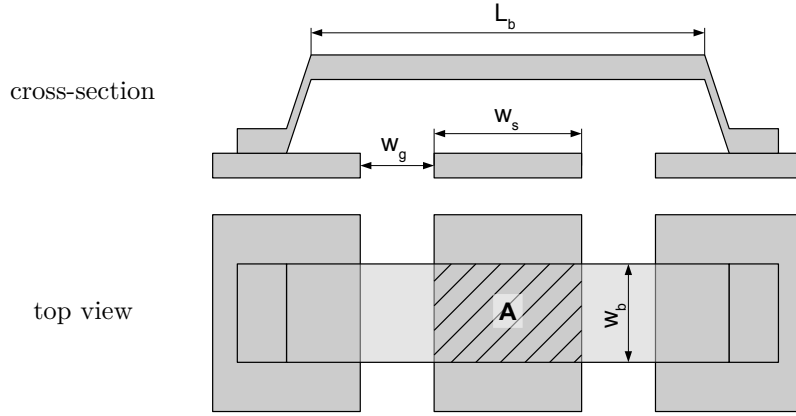
Figure 4.11: Definition of the beam and bottom electrodes dimensions.
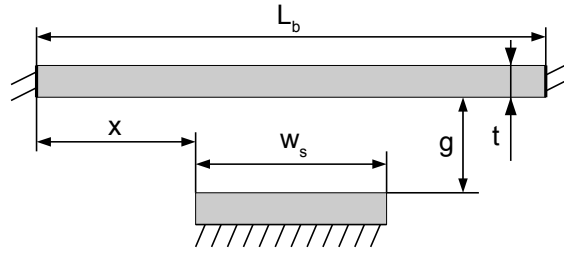
Figure 4.12: A model used to calculate the spring constant k of the clamped-clamped beam suspended above the actuation electrode.

The beam length L_b and the size of the bottom electrode w_b (i.e. the actuated portion of the beam) can be chosen during the design phase. The width of the beam w_b increases the spring constant of the beam and in the same time it increases the actuation area A. As a result, the pull-in voltage is not influenced by the width of the beam.

$$V_{pi} = \sqrt{\frac{\frac{8}{27}kg^3}{\varepsilon_0 w_b w_s}} \tag{4.3}$$

$$k = k' + k'' \tag{4.4}$$

$$k' = 32Ew_b \left(\frac{t}{L_b}\right)^3 \frac{1}{8\left(\frac{x}{L_b}\right)^3 - 20\left(\frac{x}{L_b}\right)^2 + 14\left(\frac{x}{L_b}\right) - 1} \tag{4.5}$$
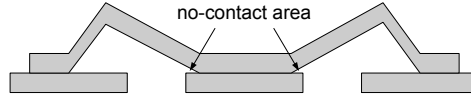
Figure 4.13: No-contact area can be a source of non-uniform trapped charge distribution.

$$k'' = 8\sigma \left(1 - \nu\right) w_b \left(\frac{t}{L_b}\right) \frac{1}{3 - 2\left(\frac{x}{L_b}\right)} \tag{4.6}$$

The parameters to be designed are w_s and L_b. The w_b can be further chosen to keep the C_{down} as desired.

In principle, the w_s and w_g, thus the L_b as well by the pull-in relation, are linked by the RF properties of the switch. The w_g and w_s determine the characteristic impedance of the CPW. The RF properties of the test structures are out of the interest of this work and the C_{down} is limited only by the sensitivity and resolution of the test equipment ($>$1pF). Therefore, the focus of the design was to find the w_s/L_b ratio concerning the reliability issues.

It was mentioned (section 2.5.5) that non-uniform charge trapping can generate unwanted effects limiting the reliability of the switches. One of the non-uniform charge trapping sources can be not complete contact of the beam and dielectric layer in down-state (Figure 4.13).

To find the optimal w_s/L_b ratio a number of FEM simulations were performed. The simulations were performed by Caroline Chen and the MARC MENTAT (MSC software) tool was used (Figure 4.14).

The electrostatic actuation was mimicked by applying a uniform pressure on the beam in the region overlapping with the actuation electrode. This only partially represents the reality of the complex electrostatic actuation. However, it helps to grasp the problems related to the contact.

FEM simulations results

First, three structures of fixed V_{pi} and different values of the w_s/L_b ratio were simulated. The results show that the higher w_s/L_b ratio generates a non-contact area (Figure 4.15). The portions of the beam that do not touch the dielectric become short and stiff. The electrostatic force is not high enough to attract them to the surface of the dielectric. Lowering the w_s/L_b ratio improves the contact (smaller non-contact area). However, at the same time the beam length increases
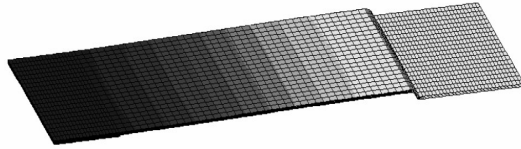
Figure 4.14: An example of the FEM result: the beam deformed under applied pressure.
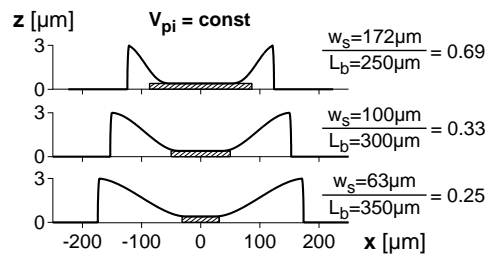
Figure 4.15: Changing the w_s/L_b ratio can modify the quality of the contact.

degrading the dynamic properties of the switch. The longer the beam, the lower is the resonance frequency, and the longer are the switch on and off times are.

Changing the w_s/L_b ratio can be done in two ways:

- by changing the length of the beam with the size of the bottom electrode fixed,

- by changing the size of the bottom electrode with the length of the beam fixed.

The results of FEM simulations of the two cases are presented in Figure 4.16. Decreasing the size of the bottom electrode improves the contact area at the cost of a lower C_{down}. Increasing the beam length improves the contact area at the cost of the dynamic properties of the structure. The $w_s/L_b = 1/3$ ratio seems a good compromise. The beam is not too long and creates a contact of more than 90% of the total dielectric area.
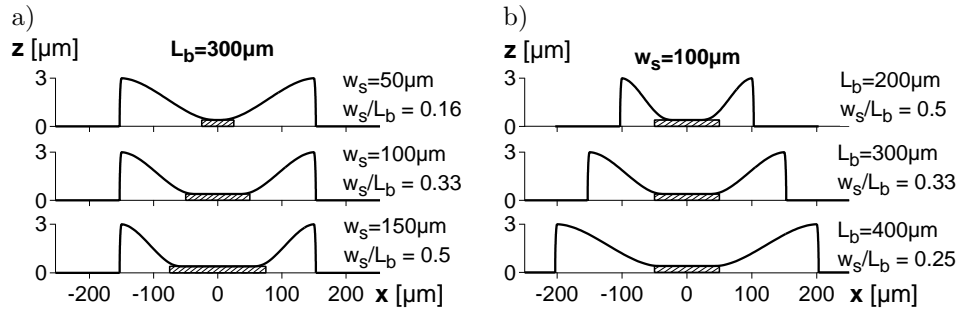
Figure 4.16: The w_s/L_b ratio can be modified by changing the size of the bottom electrode a) or the length of the beam b). $w_s/L_b = 1/3$ seems a good compromise between the size of the beam and the contact quality.

The complete structure

The dimensions of the designed test structures are presented in Table 4.1. The C_{down} is intentionally designed much higher than the assumed 1pF. Indeed, previous experiments show that often the measured down-state capacitance is much lower than the designed value. The origin of this effect was not clear. The finite roughness of the interposer dielectric and the beam material are only two of possible causes. For this reason, the C_{down} was designed a factor of ten higher in order to avoid eventual measurements difficulties. The C_{down} values listed in Table 4.1 are calculated for a dielectric material exhibiting a permittivity of 30. The foreseen use of different dielectric materials with possibly lower ε will result in a lower C_{down}. The designed dimensions should assure a measurable capacitance in case of different processing variations.

Additionally, switches with $480\mu m$ and $840\mu m$ long beams of 200 μm width ($n_w = 6$) are designed.

Every test structure should allow probing. Since no RF measurements were planned, standard $100\mu m$ x $100\mu m$ square-shaped contact pads, for needle-type probes, were added. The distance between the contact pads is in general not limited. However, a large number of the test structures and a possibility of automated probing led to the design of the contact pads as presented in Figure 4.17. The ground pads are extended to allow probing most of the test structures on a wafer with fixed positions of the probes. Two ground pads were designed to increase the probing flexibility.

Table 4.1: The results of the calculations of the dimensions of the bottom electrode w_s and the beam L_b with different beam metal thickness t and internal tensile stress σ. The corresponding V_{pi} are listed as well.

t $[\mu m]$	σ $[MPa]$	L_b $[\mu m]$	w_s $[\mu m]$	V_{pi} $[V]$	n_L	n_w	w_b $[\mu m]$	C_{down} $[pF]$
1	50	480	144	47.1	16	4	140	26.8
1	100	480	144	66.2	16	4	140	26.8
1	200	480	144	93.2	16	4	140	26.8
1	50	840	252	26.7	28	4	140	46.8
1	100	840	252	37.6	28	4	140	46.8
1	200	840	252	53.1	28	4	140	46.8
1	50	1680	504	13.3	56	2	80	53.5
1	100	1680	504	18.8	56	2	80	53.5
1	200	1680	504	26.5	56	2	80	53.5
1	50	1980	594	11.3	66	2	80	63.1
1	100	1980	594	15.9	66	2	80	63.1
1	200	1980	594	22.5	66	2	80	63.1
2	50	480	144	69.7	16	4	140	26.8
2	100	480	144	95.7	16	4	140	26.8
2	200	480	144	133.4	16	4	140	26.8
2	50	840	252	38.3	28	4	140	46.8
2	100	840	252	53.6	28	4	140	46.8
2	200	840	252	75.4	28	4	140	46.8
2	50	1680	504	18.9	56	2	80	53.5
2	100	1680	504	26.6	56	2	80	53.5
2	200	1680	504	37.6	56	2	80	53.5
2	50	1980	594	16.0	66	2	80	63.1
2	100	1980	594	22.5	66	2	80	63.1
2	200	1980	594	31.9	66	2	80	63.1
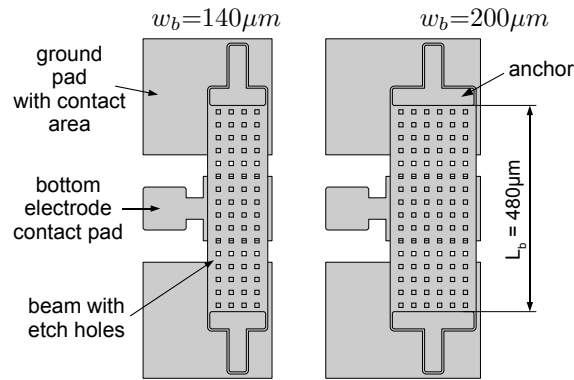
Figure 4.17: The designed structures contain the bottom actuation electrode, the beam and the ground pads that allow actuating most of the test structures on a wafer with fixed probes positions.
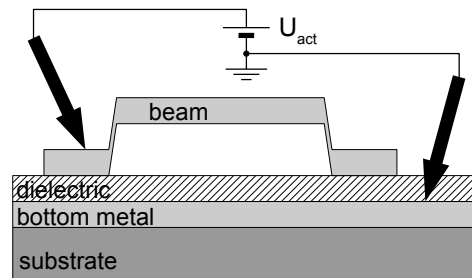
Figure 4.18: Simplified test structures - beams on non-patterned metal and dielectric layers - allow testing charging properties of different dielectric materials.

The anchors

The anchors of the test structures were extended laterally on purpose.

The test structures should allow actuation of the structures fabricated with a variety of processing conditions. One of the foreseen ENDORFINS experiments was testing simplified test structures to study charging properties of different dielectric materials. The structures contain beams fabricated on a substrate fully covered with a metal layer (bottom actuation electrode) and dielectric layer (interposer dielectric) (Figure 4.18). Actuation of such test structures requires probing the anchor of the beam. In order to avoid damaging the beams and inducing unwanted stress in the beams, the anchors were designed as presented in Figure 4.19. Probing the bottom electrode involves scratching through the dielectric layer.
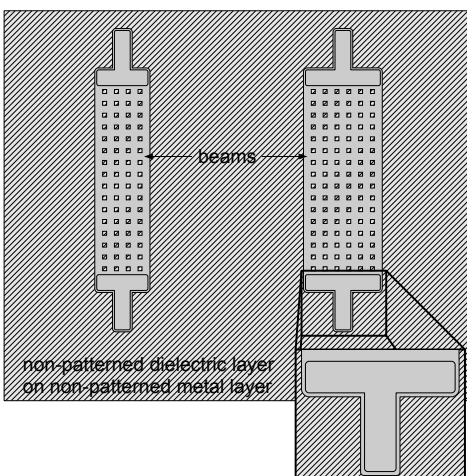
Figure 4.19: In order to avoid damaging the beam during probing, the anchors were extended with T-shaped areas.

4.4.4   Wafer mapping

The test structures are placed in 1cm x 1cm cells. Each cell contains a number of similar test structures (Figure 4.20a). The cells are organized in 4 quarters. Each quarter includes the same number of cells. In the central part, along the X and Y symmetry axes, a number of packaging dedicated test cells are placed (Figure 4.20b). Several process check modules (PCM) and alignment modules complement the test structures placed on the whole 6" wafer mask set.

Many more test structures were designed dedicated to a number of various reliability related experiments. However, several processing issues did not allow performing all the foreseen experiments. Most of the experiments performed in the frame of this work were performed on the presented test structures (Figure 4.21).

a)
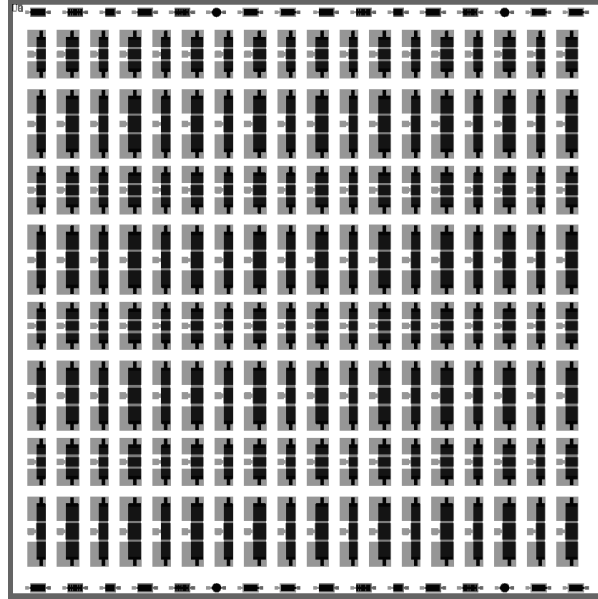
b)
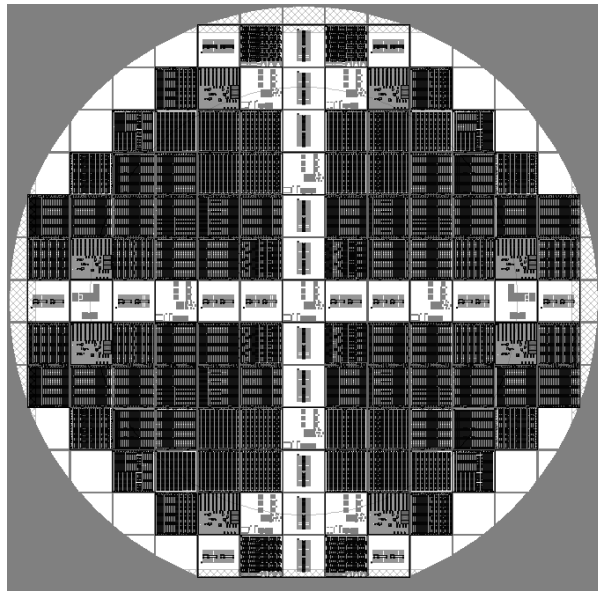
Figure 4.20: Structures organized in cells a) are placed in 4 similar quarters b). A number of cells dedicated to packaging experiments are placed along the X and Y symmetry axes.
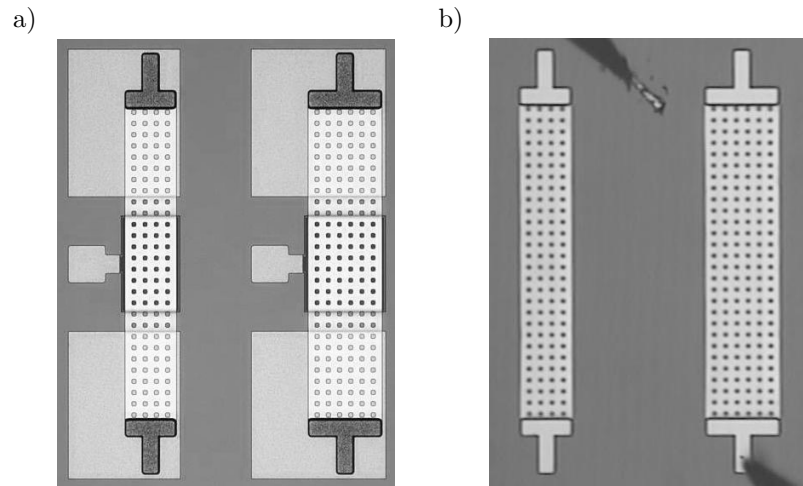
Figure 4.21: Microphotographs of fully processed a) and simplified b) (no bottom metal and dielectric patterning) ENDORFINS test structures. Visible scratch after probing the bottom metal layer.

Chapter 5

Instrumentation

Most of the experiments performed in the frame of this work are based on observations of the device's response to an applied stimulus. The response depends on the actual state of the device, which is directly linked to the amount of and distribution of trapped charges. Differences in the response recorded before, during and after stressing with various actuation voltages and under different environmental conditions can bring valuable information about the physics of the failure mechanisms. The response of the switch (beam displacement) can be observed using several techniques classified in two groups: optical and electrical.

This section presents the techniques that were used to characterize and test the capacitive RF MEMS switches in the frame of this work.

First, the optical methods are briefly introduced.

The electrical methods, including the dedicated ELT system, used in the reliability study presented in this work, are describe in more detail in the second part of this section.

5.1   Optical methods

This section presents the basics of two optical methods that can be used in reliability studies of the capacitive RF MEMS devices. The white light interferometry and laser Doppler vibrometry techniques are described.
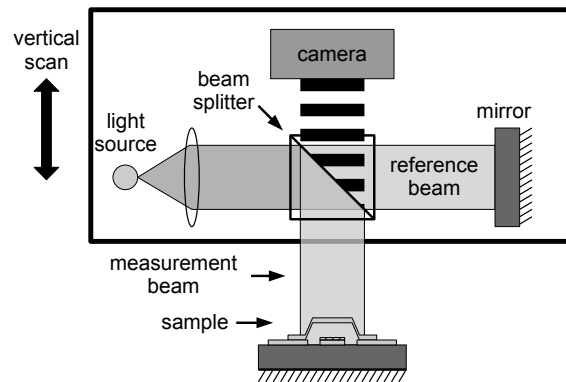
Figure 5.1: The idea of the white light interferometry.
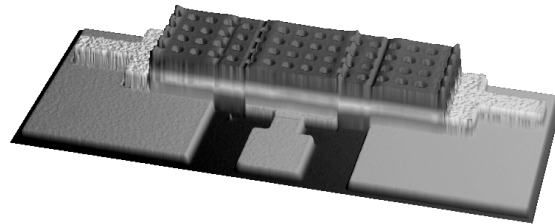
Figure 5.2: White light profilometry allows topography measurements.

5.1.1 White light interferometry

The white light interferometry measurement technique is based on the interference of two light beams. Classical interferometry uses monochromatic light usually generated by a laser. The difference between the classical and the white light interferometry is the use of non-monochromatic (white) light. The white light improves resolution and measurement range of the measurements and reduces additional unwanted interferences e.g. caused by eventual dust particles on the surface [426].

The idea is presented in Figure 5.1. The light beam is split into two beams. The reference beam is reflected from a fixed mirror. The measurement beam illuminates the sample. The reflected beams (the reference from the mirror and the measurement from the sample) interfere and the interference fringes can be observed with the camera. The interferometer is moved along the Z axis in a certain range. Detection of the interference fringes during scanning allows topography measurements (Figure 5.2).

Main features:
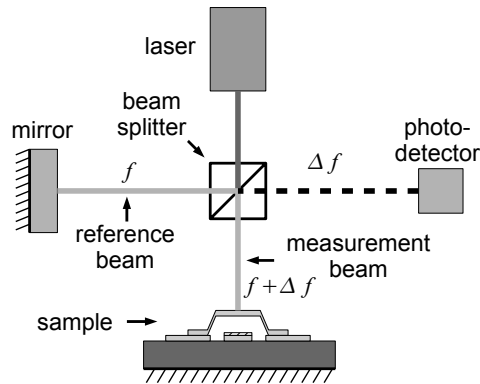
Figure 5.3: The idea of the laser Doppler vibrometry: interference of two beams allow detection of the frequency shift Δf.

- measurements of the whole specimen at the same time,

- high XY spatial resolution ($\sim 1 \ \mu m$),

- high Z resolution ($\sim 1 \ nm$),

- relatively long measurement time ($\sim$ several to tens of seconds),

More information about the white light interferometry can be found in [427] and [428].

5.1.2 Laser Doppler vibrometry

Laser Doppler vibrometry (LDV) is a technique based on the Doppler Effect. The Doppler Effect is a change of the wavelength (thus the frequency) of any wave reflected from an object moving with respect to the source of the wave. In case of the LDV a laser (HeNe) is the source of a light wave. As the frequency of the light is in the order of PHz the direct measurement of the frequency shift Δf is impossible.

To detect the change of the frequency interference of the incident of frequency f and the reflected beam of frequency $f + \Delta f$ is used. As a results a modulated light beam of frequency Δf is obtained (Figure 5.3). Based on the frequency shift measurement, the velocity of the moving object and traveling distance is calculated.

The simple interferometer does not allow distinguishing the direction of the movement. Therefore, more advanced systems e.g. heterodyne or homodyne
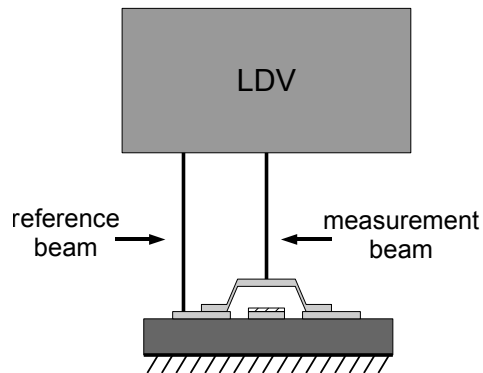
Figure 5.4: Two beam mode allows reducing the sensitivity to external vibrations.

interferometers are used. The detection of the direction of the displacement is possible. The sensitivity to hum and noise is additionally decreased [428].

The LDV can work in a differential mode in order to cancel parasitic vibrations from the environment. Two laser beams are focused on the sample. One of the beams is a reference beam and should be focused on a static part of the sample. The second beam (measurement beam) should be focused on the moving portion of the sample. The calculated difference gives information of the movement of the moving portion with respect to the non-moving part of the sample (Figure 5.4).

The position of the measurement beam can be controlled (Figure 5.5). Measurements of more than one point allow reconstructing the movement of a movable surface (Figure 5.6).
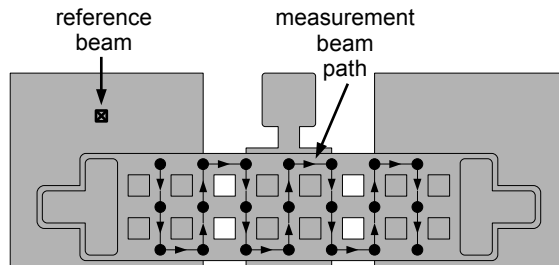
Figure 5.5: Controlling the position of the beam allows reconstruction of a movable surface.

Main features:

- out-of-plane movement measurements,

- one point real-time measurement,

- high XY spatial resolution $\sim 1\ \mu m$

- very high Z resolution of tens of picometers,

- possibility of surface movement measurement by point-by-point scanning.
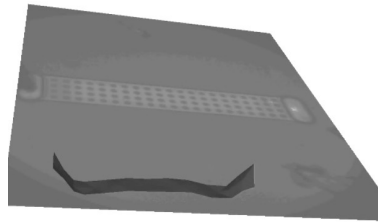
Figure 5.6: A Laser Doppler vibrometer measurement result.

5.2 Electrical methods

5.2.1 RLC meters

The commercially available RLC meters allow measurements of the capacitance with the resolution of fF [429]. The capacitance measurement resolution and range of such meters are satisfactory. However, the measurement time (tens of ms) is too long for the transition observations of the capacitance of the switches. The RLC meters allow actuating the MEMS devices. Though, the ability of generation actuation waveforms is limited.

Nevertheless, a number of measurements using the Agilent E4980a RLC meter were performed in the frame of this work.

5.2.2 RF based techniques

A natural way of testing the performance of an RF-MEMS switch would be embedding it in a real system including RF power transmitters and receivers. This approach makes the measurements expensive and complex. Another way is to use RF equipment, e.g. network analyzers, to measure the RF characteristics of the switches. The resolution of the S-parameters measurements is satisfactory. However, the time resolution is not high enough to detect the transitions.

A number of modified RF-based test techniques have been presented [44, 50, 132, 141, 327, 334, 430–432]. They all employ a source of an RF signal and a power detector. In this approach the power reflected (one port measurement) or transmitted (two port measurements) is measured. Based on the power level the state of the switch can be determined. The technique is less precise than the S-parameters measurement, though it allows for fast transitions measurements. Nevertheless, they are interesting methods for reliability experiments.

Main features:

- measurements of the real RF properties of the switch,

- limited use of biasing schemes,

- high cost.

5.3   The ELT system

The lack of commercially available dedicated test equipment led to development of the electronic lifetime test (ELT) system presented by van Spengen [433]. The idea of the system is presented in Figure 5.7. The actuation voltage U_{act} and the high frequency sensing signal U_{HF} are mixed and fed to a device via a known resistor R. The capacitance of the switch C_{switch} and the resistance R create a voltage divider. The amplitude of the high frequency signal is modulated by changes of the capacitance of the switch. The signal is further demodulated. The amplitude of the output signal is related to the capacitance of the switch.

The idea allows building a small and simple, yet powerful, test set-up. However, the relatively low frequency of the sensing signal (~ 10MHz) makes the system sensitive to the influence of the substrate material. Figure 5.8 shows an example of a C-V characteristic of a device fabricated on a high resistivity silicon wafer. The C-V curve as measured by the ELT shape is distorted due to the polarity dependent influence of the substrate.

Main features:

- low complexity and price,

- tens fF resolution,

- possibility of measurements in switch and relay configurations,

- 10 μs measurement time allows transition measurements,

- limited amplitude of the actuation voltage,
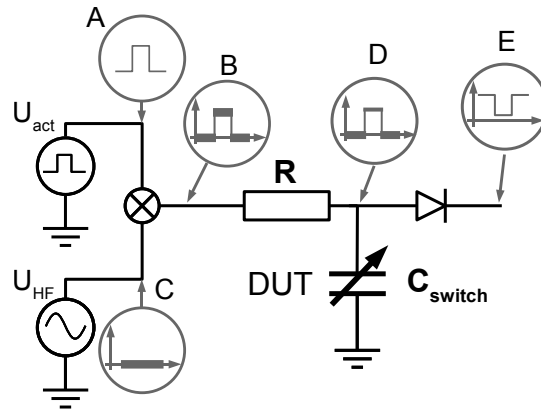
Figure 5.7: The idea of the ELT system: a voltage divider built of a known resistor R and the tested capacitive RF MEMS switch C_{switch}. The actuation (A) and sensing (B) signals are mixed and the sum (C) is fed to the tested device via a known resistor R. Changes of the capacitance of the switch (C_{switch}) result in modulation of the sensing signal (D). The demodulated signal (E) is proportional to the capacitance of the switch.
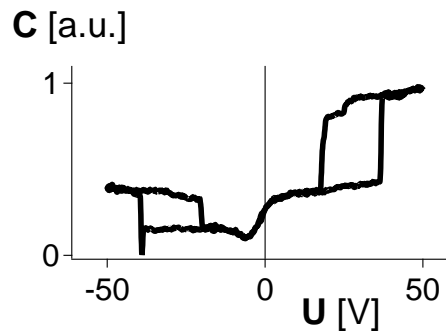
Figure 5.8: Relatively low frequency of the sensing signal ($\sim$ 10MHz) make the output signal sensitive to the substrate material influence. The distorted shape of the C-V curve is caused by the influence of the silicon substrate.

- fixed frequency of the carrier signal,

- relatively low frequency of the carrier signal ($\sim$10MHz) makes the system sensitive to the substrate material of the device,

The limitations of the first implementation led to building an improved version presented in the next section.

5.4 The HSF ELT system

5.4.1 The high frequency concept

The improved implementation of the previously introduced ELT system, the HSF ELT (High Sensing Frequency Electronic Lifetime Test) is based on the same idea of the voltage divider. However, shifting the frequency of the sensing signal to higher range ($\sim$ 500MHz) allowed improving the sensitivity and reducing impact of silicon substrates on the output voltage. The higher frequency also allows reducing the measurement time to less than 1 μs. The components used for building the new ELT system allow application of higher amplitudes of actuation voltages (tested up to 150V vs. 40V in the low frequency ELT). Another significant change included miniaturization of the sensing head (Figure 5.9). In order to reduce the influence of parasitic capacitances, it was decided to place the sensor as close to the tested device as possible. The sensing part is combined with a probe needle that is directly connected to the signal detector. Thanks to that, the sensing head is placed approximately 2 cm from a device. The source of the high frequency signal is a voltage controlled oscillator (VCO). The frequency of the signal can be tuned to obtain optimal sensitivity. The used VCO allowed tuning the frequency in the range from 400 to 700MHz.

5.4.2 The ELT output signal interpretation

The output signal of the ELT is proportional to the impedance of the tested device (Figure 5.10a). As the impedance of the capacitive RF MEMS switch is mainly modified by the changes of its capacitance, the results are presented as changes of capacitance. Although there is a possibility of a calibration of the system, the results are influenced by the impedance of the substrate. The system needs to be calibrated for each substrate material.

It was mentioned that modification of the up- and/or down-state capacitance can be identified as reliability problems. However, in the first phase of the study, the stiction and/or lack of the actuation were dominant effects. Therefore, detection of
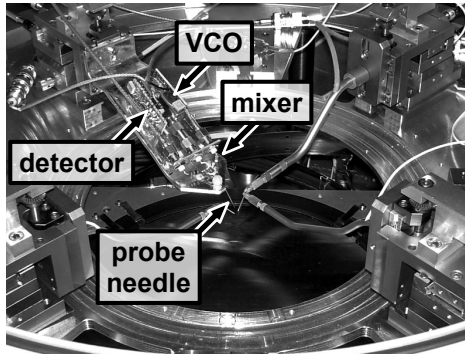
Figure 5.9: The sensing head, integrated with a probing needle, consists of the VCO, mixer and detector.
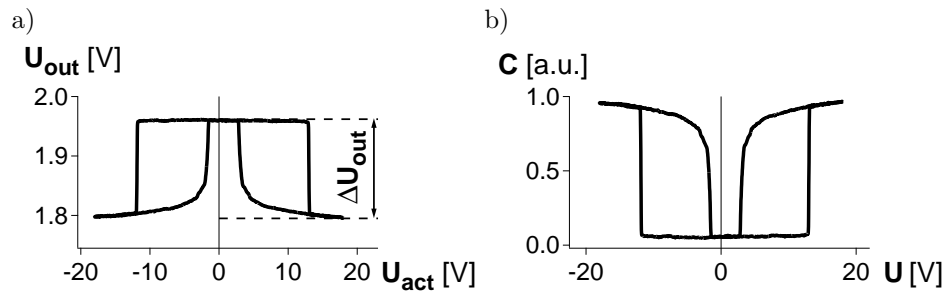
Figure 5.10: The C-V characteristic as measured: the change of the ELT output voltage ΔU_{out} represents changes of the capacitance of the switch during the C-V measurement a). The C-V characteristic measurement is presented as the capacitance C as the signal output follows the changes of the capacitance of the tested switch b).

the presence of pull-in and pull-out (i.e. fast significant change of capacitance) is the most important issue. Information about the absolute capacitance value is less essential. For this reason the calibration was usually omitted.

Nevertheless, as the change of the signal is mainly related to the capacitance changes, the results are presented as capacitance vs. cycles/time (lifetime experiments) or voltage (C-V measurements) with arbitrary units (Figure 5.10b).

5.4.3 Actuation voltage source

In the previous implementation from van Spengen an arbitrary waveform generator (e.g. Agilent 33120A) with a voltage amplifier were employed. The generator is able to generate a wide range of waveforms used for stressing (unipolar and bipolar rectangular with variable amplitude, frequency and duty cycle) as well as the triangular waveform for the C-V characteristic measurements. An arbitrary waveform can be constructed out of limited number of 32000 points. However, switching between different waveform during a lifetime experiment causes unwanted perturbations:

- the time to switch between the waveforms ($\sim 1s$) can influence results of experiments,

- voltage spikes present at the output of the generator can inject additional amount of charge or cause de-trapping of it leading to a misleading result.

The need for limiting the time to switch the waveforms led to the implementation of a data acquisition card (DAQ) with a 16-bit analog output. This results in a waveforms switching time below 100ms and eliminated the problem of the limited number of sample points.

The actuation signal from the data acquisition card is amplified with a voltage amplifier stable (no oscillations) under a capacitive load. Examples of the square waveforms generated by the DAQ + amplifier system are presented in Figures 5.11. To assure high precision of the C-V characteristic measurements, a high linearity of the amplifier is required. The transfer characteristic of the amplifier (Figure 5.12a) shows a high linearity of the amplifier. That results in a shape of the generated triangular waveform as presented in Figure 5.12b.

Another important parameter is the switching speed of the amplifier. The switching time of the voltage actuation source should be lower than the switching time of the tested switches. Preliminary experiments showed switching times of about 100 μs (at 1 atm). The aim was to achieve the switching speed of the amplifier below 10 μs. The results of the switching times measurements are presented in Figures 5.13 and 5.14. The obtained switching on t_{on} and off t_{off} times are 3.65 μs and 3.55 μs, respectively.

5.4.4 System stability

The long term stability of the measurement setup is a key issue for the reliability study. The testing system should give reliable readout throughout the whole experiment time. There are two possible sources of uncertainty in the presented system: the ELT output voltage and the actuation voltage instability.
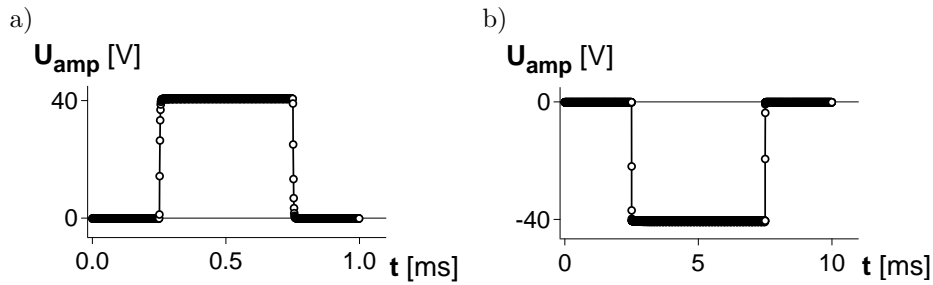
Figure 5.11: Examples of unipolar positive a) and negative b) square waveforms generated by the DAQ+amplifier actuation voltage source.
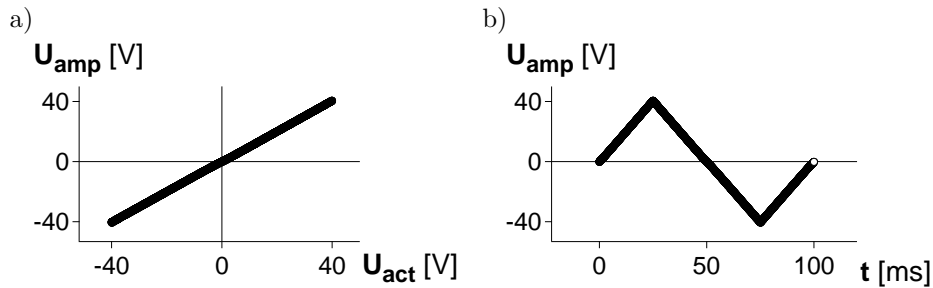
Figure 5.12: High linearity of the DAQ+amplifier system, indicated by the transfer characteristic a), results in a high quality shape of the triangle waveform b) used for C-V characteristic measurements.

The ELT readout stability

To test the stability of the ELT readout, the output voltage U_{out} was measured without any switch connected. The result is presented in Figure 5.15. The U_{out} changed with about 36mV during 310h (14 days) of testing which is more than 20% of the typical voltage swing (100-200mV) observed during a C-V characteristic measurement. The change is relatively large. However, as long as the difference between the C_{up} and C_{down} can be distinguished and the V_{pi} and V_{po} can be defined, the ELT readout instability is not such a big issue. The more important one is the stability of the actuation voltage generation circuit.

The actuation generation stability

The DAQ + amplifier system stability was tested by generating a triangular waveform (bipolar, 10V, 10Hz) and measuring the amplifier output voltage. The experiment was conducted for 310h (14 days) with the output voltage recorded every 1h. The results are presented in Figure 5.16.
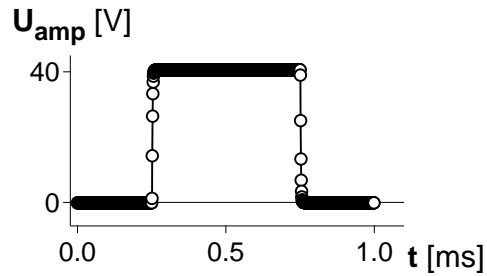
Figure 5.13: A 1kHz 40V square waveform used for the switching time measurements.

a)

b)
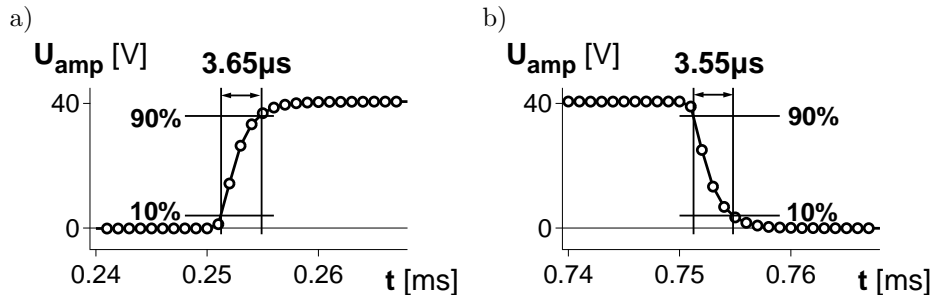
Figure 5.14: The amplifier's switching on t_{on} a) and off t_{off} b) times are equal 3.65 μs and 3.55 μs, respectively.
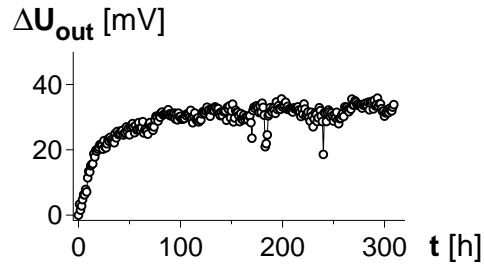
Figure 5.15: The ELT output voltage changed about 36mV during 310h observation.

The drift of 0V, 10V, and -10V potentials were monitored. The mentioned values do not change more than 50mV from the initial value.

a)   b)   c)

$\Delta\mathbf{U_{amp}}$ [mV]
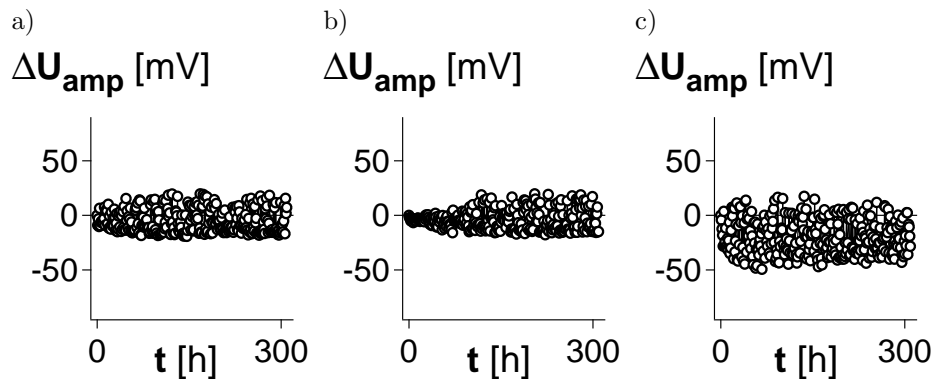
Figure 5.16: The actuation voltage stability test results. The set 0V a), 10V b) and -10V c) voltages drift less than 50mV during 310h observation.
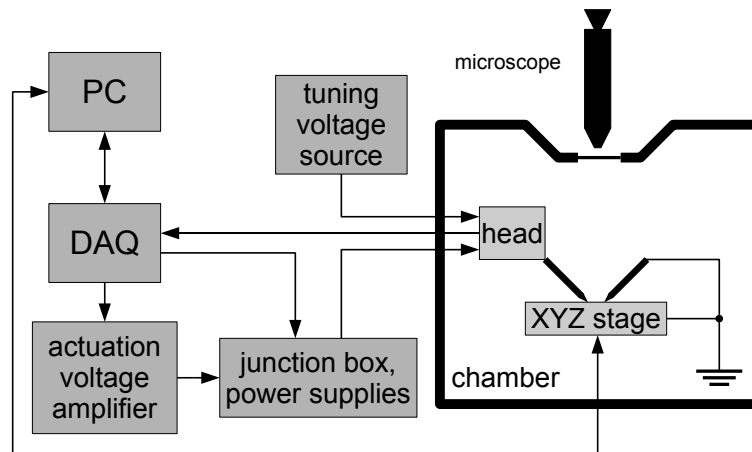
Figure 5.17: The ELT in the PAV.

5.4.5   The ELT setup

The ELT sensing head is only a part of the ELT system. The block diagram is presented in Figure 5.17. The actuation voltage is generated by the DAQ card and is amplified by the voltage amplifier. It can be connected and disconnected from the sample by a relay in the junction box. The junction box contains a power supply for the head. The VCO tuning voltage is supplied by an additional voltage source and modified manually. The measurement signal from the head is fed to an analog input of the DAQ card and collected and processed by the PC. The PC controls the whole ELT+chamber system.
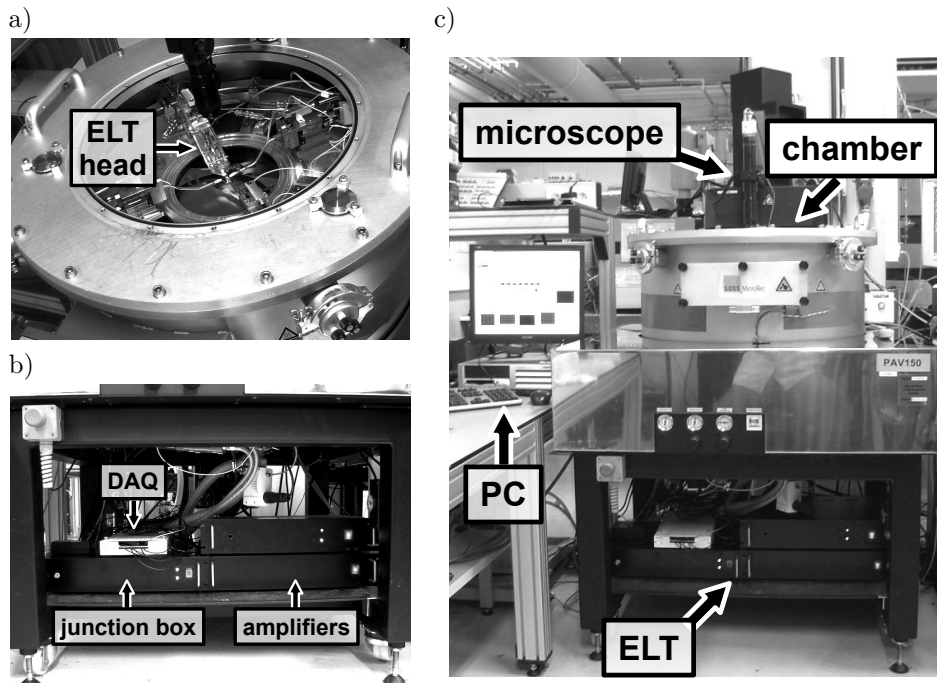
Figure 5.18: The sensing head of the ELT is placed inside an environmental chamber a). The data acquisition card, the voltage amplifiers and the junction box are placed underneath the chamber to minimize the length of the connecting cables b). The system is controlled with a PC c).

5.5 Combination of the ELT and the chamber

In order to assure stable and repeatable test conditions and allow testing the switches under various environmental conditions (temperature, pressure, atmosphere composition), the ELT system is combined with an environmental chamber. The ELT sensing head is placed inside a SussMicrotec PAV-150 environmental chamber (Figure 5.18). The chamber allows DC and RF probing, controlling the temperature and pressure of different gases. The required equipment (DAQ card, voltage amplifiers, junction box, etc.) is placed underneath the chamber to minimize the length of the connecting cables in order to minimize hum and noise.

The automated XYZ stage of the PAV-150 chamber creates the opportunity of automating the measurements. A PC with the National Instruments LabView software allows development of programs that can control the whole experimental setup. The main features of the LabView program (Figure 5.19):

- fully automated wafer screening (C-V measurements),

- fully automated lifetime experiments with several end-of-life criteria,

- observation of the parameters of a tested device (evolution of C_{up}, C_{down}, V_{pi} and V_{po} during an experiment,

- devices stressing with any actuation waveform,

- C-V measurements before, during and after experiments,

- manual and semi-automatic experiments.

The program is open to modifications. It was adopted depending on the performed experiments, to maximize its functionality.
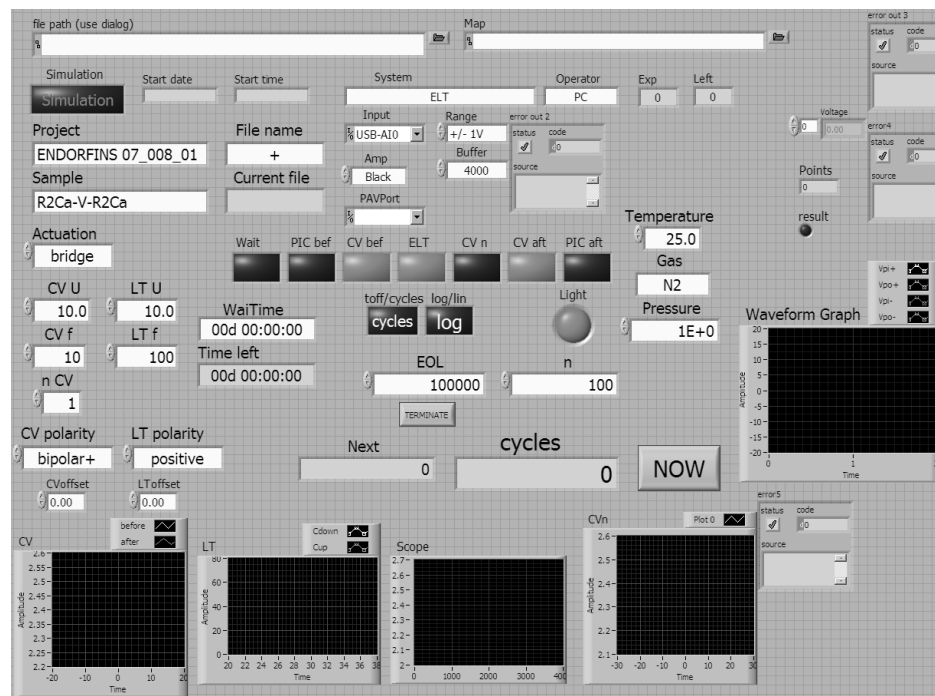
Figure 5.19: A screenshot of the LabView program controlling the ELT+chamber setup.

Chapter 6

Preliminary experiments

This chapter presents results of a preliminary study on the reliability of the capacitive RF MEMS switches. A number of experiments on MIPA and MEMS2TUNE test structures were performed. The presented experiments were chronologically the first experiments performed within the frame of this work. The results pointed to many interesting aspects of charging in capacitive RF MEMS switches. Valuable experience and insight were gained from these experiments. This was used and extended during the later experiments presented in the next sections.

6.1 Influence of biasing: actuation voltage amplitude

6.1.1 Introduction

The goal of the first experiments was to test the lifetime of the MEMS2TUNE capacitive switches. As testing of the devices can take time, an accelerated testing method is desired. However, the accelerated testing requires at least basic knowledge about the mechanism limiting the lifetime.

Assuming the Poole-Frenkel conduction mechanisms governing the dielectric charging, the Goldsmith's model to predict the lifetime can be used. The experiments performed at higher amplitudes of the actuation voltage, when devices fail within a relatively short time, allow plotting the LT vs. U_{act} graph and finding the lifetime at the desired U_{act}. In the same time, the obtained results allow checking the agreement with the model.

6.1.2 Results of the experiments

A number of MEMS2TUNE devices with actuation voltages with an amplitude ranging from +16V to +31V were stressed. The unipolar actuation waveform of 100Hz and 50% duty cycles was used. The EOL90%Δ C criterion was used to determine the lifetime.

Figure 6.1 shows examples of the obtained results. The lifetime experiments at +16V actuation voltage was stopped before the end-of-life point was reached (Figure 6.1a). The lifetime of the switch stressed with +20V was ambiguous (Figure 6.1b). The ΔC decreased after some time, however, not due to an increase of the C_{up}. Therefore, the failure was not caused by the stiction of the beam to the interposer dielectric. The EOL of the switch tested at +26V (Figure 6.1c) was due to stiction: the C_{up} increased significantly.

Figure 6.2 shows the LT vs. U_{act} graph. The lifetime of the switches stressed with a higher actuation voltage is lower than the lifetime of the switches actuated with a lower actuation voltage. The trend is similar to the one predicted by the charging model of Goldsmith [3]. That points to the Poole-Frenkel conduction mechanism as a possible one limiting the lifetime of the switches.

6.1.3 Summary

The slope of the log LT vs. U_{act} curve is not clear. The scattered lifetime results show non-uniformities in the tested structures. E.g. non-uniform thickness of the dielectric layer results in different charging properties. Therefore, an eventual prediction of the lifetime at lower U_{act} can be loaded with a significant error. The limited number of available test structures did not allow performing more experiments.

6.2 Influence of biasing: polarity

6.2.1 Introduction

The next parameter of the actuation voltage that can affect the lifetime of the capacitive RF MEMS switches is the polarity. The structure is highly asymmetric. The dielectric is deposited on the metallic bottom electrode. The top surface of the dielectric layer is exposed to gas (air). The beam touches the dielectric in the actuated state. Though, the top contact can be different than the bottom one. The gas, humidity and contamination, finite roughness, additional oxides on the surface of the beam metal etc. can affect the contact quality changing the charging

a) unipolar, +16V, 100Hz, 50%d.c.

b) unipolar, +20V, 100Hz, 50%d.c.

c) unipolar, +26V, 100Hz, 50%d.c.
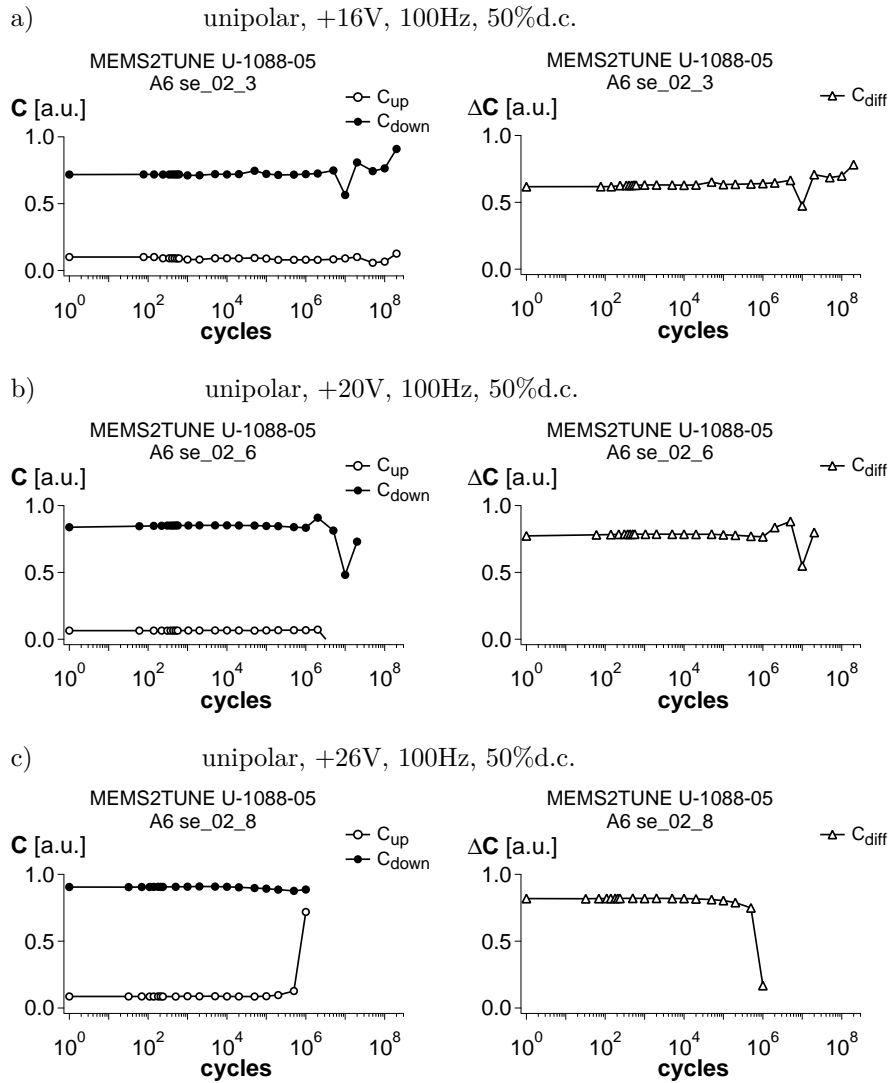
Figure 6.1: Examples of lifetime test results on MEMS2TUNE switches. The switches were tested with various amplitudes of the actuation voltage. The lifetime of the switch tested with the lowest amplitude a) was higher than the lifetime of the switch tested with the highest amplitude c). Test conditions: $25°C$, N_2, 1atm, light on.
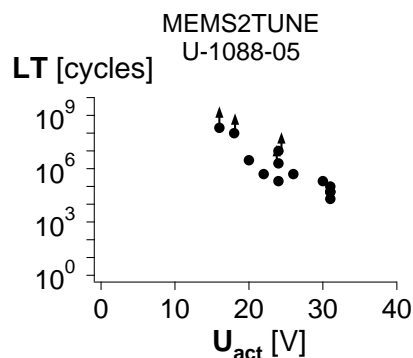
Figure 6.2: The lifetime experiments performed on the MEMS2TUNE switches show an agreement with Goldsmith's charging model. The lifetime of the switches follows the log-lin relation with the amplitude of the actuation voltage. Arrows indicate experiments stopped before end-of-life was reached.

properties. The differences can make the lifetime sensitive to the polarity of the actuation voltage.

6.2.2 Experimental results

To verify the hypothesis, two lifetime experiment with different biasing schemes were performed using the MEMS2TUNE structures. The different senses of the electric field in the gap were obtained by applying an actuation voltage of the same polarity (positive) to either the bottom electrode (Figure 6.3a) or to the beam (Figure 6.3b). That is equal to application of the positive and negative voltages to the bottom electrode. The obtained results are presented in Figure 6.3c-f.

The observed lifetime of the switches stressed with the equivalent positive and negative actuation voltages is 200 and 5000 cycles, respectively. The different lifetime can point to possible different charging time constants. However, it does not say anything about the types of charges trapped in the switch.

More information about the charge trapped in the switches during stressing can be obtained by introducing C-V characteristic measurements. The C-V characteristic is measured before and after the stressing. Changes of the curve can give information about the type of trapped charges (see section 2.5). In this case, different senses of the electric field cause a shift towards positive (Figure 6.3g) or negative (Figure 6.3h) voltage indicating negative and positive charge trapping, respectively.
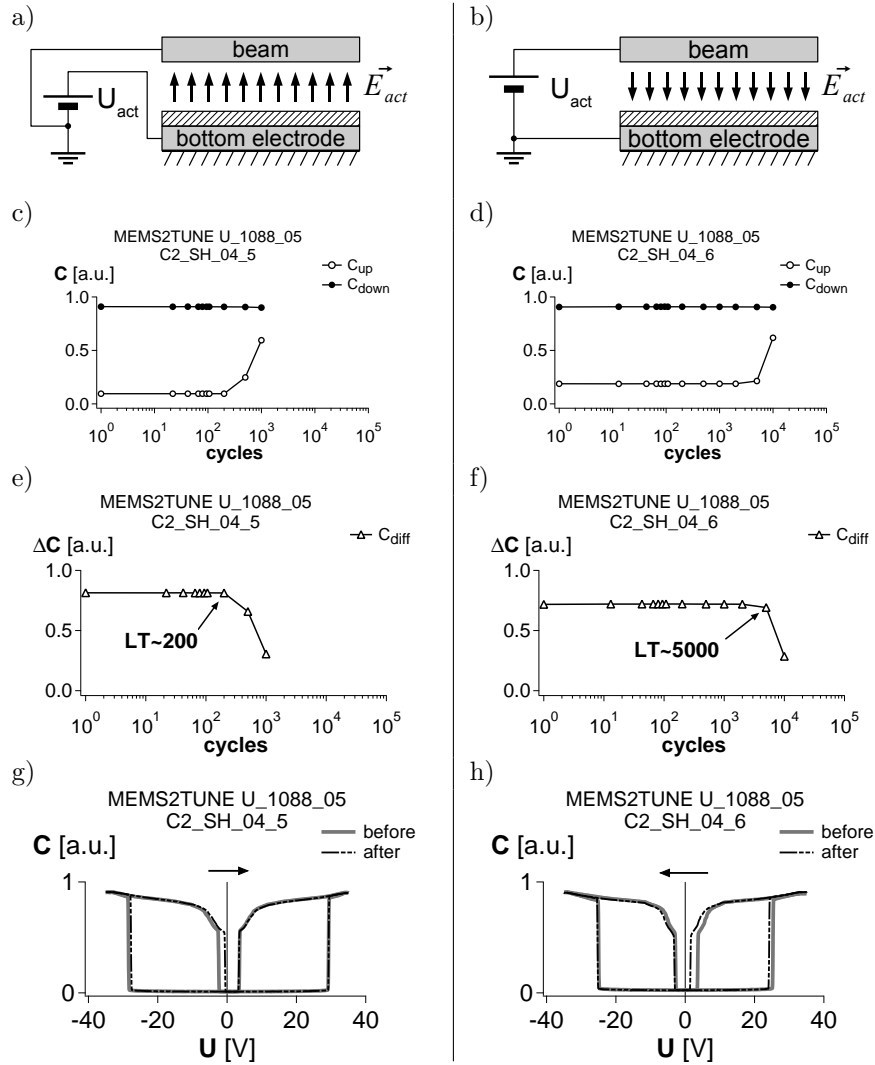
Figure 6.3: The actuation voltage (positive) applied to either the beam a) or to the bottom electrode b) results in the electric field of opposite senses in the gap. The devices stressed with different senses of the electric field exhibit different lifetimes c-f). The direction of the C-V characteristic shift depends on the sense of the electric field as well g-h). Test conditions: 25°C, N_2, 1atm, light on.

6.2.3   Discussion and summary

A shift towards positive voltages is observed when a positive actuation voltage was applied to the bottom electrode. That indicates trapping of negative charges. The negative actuation voltage (i.e. positive voltage to the beam) caused a shift towards negative voltages indicating the positive charge trapping.

The direction of the C-V curve shift, thus the type of the trapped charges, depends on the polarity of the used actuation voltage. The polarity dependent direction of the C-V curve shift was expected. The observed difference in lifetime is attributed to different time constants of trapping positive and negative charges.

6.3   Influence of biasing: waveform shape

6.3.1   Introduction

The previous sections shows the results of experiments performed using actuation voltages of one polarity at a time, i.e. unipolar. However, that is not the only possible way of actuating the capacitive RF MEMS devices.

A bipolar actuation voltage is often proposed as a remedy for the charging. For example, an improvement of the switches' lifetime actuated using the bipolar actuation waveforms is observed by the Lincoln Laboratories and the University of Michigan [4].

The results of experiments presented in this section were supposed to verify the proposed method.

6.3.2   Unipolar vs. bipolar waveforms

The influence of the type of the biasing waveform (uni- vs. bipolar) on the lifetime of the switches was checked using the MIPA switches. Two structures were tested using unipolar and bipolar actuation waveforms (Figure 6.4a and b). The results of the lifetime tests are presented in Figure 6.4c-h.

First, the unipolar actuation voltage was used and a lifetime of $2 \cdot 10^6$ cycles was observed (Figure 6.4c). The increase of the C_{up} indicates the stiction of the beam to the dielectric (Figure 6.4e). The C-V characteristic measurement performed after stressing shows the negative pull-out voltage crossing the 0V point (Figure 6.4g).

Next, a switch was stressed with the bipolar actuation voltage. In this case a decrease of the ΔC was observed as well (Figure 6.4d). However, the C_{up} and C_{down} plots and the C-V characteristic (Figure 6.4f and h) show that the change of the ΔC was not caused by a stiction or a lack of actuation. Both, positive and negative pull-out voltages did not cross the 0V point. The pull-in voltages did not become higher than the actuation voltage. Therefore, the lifetime of the switch stressed with the bipolar actuation voltage is more than the tested $17 \cdot 10^6$ cycles.

The higher lifetime obtained during stressing the devices with the bipolar stressing shows that the use of a bipolar waveform can indeed improve the reliability of the capacitive RF MEMS switches. However, the changes in the C-V characteristic (W_{pi} decrease) allow drawing a conclusion that some kind of charging still takes place. This kind of C-V deformation is described by Rottenberg [305, 309]. The visible narrowing of the C-V curve is attributed to either a non-uniform distribution of the charge or trapping of both, positive and negative, type of charges at the same time. Nevertheless, a failure still can occur.

6.3.3 Fast-switching bipolar actuation waveforms

Another group of actuation waveforms improving the reliability of the switches is proposed in literature [4]. The idea is to apply an alternating actuation voltage as presented in Figure 6.5a. If the time to switch between the polarities is lower than the time-to-off of the switch, then the beam does not react and remains in the down position. Keeping the time of each positive and negative part low is supposed to prevent charge trapping. The t_{off} of the MEMS2TUNE switches is about 150μs (Figure 6.5b) and is much longer than the switching time of the DAQ+amplifier (section 5.4.3). The time of each positive and negative part is set to 50μs. The generated actuation waveform is able to keep the beam in the bottom position during the on-state (Figure 6.5c). The device was stressed for $5 \cdot 10^6$ cycles with the switching frequency of 100Hz and the amplitude of 35V. The capacitance vs. cycles curves (Figure 6.5d and e) show that the switch did not fail during stressing. However, the C-V characteristic measurements show a narrowing of the curve indicating degradation of the switch (Figure 6.5f).

6.3.4 Understanding of the influence of the bipolar waveforms

To understand the functioning of the bipolar actuation waveform a two-phase experiment was proposed. A switch was first stressed with a positive actuation waveform and after some time it was immediately switched to a negative one. The evolution of the C-V characteristic was observed by C-V measurements every $50 \cdot 10^3$ cycles. The positive and negative pull-in and pull-out voltages were extracted and plotted as a function of cycles (Figure 6.6).

a)

b)

c)

MIPA M3.17-IV
BZB

C_{diff}

ΔC [a.u.]

LT~2·10^6

cycles

d)

MIPA M3.17-IV
BYB

C_{diff}

ΔC [a.u.]

cycles

e)

MIPA M3.17-IV
BZB

C_{up}
C_{down}

C [a.u.]

cycles

f)

MIPA M3.17-IV
BYB

C_{up}
C_{down}

C [a.u.]

cycles

g)

MIPA M3.17-IV
BZB

before
after

C [a.u.]

U [V]

h)

MIPA M3.17-IV
BYB

before
after

C [a.u.]

U [V]
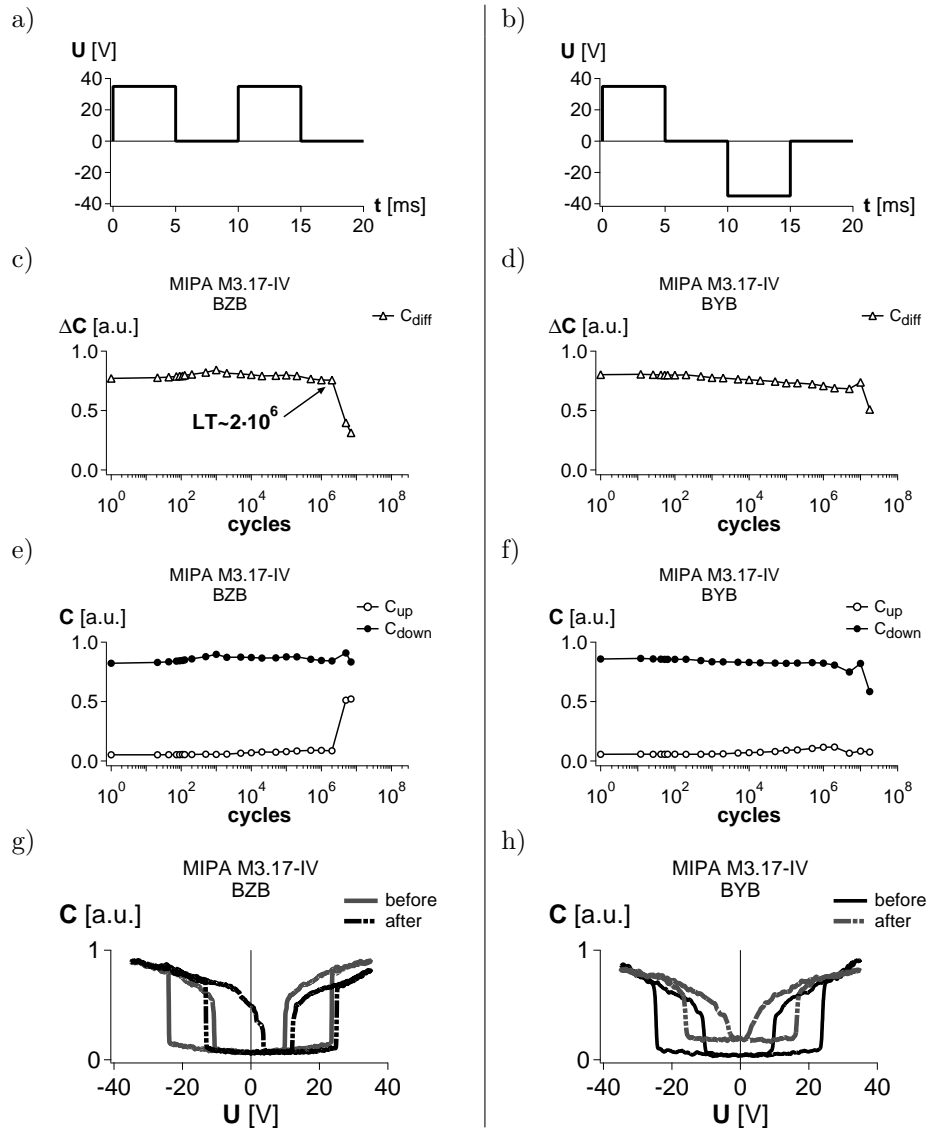
Figure 6.4: The lifetime results obtained during stressing with unipolar a) and bipolar b) actuation waveforms are $2 \cdot 10^6$ e) and more than $17 \cdot 10^6$ f) cycles, respectively. The EOL is caused by the shift g) or the narrowing h) of the C-V characteristic. That indicates different mechanisms responsible for the failures. Test conditions: $25^\circ C$, N$_2$, 1atm, light on.

a)

U [V]

50µs

40
20
0
-20
-40

0   5   10   15   20   **t** [ms]

b)

MEMS2TUNE U-1088-05
A6 se_02_3

C [a.u.]

150µs

1.0
0.5
0.0

4.8   5.0   5.2 **t** [ms] 5.4

c)

C [a.u.]

1.0
0.5
0.0

0   5   10   **t** [ms]

d)

MEMS2TUNE U_1088_05
C2 sh_04_4

C [a.u.]

C_{up}
C_{down}

1.0
0.5
0.0

10^0 10^2 10^4 10^6 **cycles**

e)

MEMS2TUNE U_1088_05
C2 sh_04_4

Δ**C** [a.u.]

C_{diff}

1.0
0.5
0.0

10^0 10^2 10^4 10^6 **cycles**

f)

MEMS2TUNE U_1088_05
C2 sh_04_4

C [a.u.]

before
after

1
0

-40   -20   0   20   40   **U** [V]
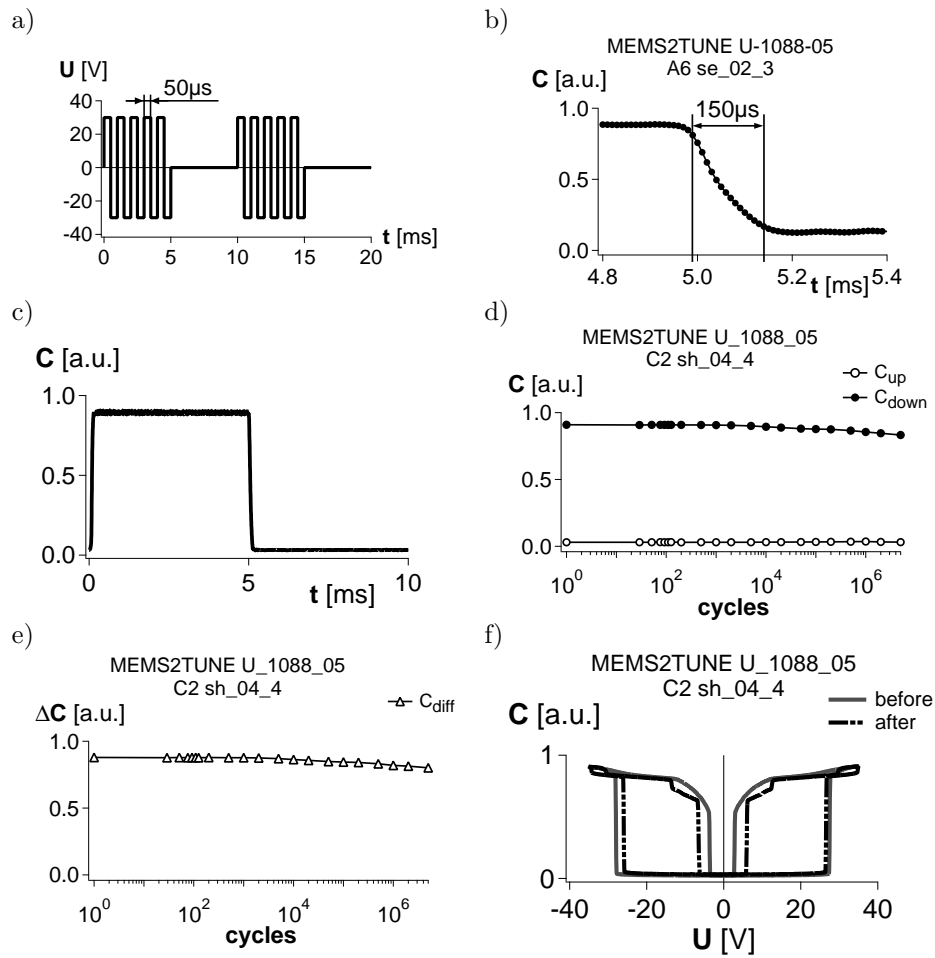
Figure 6.5: The high capacitance in the on time shows that the beam remains in the down position during switching with the fast bipolar actuation voltage. Test conditions: $25°C$, N_2, 1atm, light on.
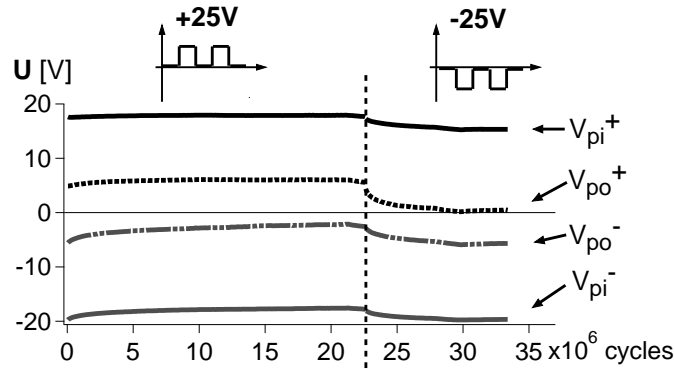
Figure 6.6: The C-V shifts towards positive voltages during the first phase (positive stressing). During the second phase (negative stressing) the C-V shifts back to the center and further, towards the negative voltages. The narrowing of the C-V characteristic, decrease of the pull-in and pull-out window, is attributed to trapping both types of charges at the same time. Test conditions: $25°C$, N_2, 1atm, light on.

The C-V curve shifts towards positive voltages during the first phase. Then, the negative actuation part causes a shift of the C-V towards the negative voltages. The positive charge causing the shift during the positive stressing phase seems to be de-trapped and replaced with charge of opposite polarity during the second phase. Yet, not all the charge is de-trapped. The visible narrowing of the C-V curve indicates some remaining charge. The narrowing of the C-V characteristic is attributed to trapping of two types of charges (see section 2.5.4). It is highly possible that after some time of stressing a failure will occur.

6.3.5 Summary and conclusions

It is shown that the bipolar actuation waveforms can improve the reliability of the capacitive RF MEMS switches, i.e. enhance their lifetime. However, the presented method does not solve the charging problem. The narrowing of the C-V characteristic observed during stressing is attributed to trapping of two types of charges. As one part of the stressing waveform (e.g. positive) causes trapping of one type of charges, the second part (e.g. negative) can let part of the trapped charge escape. However, it causes additional trapping of charge of opposite polarity in the same time.

a)

V_{po}^- [V]

b)

V_{po}^- [V]
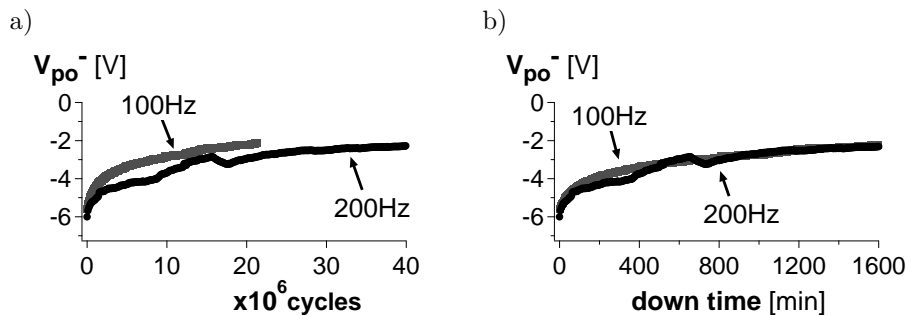
Figure 6.7: The results of lifetime experiments performed at different frequencies of the actuation voltage. The lifetime expressed in the number of cycles shows different results a). However, the results are the same when expressed in the down-time b). Test conditions: $25°C$, N_2, 1atm, light on.

6.4 Influence of biasing: frequency

6.4.1 Introduction

A study of the influence of the actuation waveform frequency on the lifetime of the capacitive switches was presented by van Spengen [313]. The results show that the lifetime of the switches is determined by the total down state and not the number of switching cycles.

To confirm the observations, the MEMS2TUNE devices were stressed with actuation waveforms of various frequencies. The degradation of the devices was monitored using the technique introduced in the previous section: C-V characteristic measurements during stressing.

6.4.2 Results

Figure 6.7 shows the evolution of the negative pull-out voltage as a function of switching cycles (a) and the down-state time (b). In both cases, the V_{po}^- is approaching the 0V level indicating charge trapping.

The pull-out voltage recorded during stressing a device with 100Hz seems to change faster than when the 200Hz waveform is used. However, it can be illusive. When the pull-out evolution is showed as a function of the down-state time then a similar degradation of the devices (C-V characteristic shift) is observed.

6.4.3 Summary and conclusions

The results show that the charge trapping can be a mechanism governed by the time and not the number of switching cycles. Charge trapping occurs when an electric field across the dielectric is present. That happens when an actuation voltage is applied and the beam is in the down position touching the dielectric.

The difference between the lifetime expressed in cycles and time shows that a comparison of lifetime of two different switches cannot be made based only on the reported number of switching cycles. Devices tested at different switching frequencies may exhibit different lifetime, although, suffering from the charge trapping in a similar way.

The information about the frequency of the stressing actuation voltage is important. Two different devices should be tested at the same frequency, the obtained lifetime should be expressed in the down-state time or the testing conditions should be at least mentioned.

6.5 Influence of biasing: duty cycle

6.5.1 Introduction

The bipolar actuation experiment showed that the trapped charge can be (partially) de-trapped by applying an external field of opposite polarity. However, it is possible that the charge can be released if a previously stressed switch is not actuated. A switch that reached end-of-life could recover when not actuated for some time. An experiment to check that issue was proposed and discussed in the following.

6.5.2 Irregular C-V measurements

As the full C-V characteristic is measured using the bipolar triangular waveform, the C-V measurement itself could cause a release of the trapped charge. Therefore, the C-V curve was measured not every 30 minutes as commonly done (Figure 6.8a). The measurements were taken in consecutive 10 and 50 minutes periods (Figure 6.8b).

C-V measurements performed in regular time periods do not allow distinguishing between the spontaneous and C-V measurement induced charge de-trapping. A plot of V_{po}^{+} evolution in time obtained from C-V measurements taken every 30 min would show a continuous decrease (Figure 6.8c). That can be observed when either of the two de-trapping mechanisms occurs.

The (10+50) method clearly differentiates the two mechanisms. If the charge was de-trapped mainly due to the negative part of the C-V measurements then the change of the pull-in and pull-out voltage would run in steps (Figure 6.8d).

6.5.3 Charge de-trapping observation

First, a MEMS2TUNE switch was stressed for a number of cycles. A unipolar actuation voltage was used and the C-V characteristic before and after stressing was measured. The C-V curve changes indicate that some charge is trapped during stressing (Figure 6.9). Next, the device was kept un-actuated and the C-V characteristic was monitored every 10 and every 50 min.

The evolution of the V_{pi} and V_{po} are presented in Figure 6.10a. The C-V characteristic, shifted towards the positive voltages during stressing, shifts back to 0V and becomes symmetric, indicating de-trapping of the trapped charge. A closer look to the C-V evolution (Figure 6.8d) shows that the change of the e.g. positive pull-out voltage between two C-V measurements taken in 10 minutes slightly shifts towards positive voltages (Figure 6.10b). The C-V measurement causes additional trapping of the charge that is not fully released before the next measurement performed 10 minutes later. The 50 minutes time distance seems long enough to de-trap the charge trapped during the C-V measurement and part of the charge trapped during initial stressing. This confirms that the C-V measurement, although it is very fast, affects the measurement.

Despite the impact of the C-V measurements, the experiment shows that the charge trapped during stressing can be de-trapped when the device is not actuated. In that case, the duty cycle of the actuation voltage waveform should have an impact of the lifetime of the switches. This is verified in the following experiment.

6.5.4 Impact of the duty cycle

Two more MEMS2TUNE switches were stressed with unipolar actuation voltages. A duty cycle of 50%, 80% and 100% was used. The amplitude of 25V and frequency of 100Hz were fixed. The evolution of the C-V characteristic was observed by C-V measurements every $50 \cdot 10^3$ cycles (i.e. 8.3 min). Figure 6.11 shows the obtained relative changes of the negative pull-out voltages as a function of the down-state time obtained during a 50% duty cycle lifetime test. The V_{po}^- changes faster when waveforms of a higher duty cycle are used, even if compared within the same down-state time.
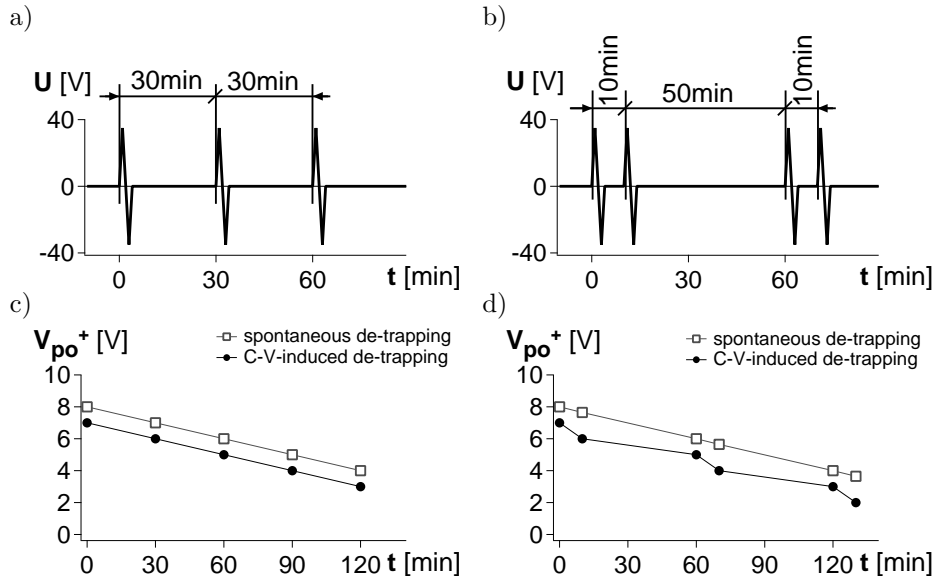
Figure 6.8: The simulations of the V_{po}^+ evolution expected with regular a) and irregular b) C-V characteristic measurements. The (10+50) minute method allows distinguishing between the spontaneous and C-V measurement induced charge de-trapping d).
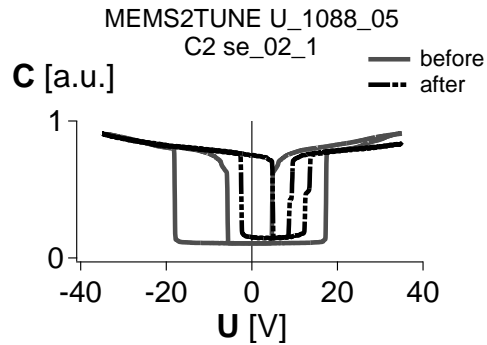
Figure 6.9: The C-V characteristic of the device measured before and after stressing with a positive actuation voltage (25V, 100Hz, 50%d.c.). Test conditions: $25°C$, N_2, 1atm, light on.

a)

b)
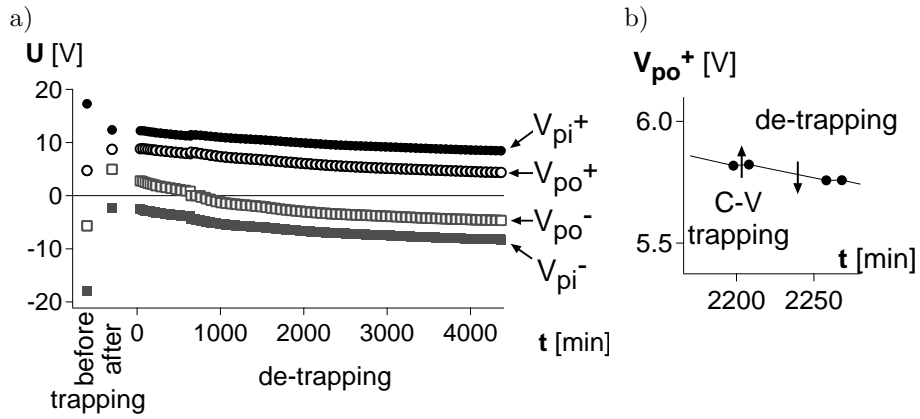
Figure 6.10: The shift of the C-V curve disappears. The C-V curve center shifts back to the 0V position indicating release of the charge a). A closer look at the evolution of the positive pull-out voltage b) shows that the measurement of the C-V characteristic causes trapping of a small portion of charge. Test conditions: $25°C$, N_2, 1atm, light on.
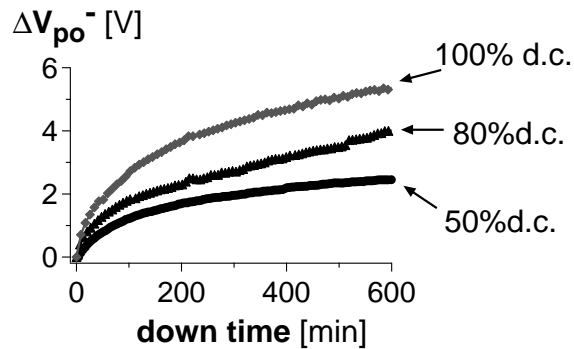
Figure 6.11: Stressing with waveforms of higher duty cycle results in faster changes of the C-V characteristic. Test conditions: $25°C$, N_2, 1atm, light on.

6.5.5 Summary and conclusions

The presented results impair the hypothesis about the down-state time determining the lifetime. It is observed that the up-to-down time ratio, determined by the duty cycle of the actuation voltage waveform, can also influence the lifetime. The charge trapped during the on-state can be released during the off-state. The higher the up-to-down time ratio is, the higher lifetime of the switch can be obtained.

The observed effect proves that the lifetime of the capacitive RF MEMS switches is sensitive to the up-to-down time ratio. That will have an impact on the use of the switch in different applications. The use of the switches in particular systems should be optimized in order to obtain a high lifetime.

6.6 Impact of environment: atmosphere composition

6.6.1 Introduction

It has been pointed out that the lifetime of the switches can be influenced by the environment [336]. The observed lower lifetime of switches tested in ambient air, with respect to the results obtained in N_2, is attributed to the humidity present in the air. The humidity can enhance charge trapping. To verify the hypothesis, a similar experiment was performed. The influence of the atmosphere on the lifetime of the capacitive switches was tested. The results are discussed in the following section.

6.6.2 Results

Two MIPA switches in dry N_2 and ambient air atmosphere using the same amplitude of the actuation voltage were tested. The results are presented in Figure 6.12a. The lifetime of the switch tested in ambient air is about 500 times lower than the lifetime of the switch tested in N_2.

The hypothesis about the humidity influencing the lifetime can be further verified by testing a switch in a different, yet dry, gas atmosphere. Out of a large number of possibilities, helium was chosen. It was a relatively easy-accessible and safe candidate.

Another MIPA device was tested in He atmosphere. Due to observed disturbances, the lifetime experiment was performed using a lower actuation voltage Ű 30V. The result, compared with the one obtained in dry N_2 atmosphere, is presented in

Figure 6.12b. The lifetime of the switch tested in He is lower (a factor of 10) even though it was tested with a lower actuation voltage.

As the used He was dry, humidity could not be the (only) cause of the lower lifetime.
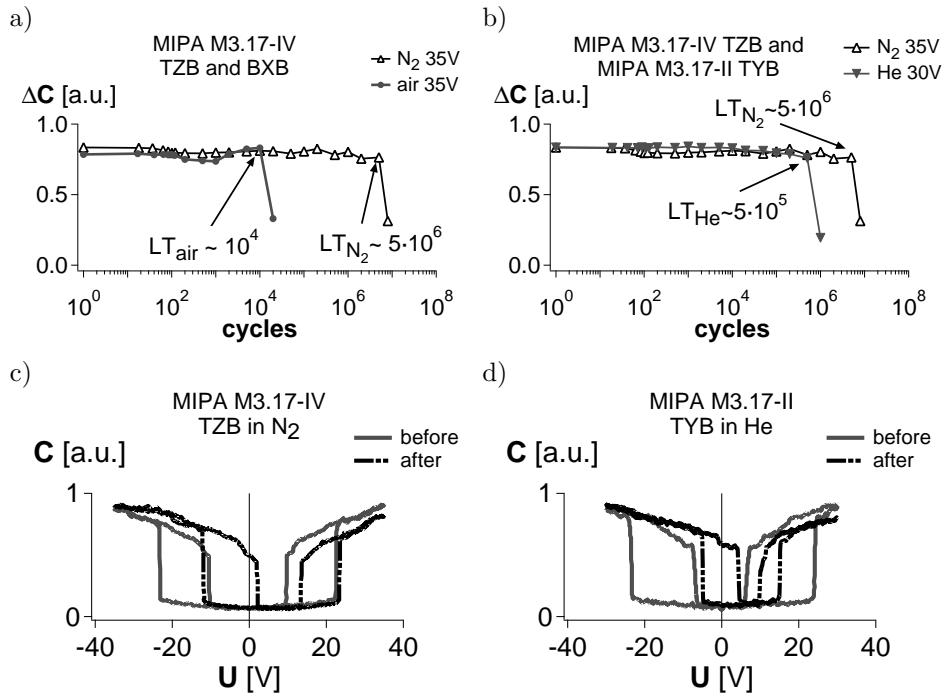
Figure 6.12: Lifetime of a switch tested in ambient air is lower than the lifetime of a switch tested in N_2 atmosphere at the same amplitude of the actuation voltage a). The lifetime of a switch tested in He atmosphere is lower than the lifetime of a switch tested in N_2 atmosphere b). The lifetime of the switch tested in He was expected to be higher due to lower actuation voltage. The shift and narrowing of the C-V characteristics indicate EOL due to charging c) and d). Test conditions: $25°C$, light on.

6.6.3 Discussion

Another difference between the two gases lies in their electrical properties. That can be a possible factor influencing the lifetime of the switches.

Indeed, there is a significant difference in electric strength of helium and nitrogen gases. The nitrogen electric strength is about 1kV/mm and the helium electric

strength is about 150V/mm [437]. The lower breakdown voltage of He corresponds to the observed lower lifetime.

The electric strength of the ambient air can also be different. It may vary between 0.4kV/mm and 1.5kV/mm as reported by Vijh, Kubuku and Al-Arainy [437]. Moreover, it depends on the humidity of the air: the higher the air humidity is, the lower the breakdown voltage is. The breakdown voltage depends on the type of atmosphere [440], shape and material of the electrodes [438] and the surface conditions (roughness, pollution etc.) as well [439].

Ionization of the gas, due to the electric breakdown, generates ions that can be trapped on the surface of the dielectric layer. In a system of two electrodes, one covered with a dielectric layer, a back discharge can occur resulting in the dielectric charging as well.

The phenomenon is used for electrets formation. Dielectric material is placed close to two electrodes and a gas discharge, usually corona discharge, is invoked [441–445].

The breakdown of the gas can be influenced by charge trapped in the dielectric due to other mechanisms. The charge modifies the distribution of the electric field and can initiate the gas discharge even if it could not occur when no charge was trapped [446, 447].

A more detailed study of this phenomena was foreseen. A number of test structures to study this phenomenon were designed. However, the test structures could not be used due to processing problems.

6.6.4 Summary and conclusions

The influence of the composition of the ambient atmosphere on the lifetime of the capacitive RF MEMS switches has been presented. A stable and humidity-free environment should be assured for reliable operation of the switches. A hermetic package, filled with a gas (or a mixture of gases) of a high electric constant, seems to be necessary. That requirement may have a big impact of the design and fabrication of not only the capacitive RF MEMS switches. Reliability of any electrostatically driven MEMS device can be affected by the environment.

6.7 Impact of environment: gas pressure

6.7.1 Introduction

The previous section presents the influence of the ambient gas on the lifetime of the capacitive RF MEMS switches. The observed difference in the lifetime of switches tested in different environmental conditions was attributed to mainly two aspects: humidity and gas breakdown. Both are possible sources of additional charge trapping lowering the lifetime of the switches.

The lifetime of the switches seems proportional to the electric strength of the ambient gas: the lower the electric strength is, the lower the lifetime of the switch is. Different breakdown voltages can be obtained by changing the ambient gas.

The electric breakdown between two electrodes separated with a gap filled with a particular gas occurs at a breakdown voltage V_{br}. V_{br} depends on the pressure of the gas and the distance between the electrodes. The relationship between the breakdown voltage, pressure and gap size (6.1) was presented by Paschen in 1889 [452]. Figure 6.13 shows the V_{br} vs. $p \times d$ curve. The breakdown voltage decreases with decreasing $p \times d$ product until it reaches a minimum. Further decreasing of the $p \times d$ causes an increase of the breakdown voltage.

$$V_{br} = \frac{a(p \times d)}{ln(p \times d) + b} \qquad (6.1)$$

where:
V_{br} - breakdown voltage,
p - gas pressure,
d - distance between the electrodes,
a, b - gas composition dependent constants.

6.7.2 Lifetime vs. pressure

The lifetime of several MEMS2TUNE switches was tested under various pressure of N_2. The devices were stressed using a positive 100Hz, 50% d.c. actuation voltage applied to the bottom electrode. Figure 6.14a shows results of the experiment.

The lifetime of the devices depends on the pressure. It decreases with decreasing gas pressure. Below 20mbar the lifetime of the tested switches was about 100 cycles. A further decrease of the pressure did not show any change. At 10^{-8} bar the lifetime of the tested switch was similar to the one obtained at 20mbar (Figure 6.14b). If the lifetime was limited due to the breakdown of the gas following
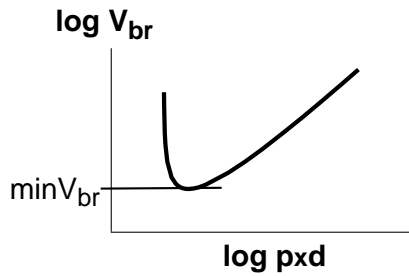
Figure 6.13: Paschen's curve shows that decreasing $p \times d$ results in a decrease of the breakdown voltage V_{br}. There is a minimal breakdown voltage for a certain $p \times d$ value. Further decreasing the pressure or distance causes an increase of the V_{br}.
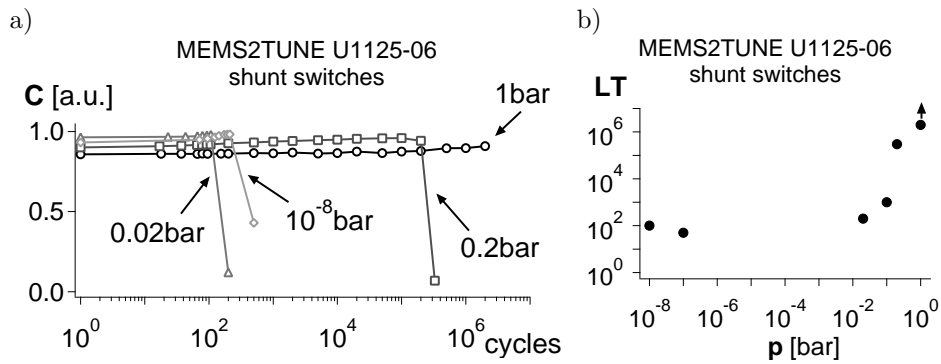
Figure 6.14: Lifetime of the switches is related to the pressure of the ambient gas. Lowering the pressure of the gas resulted in a decrease of the lifetime a). No lifetime improvement is observed at $10^{-7} - 10^{-8}$ bar pressure. Test conditions: 35V, positive actuation voltage, 100Hz, 50%d.c., 25°C, light on.

Paschen's law, then an improvement in lifetime should be observed at very low pressure (thus the $p \times d$).

6.7.3 Deviation from Paschen's law

According to Paschen's law, an increase of the breakdown voltage should be observed at a $(p \times d)$ left from the min V_{br} point. Therefore, the breakdown of the gas was not expected to take place in MEMS. Dimensions in the order of μm guaranteed operating in the safe area left from the minimal breakdown voltage.
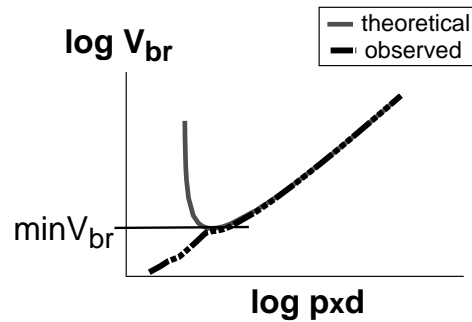
Figure 6.15: The observed V_{br} vs. $p \times d$ curve for low gaps is different than the theoretical Paschen's curve. The breakdown voltage does not increase when the $p \times d$ product is decreased below the min V_{br} point [448–450].

However, a discrepancy between the theoretical model and the observed results has been shown in literature as well. If the distance between the electrodes is lower than about 4-5 μm, then there is no increase of the breakdown voltage with decreasing the $p \times d$ product (Figure 6.15) [448–450]. The breakdown, in the case of 4-5μm air gaps, is similar to the breakdown of vacuum gaps of less than $200\mu m$. Breakdown of vacuum is mainly attributed to the electron field emission as the gas ionization is less probable.

In the case of the gaps higher than the mentioned 4-5μm, the ionization can be induced by electron field emission from the electrodes. The electron field emission is strongly related to the material of the electrodes. Therefore, the breakdown voltage, for low gaps, may depend on the electrodes material as well [451].

6.7.4   Influence of biasing scheme

The observed degradation of the lifetime of the capacitive RF MEMS switches with decreasing ambient pressure is attributed to the breakdown of the gas. Therefore, the biasing scheme is expected to have a big impact on the lifetime.

First, the influence of the polarity (positive and negative) and type of biasing waveform (unipolar and bipolar) on the lifetime of the switches at lower pressure was tested. Several lifetime experiments using the MEMS2TUNE switches under various conditions were performed. The results are presented in Figure 6.16.

No significant difference between the lifetimes of the switches tested using the positive and negative actuation voltage was observed. The switches stressed with the unipolar and bipolar waveforms achieved similar lifetimes. The difference (a factor of 10) is similar to the one observed at atmospheric pressure.
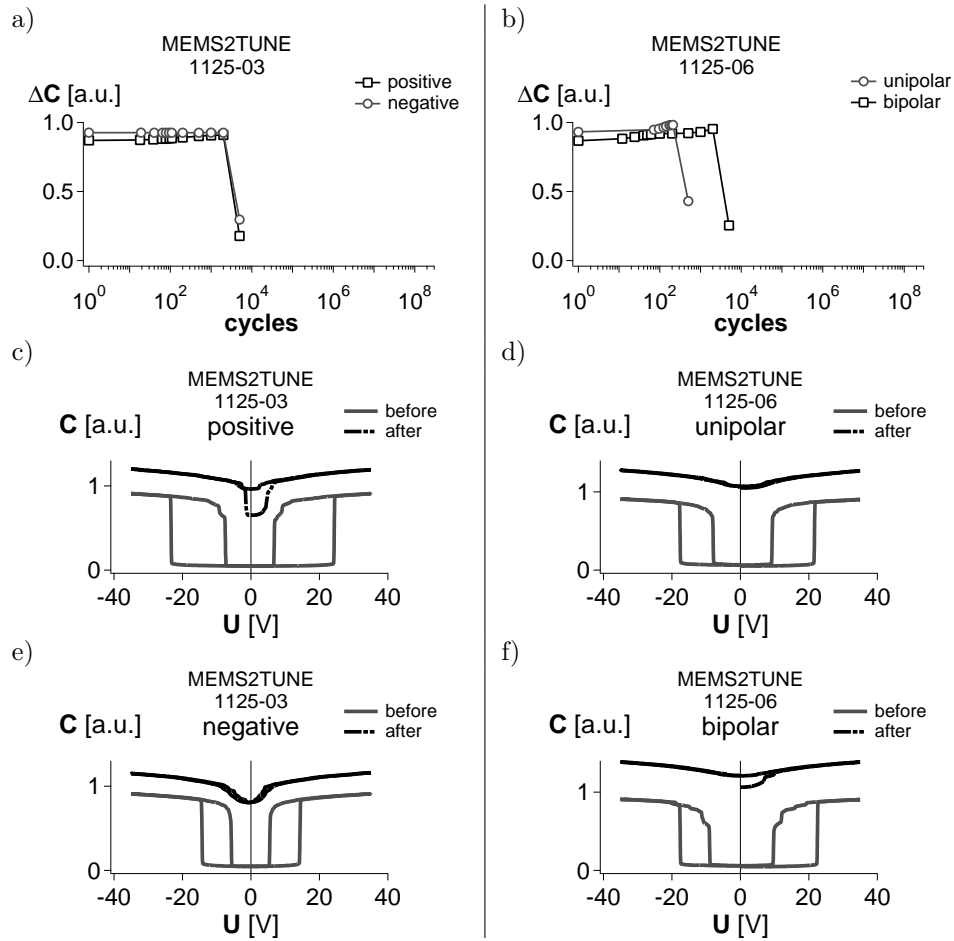
Figure 6.16: No difference in lifetime of the devices stressed with the positive and negative actuation voltages at 0.1bar is observed a). The difference between the lifetime of the devices actuated with the unipolar and bipolar waveforms at 10^{-8}bar (a factor of 10) is similar to the one observed at atmospheric pressure. Distinguishing the type of charges causing the failure is difficult as mainly the narrowing of the C-V characteristic is observed c-f). Test conditions: N_2, 35V, 100Hz, 50% d.c., 25°C, light on.
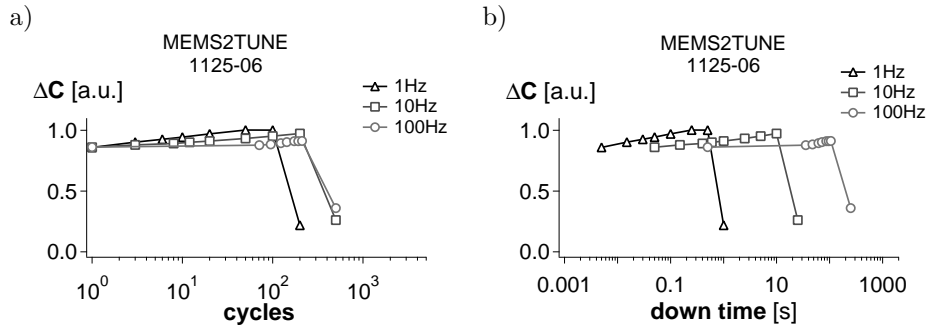
Figure 6.17: At 10^{-8}bar the lifetime of the switches is determined by the number of up-to-down (or down-to-up) transitions independently on the down state time. Test conditions: 35V, 50%d.c., 25°C, light on.

More experiments to understand the influence of the polarity of the actuation waveform on the lifetime at low pressure should be performed.

6.7.5 Influence of frequency and duty cycle

No big impact of the polarity (positive vs. negative) and shape (unipolar vs. bipolar) of the actuation voltage is observed. However, there are other properties of the actuation voltage that may have an influence on the lifetime of the switches. Therefore, a number of experiments including stressing the devices with various values of the frequency and duty cycle of the actuation waveform were performed.

First, lifetime of a number of MEMS2TUNE switches using waveforms with frequencies of 1Hz, 10Hz and 100Hz was tested. The devices obtained similar lifetime expressed in number of cycles (Figure 6.17a). However, the lifetime is different if plotted as a function of the down-state time (Figure 6.17b). This is opposite to what was observed at atmospheric pressure (see section 6.4). This observation points to the transitions, up-to-down or down-to-up, being responsible for the failure.

An experiment that could help verifying this hypothesis was proposed. Two devices were stressed using actuation waveforms emphasizing charging either during the transitions or during the down position. The first waveform mimics the initial part of the up-to-down transitions (Figure 6.18b). It contains a number of pulses, short enough to avoid the beam-dielectric contact. Keeping the period of the pulses shorter than the t_{on} makes the beam stay in the up position. So, charge trapping due to high field across the dielectric should be reduced. The t_{on} at $2 \cdot 10^{-8}$bar was determined from one of the previous experiments and is equal to about $40\mu s$

(Figure 6.18a). Therefore, $10\mu s$ wide pulses are adequate. The standard frequency of 100Hz was used.

Figure 6.18d shows that the capacitance of the device remains low during the experiment, indicating a lack of the beam-dielectric contact, as intended. Nevertheless, the device failed after 300 pulses due to narrowing of the C-V characteristic (Figure 6.18f). In the second part of the experiment a DC voltage of 35V for a period of 98s was applied to the device (Figure 6.18c). The device stayed in the bottom position during the measurement (Figure 6.18e). The C-V characteristic measured after the stressing shows no changes with respect to the curve measured before the experiment (Figure 6.18g).

Considering the duty cycle of the waveforms, the results are opposite to the ones obtained at atmospheric pressure (see section 6.5). The dielectric of the switch actuated with the $10\mu s$ pulses, was effectively stressed with 0% duty cycle voltage. Though, it showed more changes than the switch actuated with the DC actuation voltage.

6.7.6 More experiments

The lifetime of more MEMS2TUNE devices was tested under various pressures and amplitudes of the actuation voltage. Changing the amplitude allows obtaining "high" ($> 10^5$ cycles) and "low" ($< 10^3$ cycles) lifetime at each pressure level (Figure 6.19a). I.e. it is possible to improve the lifetime at the same amplitude of the actuation voltage by changing the pressure.

Figure 6.19b shows a comparison of the data obtained at 1mbar and 1bar. The slope of the LT vs. U_{act} curves is different. That may indicate an additional mechanism limiting the lifetime.

6.7.7 Discussion

Section 6.6 describes the observed impact of the ambient atmosphere composition on the lifetime of the capacitive RF MEMS switches. A different lifetime is observed when devices are tested in various types of gases. Switches tested in He exhibit a lower lifetime than the ones tested in N_2. The two gases have different breakdown voltage: 150V/mm and 1kV/mm for He and N_2, respectively. Therefore, the lifetime limitation is attributed to the gas breakdown that can occur during actuation of the switch. Charges generated during the breakdown (ionization) may be trapped and limit the lifetime of the switches.

The breakdown voltage of one type of gas can be modified by changing its pressure. According to Paschen's law, the breakdown voltage changes with the changing
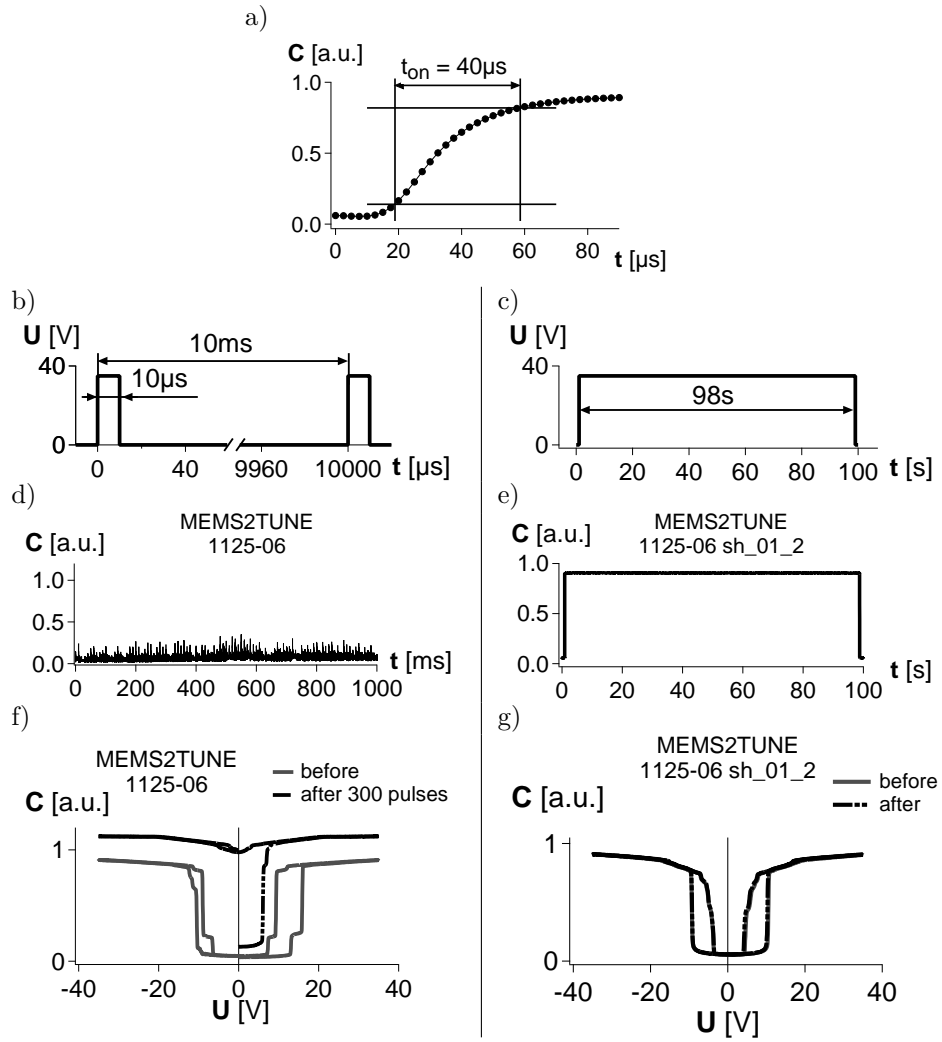
Figure 6.18: The pull-in (up-down) transition time t_{on} in vacuum is reduced to about $40\mu s$ a). The short-pulses waveform b), keeping the beam remaining in the top position (low capacitance d), causes a failure after about 300 cycles due to narrowing of the C-V characteristic f). A DC voltage c) makes the beam touch the dielectric (high capacitance e). However, even after 98s the changes of the C-V curve are minor g). Test conditions: $25°C$, light on.
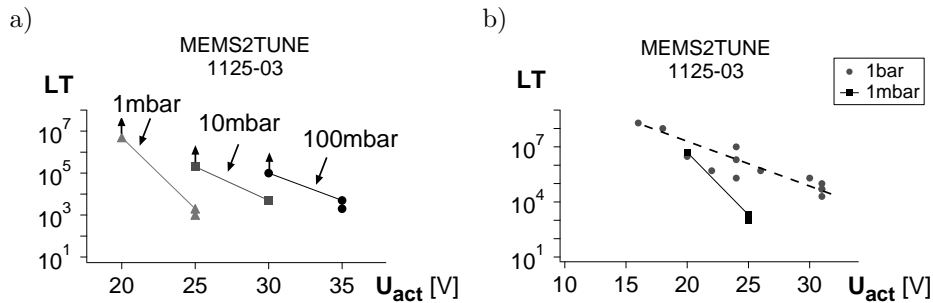
Figure 6.19: "High" ($> 10^5$ cycles) and "low" ($< 10^3$ cycles) lifetime is observed at each pressure level if the U_{act} amplitude is changed a). The slope of the LT vs. U_{act} curve depends on the pressure indicates additional factor limitting the lifetime b).

pressure of the gas. The observed relation between the lifetime and the pressure of the ambient gas seems to prove the hypothesis about the breakdown limiting the lifetime.

Paschen's law describes an increase of the breakdown voltage left to the minimum. This was not observed. The experiments show no improvement of lifetime at low values of the $p \times d$ component. However, that corresponds to the modified Paschen curve for low gaps ($< 4\mu m$). The breakdown voltage decreases with decreasing $p \times d$ component. This is due to electron emission initiating gas ionization.

It is shown that the degradation of the devices at low pressure (10^{-8} mbar) is not due to charging of the interposer dielectric in the actuated state. The lifetime is limited by the number of up-down transitions of the switch independently on the frequency and duty cycle. A failure is observed even if the beam is not touching the dielectric during stressing.

The link between the gas composition, pressure and amplitude of the actuation voltage points to a gas breakdown. It is highly possible that the breakdown is initiated by an electron emission from the electrodes. Performing more experiments would help in plotting a Paschen's curve and determining the d parameter at which breakdown occurs. The known value of the gap size would help in finding the breakdown place. The breakdown does not have to occur always in the same place. The position of the breakdown may also depend on the pressure and the applied voltage. The gap between the beam and the dielectric is not the only possible place. The breakdown can occur in any place between the electrodes as well (Figure 6.20).
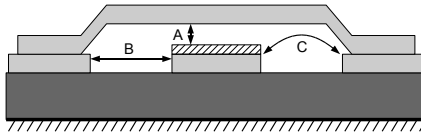
Figure 6.20: The breakdown can occur in different places: between the beam and the dielectric A, between the actuation electrode and the ground plane B. It can occur even if the shortest distance between the edges of the electrodes is lower than the critical distance at given pressure and voltage. Particles can travel along longer field lines C d).

6.7.8   Summary and conclusions

The results presented in this section show that the MEMS devices can be sensitive to the environmental conditions. The earlier presented impact of humidity is not the only environment related factor influencing the reliability of the devices. The type of used atmosphere and its pressure may also have a huge impact on the lifetime. Some part of the environment related issues can be solved by a proper design and choice of material. However, in some cases a need for a use of hermetic packages seems mandatory.

6.8   Summary and conclusions

The preliminary experiments presented in this chapter were performed on a limited number of available devices. However, it is shown that he lifetime of the capacitive RF MEMS switches can depend on many factors influencing charging. The amplitude, polarity, shape, frequency, duty cycle need to be taken into account during designing a switch. The influence of the environment cannot be neglected. The lifetime can depend on the environmental conditions that cannot be forgotten during the design phase.

The presented results show that the Poole-Frenkel mechanism, considered the main source of failures, is a possibility. However, the lifetime can depend on many other factors as well.

Finally, these first experiments allowed development of new testing techniques. The C-V measurements proved to be a powerful tool. The actual condition of the tested device can be easily checked. However, the influence of the C-V measurements on the actual condition of the tested device cannot be neglected.

The experiments presented in the next part of this work were performed using mainly the ENDORFINS devices. The structures were foreseen for a reliability

study focused on aspects of charging.

Chapter 7

Evaluation of the ENDORFINS test structures

Based on the results of the preliminary experiments presented in chapter 6, several test structures were designed and processed within the frame of the ENDORFINS project (see chapter 4).

Before starting any lifetime experiments, the basic parameter of the devices, the V_{pi}, should be identified. Often, the parameters are provided by the designers. However, due to discrepancies between the designed and obtained material properties, the real V_{pi} can differ from the designed value. Therefore, the V_{pi} value should be confirmed by a C-V characteristic measurement.

The C-V characteristic of a real device is presented and compared to the theoretical one in this section. An attempt to understand the possible sources of discrepancy is taken. Next, the influence of test conditions on the results of the C-V characteristic is discussed and the usefulness of the ENDORFINS structures in the reliability study is verified.

The reliability study requires a number of similar devices. The differences in the parameters of the devices on one wafer are caused by non-uniformities of the processing steps. Results of wafer screening are further presented.

7.1 The C-V characteristic of a real device

Figure 7.1 shows a comparison of the theoretical (a) and measured (b) C-V characteristics of a capacitive RF MEMS switch. There are several differences
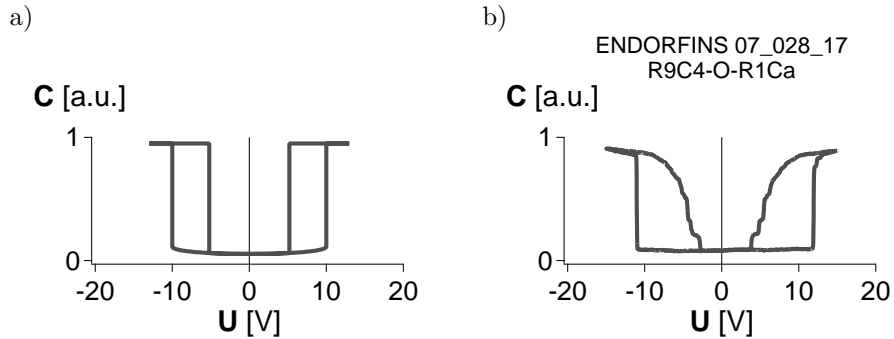
Figure 7.1: A comparison of the theoretical a) and measured b) C-V characteristics.

visible. Starting from the 0V point, the capacitance of the real switch increases as the theoretical model predicts. After crossing the V_{pi} voltage, the beam is attracted to the bottom electrode and a significant increase of the capacitance is observed. Increasing the voltage above the pull-in causes an increase of the capacitance of the switch. That can be caused by a lack of full beam-dielectric contact due to the shape, stress and stress gradient in the beam. The beam in the down state does not touch the dielectric in the entire area (Figure 7.2a). Increasing the actuation voltage (above the V_{pi}) causes an increase of the electrostatic force in the non-contact regions (Figure 7.2b-c). The improved contact is observed as a higher capacitance (Figure 7.2d).

A similar situation takes place when the actuation voltage is decreased from a magnitude higher than the V_{pi} to values below the V_{po}. In the case of the theoretical, parallel plate model, the capacitance should remain constant until the $U_{act} < V_{po}$ is reached. In the real switch the capacitance gradually decreases with decreasing actuation voltage. The electrostatic force attracting the beam decreases and smaller and a smaller part of the beam touches the surface of the interposer dielectric. At a certain point, the electrostatic force is lower than the mechanical restoring force, and the pull-out occurs. The effect reminds pealing-off. The observed transition is not as sharp as during the pull-in. Therefore, the localization of the pull-out voltage is more difficult.

7.2 V_{pi} and V_{po} in charging studies

Observations of charge trapping and de-trapping require the use of an indicator that does not misrepresent the information about the trapped charge. The response of the indicator should be as linear as possible. As the pull-in and pull-out voltages

a)

b) $|U_{act1}| > |V_{pi}|$

c) $|U_{act2}| > |U_{act1}| > |V_{pi}|$

$C_{down1} < C_{down2}$

d)

C [a.u.]

1

0

-20   -10   0   10   20   **U** [V]

C_{down2}

C_{down1}

U_{act2} U_{act1}

e)

C [a.u.]

1

0

-20   -10   0   10   20   **U** [V]

no sharp pull-out
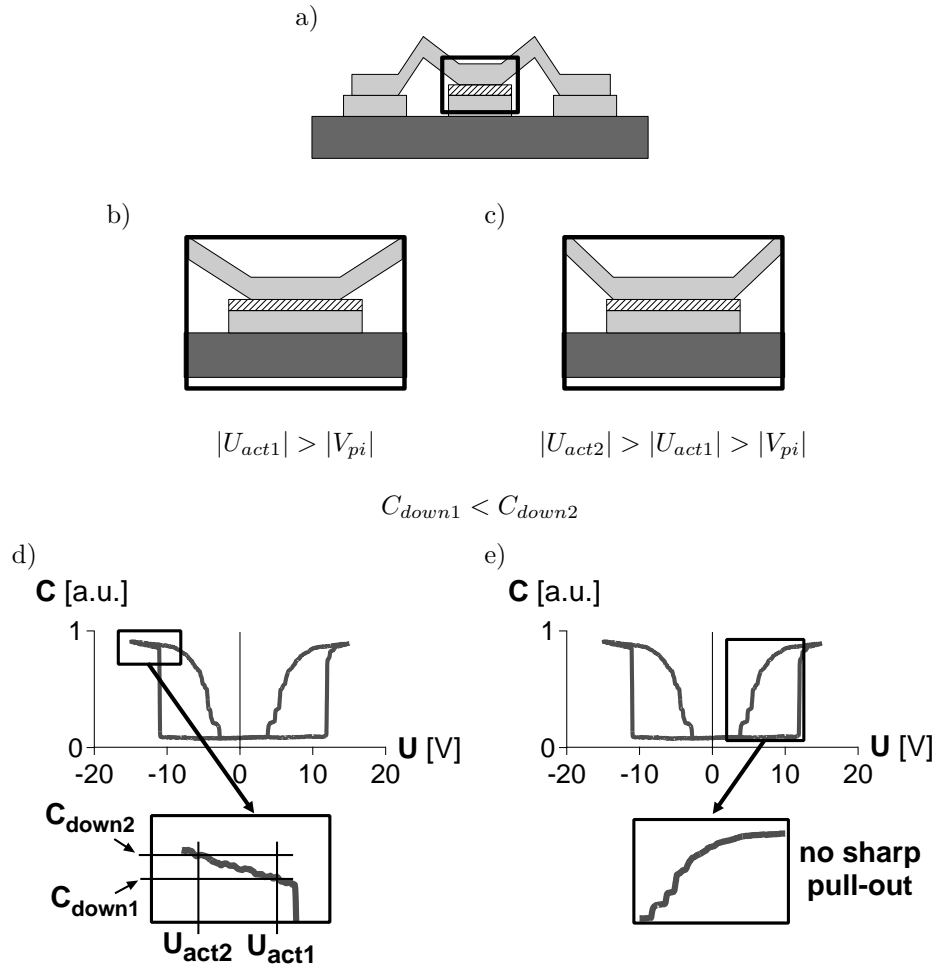
Figure 7.2: Lack of the perfect beam-dielectric contact in the down-state a) is a possible cause of the observed increase of the capacitance with increasing U_{act} above the V_{pi}. The contact area depends on the amplitude of the applied actuation voltage. Higher U_{act} generates more electrostatic force improving the contact and the C_{down} (b and c). The effect can be observed in the C-V characteristics (d). A similar situation is observed during the pull-out transition. The beam is not released at once. The contact area (thus the capacitance) gradually decreases until the electrostatic force is lower than the restoring mechanical force (pull-out point) e).

are charge sensitive parameters of the switch, both can be used as the charge indicators. However, they can be modified differently, e.g. in case of a non-uniform distribution of charge.

As presented by Rottenberg [305], the positive and negative V_{po}'s are influenced more than the V_{pi}'s. I.e. the pull-out window W_{po} is narrowed more than the pull-in window W_{pi}. Moreover, the pull-in and pull-out voltages are additionally modified by the gap non-uniformities in the presence of a non-uniformly distributed charge [310]. The beam in the up position creates less non-uniformities than when it is in the down position. It is clear that V_{po} is much more influenced than V_{po} by various parameters such a beam shape, non-uniformity of the gap etc. For that reason, the V_{pi} is a more reliable charge indicator than the V_{po}. Even though mainly changes of the pull-out voltages limit the lifetime of the switches.

7.3 Optimal C-V measurement conditions

The C-V characteristic measurement should not disturb the lifetime experiments. The effect of the C-V measurement should be as low as possible. Still, it should provide reliable information about the actual switch condition. There are mainly two parameters that can be tuned to optimize the C-V measurements: the measurement time t_{CV} and the voltage amplitude U_{CV}.

7.3.1 Measurement time

To assure a minimal influence of the C-V measurement, the total measurement time t_{CV} should be kept as low as possible. However, a too short measurement time can result in deformations of the C-V curve. Figure 7.3 shows results of C-V measurements performed too fast. The positive and negative pull-out voltages crossed 0V point on the curve (Figure 7.3a). It can be misinterpreted as a failure. The curve in Figure 7.3b shows a lack of the pull-outs. The position of the beam, deducted from the measurement (Figure 7.4), shows that the beam does not follow the actuation voltage. The beam does not have enough time to go to the up position. At the moment when the applied voltage is 0V, the beam still partially touches the dielectric. When the voltage increases again, after switching the polarity, the electrostatic force attracts the beam back towards the bottom electrode. After the first pull-in, the beam stays in the bottom position during the entire measurement. That can be wrongly interpreted.

To distinguish whether the observed C-V curve is a result of a too fast measurement or of charging during the measurement, another C-V measurement, with a longer time, should be performed. Figure 7.5 shows the result of a measurement with much longer time. The pull-out's can be very well defined. However, the long t_{CV}

a) ENDORFINS 06_252_05 R3C4-O-R2Ca

b) ENDORFINS 06_252_05 R3C4-O-R2Cb
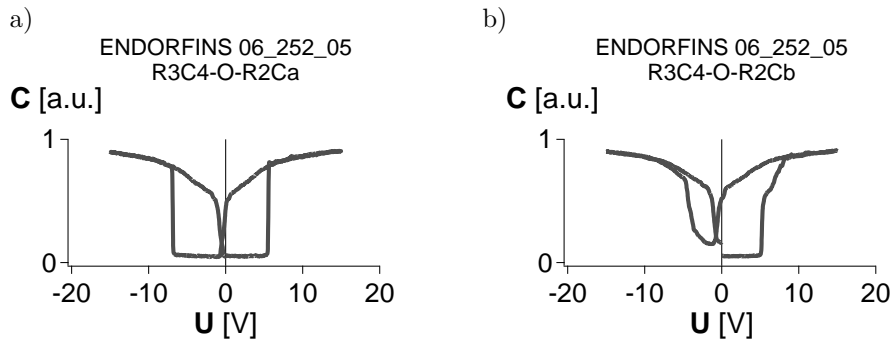
Figure 7.3: Examples of the C-V characteristics measured with too short measurement time. The observed failure mode - the pull-out voltage crossing 0V point - is caused by a too fast measurement a). The pull-out voltage can disappear leading to a wrong conclusion that the stiction takes place b). Test conditions: $25°C$, N_2, 1atm, light on.
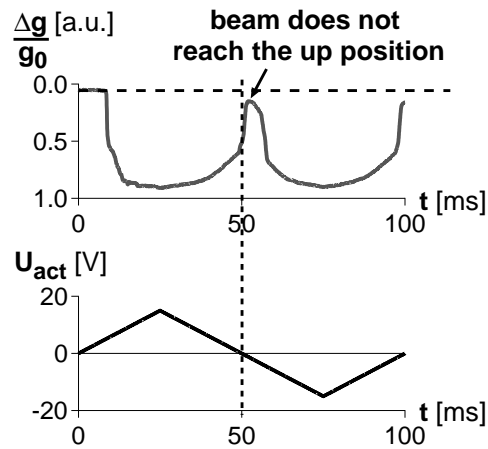
Figure 7.4: The beam does not reach the up position when the actuation voltage is 0V and even low voltage, after switching the polarity, keeps the beam in the down position.

(1s in this particular case) can cause significant trapping or de-trapping of the charges.

The measurement time should be experimentally chosen for each type of device. Figure 7.1b shows a C-V curve of an ENDORFINS switch measured with $t_{CV} = 100ms$. It seems to be a good compromise between the obtained shape of the curve and the measurement time. 100ms is a time equal to 10 switching cycles with the

ENDORFINS 07_144_04
R2C4-T-R1Cf

C [a.u.]
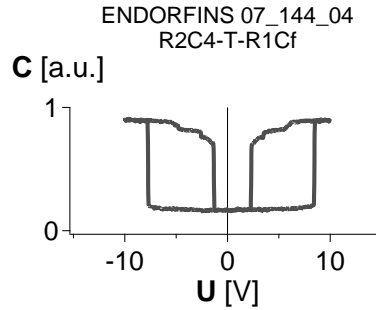
Figure 7.5: A longer measurement time ($t_{CV} = 1sec$) allows better pull-out voltage definition. However, it can introduce more disturbances in the trapped charges. Test conditions: $25°C$, N_2, 1atm, light on.

frequency of 100Hz typically used in lifetime experiments. 10 cycles are negligible if compared with lifetimes of minimum thousands of cycles observed. In the same time, the shape of the C-V curve shows that the beam reaches the up position when the actuation voltage drops below the pull-out voltage. The fuzzy pull-out transition does not allow for precise pull-out voltage extraction. Nevertheless, it is acceptable since it was decided to use the pull-in voltages for lifetime monitoring (see 7.2).

The ELT system data acquisition card allows measurements of the C-V characteristic with the total time of less than 1ms. Though, the V_{pi} and V_{po} resolution drops. The C-V characteristic measured during 1ms allows pull-in and pull-out voltage extraction with the resolution of 0.25% of the U_{CV}. Typically, the C-V measurements were performed with $t_{CV} = 100ms$ resulting in the resolution of 0.1% of the amplitude. E.g. $t_{CV} = 100ms$ and $U_{CV} = 40V$ allows extracting the pull-in/pull-out with a resolution of 40mV.

7.3.2   Amplitude

The choice of the U_{CV} should be made taking all the possible changes of the pull-in voltage during stressing into account. I.e. the applied voltage must be higher than the V_{pi} during the whole lifetime test. On the other hand, it should not be too high in order to avoid influencing the lifetime test results.

Most of the C-V characteristics, presented in this work, were measured with the amplitude of the C-V actuation voltage significantly higher (30-50%) than the pull-in voltage. It was not modified during the experiments. The required minimal impact of the C-V measurements was achieved by minimizing the measurement time.

ENDORFINS 07_144_04
R2C4-T-R1Cf

U [V]

C [a.u.]

10

1

5

0

0

0   50   100
                    t [ms]

-10   0   10
           U [V]
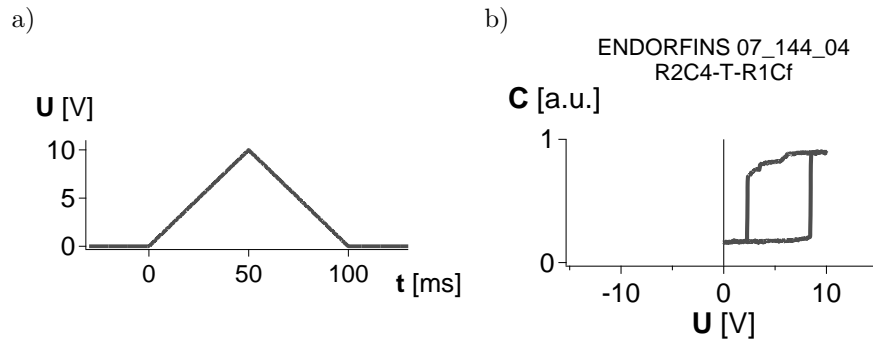
Figure 7.6: In some cases a unipolar C-V characteristic can be measured using the positive part of the triangular waveform only a). However, the obtained C-V curve can give limited information b).

There is a possibility of smart C-V measurements. The capacitance of the switch can be observed while increasing the actuation voltage. The measurement should be stopped immediately after detection of a significant increase of the capacitance, indicating the pull-in occurrence. This type of measurements could be implemented in the ELT program in the future.

In some cases, a unipolar C-V characteristic can be used (Figure 7.6). However, it does not give the full information about the trapped/de-trapped charge. It is not possible to distinguish whether the pull-in voltage changes due to the shift or narrowing of the C-V curve.

7.4 Designed and measured V_{pi} discrepancy

The measured pull-in voltage differs from the calculated/designed value. The calculated pull-in of a 140umx480um beam switch (3um gap, 1um thickness, AlCu), is about 47.1V taking the lowest considered initial stress (50MPa) into account (see Table 4.1). The measured value of about 14V is much lower. The difference between the designed and measured value of the pull-in voltage can be caused by several factors.

7.4.1 Initial stress

The deposition condition of the beam material may differ resulting in a different initial stress. On top of that, the value of the internal stress provided for the pull-in voltage calculations is measured in layer deposited directly on a silicon or

glass wafer [434, 435]. The beam metallization of the switches is deposited on the sacrificial layer. In the end the beam is released. Therefore, the resultant internal stress may vary (Figure 7.7).
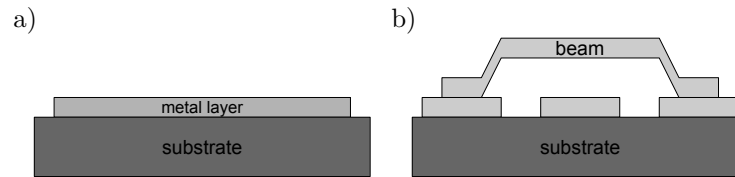
Figure 7.7: The internal stress in the metal layer is measured in a layer deposited directly on the substrate a). The beam of the switch is deposited on the sacrificial layer and finally released b).

7.4.2   Bowing and plies

The fabricated beams are not flat due to a finite stress gradient. The bowing can change the distribution of the electrostatic force and spring constant influencing the pull-in voltage (Figure 7.8a). The picture shows visible discontinuities (plies) in the beam, created by non planar layers below the beam. The discontinuities can be considered as a type of corrugations affecting the spring constant of the beam (Figure 7.8b).

7.4.3   Influence of anchors

The model used for the V_{pi} calculations assumes perfect anchoring (Figure 7.9a). The beam anchors in the real switch can bend (Figure 7.9b). That can change the
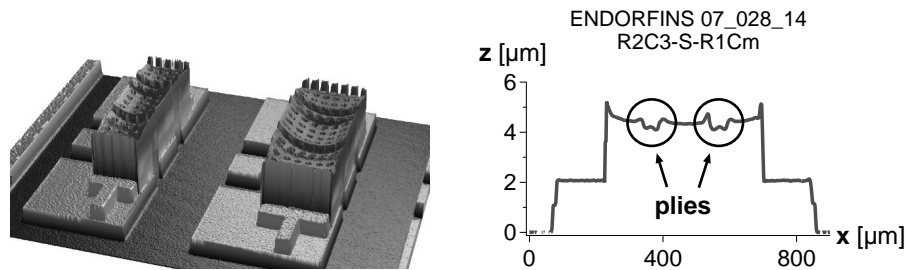
Figure 7.8: Finite initial-stress gradient causes bowing of the beams a). Non-planar layers below the beam results in discontinuities (plies) in the beam b). Both can affect the pull-in voltage.

spring constant of the beam, thus the pull-in voltage, as well.
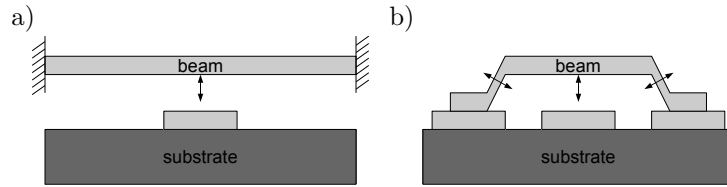
Figure 7.9: The model considers a perfect clamping of the beam a). The anchors of the real structure can bend changing the spring constant of the beam b).

7.4.4 Presence of substrate

The used model does not take into account the presence of the substrate. The dielectric substrate changes the distribution of the electrostatic force between the actuation electrode and the beam and may influence the pull-in voltage (Figure 7.10).
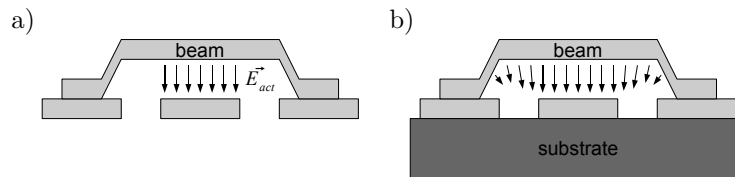
Figure 7.10: The used model takes only the perpendicular component of the electric field between the actuation electrode and the beam into account a). The modifications of the electric field due to the presence of the substrate (dielectric material) are neglected b).

7.4.5 Impact of CTEs mismatch

The used model does not take the influence of the thermal expansion of the beam and the substrate into account. During the design, a certain tensile stress is considered. At $25\,^\circ C$ the internal stress is indeed tensile. However, the situation changes when the temperature of the wafer is elevated. Different coefficients of thermal expansion (CTE) cause higher elongation of the beam than the substrate. The internal stress changes from tensile to compressive causing buckling of the beam. Figure 7.11a shows results of a profile measurement performed at different temperatures. At $50\,^\circ C$, the distance between the beam and the bottom electrode can change by more than $7\mu m$. That significantly changes the pull-in voltage.
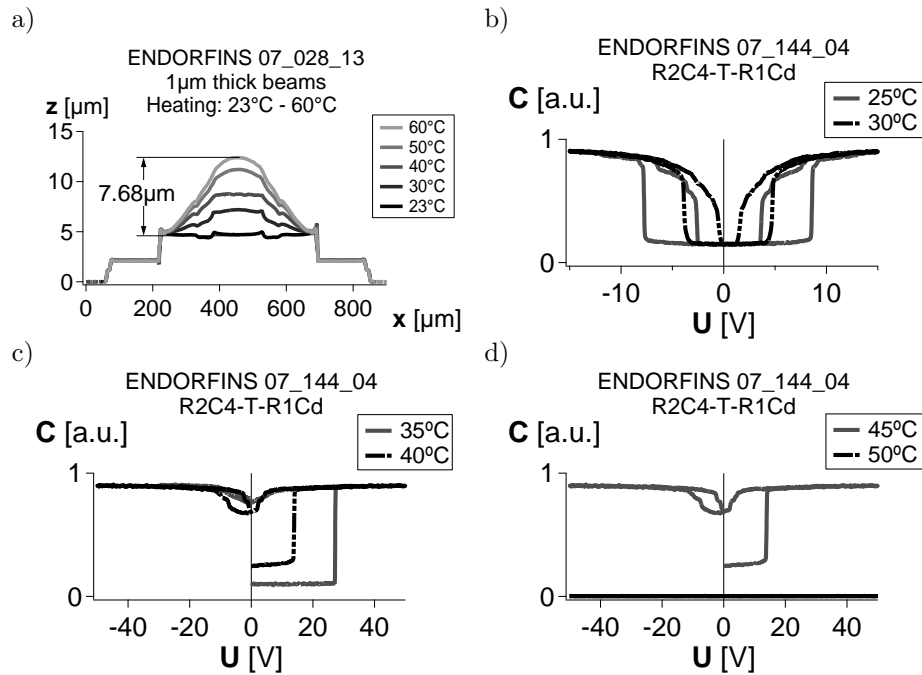
Figure 7.11: Profile and C-V measurements show a high sensitivity to elevated temperatures. The beam expands more than the substrate resulting in compressive stress causing the beam buckling a). A small change of temperature can result in downward buckling of the beam decreasing the V_{pi}. In some cases, the actuated beam changes the concave to convex shape and stays in the bottom position c). At $50\,^{\circ}C$ the pull-in increases to more than $50V$ d) C-V measurements were performed in N_2, 1atm atmosphere with light on. The profilometry was performed in ambient air.

The profilometry results were compared with C-V characteristic measurements of the devices at various temperatures. The pull-in voltage of the switch drastically changes with temperature. The V_{pi} observed at 30C is lower than the V_{pi} at $25\,^{\circ}C$ (Figure 7.11b). That is a result of a possible downward buckling of the beam. The resultant gap is lower, thus the pull-in decreases. At higher temperatures, the beam is buckled upwards increasing the pull-in. However, only one part of the C-V characteristic could be measured. The initially concave shaped beam can flip to a convex shape due to the compressive stress. It may remain in the down position even after actuation voltage removal (Figure 7.11c). At $50\,^{\circ}C$ the gap increases to a level that the pull-in voltage is higher than $50V$ (Figure 7.11d).

The high sensitivity of the pull-in voltage on temperature make lifetime experiments under various temperatures very complicated.

Nevertheless, the thermal stability of the capacitive MEMS switches can be assured by a proper design [436].

7.4.6 Influence of holes

The beam holes are neglected during the design phase. The holes can change the mechanical properties of the beam due to changing the total cross section area and modifications of the internal stress.

7.5 Exemplary lifetime test results

Figure 7.12 shows exemplary results of lifetime tests performed on ENDORFINS structures, both simplified and fully processed (see 4.4.3). In both cases, the C-V characteristics are measurable (Figure 7.12a and b). The beam follows the applied actuation signal (Figure 7.12c and d) and the up- and down-states are detectable (Figure 7.12e and f). The change of the ΔC is high enough to determine the end-of-life of the device (Figure 7.12g and h).

Therefore, the ENDORFINS devices, both simplified and fully processed, can be used for in depth reliability studies.

7.6 Wafer uniformity and wafer-to-wafer repeatability

A reliability study requires the use of a large number of similar devices. A high repeatability of the parameters of the fabricated devices is determined by the uniformity of the processing steps. The key parameters influencing the pull-in voltage are the thickness of the sacrificial layer and the thickness and internal stress of the beam metal layer. The uniformity (or non-uniformity) is directly mirrored in the distribution of the V_{pi} across the wafer. The uniformity of all ENDORFINS wafers was verified by monitoring the distribution of the pull-in voltage.

The C-V characteristics of a number of devices were measured. Figure 7.13 shows the positions of the tested devices. The devices are organized in cells.

In both cases, the simplified and fully processed structures of two sizes of beams were measured. The dimensions of the beams:
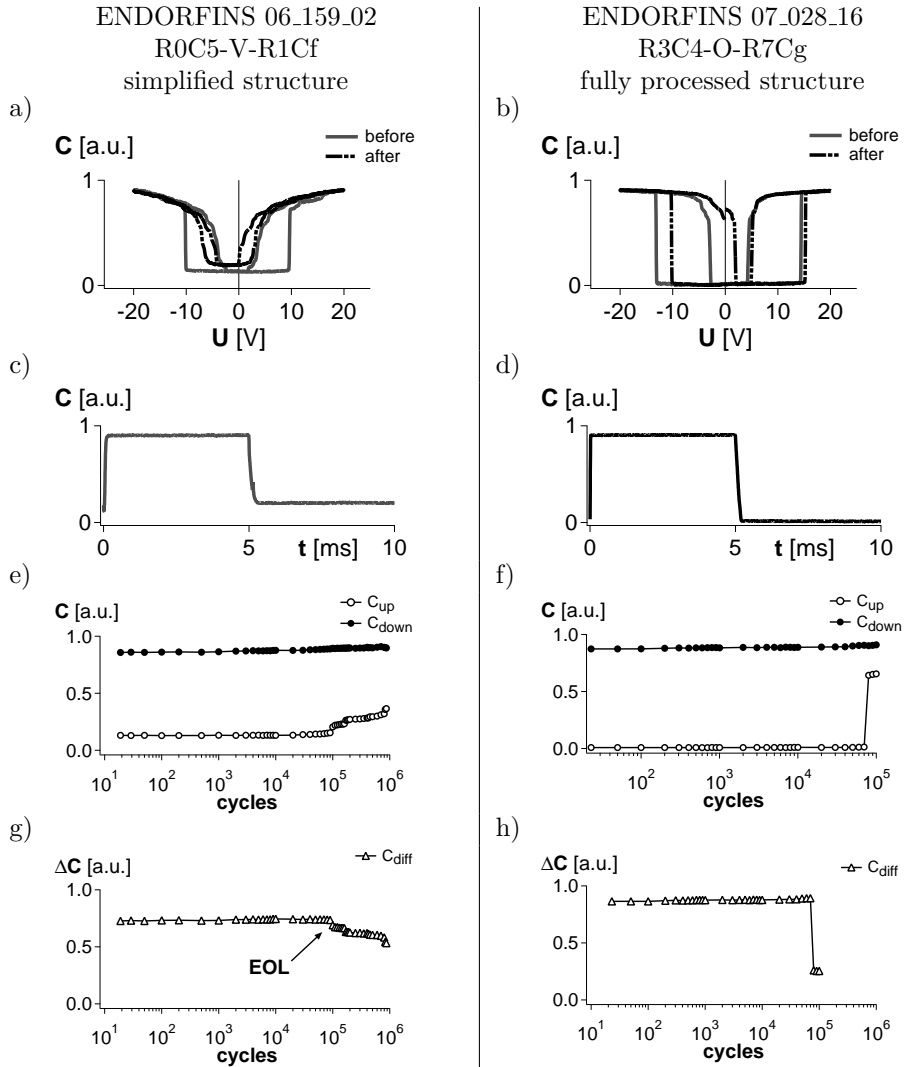
Figure 7.12: Examples of lifetime tests results of ENDORFINS simplified and fully processed devices. The C-V characteristic is measurable a) and b). The response of the switch on the applied actuation voltage (rectangular, unipolar, 50% d.c., 100Hz) c) and d) allows detection of the up- and down-states e) and f). The end-of-life, change of the ΔC is detectable as well g) and h). Test conditions: $25°C$, N_2, 1atm, light on.
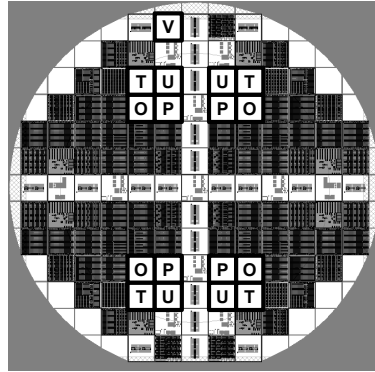
Figure 7.13: Location of the tested devices on the ENDORFINS wafer.

- simplified: $80\mu m$ and $140\mu m$ wide, 600 μm long (V cell),

- fully processed: 140 μm and $200\mu m$ wide, 480 μm long (O, P, T, U cells).

Figure 7.14a shows the distribution of the V_{pi} of the simplified structures placed in the V-cell. The pull-in voltage of the structures is 8.5 ± 0.20V and and 7.7 ± 0.19V for $80\mu m$ and $140\mu m$ beams, respectively.

The distribution of the V_{pi} of the fully processes structures placed in cells O,P,T and U is presented in Figure 7.14b. The pull-in voltage of most of the devices on the ENDORFINS 07_028_13 wafer is 14.0 ± 0.18V and 14.2 ± 0.21V for $140\mu m$ and $200\mu m$ wide beam, respectively. Similar results are obtained on the other wafers fabricated within the ENDORFINS project.

A comparison of pull-in voltage fabricated on different wafers show a high repeatability of the processing. There is a difference of about 1V between the wafers with the simplified test structures (Figure 7.14c and e). The structures on two fully processed wafers exhibit the same pull-in voltage (Figure 7.14d and f).

The observed difference in the V_{pi} of the narrow and wide beams is caused by the bowing of the beams. Theoretically, the pull-in voltage of clamped-clamped beam switches should be independent on the width of the beam as long as it is equal to the width of the bottom electrode. The electrostatic force, thus the pull-in voltage, is slightly different due to the different shapes of the beams.
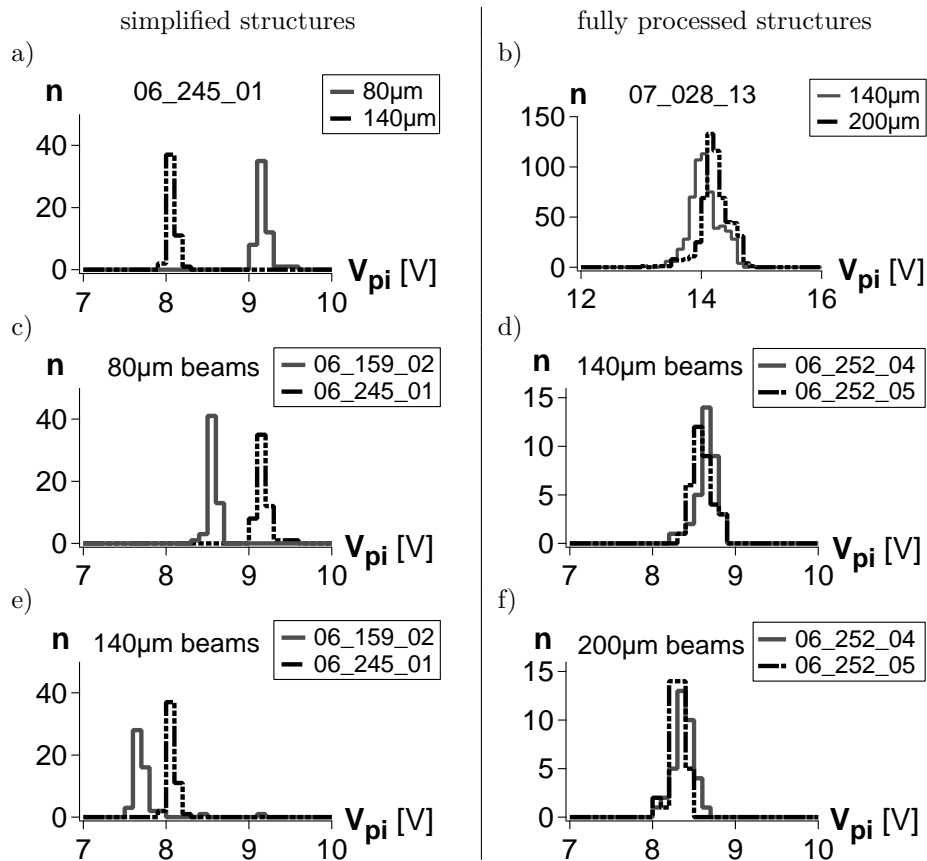
Figure 7.14: The C-V measurements results show a high uniformity of the devices on wafers a-b). The high wafer-to-wafer repeatability allows comparison of devices fabricated on different wafers c-f).

7.7 Summary and conclusions

Both simplified and fully processes ENDORFINS structures can be used as test structures in the charging study. The C-V characteristic is measurable and the failure (stiction) is detectable with the ELT system. High uniformity and repeatability allow obtaining statistical data of high confidence.

The observed pull-in voltage differs from the designed values. However, that does not disqualify the test structures.

Chapter 8

Interposer dielectric charging

One of the goals of the ENDORFINS project was to find an optimal set of materials in order to improve lifetime of the capacitive RF MEMS switch. Therefore, a study of charging properties of different types of dielectric materials was proposed.

First, a number of simplified ENDORFINS structures were fabricated with four types of dielectrics:

- Ta_2O_5 sputtered (TaO1) and anodized (TaO2),

- AlN sputtered using two recipes (AlN1 and AlN2).

A number of lifetime experiments using various biasing schemes were performed. The obtained results were completed with I-V measurements of MIM capacitors made with the same materials. Both types of measurements helped in the choice of the best dielectric candidate.

Next, a study on the fully processed ENDORFINS structures with the chosen dielectric materials was done. The lifetime experiments were intended to give more insight into the dielectric charge trapping mechanisms.

However, an unusual behavior of the devices during stressing was observed. This is discussed in the last part of this chapter.
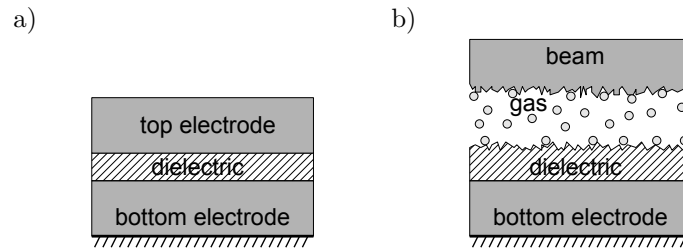
Figure 8.1: The main difference between the MIM (metal-insulator-metal) capacitor a) and the MEMS structure b) is the different top metal-dielectric interface. The gap between the dielectric and the beam is filled with gas (air, nitrogen) and moisture that can affect the charge trapping. The interface is exposed to an etchant during the release step that can modify the charging properties of the dielectric.

8.1 Evaluation of dielectric materials

8.1.1 Introduction

A study of different dielectric materials for the capacitive RF MEMS switches was done within the frame of the ESA/ESTEC ENDORFINS project. It contained an evaluation of four dielectric materials. First, the use of the MIM capacitors was considered. The MIM (metal-insulator-metal) capacitors are often proposed as test structures to evaluate charging properties of dielectric materials. However, the main difference between the MEMS and MIM structures is the presence of an air (gas) gap between the dielectric and the beam, allowing to obtain only limited information. The MIM capacitors may be insensitive to several charging mechanisms related to the surface of the dielectric being exposed to air (gas) (Figure 8.1). Therefore, it was decided to use MEMS devices as the main test vehicles. The MIM structures can complement the MEMS devices.

The use of simplified test structures was proposed by Xavier Rottenberg. The simplified devices are fabricated by omitting several processing steps. Still, they consist of the most important elements: the bottom electrode, the dielectric and the beam (see section 4.4, Figure 4.18, 4.19). Actuation and observation of lifetime and C-V characteristic changes are possible.

As the actuation of the simplified test structures requires application of the actuation voltage to the beam, the sense of the electric field vector is opposite to the one in the case of bottom electrode actuation. To avoid confusion, the results are presented as if the devices were actuated on the bottom electrode. E.g. a positive actuation voltage is in reality a negative actuation applied to the beam.
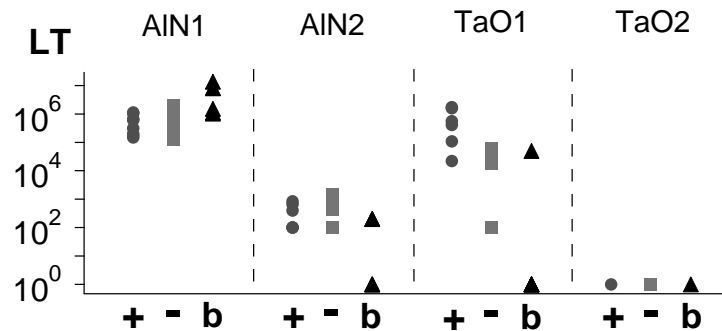
Figure 8.2: Comparison of the lifetime of structures with four types of dielectrics: AlN1, AlN2, TaO1 and TaO2. The lifetime experiments were performed using positive (+), negative (-) and bipolar (+) actuation waveforms. The end-of-life was determined using the EOL90% procedure. Test conditions: 13V, 100Hz, 50%d.c., 1atm N_2, 25°C, light on.

8.1.2 Lifetime results

Figure 8.2 shows the lifetime test results. The EOL was determined using the EOL90% criterion. The lifetime of a number of test structures on four wafers with the TaO1, TaO2, AlN1 and AlN2 dielectrics was tested. The test procedure includes lifetime tests using unipolar, positive and negative, and bipolar actuation waveforms of fixed amplitude (13V), frequency (100Hz) and duty cycle (50%). To monitor the condition of the devices, C-V characteristics before and after stressing were measured. The experiments were performed in dry nitrogen atmosphere under atmospheric pressure and at 25°C temperature.

8.1.3 AlN1

The lifetime of the test structures with the AlN1 dielectric is observed to be the highest. The C-V characteristic of the devices stressed with the unipolar actuation voltages show a positive or negative voltage shift depending on the polarity of the actuation voltage (Figure 8.3a and b). Additionally, the C-V characteristic of the device stressed with the negative actuation voltage is more narrowed that in the positive stressing case. The bipolar actuation voltage improves (with a factor of 10) the lifetime of the devices. The C-V curve measured after stressing is narrowed (Figure 8.3c). That may be due to a partial release of charge trapped during one polarity cycle by the cycle of the opposite polarity.

The AlN1 dielectric seems to be the best candidate. The highest observed lifetime is further supported by the I-V curve of a MIM capacitor with the AlN1 dielectric.

The small hysteresis indicates a low charge trapping in the dielectric (Figure 8.3d).

8.1.4 AlN2

The lifetime of the AlN2 structures is lower than the lifetime of the AlN1 and TaO1 structures. However, often the lifetime was very short because of dielectric breakdown and not because of stiction. The AlN2 is attacked during one of the processing steps after its deposition. Therefore, the thickness of the dielectric layer is lower than the thickness of the AlN1 or TaO1 dielectrics - about 160nm instead of 200nm. This might explain the lower breakdown voltage.

The C-V characteristic shows that the direction of the voltage shift is dependent on the polarity of the actuation voltage (Figure 8.4a and b). The bipolar actuation waveform causes narrowing of the C-V curve (Figure 8.4c). The I-V curve of a MIM structure with the AlN2 dielectric shows a similar hysteresis to the one observed in the case of the AlN1 dielectric (Figure 8.4d).

The lifetime of several additional AlN2 devices was tested at a lower amplitude of the actuation voltage (11V) to avoid breakdown. The obtained lifetime was more than 10^6 cycles and more than 10^7 cycles with unipolar and bipolar actuation voltage, respectively.

The AlN2 dielectric was promoted as a candidate for further experiments due to its promising properties.

8.1.5 TaO1

The lifetime of the TaO1 devices is lower with about one order of magnitude than the AlN1 structures. However, the C-V characteristics measured before and after stressing show relatively small changes (Figure 8.5a and b). The pull-out voltage of the TaO1 structures is lower than AlN1 and AlN2 devices. Therefore, a smaller amount of trapped charge can cause one of the pull-out voltage reaching the 0V point and resulting in stiction.

The shift of the C-V characteristic of the devices stressed with the unipolar, positive and negative, actuation waveform is always positive. That indicates trapping of one type of charge (negative) independently on the polarity of the actuation voltage. The C-V characteristic of the devices stressed with a bipolar waveform is narrowed (Figure 8.5c).

As the goal of the study was to point out the best candidate, the TaO1 dielectric was rejected. However, the observed low lifetime of the devices is caused not only by high charge trapping. The low pull-out voltage creates a small margin for the V_{po} changes. Still, there is some charge trapped in the dielectric indicated by the

shift of the C-V curve. The I-V curve of a MIM capacitor with the TaO1 dielectric confirms that the dielectric traps charges (Figure 8.5d).

8.1.6 TaO2

The switches with the TaO2 dielectric stuck during the first part of the first C-V characteristic measurement. An example is presented in Figure 8.6a. There are several possible causes for the immediate stiction of the beam besides charging. One of the possibilities is a very low restoring mechanical force. The actuated beam touches the surface of the dielectric when actuated and it cannot go back to the up position. The capillary forces (remaining water on the surfaces) or van der Waals forces are strong enough to keep the beam in the down position. Charge trapped during processing can be another source of force keeping the beam in the down position. However, the pull-in voltage of the structures fabricated with the TaO2 dielectric is similar to the pull-in voltages of the structures fabricated on the other wafers. This indicates that the mechanical properties of the beam, therefore the restoring force should be similar. The charge trapped during processing should influence the pull-in as well. The most probable cause of the failure is for this reason high charging after pull-in.

To confirm this hypothesis two more wafers were fabricated: one with $2\mu m$ thick beams and one with an additional step roughening the surface of the dielectric. The structures on both wafers stuck during the first part of the first C-V measurements. This confirms that insulator roughness or mechanical properties of the beam are not the cause of this fast stiction. Figure 8.6a shows the I-V characteristic of MIM structures fabricated using the TaO2 dielectric. There is a noticeable hysteresis visible in the I-V curves of the TaO1 and TaO2 dielectric. The hysteresis indicates charge trapping. Even though the level of current is much lower in the case of the TaO2 dielectric, the visible hysteresis indicates considerable charge trapping.

8.1.7 Summary and conclusions

Four types of dielectrics using simplified MEMS and MIM test structures were compared. Lifetime tests using positive, negative and bipolar actuation waveforms were performed. The results promoted one candidate for further processing of complete devices. The AlN1 devices showed the highest lifetime. For this reason, fully processed devices with the AlN1 dielectric were fabricated for further experiments. In addition, the AlN2 material was chosen. This type of dielectric showed a decent performance though at lower amplitudes of the actuation voltage. The material was chosen because the devices with this dielectric showed good lifetime even though the thickness of the dielectric layer was lower than the thickness of the other candidates.
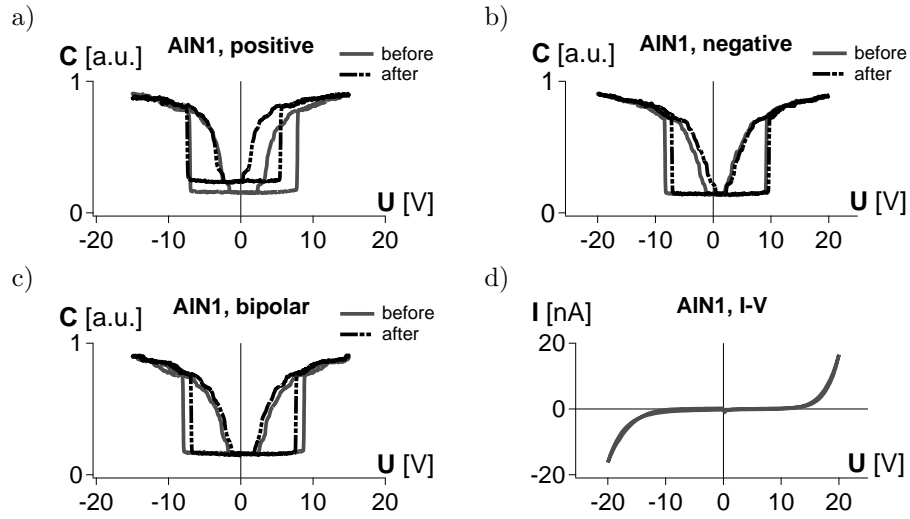
Figure 8.3: The results of lifetime tests of the ENDORFINS simplified AlN1 structures: positive a), negative b) and bipolar c) actuation waveforms, and the I-V curve of a AlN1 MIM capacitor d). Test conditions: $25°C$, N_2, 1atm, light on.
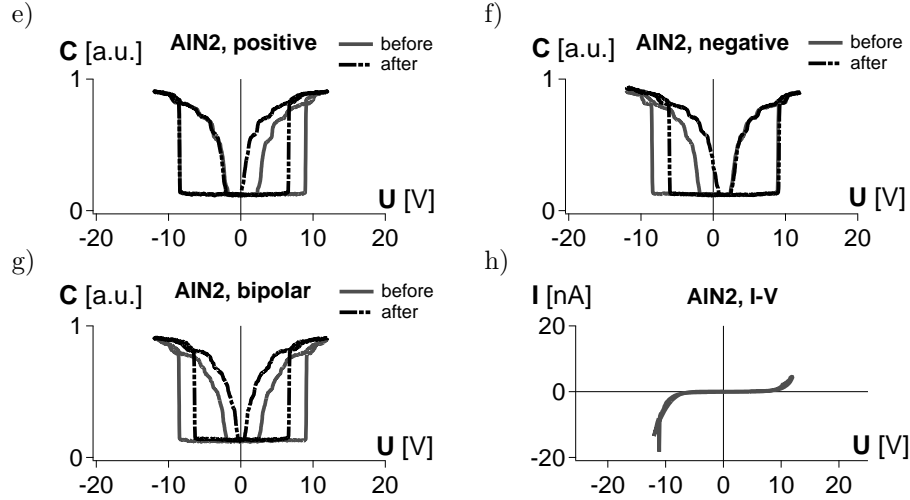
Figure 8.4: The results of lifetime tests of the ENDORFINS simplified AlN2 structures: positive a), negative b) and bipolar c) actuation waveforms, and the I-V curve of a AlN2 MIM capacitor d). Test conditions: $25°C$, N_2, 1atm, light on.
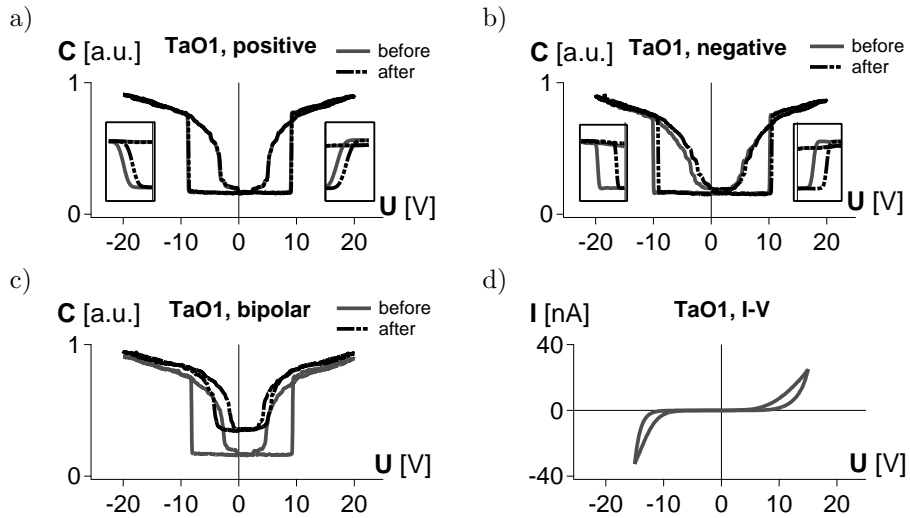
Figure 8.5: The results of lifetime tests of the ENDORFINS simplified TaO1 structures: positive a), negative b) and bipolar c) actuation waveforms, and the I-V curve of a TaO1 MIM capacitor d). Test conditions: $25°C$, N_2, 1atm, light on.
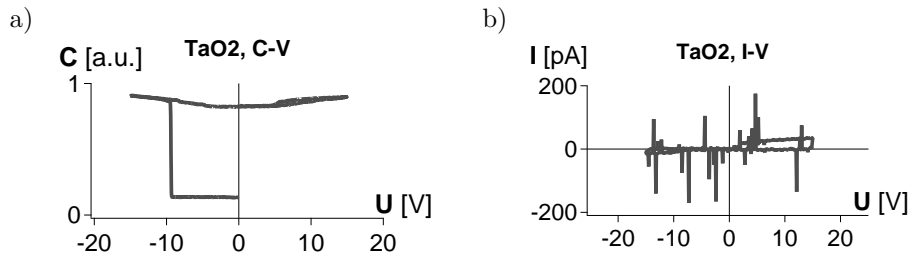
Figure 8.6: The ENDORFINS simplified TaO2 structures fail during the first C-V measurement a). The large I-V hysteresis indicates significant charge trapping d). Test conditions: $25°C$, N_2, 1atm, light on.

8.2 The EOLxV criterion

As the lifetime of the devices improves, testing using the EOL90%ΔC criterion causes an increase of the testing time. Techniques for faster testing are needed.

The EOL90%ΔC criterion is based on the difference between the up- and down-state capacitance. The decrease of the ΔC, due to an increase of the C_{up}, indicates stiction of the beam. The stiction of a capacitive switch occurs when one of the pull-out voltages, positive or negative, reaches the 0V point of the C-V characteristic, i.e. the change of the pull-out voltage is equal to the initial value (Figure 8.7a and c). However, to study the charge trapping there is no need to wait until the stiction occurs. The charge trapped causes changes of the C-V characteristic before the stiction as well.

Thus, the EOL criterion can be defined as a change of the V_{po} with a given value. It was already mentioned that the V_{pi} is a better indicator than the V_{po}. Therefore, the final definition of the EOLxV is the following: The end-of-life is defined when the pull-in voltage of the tested device is modified with more than x volts of the initial value (Figure 8.7b and d). E.g. EOL2V denotes the end-of-life when the pull-in voltage is modified with more than 2V from the initial value. This EOLxV does not give the exact end-of-life but indicates the sensitivity to charging.

Additional advantage of using the EOLxV criterion is that the C-V characteristic is not distorted by the stiction of the beam. Therefore, the pull-in and pull-out voltages are determined more precisely.

8.3 A comparizon using the Weibull plot

A comparison of the two dielectric materials can be done using the lifetime of devices. To find the characteristic lifetime of a population in a reasonable time a representative group can be tested. The obtained results are used to find the characteristic lifetime. As the probability of a failure is related to stressing time (non-stressed devices do not fail), the distribution of failure can be probably described with the Weibull distribution [453].

The Weibull distribution describes a distribution of failures, where the failure rate is proportional to a power of time. The Weibull plot provides useful information about the tested devices. E.g.:

- it can verify if they follow the Weibull distribution,

- it can verify if two sets of samples are statistically independent, i.e. the difference between the two sets of samples is not due to a non-uniformity,
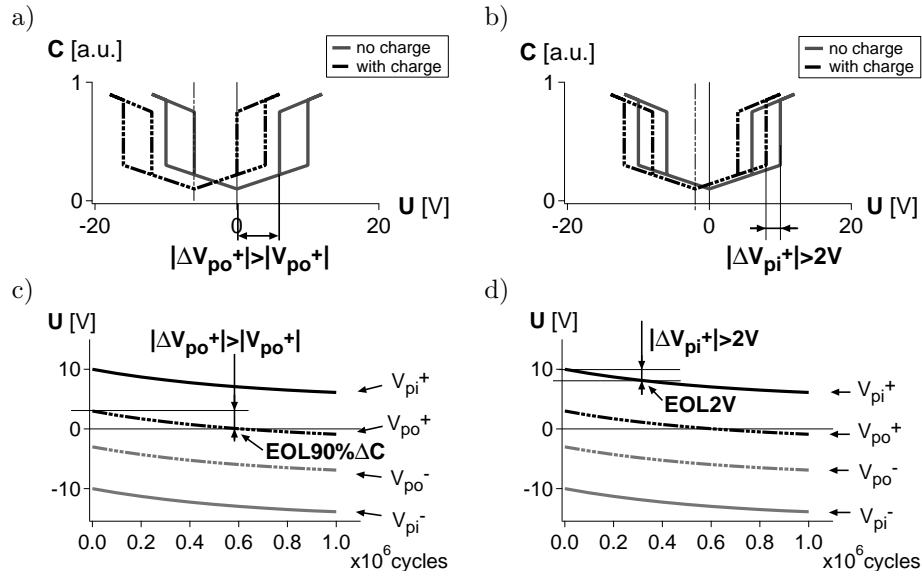
Figure 8.7: The EOL90%ΔC criterion is based on the change of the difference between the up- and down-state capacitance. The change of the capacitance indicates stiction of the beam a) and c). The EOLxV criterion is based on the pull-in voltage changes. It allows faster testing and better lifetime definition due to lack of distortions of the C-V curves b) and d).

- it allows to determine the characteristic lifetime of a population based on a limited number of devices, i.e. the time (number of cycles) after 63% of the devices will fail.

A number of ENDORFINS devices with AlN1 and AlN2 dielectrics were tested. Each group contained of 34 devices. The lifetime was determined using the EOL2V criterion. Figure 8.8 shows Weibull plots for the two groups of devices. They are statistically independent. All the points are within a relatively narrow confidence band. That confirms that the failure are time related and can be described with the Weibull distribution. The characteristic lifetimes are about 3200 and 10400 cycles for AlN1 and AlN2 devices, relatively. The AlN2 seems to be a better candidate than AlN1.

The results presented in section 8.1 shows that the AlN1 devices show a higher lifetime than the AlN2 switches. The discrepancy is attributed to a slightly lower thickness of the AlN2 layer on the wafers used in the first experiment.

The relatively high values of the β parameter indicate a high uniformity of the devices.
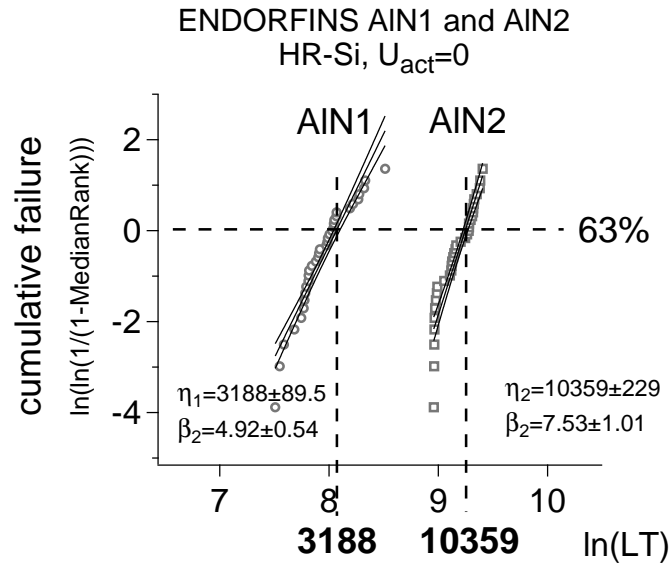
Figure 8.8: A Weibull plot can be used to compare the devices with the AlN1 and AlN2 dielectrics. Lifetime test conditions: $25°C$, N_2, 1atm, light on.

8.4 The Goldsmith's model agreement verification

In the next step, an agreement with the Goldsmith's model was verified. A number of fully processed ENDORFINS test structures with both AlN1 and AlN2 dielectrics were tested. The amplitude of the actuation voltage was changed and the C-V characteristic during stressing was observed. The EOLxV to determine the lifetime was used. The lifetime of AlN2 devices fabricated on the ENDORFINS 07_028_16 wafer was determined using the EOL1.3V criterion as the pull-in voltage did not change more than 2V during stressing. The lifetime of the remaining devices was determined using the EOL2V criterion. The results are presented in Figure 8.9.

The results of the lifetime test of the two AlN1 wafers are as expected ad in agreement with Goldsmith's model. The lifetime of the devices depends on the actuation voltage and decreases with increasing amplitude of U_{act}. However, in the case of the AlN2 wafers an unusual behavior is observed. The lifetime, when tested at higher actuation voltage, is higher than when tested at lower amplitudes. The extraordinary LT vs. U_{act} curve was studied in more details.

The unusual behavior is not observed when a negative actuation voltage is used (Figure 8.9e).
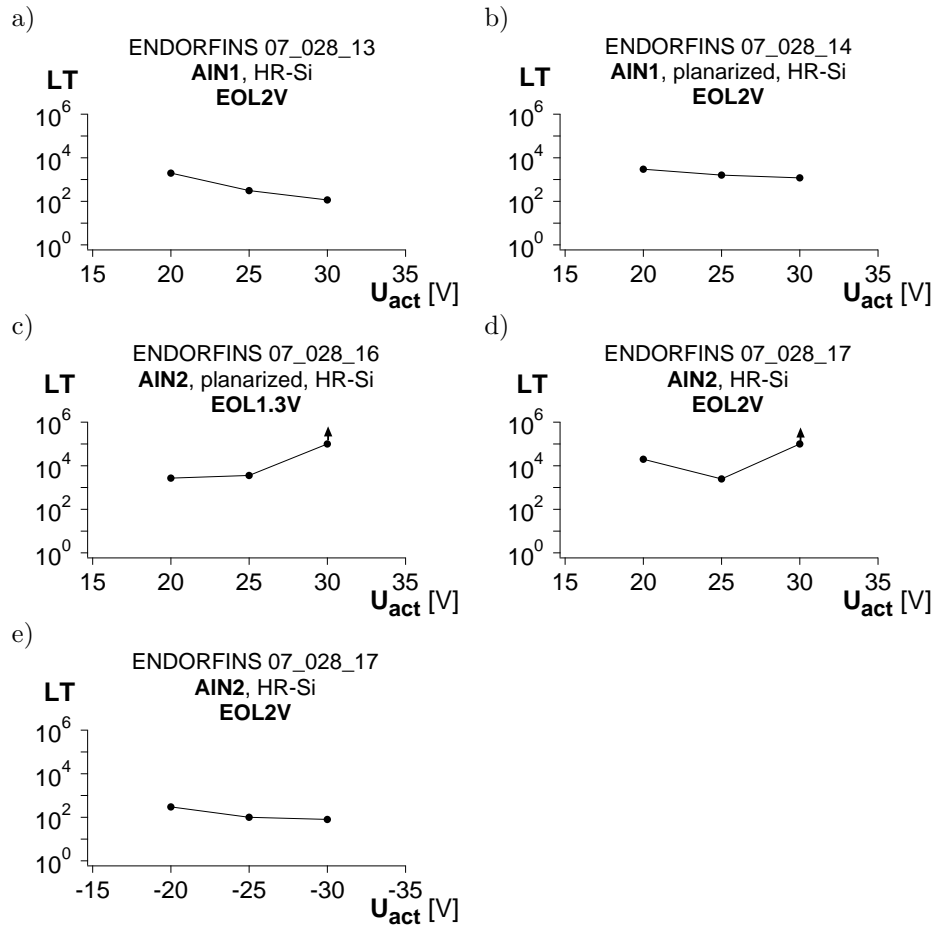
Figure 8.9: The lifetime of the two AlN1 wafers is in an agreement with the Goldsmith's model: the lifetime decreases with increasing amplitude of the actuation voltage a) and b). The lifetime of the two AlN2 wafers can be higher at higher actuation voltage than at lower amplitude of the U_{act} c) and d). The unusual behavior is not observed when the negative actuation voltage is used e). Test conditions: $25°C$, N_2, 1atm, light on.

8.5 A detailed study of the unusual behavior

8.5.1 Introduction

The unusual behavior observed during stressing with the positive actuation voltages required a more detailed study. More experiments using various amplitudes of actuation voltage were done. The C-V characteristic was monitored before, during and after stressing.

8.5.2 Positive actuation voltages

A number of the ENDORFINS AlN2 devices were stressed using positive actuation voltages with the amplitude ranging from 15V to 30V. The C-V characteristic was measured during stressing to monitor the V_{pi}. Figure 8.10a and b show two examples of the C-V characteristic development measured at various U_{act} amplitudes. The C-V curve shifts towards negative voltages when $U_{act} = 15V$ and it shifts towards positive voltages when an amplitude of 27V is used. The lower U_{act} causes a decrease of the V_{pi}^+ with more than 1.3V and the EOL according to the EOL1.3V is observed (Figure 8.10c). The V_{pi}^+ of the device tested at higher U_{act} did not decrease of more than 1.3V. It increases. Therefore, no EOL is detected according to the EOL1.3V criterion (Figure 8.10d).

Initially, the EOLXV criterion was based on observations of changes of only one pull-in voltage. The direction of the C-V curve shift was expected to be dependent on the polarity of the actuation voltage, e.g. a shift towards negative voltages when a positive actuation is used. However, the sign of the C-V shift turns out to be sensitive to the amplitude of the actuation voltage as well in these devices. A shift towards both, positive and negative, voltages can be observed when an actuation voltage of only one polarity is applied. That was never reported in literature.

In this case, the lifetime should be determined using both, positive and negative, pull-in voltages. Figure 8.10e shows the lifetime of the devices determined using both pull-in voltages. The lifetime is determined by V_{pi}^+ at the lower actuation voltages (<20V) and by the V_{pi}^- at the higher actuation voltages (>25V). There is a range of the actuation voltage amplitude, between 20V and 25V, where the EOL is not reached.

Figure 8.11a shows the extracted voltage shift V_s. Both, positive and negative shifts are possible when the same polarity of the actuation voltage is used.

The voltage shift at 21V seems to stabilize after the first few thousand cycles pointing to a charge saturation (Figure 8.11c). If this was the case, then the lifetime of the devices tested with this amplitude of the actuation voltage would
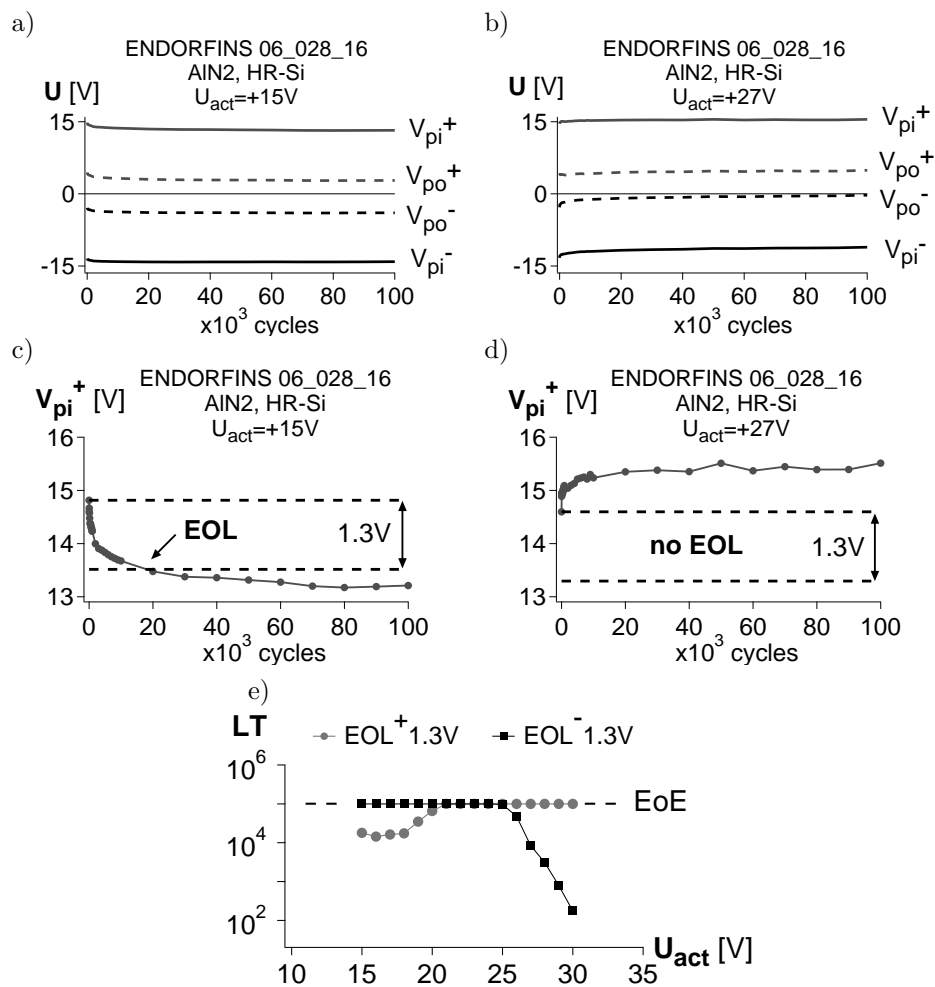
Figure 8.10: Evolution of the C-V characteristic observed during stressing devices with positive actuation voltage. The C-V curve shifts towards negative voltages when +15V is applied a) and towards positive voltages when +27V is applied b). In the first case, the V_{pi}^+ decreases more than 1.3V and the EOL is observed c). The higher U_{act} amplitude causes a shift in the opposite direction. The pull-in voltage increases and no EOL is detected d). The lifetime is determined by the V_{pi}^+ at lower (<20V) actuation voltages and by the V_{pi}^- at higher (>25V) actuation voltages e). Test conditions: $25°C$, N_2, 1atm, light on.

be infinite. However, the narrowing of the pull-in window shows still some charge being trapped (Figure 8.11b).

If the amplitude of the actuation voltage is increased to 23V, then a negative shift during the first few thousand of cycles is observed and then a positive shift occurs (Figure 8.11c). The narrowing of the C-V curve indicates continuous charging (Figure 8.11d).

8.5.3 Negative actuation voltages

Stressing the devices with negative actuation voltages does not show the unusual behavior (Figure 8.12). However, when the V_s and the ΔW_{pi} are investigated then one can see a decrease of the voltage shift after some time of stressing at the -30V actuation voltage. The evolution of the ΔW_{pi} is similar to the observed one at -20V and -25V. That can indicate charge redistribution rather than trapping of other charges.

8.5.4 Discussion and summary

The presented results show that a C-V shift of both, positive and negative, sign can occur during stressing a device with an actuation voltage of one amplitude and polarity. The sign of the shift indicates the type of trapped charges. Therefore, both types of charges, positive and negative, can be trapped during stressing a device with one polarity of the actuation voltage. The presence of both types of charges is confirmed by the narrowing of the C-V characteristic.

This kind of behavior has never been observed before. The previous experiments reported in literature showed a voltage shift of the sign dependent on the polarity of the actuation voltage. A shift of only one sign during stressing with one polarity of the actuation voltage was observed.

It is possible that the bipolar C-V measurement itself can introduce charges of both types. However, all the experiments were performed in a similar way, i.e. the same number of C-V measurements of the same amplitude and period. That excludes the impact of the C-V measurement as the effect was observed only under particular stressing conditions.

The two charging mechanisms can cancel each other's impact on the shift of the C-V curve. A similar effect can be observed when the charge is trapped and immediately de-trapped. However, that is excluded by the observed narrowing of the C-V characteristic. Charge trapping and de-trapping would be observed as no changes of the pull-in window. The W_{pi} evolution recorded during the experiments shows only trapping of charges.
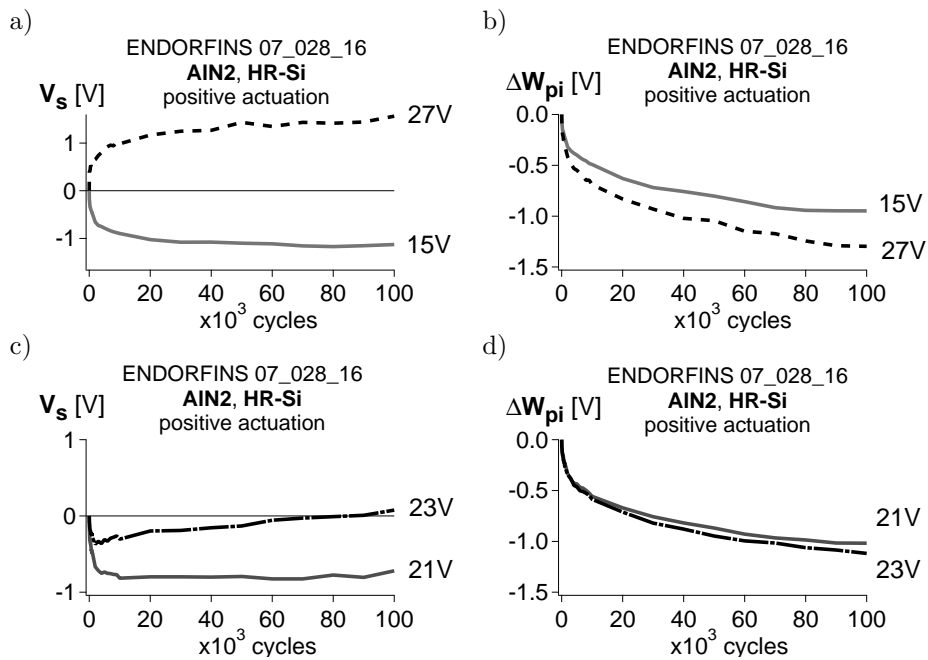
Figure 8.11: The voltage shift a) and c) and the pull-in window change b) and d) observed during stressing the AlN2 devices with positive actuation voltages. Test conditions: $25°C$, N_2, 1atm, light on.
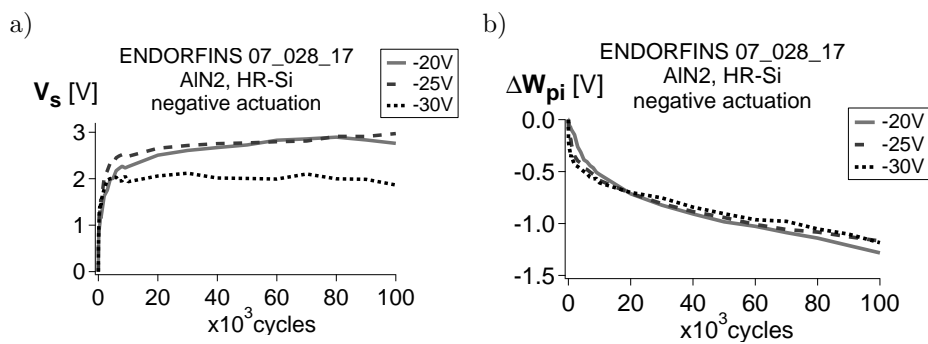
Figure 8.12: The voltage shift a) and the pull-in window change b) observed during stressing the AlN2 devices with negative actuation voltages. Test conditions: $25°C$, N_2, 1atm, light on.
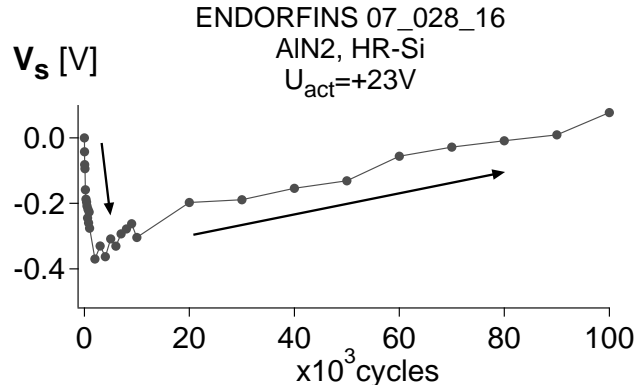
Figure 8.13: First, a negative shift and then a positive shift are observed during stressing a device with $U_{act} = +23V$.

The results show the presence of more than one charging mechanism limiting the lifetime of the capacitive MEMS switches with AlN2 dielectric.

8.6   A "fast" and "slow" charging evidence

Figure 8.11 showed that the voltage shift of an AlN2 device tested at +23V shifts first towards negative and then towards positive voltages. This is shown more in detail in Figure 8.13. Both, positive and negative, charge trapping mechanisms are observed during this one experiment. One of the mechanisms, (the positive charge trapping causing the negative shift) seems to be faster than the other one (the negative charge trapping cause the positive shift). The "slow" shift causes the center of the C-V characteristic return to 0V point indicating charge release.

8.6.1   Two-components representation

The evolution of the V_s in time as observed in Figure 8.13 can be presented as a sum of two components. It is assumed that both components are exponential functions of time (Equation 8.1).

$$A(t) = A_1 exp\left(\frac{-t}{\tau_1}\right) + A_2 exp\left(\frac{-t}{\tau_2}\right) + A_3 \tag{8.1}$$

Figure 8.14 shows the results of the fit of this equation to the data presented in Figure 8.13. There are two component with different time constants τ_1 and τ_2 visible.
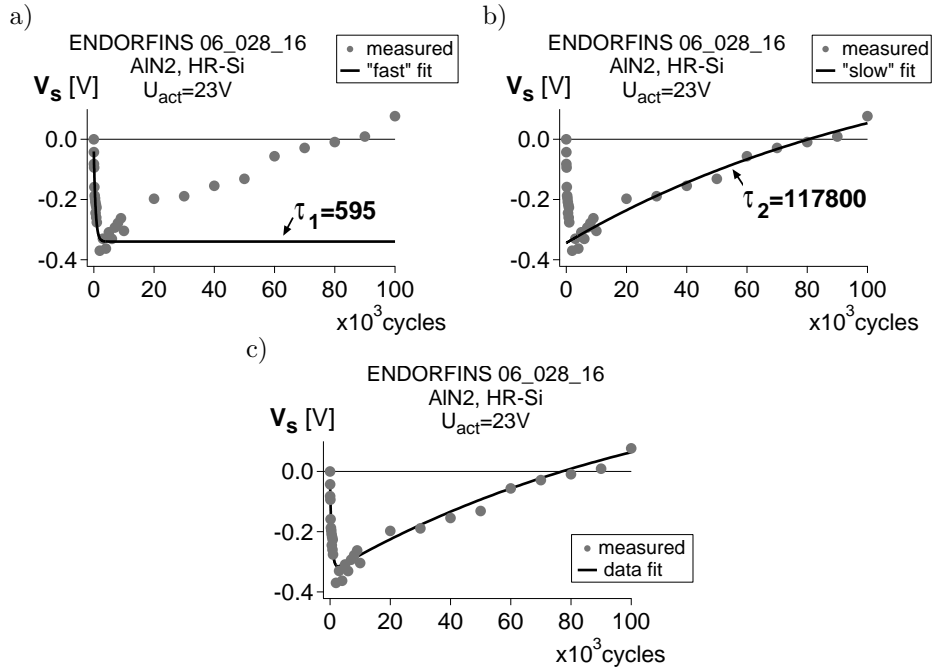
Figure 8.14: The measured V_s can be represented as a sum of two components of two different time constants c): a fast one a) and a slow one b).

8.6.2 Observation of the "slow" and "fast" components

It was shown that there are two charge trapping components with different time constants. There is a possibility that the first trapped charge is released with a different speed as well. Therefore, an experiment to separate the two mechanisms is proposed.

The fully processed AlN2 devices were stressed with positive and negative actuation voltages for 10^5 cycles. The C-V characteristics were measured before and immediately after stressing. Next, the stressed devices were un-actuated for a period of 1 minute and the C-V characteristics were measured again.

Figure 8.15 shows the measured C-V characteristics. A negative and positive shift is observed immediately after stressing with positive and negative actuation voltages,
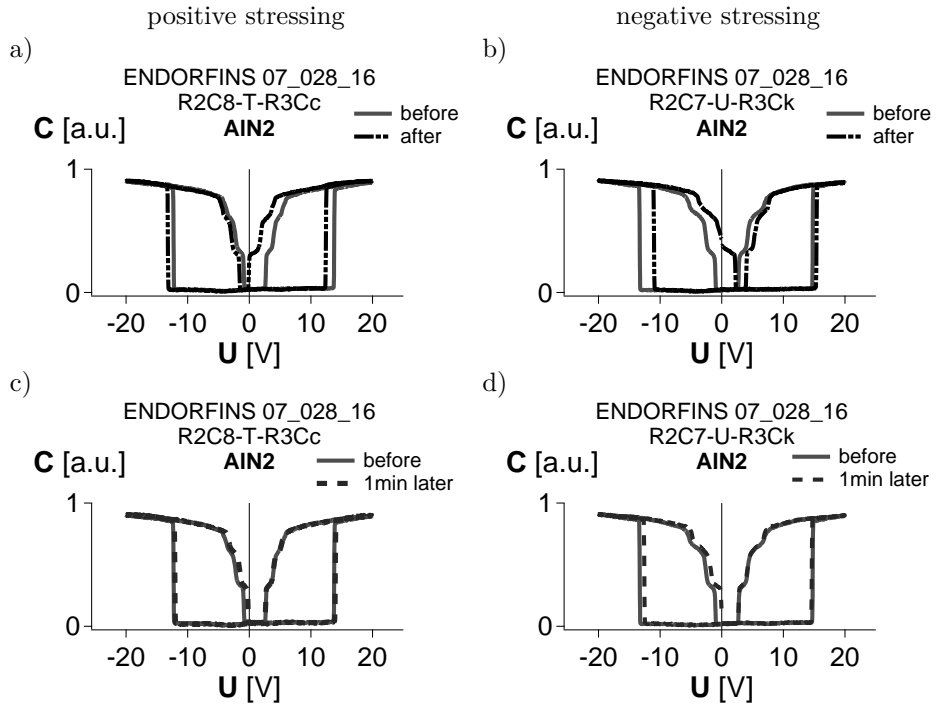
Figure 8.15: The C-V measurement performed immediately after stressing shows a voltage shift of a sign depending on the polarity of the applied actuation voltage a) and b). After 1 min of idling the C-V curves of the devices stressed with positive and negative actuation voltage are shifted in the same direction c) and d). Test conditions: $25°C$, N_2, 1atm, light on.

Table 8.1: The voltage shift V_s of the C-V characteristic observed immediately after stressing and after 1min idling.

	positive stressing	negative stressing
before	0.00V	0.00V
immediately after	-1.13V	+1.47V
1min later	+0.20V	+0.30V

respectively. However, after 1 minute of idling a positive shift in both cases was noticed (Table 8.1).

8.6.3 Discussion and summary

The presented results show the presence of two charging mechanisms. The mechanisms exhibit different time constants. One of the mechanisms, the "fast" one, seems polarity dependent. It causes a negative shift during positive stressing and a positive shift during negative stressing. The "slow" mechanism seem to be actuation polarity independent. It causes a positive shift in both cases.

8.7 Summary

First, a comparison of four types of dielectric materials as candidates for interposer dielectric was done. Lifetime experiments of simplified ENDORFINS structures with the four dielectrics were performed and compared. Two dielectrics, AlN1 and AlN2, were chosen for further study. The devices with these two selected materials exhibit the highest lifetime. However, modifications of the C-V characteristic indicate that these best candidates can trap charges as well.

The next step was to verify the agreement with Goldsmith's model. A number of lifetime experiments were performed. However, an unusual behavior of the devices was observed. Unexpectedly, a higher lifetime of the AlN2 devices at higher U_{act} was observed.

This unusual behavior was further studied. More lifetime experiments with C-V measurements during stressing were performed. The results showed that devices can achieve a higher lifetime due to a presence of two charging mechanisms. The mechanisms canceled each other's voltage shift improving the lifetime. Nevertheless, the narrowing of the C-V characteristics indicated charge trapping.

The data fit showed that the two charging mechanisms have different time constants. An experiment to isolate the two was proposed. The results showed that one type of charge was released faster that the other. The sign of the C-V shift caused by the "fast" charge seems U_{act} polarity dependent. The "slow" one showed a shift of the same sign independently on the polarity of the applied stressing.

Chapter 9

Impact of the substrate

The reliability study presented in the previous chapter consisted testing the lifetime of the ENDORFINS capacitive RF MEMS switches under various electrical conditions. The experiments were performed in a controlled dry N_2 atmosphere. However, an influence of the environment on the reliability of the MEMS devices has been pointed out by van Spengen in [336]. A few aspects of the impact of the environment were addresses during the preliminary experiments with MIPA and MEMS2TUNE devices.

This part presents results of experiments performed in two types of environment: dry N_2 and ambient air. The experiments help understanding another possible charging place - the substrate. It is shown that different types of substrate react differently under different environmental conditions.

The understanding of the influence of the trapped charges, depending on the type of substrate as well, was possible thanks to finite element modeling (FEM) methods. A part of the section describes the performed simulations.

The last part shows results of a number of experiments performed in a non-contact mode. The devices were stressed with an actuation voltage with an amplitude lower than the actual V_{pi}. In that case, the beam stays in the up position not touching the interposer dielectric. Yet, modifications of the C-V characteristics were observed. The obtained results show one more possible explanation of the previously observed failure of the switches in the non-contact mode.

9.1 Storage experiment

9.1.1 Introduction

Two ENDORFINS wafers, 06_252_04 and 07_028_13, were stored in ambient air for over one week. Next, the lifetime of the switches was tested under different conditions. The same type of the interposer dielectric (AlN1) is used in both cases. The only difference is the substrate material: glass AF45 (06_252_04) and high-resistivity silicon with a 200nm layer of silicon oxide (07_028_13).

9.1.2 The experiment and results

First, the lifetime of the devices was tested with no additional conditioning, i.e. immediately after storage in ambient air. The experiments showed a drastic lifetime reduction: $10^3 - 10^4$ cycles instead of more than 10^6 (Figure 9.1). The lower lifetime is attributed to the humidity enhancing charge trapping. The visible significant narrowing of the C-V characteristic of the HR-Si device is due to a partial stiction of the beam. In both cases, the EOL is caused by stiction as the increase of the C_{up} indicates. However, the AF45 device partially recovers between the end-of-experiment and the C-V characteristic measurements and the beam returns to the up position. In the case of the HR-Si wafer, the time between the lifetime and C-V characteristic measurements is too short. The beam charge trapped is high enough to keep the beam (partially) stuck in the bottom position.

To confirm the hypothesis about the humidity causing earlier failure, a step to remove the water molecules from the surface of the wafers was done. The wafers were placed in a vacuum chamber at a pressure of about 10^{-4} mbar and the temperature was elevated to 50°C. Next, the temperature was stabilized at the level of 25°C, the chamber was filled with dry nitrogen under the pressure of 1atm and lifetime tests were performed. The results show no significant lifetime change in the case of the glass wafer and an improvement in the case of the HR-Si wafer (Figure 9.2).

The improvement of the lifetime observed in the case of the HR-Si wafer is observed after only 1min of the conditioning. The devices fabricated on the glass wafer did not show any changes even after 1 hour of conditioning.

Figure 9.3 shows a comparison of the results: lifetime of the devices fabricated on both wafers observed after the air-storage and after the conditioning.
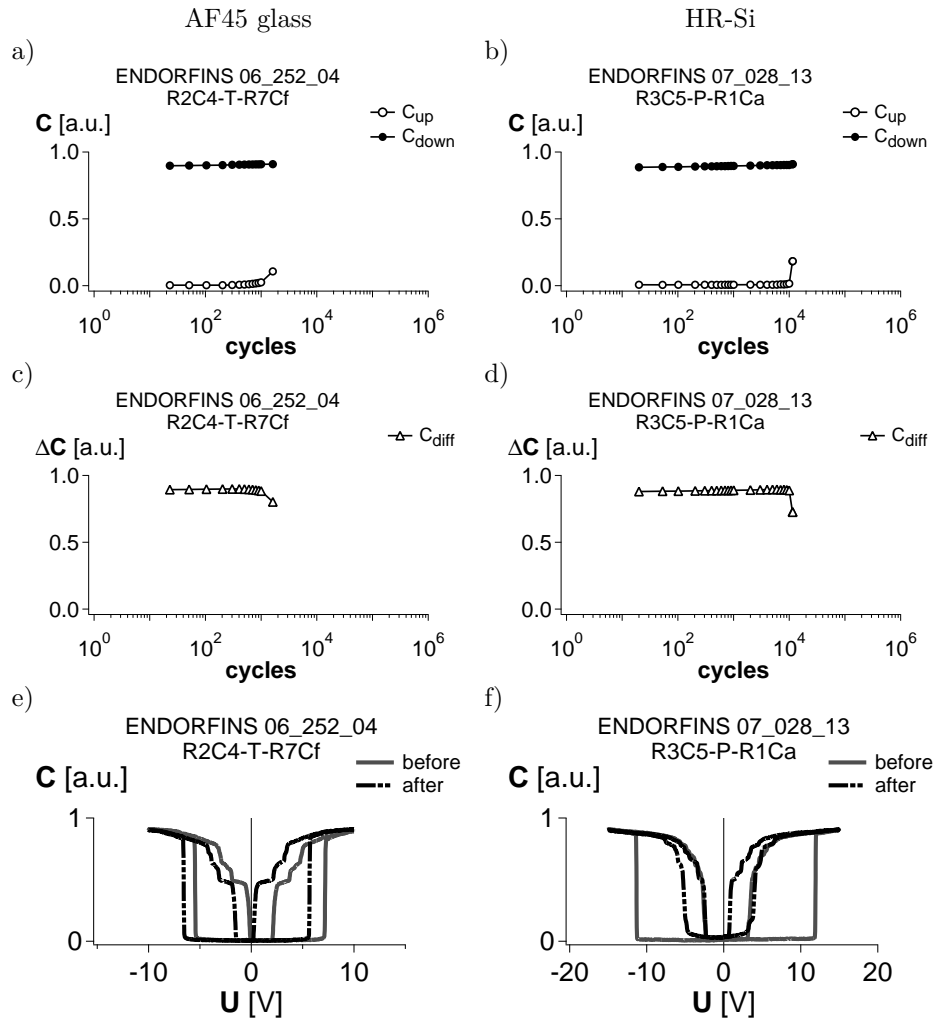
Figure 9.1: The lifetime of devices on both tested wafers was significantly lower than observed before exposing to the ambient air. The increase of the C_{up} indicates stiction as the failure cause a) and b). The C-V characteristic of the device fabricates on the glass wafer is shifted for the glass wafer device e) and narrowed in the case of the HR-Si wafer device f). Test conditions: $25°C$, N_2, 1atm, light on.
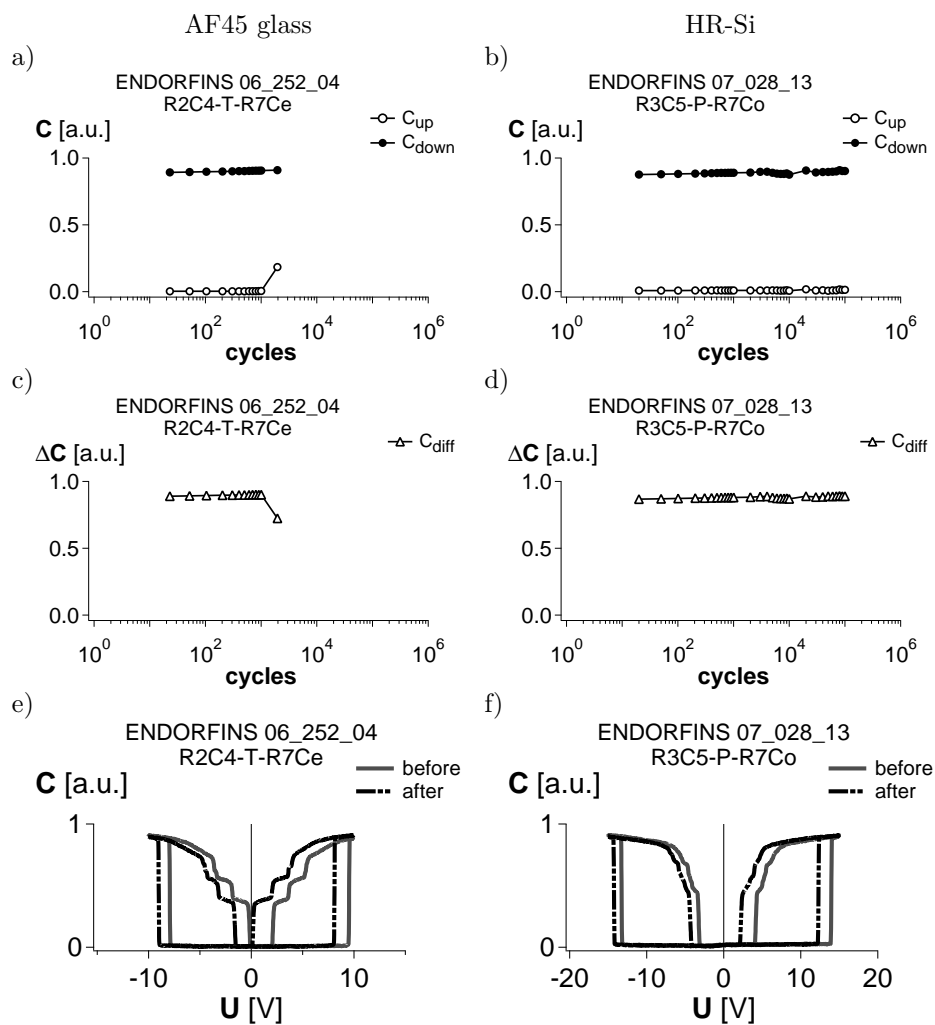
Figure 9.2: The lifetime of the devices fabricated on the glass wafer did not improve after 1 hour of conditioning in vacuum (10^{-4}mbar) at 50°C a) and c) (compare with Figure 9.1). In the case of the HR-Si wafer, only 1min of conditioning caused a significant improvement in lifetime b) and d). Test conditions: $25°C$, N_2, 1atm, light on.
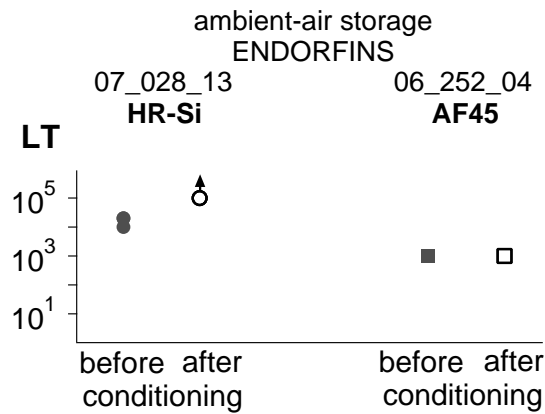
Figure 9.3: The comparison of lifetime test results performed on ENDORFINS devices fabricated on HR-Si and glass wafers. The lifetime tests were performed before and after conditioning ($50°C$, 10^{-4}mbar) after storage in air. The lifetime of the HR-Si device improved after 1min of conditioning - the arrow indicates that the measurement was stopped before reaching the EOL. The lifetime of the glass device did not improve after 1h of conditioning.

9.1.3 Discussion and conclusions

The difference between the two tested wafers is the substrate material: glass vs. high-resistivity oxidized Si. As the air storing/conditioning experiment shows, the difference in the behavior of the devices is probably caused by the humidity trapped on the surface on the wafers. The AF45 glass is an alkali-free borosilicate used for wafer level chip size packaging by anodic bonding [454]. The anodic bonding process requires hydrophilic surfaces. In the case of glass-to-silicon bonding, the silicon wafer is treated to make the surface hydrophilic. Usually, the surface of silicon wafer is hydrophobic. The hydrophobic properties of silicon help removing water from the surface. It is more difficult to remove the humidity from the AF45 glass wafers. This difference is mirrored in the presented lifetime results. That points to the substrate being another possible place of charge trapping.

9.2 The EFFA devices

Testing the lifetime of the EFFA (Electrostatic Fringing-Field Actuator) (Figure 9.4) devices presented by Xavier Rottenberg [78], showed that substrate charging can be indeed a failure cause. An EFFA device that has no interposer dielectric deposited during processing, failed (stiction observed) after a number of cycles of
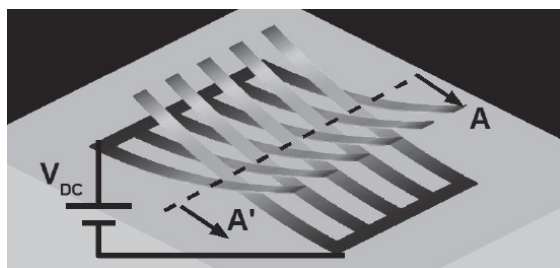
Figure 9.4: A 3D simulation of the EFFA device.
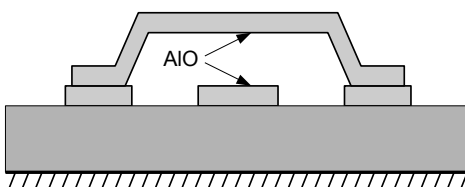
Figure 9.5: The native AlO is the only layer preventing the short-circuit between the beam and actuation pad during actuation.

stressing with a unipolar actuation voltage. The device recovered after switching the polarity of the actuation voltage. That pointed to a charging related failure. If it was due to mechanical causes, the device would not fully recover.

As the EFFA devices are fabricated with no interposer dielectric, the charge trapping can take place on or in the non-conductive substrate. These experiments were performed with the EFFA devices fabricated on a AF45 glass wafer.

That experiment showed that the substrate can indeed charge and influence the reliability of the RF MEMS devices as well as any other part of the device. The choice of the material should not be driven only by the RF properties of the devices.

9.3   Native aluminum oxide devices

The possible differences in the influence of the HR-Si and the AF45 glass wafers on the C-V characteristics of the parallel-plate type of devices were tested on two additional wafers fabricated without any additional interposer dielectric. The only dielectric barrier between the two conductive electrodes preventing short-circuiting is the native AlO (Figure 9.5). The native AlO is about 5.5nm thick and allows actuating the devices with an amplitude of the actuation voltage up to 7V.

A number of lifetime tests with C-V characteristic measurements during stressing were performed. Unipolar actuation waveforms of both polarities were used. The evolution of the C-V characteristics is presented in Figure 9.6a-d. The results show that the C-V characteristic can be both shifted and narrowed by the substrate charging.

Figure 9.6e-h show the extracted V_s and ΔW_{pi}. The pull-in window changes in a similar way. However, the voltage shift of the C-V curves is different for the devices fabricated on the glass and silicon wafers.

It has been stated that the pull-in voltage is influenced by the distribution of the electric field in around the bottom actuation electrode and the beam. As an influence of different types of substrate materials on the C-V characteristic is observed, the substrate can probably deform the electric field as well.

9.4   FEM simulations

9.4.1   Introduction

The results presented in the previous sections indicate a possible impact of the substrate material on the C-V characteristic. In order to understand this effect better, finite element modeling (FEM) is used. The methodology and results are described and discussed in the following.

The simulations of the charge influence on the C-V characteristic were performed using the Ansoft Maxwell FEM software. The software allows simulations of the electrostatic field. Combined electro-mechanical simulations are not possible. However, calculations of the electrostatic force acting on the beam are possible.

The FEM simulations of the devices fabricated on HR-Si substrate present the static case. The migration of charges in silicon is not taken into account. However, they give a feeling about the difference between the glass and silicon substrates.

9.4.2   FEM simulations methodology

The electrostatic force vs. actuation voltage, as shown in Figure 9.7, can represent the before-pull-in part of the C-V characteristic. The capacitance of the device indicates the position of the beam that is proportional to the actual electrostatic force. The F_{el} vs. U_{act} curve can be a representative indication of the influence of the trapped charges.

The F_{el} vs. U_{act} curves do not take into account the deformation of the beam (fixed in up position) and its influence on the pull-in and pull-out voltages modifications
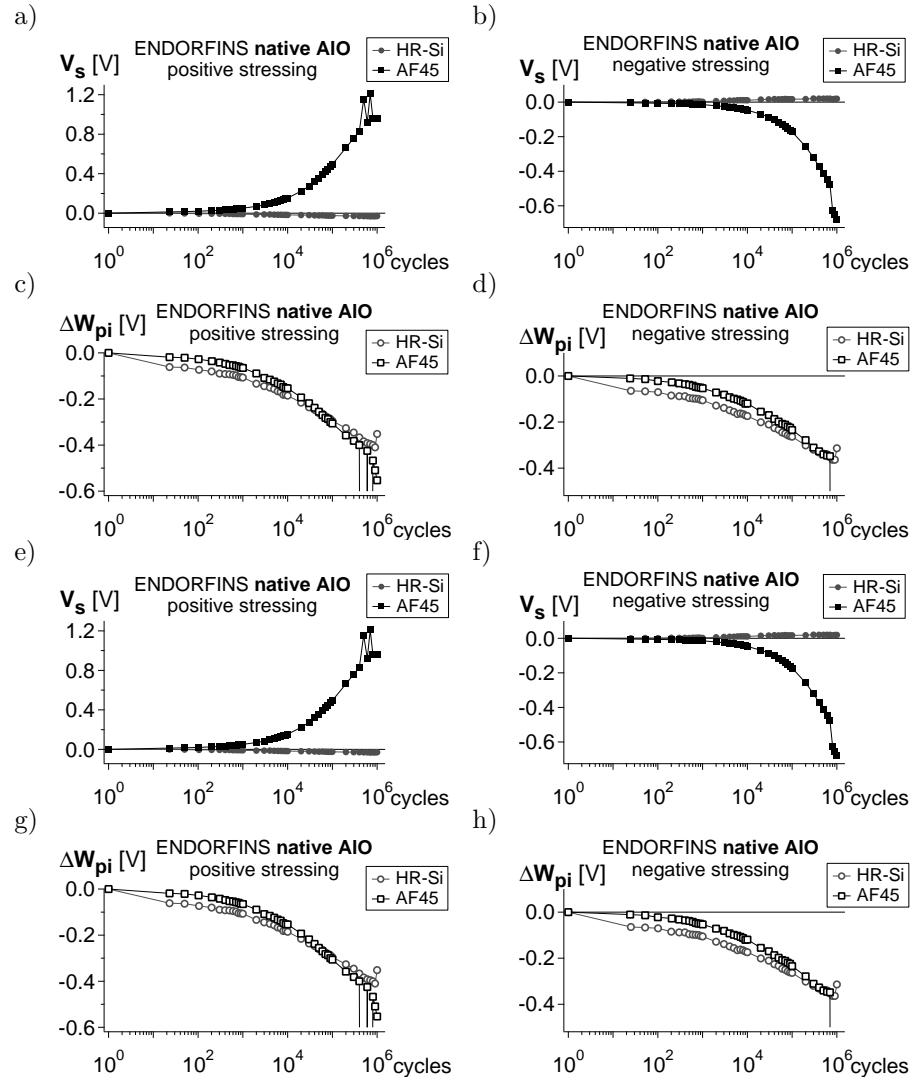
Figure 9.6: Results of experiments (C-V evolution) performed on the native AlO devices fabricated on HR-Si and AF45 glass. The V_s and ΔW_{pi} are extracted from C-V characteristics measured during stressing. Test conditions: $U_{act} = 5V$, positive and negative, 100Hz, 50% d.c., N_2, 25°C, light on.

as well as the influence of the distribution of the electric field alongside the beam. The resultant spring constant of the beam (thus the V_{pi} and V_{po}) depends on the distribution of the force that can be modified by trapped charge.

Nevertheless, the obtained results of simulations help to understand the influence of the trapped charges on the C-V curve of the devices fabricated on different types of substrates.

In the next part, the pull-in voltages were determined by finding a voltage level at a fixed value of the electrostatic force. Therefore, is it possible to show the changes caused by charges as shift and narrowing of the C-V curve. The C-V curve does not take into account the movement of the beam. However, it gives a feeling of the influence of the charge.

9.4.3 The AF45 vs. HR-Si wafer

The difference between the HR-Si and glass substrates is presented in Figure 9.8. The bottom part of the oxidized silicon wafer, even though high resistive, can be considered conductive. Therefore, the potential of the back side of the wafer is brought to the Si-SiO$_2$ interface. As a result, the voltage drop on the silicon can be neglected and most of the electric field appears across the SiO$_2$ layer. Due to the much lower thickness, the magnitude of the electric field across the SiO layer is much higher than across the $700\mu m$ of the glass.

9.4.4 FEM simulations results

No charge trapped

Figure 9.9a shows the distribution of the electric field alongside the beam in the AF-45 and HR-Si structures at 10V applied to the actuation pad with no charge trapped in the substrate. The difference is mainly due to the different distance between the actuation pad and the grounded back side of the wafers. In the AF45 glass structures the electric field penetrates much further in the slots next to the actuation pad.

Figure 9.9b shows the F_{el} vs. U_{act} curves simulated for both types of structures with no charge trapped. The different magnitude of the electrostatic force obtained at the same actuation voltage may result in slightly different pull-in voltages in real structures only due to a different substrate material. The difference becomes more visible when portions of charge is placed in the slots.
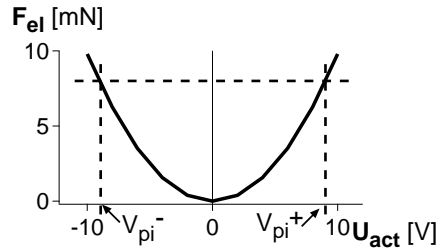
Figure 9.7: The voltage values found at a fixed electrostatic force allows determining a pull-in equivalent and observe the eventual shift and narrowing of the F-V (C-V) characteristic.
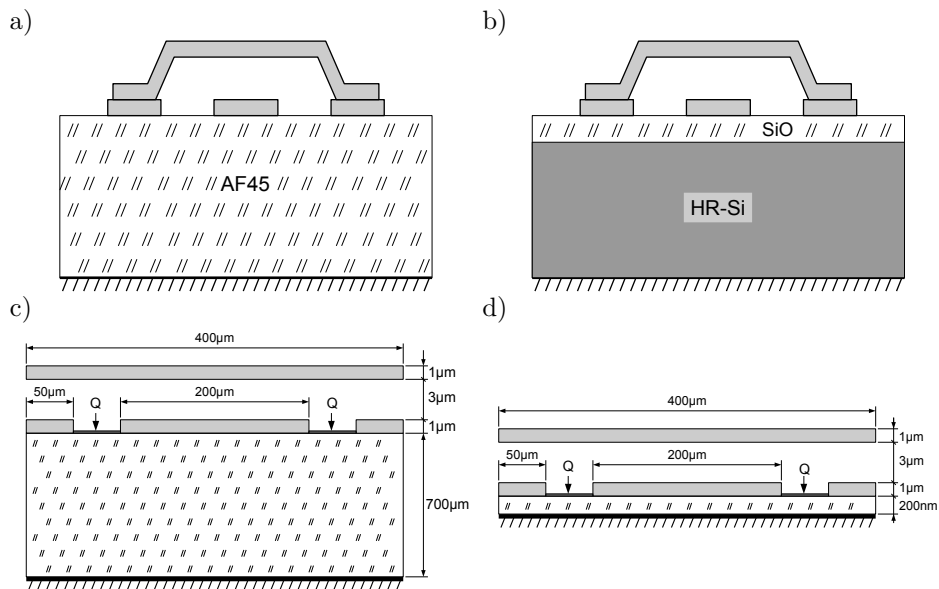
Figure 9.8: In the first approximation, the difference between the silicon and glass wafers is the thickness of the insulating layer: $700\mu m$ in AF45 a) vs. $200nm$ in HR-Si b). Therefore, the simulations can be performed using a similar structure with a conductive layer on the back side of the wafer and with a different thickness of the insulating layer c) and d). Q indicates the position of charge trapped in the slots between the bottom actuation pad and the ground pads.
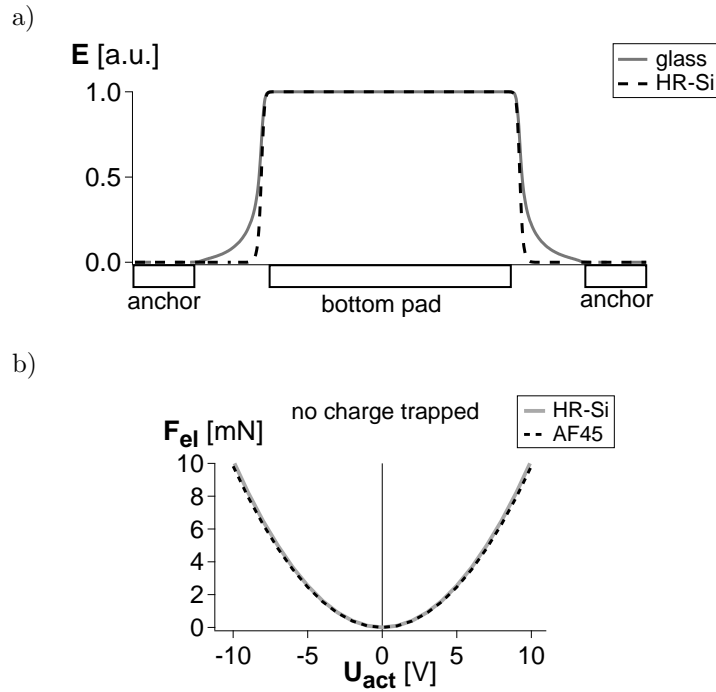
Figure 9.9: The obtained FEM simulation results show that the electric field is distributed in different ways in the structures fabricated on the glass and silicon substrates. The magnitude of the electric field along the beam shows that the electric field penetrates the slots much further in the case of the AF45 glass structures than the HR-Si devices b). The type of substrate material can modify the electrostatic force b) and the resulting V_{pi} and V_{po}.

With charge trapped in the substrate

Next, a number of simulations with portions of charge Q trapped in the slots were performed. The results are compared with the no-charge-trapped simulations results (Figure 9.10). The F_{el} vs. U_{act} curve of the AF45 glass structure show a shift and narrowing. In the case of the HR-Si structure mainly a C-V narrowing is observed.

9.4.5   Discussion and conclusions

The F_{el} vs. U_{act} curve of the AF45 structure can be shifted due to the electrostatic field penetrating the slots next to the actuation pad. The charges placed in the
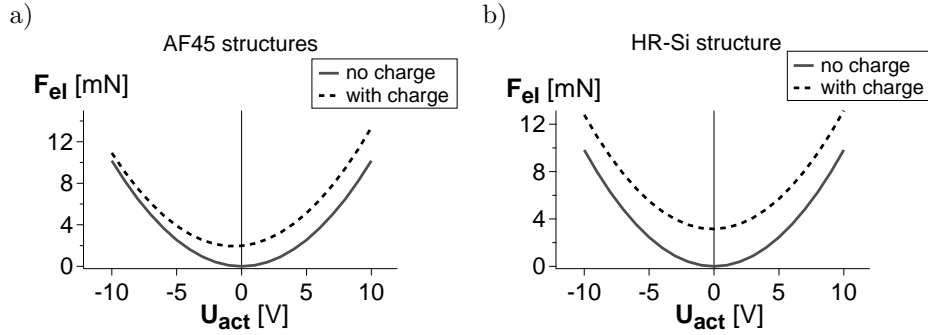
Figure 9.10: The charge trapped in the substrate can cause a visible shift and narrowing a) or mainly narrowing b) of the F_{el} vs. U_{act} curve depending on the type of the substrate material.

range of the field lines modify the component of the field created by the actuation voltage applied to the bottom pad. The modifications (mainly the sign) depend on the type of the trapped charge and polarity of the actuation voltage. Therefore, a shift of the F_{el} vs. U_{act} (C-V) curve can be observed.

In the case of the HR-Si structures, only a very small amount of the trapped charge can influence the actuation voltage field component. Most of the charge generates an additional independent force resulting in the observed narrowing of the curve.

Both experiments were performed with different quantities of the trapped charge. A charge of 2nC (in each slot) caused changes of the AF45 F_{el} vs. U_{act} curve. The same amount of charge did not show any visible changes in the HR-Si devices characteristic. The presented curve was simulated at 50nC (in each slot) of the trapped charge. That shows different sensitivity of the devices to the trapped charge depending on the used substrate material. The effect can be explained using a capacitor as a model. The voltage (generating the electrostatic force) created by charge stored in two capacitors of different capacitance is different. It lowers with increasing capacitance (Equation 9.1). The capacitance of an imaginary capacitor is much lower (due to higher thickness) in the AF45 devices than in the HR-Si structures. Therefore, a much lower amount of charge causes similar modifications of the electrostatic force.

$$U = \frac{Q}{C} \tag{9.1}$$

The charge trapped in the substrate can modify the effective actuation area. The actuation voltage field component can be focused or de-focused on a different than the designed part of the beam. That changes the distribution of the electrostatic force acting on the beam (and the V_{pi} and V_{po}). The focusing and de-focusing

depends on the mutual signs of the trapped charges and the electric field generated by the actuation voltage and can cause both the shift and narrowing of the C-V curve. Simulated distribution of the electric field alongside the beam with no charge, positive and negative charge trapped is presented in Figure 9.11.

The simulation results confirm the experimental data. The C-V characteristic of a device fabricated on the glass wafer is shifted and narrowed. The C-V characteristic of a device fabricated on the HR-Si wafer is mainly narrowed.

9.4.6 Competing mechanisms

The results presented in section 8.5 show that two mechanisms can cause a voltage shift of opposite signs and they may mutually cancel. The interposer dielectric charging is considered as one of the mechanisms. The substrate charging is another possibility.

It has been shown that the charge trapped in the substrate can cause a voltage shift. It needs to be verified whether the voltage shift caused by the charge trapped in the interposer dielectric can be canceled by the charge trapped in the substrate.

Charge can modify the C-V characteristic when the electric field component created by the applied actuation voltage is changed. The electric field in the switch fabricated on the HR-Si wafer is focused close to the actuation pad (Figure 9.9a). Therefore, it is possible that the charge trapped in the substrate close to the actuation can originate a voltage shift.

A number of FEM simulations using the test structure presented in Figure 9.12a were performed. Figure 9.12b shows a voltage shift of the C-V characteristic of a device with charge Q_{diel} trapped uniformly in the interposer dielectric. Figure 9.12c shows results of a simulation of the same structure with portions of charge Q_{sub} placed on the surface of the substrate close to the actuation pad. A shift and narrowing of the C-V curve is observed. Finally, Figure 9.12d shows results a FEM simulation with charge trapped in the interposer dielectric and in the substrate at the same time. The C-V curve is narrower with respect to the no-charge curve. The voltage shift disappears.

9.5 Non-contact stressing experiments

The substrate charge trapping can be emphasized by limiting the charging of the interposer dielectric. The interposer dielectric is charged mainly when an actuation voltage higher than the pull-in voltage is applied and the beam is in the bottom position.
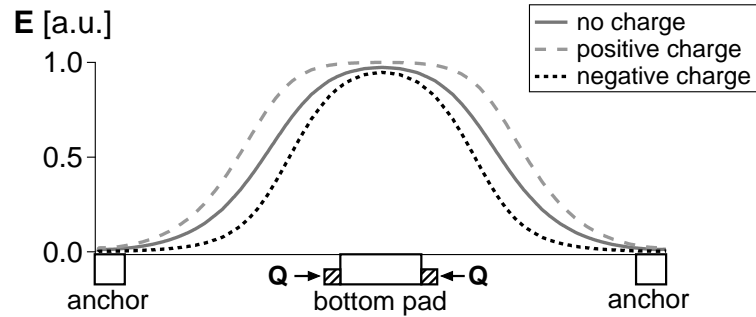
Figure 9.11: Simulated distribution of the electric field distribution alongside the beam by charge trapped in the vicinity of the bottom actuation pad with no charge, positive charge and negative charge trapped.
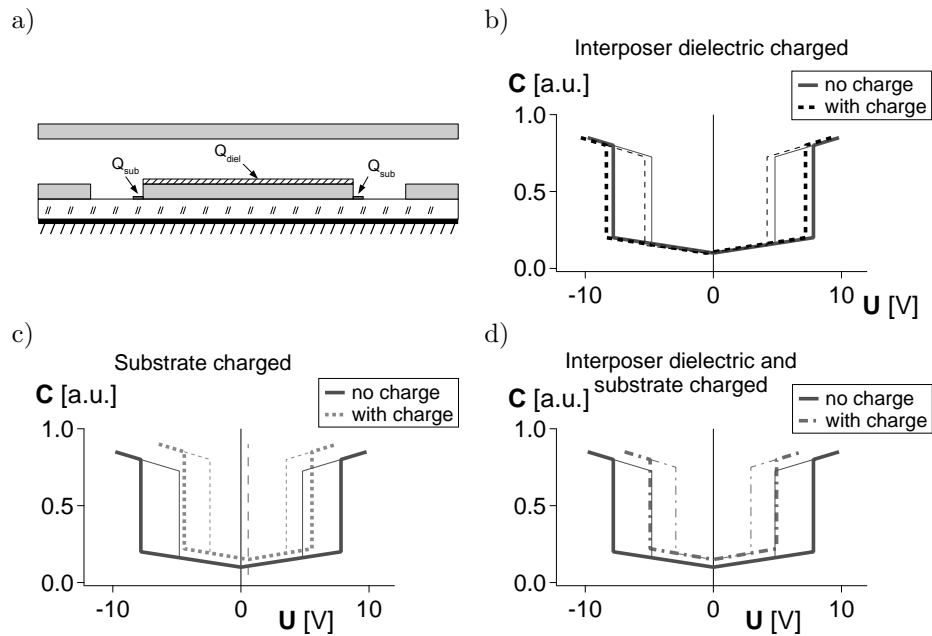
Figure 9.12: The geometry of the test structure used in FEM simulations a). The charge is trapped in the interposer dielectric Q_{diel} or on the surface of the substrate close to the actuation pad Q_{sub}. The results show that the voltage shift can be caused by both cases b) and c). The voltage shift caused by charge trapped in the interposer dielectric can be canceled by the charge trapped in the substrate d).

A voltage slightly lower than the V_{pi} keeps the beam in the up-state and thus reduces stressing of the interposer dielectric. In the same time, the substrate is stressed by the field between the bottom actuation electrode and the ground pads. If the substrate is charged by this field, then the pull-in voltage should drop and the pull-in should be observed.

To verify this, the following non-contact stressing experiments were performed.

9.5.1 Stressing of the devices under various atmospheric conditions

The ENDORFINS devices fabricated on two types of substrates, AF45 and HR-Si, were tested. In order to find the adequate amplitude of the actuation voltage the C-V characteristics of all tested devices were measured. Next, the non-contact stressing was started. To accelerate them, a DC actuation voltage was used. This actuation voltage was chosen to be about 1V lower than the observed pull-in voltage. To detect a possible pull-in, the capacitance of the devices was monitored during stressing. The experiments were performed in two types of atmosphere: dry N_2 and ambient air.

The results presented in Figure 9.13a show that indeed pull-in occurs in the case of the AF45 glass devices. The pull-in was observed after about 4min and 4h of stressing in air and dry N_2, respectively. A shift and narrowing of the C-V characteristic is observed in both cases (Figure 9.13c and e). This confirms that substrate charging takes place.

The HR-Si devices did not pull-in after 90h of stressing. No significant changes of the C-V curves are observed (Figure 9.13d and f).

9.5.2 Charge de-trapping observation

The observed changes of the C-V curves point to substrate charging being the cause of the pull-in. It has been presented that the charge trapped during stressing can be released during a period of idling.

To confirm this for substrate charging, an initially stressed device was monitored during idling. First, a DC voltage of an amplitude below the V_{pi} was applied to the devices until the pull-in occurrence (Figure 9.14a). Then, 0V was applied and the capacitance of the device was monitored. After about $4 \cdot 10^5$s the beam moved from the down to up position confirming release of trapped charge (Figure 9.14b).
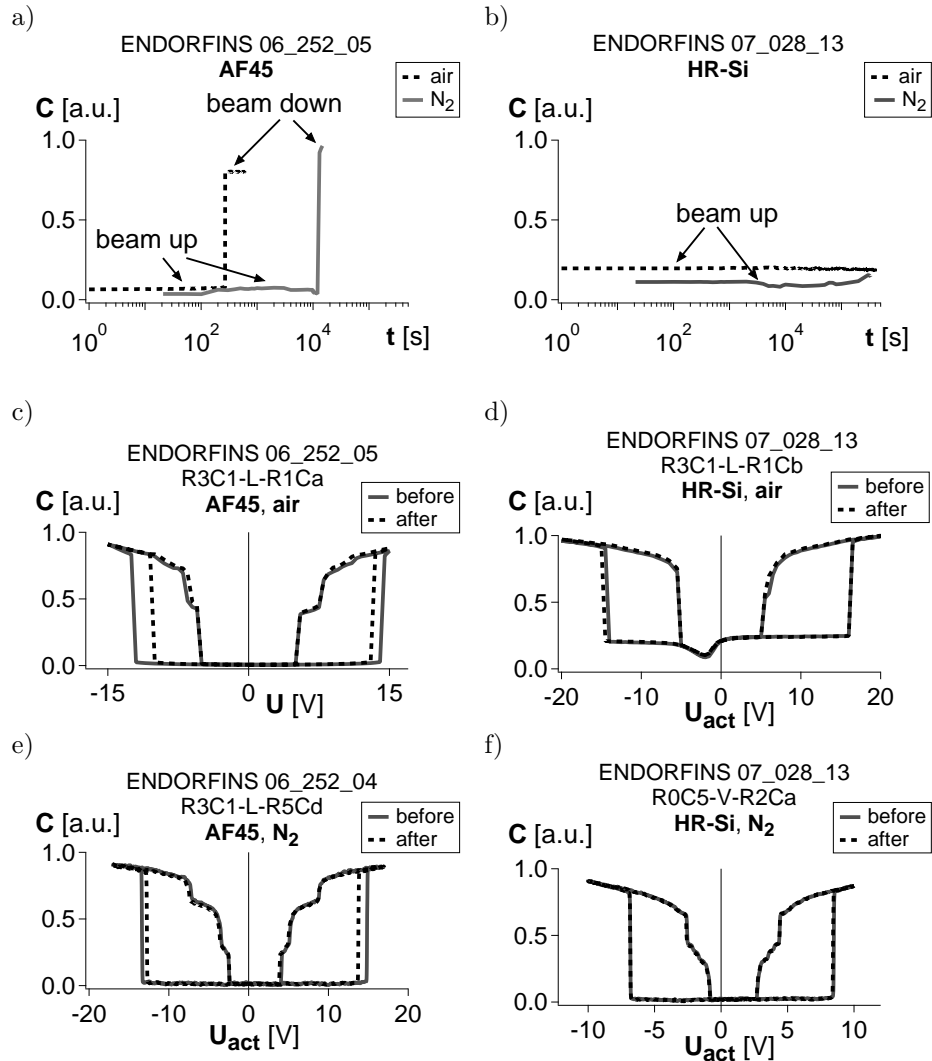
Figure 9.13: The non-contact stressing experiment results. The AF45 glass devices pull-in after a time of stressing. The time-to-pull-in depends on the atmosphere: the pull-in occurs faster in the air than in the N_2 a). A shift and narrowing of the C-V characteristic is observed c) and e). The devices fabricated on the oxidized silicon wafer did not pull-in even after about 90 hours of stressing b). Only small changes of the C-V curves are visible d) and f). Test conditions: $25°C$, light on.

a)

ENDORFINS 06_252_05
R3C1-L-R1Ce
AF45, **air**, U_{act}=10VDC

C [a.u.]

1.0

0.5

beam down

beam up

0.0

10^0 10^2 10^4 10^6 **t** [s]

b)

ENDORFINS 06_252_05
R3C1-L-R1Ce
AF45, **air**, U_{act}=0V

C [a.u.]

1.0

0.5

beam down

beam up

0.0

10^0 10^2 10^4 10^6 **t** [s]
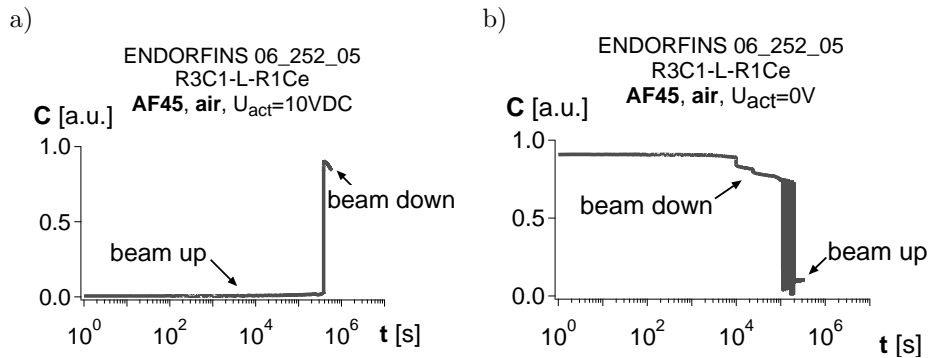
Figure 9.14: A first stressed device closed after about $4 \cdot 10^5$s a) and opened after $3 \cdot 10^5$s of idling b). Test conditions: $25°C$, light on.

t$_{pi}$ [s]

ENDORFINS 06_252_05
AF45, **air**, U_{act}<V_{pi}

10^6

10^4

10^2

10^0

8   10   12   14   **U$_{act}$** [V]
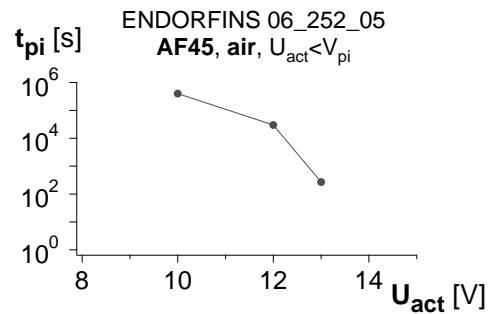
Figure 9.15: The t_{pi} depends on the actuation voltage in a similar way as the lifetime of the switches stressed using the standard rectangular actuation waveforms.

9.5.3 Voltage dependent time-to-pull-in

The charge trapping is a function of the applied amplitude of the actuation voltage. Therefore, the time-to-pull-in observed during stressing devices with the $U_{act} < V_{pi}$ can be expected to depend on the amplitude of the actuation voltage as well.

To verify this, a number of ENDORFINS AF45 devices were tested. Various amplitudes of the actuation voltage still lower than the pull-in voltage were used. The experiment was performed in the ambient air.

The results in a form of time-to-pull-in (t_{pi}) vs. U_{act} are presented in Figure 9.15. The curve shows that the t_{pi} depends on the U_{act} and, as expected, is higher when the applied voltage is lower.

9.5.4 Discussion and conclusions

The presented results show that a switch can pull-in even if the applied actuation voltage is lower than the actual V_{pi}. The pull-in occurs after some time of stressing. The pulled-in devices recover after a period of idling pointing to charge trapping being the cause of the pull-in.

The time to pull-in depends on the amplitude of the applied actuation voltage and the atmosphere. An increase of the U_{act} causes a faster pull-in occurrence. The t_{pi} is reduced when a device is tested in ambient air. That indicates the humidity enhanced charging.

9.6 Quartz as a substrate material candidate

The previous experiments show that the two types of investigated materials may impact the lifetime of the capacitive RF MEMS switches in two ways. The charging of the glass substrate is high even though the field across it is lower than in the HR-Si wafer.

The SiO_2 on top of the silicon wafer probably charges less than the glass at the same magnitude of the electric field. However, the electric field is much higher. That results in significant charging. One of the possible solutions would be to use a substrate material (MEMS compatible) that traps charges in a similar way as the thermal SiO_2 (in the HR-Si wafer) of a thickness of the AF45 glass wafer. Fused quartz can be such a candidate.

To study the charging properties of quartz substrates, a number of quartz wafers with dielectric-less (native AlO) devices as well as with the AlN2 interposer dielectric were fabricated and the lifetime of the structures was tested.

9.6.1 Dielectric-less devices

A native AlO switch fabricated on a quartz wafer was stressed for 10^6 cycles. A positive actuation voltage of 5V amplitude was used and the C-V characteristic was monitored during stressing. The V_{pi} and V_{po} were extracted and voltage shift and pull-in window were calculated. The results are presented in Figure 9.16. The C-V characteristic is both shifted and narrowed during the experiment. However, the changes are relatively low compared to the results obtained during stressing the AF45 and HR-Si devices (Figure 9.6). There is a high probability that devices fabricated on the quartz substrate can exhibit a high lifetime.
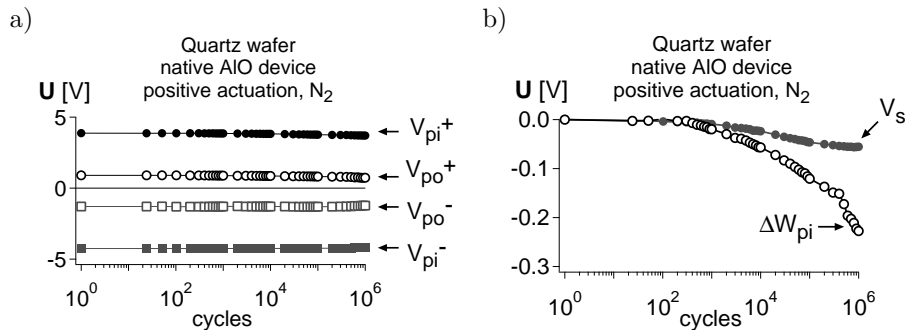
Figure 9.16: The evolution of the C-V characteristic of a native AlO device fabricated on the quartz substrate a). Boht shift and narrowing of the C-V curve are observed. Test conditions: $25°C$, N_2, 1atm, light on.

9.6.2 AIN2 devices

The lifetime of a number of AlN2 devices fabricated on a quartz wafer was tested. A positive actuation voltage with the amplitude ranging from 15 to 30V was used. The lifetime was determined using the EOL90%DC criterion and the C-V characteristic was monitored during stressing. The results are presented in Figure 9.17a. The LT vs. Uact curve seems to follow Goldsmith's model. However, the evolution of the C-V characteristic shows that the EOL is mainly due to narrowing of the C-V curve and not due to a shift (Figure 9.17b and c). The shift seems to stabilize after the first few thousands cycles (Figure 9.17d) and the pull-in window is still changing (Figure 9.17e).

This indicates that substrate charging has a significant influence on the lifetime limitation in the case of the quartz substrate. The lifetime of the quartz devices drops fast with an increasing amplitude of the actuation voltage. That makes the quartz not a very good substrate candidate.

9.6.3 Summary

Quartz was proposed as a possibly better substrate candidate for the capacitive RF MEMS switches. However, the results of the lifetime tests showed a significant charge trapping in the quartz.

The first test indicated that there is not much charging in the quartz substrate. However, the experiment was performed at a relatively low voltage. The next experiment showed that at higher voltages the lifetime of the devices drops drastically and the substrate charging is the main cause of the failure.
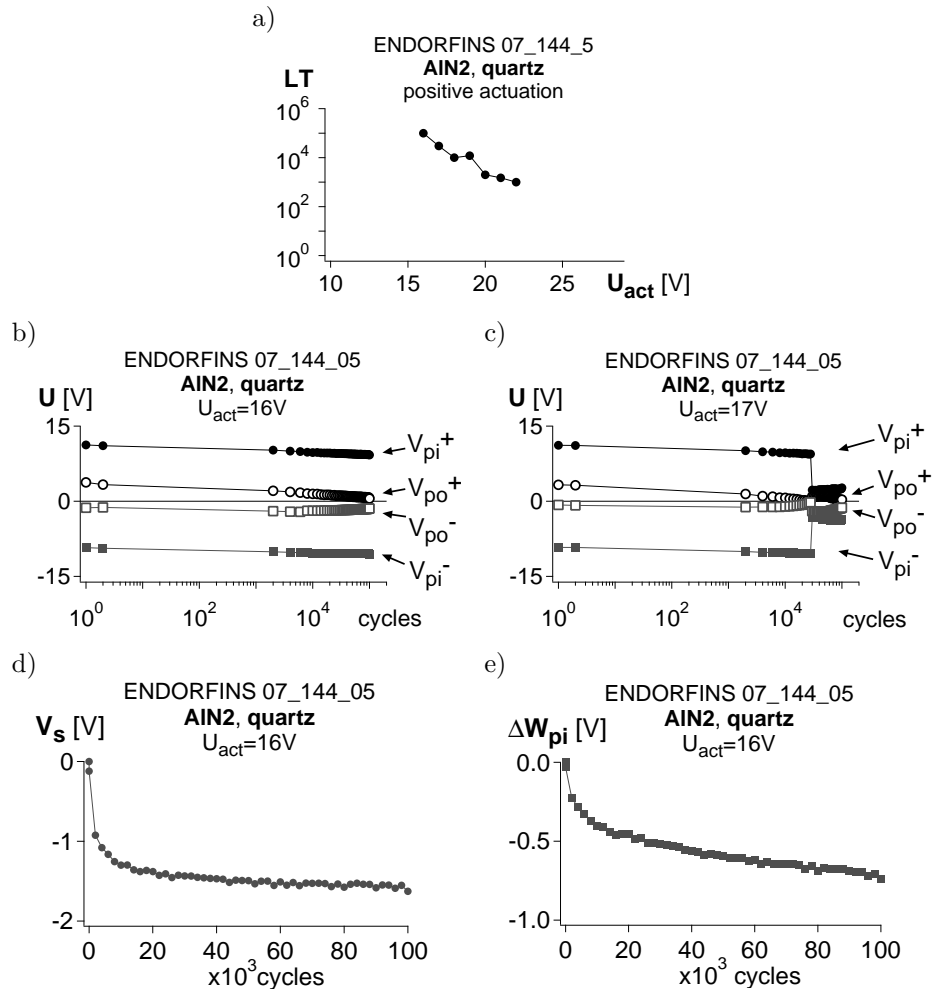
Figure 9.17: The LT vs U_{act} curve seems to be with an agreement with the Goldsmith's model a) However, the EOL is due to the narrowing of the C-V curve and not the shift b) and c). The shift seems to saturate after the first few thousand cycles d) while the pull-in window is still changing e). Test conditions: $25°C$, N_2, 1atm, light on.

However, quartz may be desired due to its low RF losses. In order to improve the lifetime of the devices fabricated on quartz substrates the geometry of the switch should be optimized to obtain a low sensitivity to the trapped charge.

9.7 Summary and conclusions

The results presented in this section show that the substrate is an important factor influencing the reliability of capacitive RF MEMS switches. The substrate, that is usually an insulating material, can trap sufficient charge to limit the lifetime of the devices.

The influence of the substrate was exposed during a study of the impact of the environment on the lifetime of the capacitive devices. The tested devices were fabricated on two types of substrates, AF45 glas and HR-Si, that respond differently on stressing under different environmental conditions (biasing+environment).

A possible explanation is the different affinity to water molecules. The AF45 glass exhibits hydrophilic properties and the silicon oxide can be both hydrophobic and hydrophilic [456]. Hydrophobicity of the silicon and silicon oxide can be changed. E.g. the surface of the silicon wafers needs to be prepared for the anodic bonding process that requires hydrophilic surfaces.

The conditioning experiment shows that it is easier to remove the humidity from the HR-Si surface than from the glass wafer.

Migration of charges on the surface of a silicon wafer was studied and presented by Shockley et al. in [455]. The authors stress a structure in dry and humid atmospheres. The charge distributes laterally on the surface next to the electrode placed on top of the oxide surface. A similar situation takes place in the case of the switches. The electric field between the actuation and ground electrode allow charge to migrate over the surface of the substrate. The charges trapped on the surface of the substrate modify the electric field distribution causing changes in the C-V characteristic and can even cause charge-induced pull-in of switches at voltages below the pull-in voltage.

The lifetime of a number of devices fabricated on another type of substrate material was tested as well: Quartz was proposed as a material that should not trap charges and in the same time exhibit low RF losses. The first results showed only small changes in the C-V characteristic during stressing indicating no severe charge trapping in the quartz. However, the lifetime of the devices drops drastically when stressed with higher amplitude of the actuation voltage. The shift narrowing of the C-V curves points to the substrate charging being a considerable lifetime limiting factor.

Chapter 10

Identification of failure mechanisms

10.1 Introduction

The previous chapter shows that there is more than one charging mechanism limiting the lifetime of the capacitive RF MEMS switches. The interposer dielectric charging is only one possibility. The substrate charging is another important mechanism that can significantly impact the performance of the switches. It has been shown that the different mechanisms can occur or can be visible under different testing conditions. The experiments performed in different environmental conditions show a different impact of different types of substrates. This chapter is focused on the identification and localization of these different charging mechanisms.

First the impact of the dielectric thickness is studied. Changing the thickness of the interposer dielectric layer allowed studying the balance between the different charging mechanisms.

Next, mechanisms with different time constants are shown. The use of different biasing methods allowed the isolation of "slow" and "fast" mechanisms. However, the methods do not provide clear information about the exact location of the mechanisms in the sample.

A method to measure and map charge trapped in the capacitive switches has been proposed in literature. However, the EFM (Electrostatic Force Microscopy) requires removal of the beam after stressing. Therefore, a number of methods that allow to locate different charging mechanisms without the need of using additional equipment and destroying the device are presented. The methods require the

introduction of an extended qualitative model of the switch.

The so far used model of the device, two parallel plates of the same size, did not take into account the presence of the substrate. Therefore, an extended model of the switch is proposed. The model consists of a simplified representation of the high-resistivity silicon substrate. The use of the model is verified with FEM simulations. Based on the results a guide that should help to locate the charging is created.

Next, the results of the FEM simulations are compared with the measurements results. The devices are stressed using non-standard actuation methods that allow emphasizing particular charging mechanisms. The obtained experimental data are different than expected, yet, are very consistent. One specific charging mechanism is pointed out. The proposed model turned out to be missing an important factor. It is discussed in the next chapter.

10.2   Impact of the dielectric thickness

Charge trapping in the interposer dielectric is recognized as the main charging mechanisms in the capacitive RF MEMS devices. The charge trapping in a dielectric layer depends on the applied voltage and the thickness of the layer. Therefore, modifications of the dielectric layer thickness may influence the lifetime. A thicker layer of the dielectric is expected to improve the lifetime. Moreover, testing devices with a thicker layer of the interposer dielectric may give some insight into the other charging mechanisms occurring in the switch. Therefore, an additional wafer with 500nm thick AlN2 dielectric layer was fabricated. The wafer contains a set of ENDORFINS fully-processed test structures.

10.2.1   Lifetime vs. actuation voltage

First, a number of lifetime experiments using various amplitudes of the actuation voltage were performed. The C-V characteristics during stressing were measured and the lifetime using the EOL2V criterion was determined. The results are presented in Figure 10.1a. The graph shows a comparison of the results obtained during testing of the 200nm AlN2 and 500nm AlN2 devices.

The lifetime of the 500nm AlN2 devices was determined by a negative C-V shift only (Figure 10.1b). No positive shift was observed. Hence, the EOL was caused by one mechanism only.

The amplitude of the voltage shift is higher than in the case of the 200nm AlN2 devices (Figure 10.1c and d). An opposite situation was expected as the thicker

dielectric is supposed to trap less charge. However, the amplitude of the voltage shift of the 200nm devices decreases with increasing U_{act}. That is due to a second mechanism that is present in the 200nm AlN2 devices. Both compensate each other's voltage shift.

One of the mechanisms does not appear (is less significant) in the case of the 500nm AlN2 structures. The lifetime of the 500nm AlN2 devices decreases with increasing amplitude of the actuation voltage due to an increasing voltage shift. Lower changes of the ΔW_{pi} show that the 500nm AlN2 devices trap mainly one type of charge (Figure 10.1e and f).

10.2.2 Beyond-EOL observations

One of the 500nm AlN2 ENDORFINS devices was stressed for a longer time and the C-V characteristic was observed. The experiment was continued even though the EOL, indicated by one of the pull-out voltages crossing the 0V point, was reached. The C-V characteristic was monitored and the V_s and ΔW_{pi} were extracted. The results are shown in Figure 10.2.

First, a shift towards negative voltages is observed. The amplitude of the charging component causing this negative shift is high enough to cause the V_{po}^+ crossing the 0V point (Figure 10.2a). Further stressing causes a positive shift component to become visible (Figure 10.2b). The observed C-V shift back to the center position could be due to a release of the trapped charge. However, the narrowing of the C-V characteristic shows that there is charge trapping during the entire experiment (Figure 10.2c).

10.2.3 Observations during idling after stressing

The experiment presented in the previous section was extended with observations of the C-V curve during idle after stressing. The device was un-actuated and the C-V measurements were performed. Figure 10.3a shows the C-V characteristic recorded before and immediately after stressing. A shift towards negative voltages is observed. Figure 10.3b shows the C-V curves recorded before stressing and after stressing plus 25min idling. The dominant negative shift is gone however a small positive shift component becomes visible and remains present. Figure 10.3c shows the evolution of the V_s during idling. Most of the negative shift disappears during 5 min of idling and only the positive shift remains. The release of the "fast" charge is confirmed by the increase of the pull-in window (Figure 10.3d). The positive shift of the C-V curve observed after idling indicates that negative charge remains trapped.
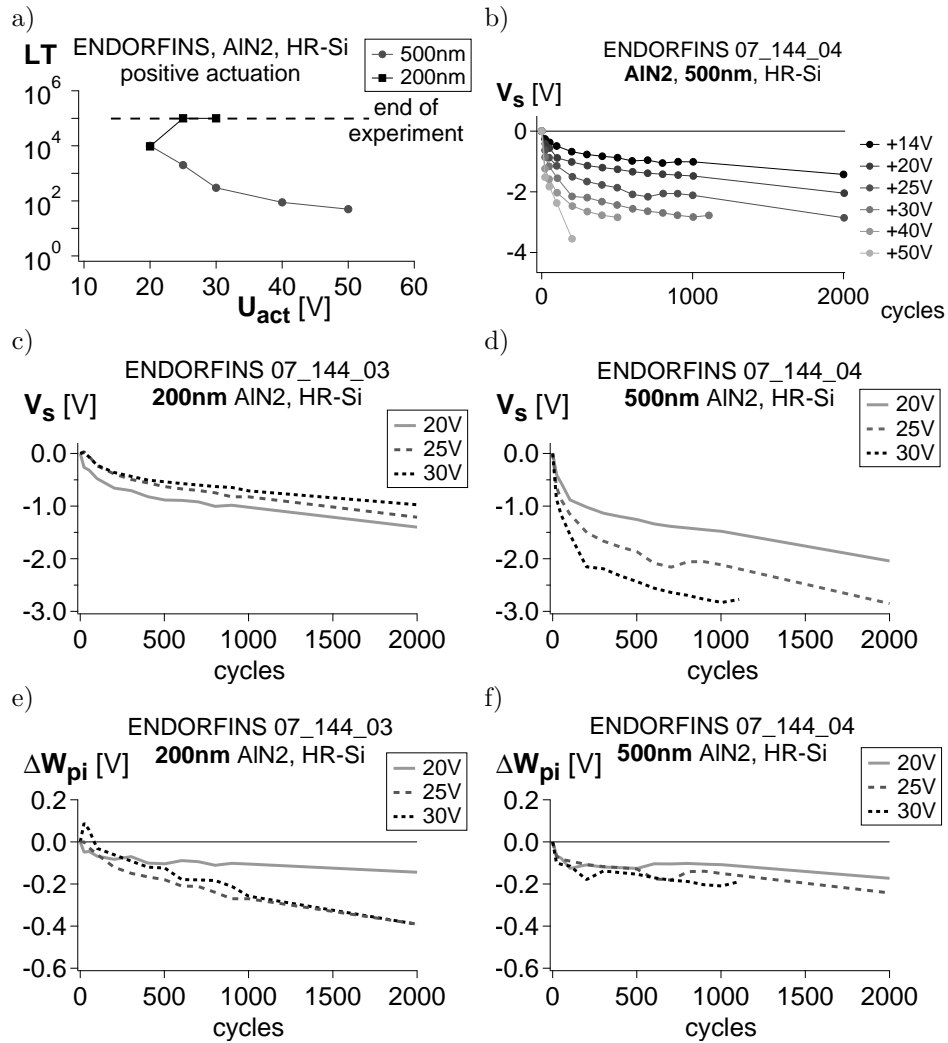
Figure 10.1: A comparison of lifetime test results of 200nm AlN2 and 500nm AlN2 ENDORFINS devices a). The amplitude of V_s increases with increasing U_{act} b). The differences in evolution of the V_s and Δw_{pi} shows that one charging mechanisms is reduced c-f). Test conditions: positive actuation voltage, 100Hz, 50%d.c., 1atm N_2, 25°C, light on.
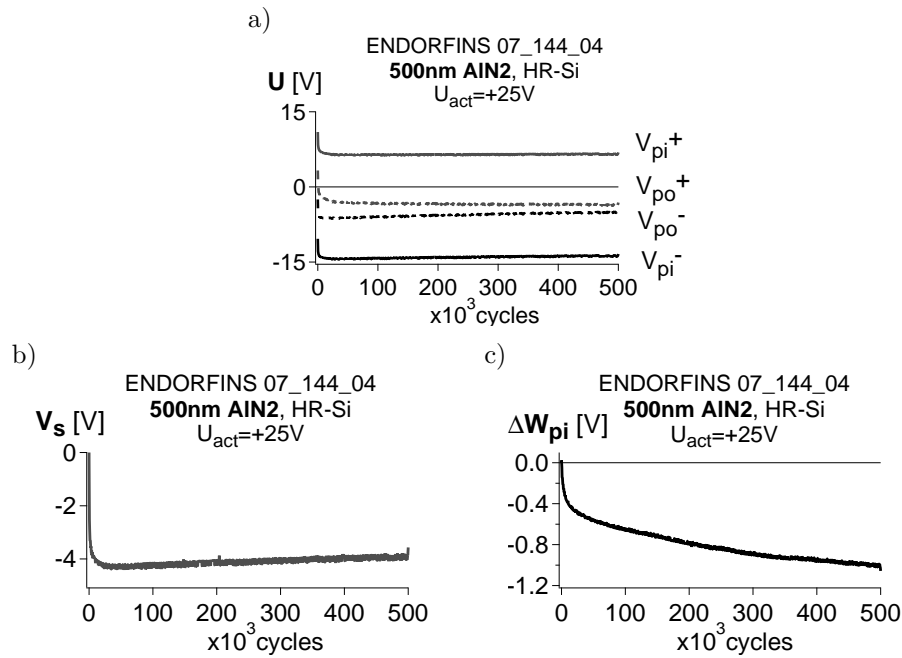
Figure 10.2: The C-V characteristic observations of a 500nm AlN2 device. The experiments was continued even though the EOL was reached a).The C-V characteristic first shift towards negative voltages. After some time a positive V_s is visible as well b). The narrowing of the C-V curve show that both components are due to charge trapping c). Test conditions: $25°C$, N_2, 1atm, light on.

10.2.4 I-V characteristic of a MIM structure

To verify the type of charge trapped in the interposer dielectric an I-V curve of a 200nm AlN2 MIM capacitor was measured (Figure 10.4). The observed hysteresis indicates indeed negative charge trapping.

10.2.5 Summary and discussion

The presented results show that the lifetime of the devices with the AlN2 dielectric depends on the thickness of the interposer dielectric layer. However, a lifetime reduction instead of an improvement with increasing thickness is observed. An understanding of the effect requires a closer look at the obtained results.

The un-usual behavior, previously observed in the 200nm samples, is not noticed in the 500nm devices. The C-V characteristic is shifted towards one direction only, i.e.

a)

ENDORFINS 07_144_04
500nm AlN2, HR-Si
U_{act}=+25V

C [a.u.]

b)

ENDORFINS 07_144_04
500nm AlN2, HR-Si
U_{act}=+25V

C [a.u.]

c)

ENDORFINS 07_144_04
500nm AlN2, HR-Si
U_{act}=+25V

V_s [V]

d)

ENDORFINS 07_144_04
500nm AlN2, HR-Si
U_{act}=+25V

ΔW_{pi} [V]
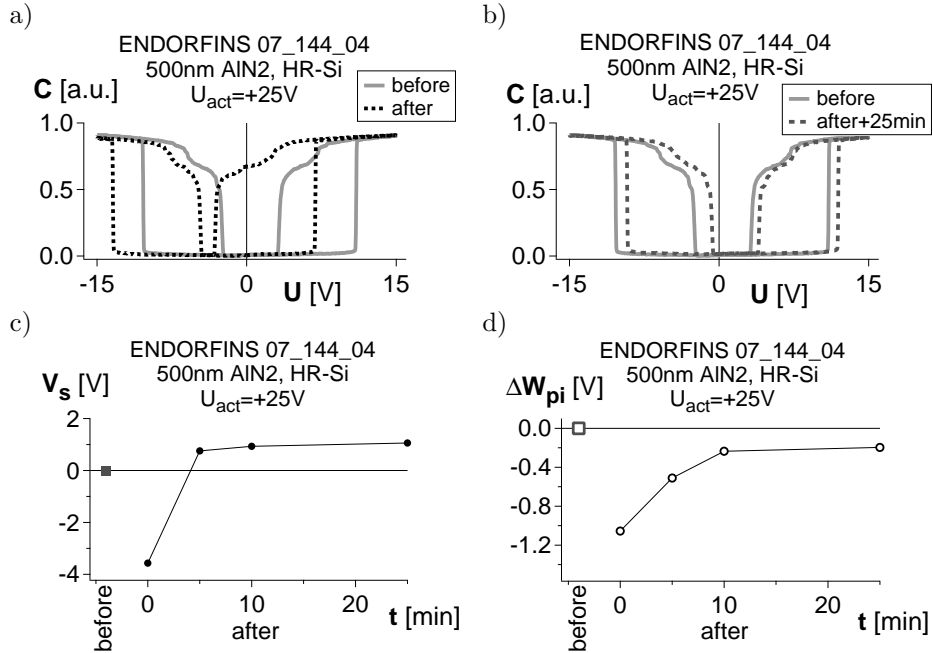
Figure 10.3: The C-V characteristics recorded before and after stressing a) and after 25min of idling b). The negative shift disappears during first 5 min and only a positive shift is visible c). The change of the pull-in window indicates release of trapped charge d). Test conditions: $25°C$, N_2, 1atm, light on.

I-V measurement
MIM capacitor

I [a.u.]
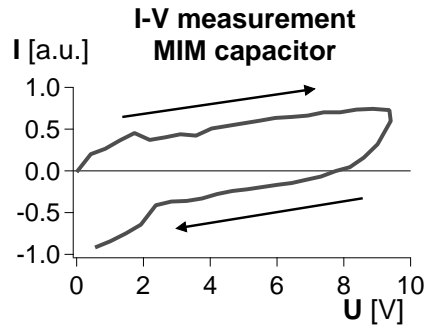
Figure 10.4: The hysteresis on the I-V measurement of an AlN2 MIM capacitor indicates negative charge trapping. Test conditions: $23°C$, ambient air, 1atm, light off.

a voltage shift of one sign is observed, during stressing the devices with positive actuation voltage of amplitudes up to 50V. The amplitude of the V_s increases with increasing amplitude of the actuation voltage. The EOL can be determined by monitoring of only one, positive, pull-in voltage up to 50V of the U_{act}.

This voltage shift of only one sign indicates one dominant charging mechanism.

It has been shown that two charging mechanisms can cancel each other's impact on the voltage shift of the C-V characteristic. If both are equal, then no shift is observed. However, the change of the pull-in window indicates the presence of the two mechanisms. If one of the mechanisms becomes dominant, then a voltage shift of one sign is observed. The domination of a mechanism can be observed if one of the mechanisms is enhanced or another one reduced. The enhancement of one of the mechanisms is mirrored in a higher change of the pull-in window. A lower ΔW_{pi} indicates the reduction.

The magnitude of the V_s observed during stressing the 500nm AlN2 devices is higher than the one observed during stressing the 200nm AlN2 ENDORFINS switches. At the same time, the pull-in window is affected less pointing to a reduction of one of the mechanisms. The reduction of one charging mechanism is linked to the use of the thicker interposer dielectric layer. The thicker interposer dielectric is expected to trap less charge. Only a negative voltage shift, indicating positive charge trapping, is observed. The magnitude of the positive shift, related to negative charge trapping, seems to depend on the thickness of the interposer dielectric. The stressing-after-EOL experiment shows that the second mechanism is still present, though it is significantly reduced.

The I-V characteristic of a MIM capacitor with the AlN2 dielectric indicates negative charge trapping in this type of dielectric.

The introduction of the thicker interposer dielectric layer caused a reduction of one charging mechanism in the ENDORFINS switches. However, the other mechanism, probably the substrate charging, is still present. Not compensated voltage shift caused by charge trapped in the substrate lowers the lifetime of the devices.

In conclusion, there are clearly two charging mechanisms. The interposer dielectric traps negative charges as confirmed with the I-V measurements of MIM capacitors. For a thin dielectric, the negative charging of the interposer dielectric dominates the second charging behavior. For a thick dielectric, the second charging mechanism becomes more visible.

10.3 "Fast" and "slow" components

10.3.1 Introduction

The presence of charging mechanisms with different time constants has been presented in section 8.6. Thus these different mechanisms can be separated in the time domain.

The observations of the "fast" and "slow" V_s and ΔW_{pi} components can help distinguishing the different charging mechanisms. The method can be used when different mechanisms exhibit different time constants. More experiments using the method were performed and are discussed in the following sections.

10.3.2 Experimental results

An ENDORFINS 200nm AlN2 device fabricated on the HR-Si wafer using positive actuation voltage was stressed. The C-V characteristic was monitored at regular intervals during stressing and during idling after stressing. The results are presented in Figure 10.5.

Two mechanisms are visible: "fast" and "slow". Both cause a voltage shift of opposite signs. Most of the "fast" charge is released during the first 1-2 minutes of idling. Further, only a positive shift caused by the "slow" charge is visible.

It is clear that the "fast" charge is trapped and released in much shorter time period than the "slow" one. That helps in observations of both mechanisms.

10.4 "Fast" component observations

10.4.1 Introduction

The results presented in section 8.5 show that depending on the amplitude of the actuation voltage, different mechanisms can be dominating. One of the components, the "fast" one seems to be more visible when low amplitudes of the U_{act} (below the U_{opt}) are used. This effect is used to study this particular component more in detail.

a)

b)
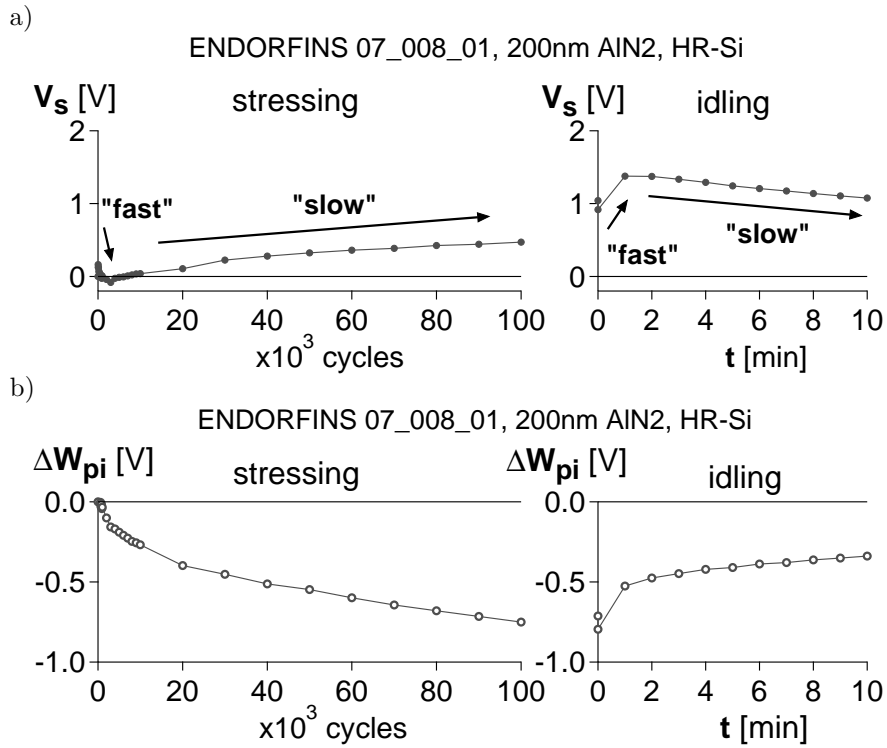
Figure 10.5: The V_s and ΔW_{pi} observed during and after stressing ENDORFINS AlN2 devices with a positive actuation waveform. The "fast" and "slow" components are visible. Test conditions: U_{act}=25V, 100Hz, 50%d.c., 1atm, N$_2$, 25°C, light on.

10.4.2 Experiments

Two groups of 500nm AlN2 ENDORFINS devices using positive and negative actuation voltages of 10V amplitude were stressed. The C-V characteristic during stressing was observed and V_s and ΔW_{pi} were extracted. The results are presented in Figure 10.6.

10.4.3 Discussion

The positive and negative low actuation voltages cause a fast voltage shift of opposite signs and similar magnitude. The pull-in window of the C-V characteristic is modified in a similar way in both cases. The same magnitude of the V_s and W_{pi} point to a similar quantity and distribution of charges. However, the different voltage shift signs indicate trapping of both, positive and negative, types of charge.
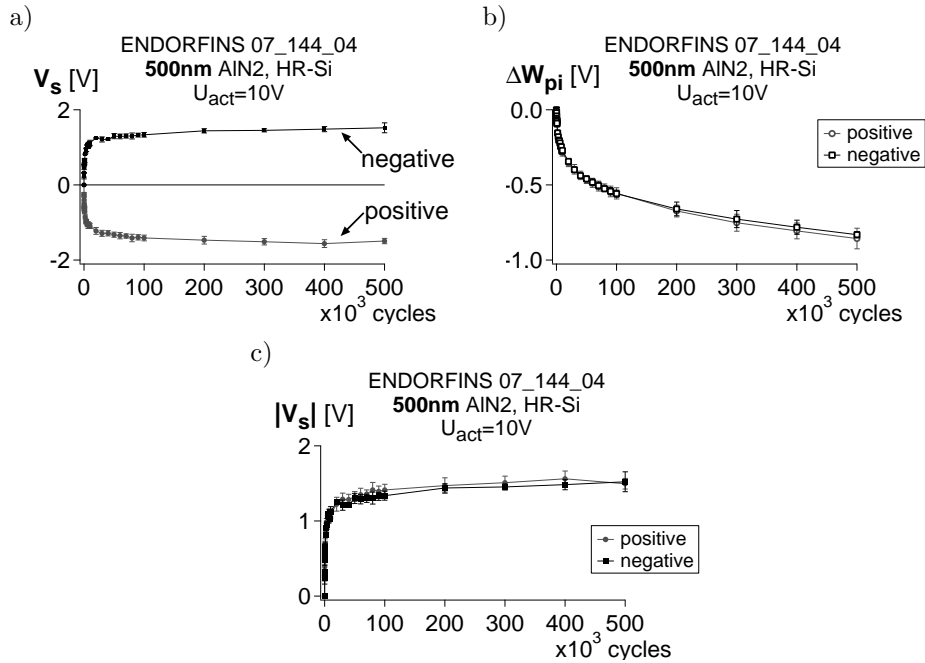
Figure 10.6: Positive and negative actuation voltage of 10V amplitude cause a voltage shift of opposite signs. However, the magnitude of the V_s and ΔW_{pi} are similar in both cases. Test conditions: $25°C$, N_2, 1atm, light on.

It has been shown that the interposer dielectric traps mainly one type (negative) of charges. However, even if both types of charge could be trapped in the interposer dielectric, it is highly possible that the amount and space distribution are different.

The MEMS structure, the bottom electrode, interposer dielectric, gas (air) gap and the beam, make a very asymmetric structure. Injection and/or extraction of charges from the interposer dielectric are probably asymmetric as well. Therefore, charge trapping in the interposer dielectric is less likely to cause the observed effects presented in Figure 10.6.

Another possible place for charge trapping is the substrate. The silicon oxide is known from amphoteric behavior. It can trap both types of charge [322, 343]. However, trapping positive and negative charge is expected to be asymmetric as well.

A more plausible cause of the observed voltage shift is charging (not charge trapping) of the switch capacitance. The dielectric creates a capacitor with the bottom electrode and the beam. In the down position, the capacitor is charged by the actuation voltage. However, when the actuation voltage is removed, the

capacitor does not have to be completely discharged for pull-out occurrence. As long as the voltage across the capacitor is lower than the pull-out voltage, the beam still can travel from bottom to top position. In the next cycle, a lower actuation voltage is required to move the beam to the bottom position. As a result a voltage shift is observed. Depending on the polarity of the actuation voltage, both positive and negative voltage shifts can be observed. The phenomenon is an RC circuit charging and is polarity independent.

Other possibilities are dipolar polarization of the dielectric material or charge migration [343].

10.5   "Slow" components observations

There are, at least, two techniques that allow observation of the "slow" charging components. The first technique has already been introduced: C-V characteristic measurements during idling after stressing. This technique allows observations of charge de-trapping. The second method introduces idling periods during stressing. The idling period allows releasing the "fast" charge. In the following experiment, devices are stressed for a low number of cycles (e.g. 1000) and then not actuated for a period of time (e.g. 2 min). The stressing-idling cycle is repeated several (n) times. The C-V characteristics are measured after every idling period.

10.5.1   Idling after stressing

First, the results obtained using the "idling after stressing" technique are presented and discussed.

A number of 200nm AlN2 ENDORFINS devices were stressed using positive and negative actuation voltage. However, long time stressing at high voltage causes the devices to stick and observations of the C-V characteristic are difficult. Figure 10.7 shows results of the experiment performed at an actuation voltage of +25V. This U_{act} amplitude allowed complete observations with both polarities of stress.

The C-V characteristic recovers in different ways when positive and negative actuation voltages are used. The sign of the "slow" component of the V_s depends on the polarity of the actuation voltage. The way the charge is released is different as well. The V_s and ΔW_{pi} change in different ways during idling. That may indicate the existence of two different "slow" mechanisms, activated by different polarities of the actuation voltage. It is possible that both mechanisms cause charging in both cases (positive and negative stressing) and only one is dominant at a time.
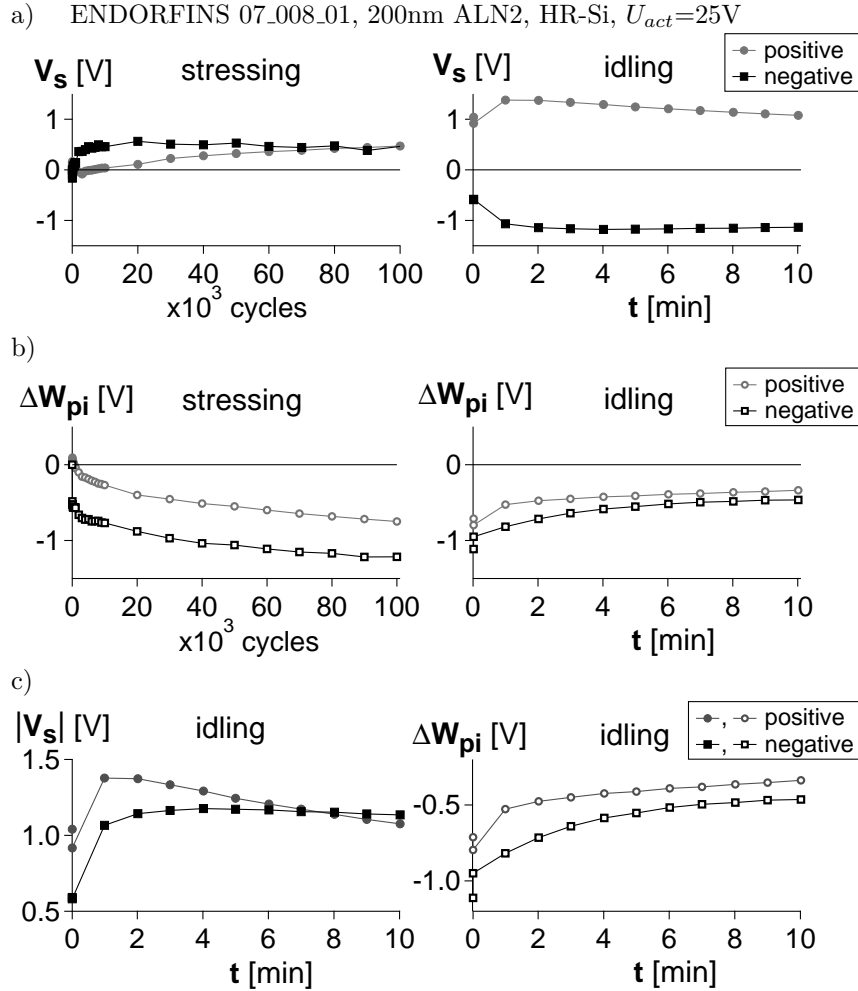
Figure 10.7: Monitoring thr C-V characteristic during idling after stressing allows observations of the "slow" charging mechanisms. The de-trapping of charge trapped during stressing the devices with positive and negative actuation voltages are different. The different evolution of the V_s and ΔW_{pi} may indicate different mechanisms activated with different polarities of the actuation voltage. Test conditions: stressing - U_{act}=25V, 100Hz, 50%d.c., idling - C-V measurements every 1 min, N_2, 1atm, 25°C, light on.

That is contrary to the results presented in section 8.6. The "slow" charging component was always of one sign independently on the U_{act} polarity. However, both experiments were performed using devices fabricated on two different wafers. The substrate material is of two different resistivity levels. The thickness of the AlN2 layer may be slightly different as well. All that may change the balance between the mechanisms and/or make one of the mechanisms not present or not visible in some cases.

The observations during idling after stressing allow the observations of the "slow" charge release. In addition, due to the long stressing period, the devices can be stuck quickly and then the C-V characteristic measurements are impossible. Therefore, another method, idling during stressing, is proposed.

10.5.2   Idling during stressing

The "slow" charge occurs at higher amplitudes of the actuation voltage ($>$20V) than the "fast" charge. To avoid obscuring the "slow" charges by the "fast" ones, idling periods during stressing were introduced. It has been shown that the "fast" charge is released in about 2 minutes (see Figure 10.5). Therefore, the devices were stressed for 1000 cycles and then stressing was stopped for 2 minutes. The C-V characteristic was observed during the experiment and the pull-in voltages were extracted. The voltage shift and pull-in window changes are presented in Figure 10.8.

A shift of the C-V characteristic depending on the amplitude of the actuation voltage is observed (Figure 10.8a and c). That is in agreement with Goldsmith's model: the higher the actuation voltage, the higher the impact on the C-V curve (i.e. lower lifetime).

The sign of the voltage shift depends on the polarity of the actuation voltage. That is contrary with the hypothesis of only one type charge being trapped in the interposer dielectric. However, if the amplitudes of the voltage shift and the ΔW_{pi} are compared, then differences are visible (Figure 10.8g). The voltage shift is lower and the C-V characteristic is more narrowed in the case of the negative actuation voltage. That may indicate two different mechanisms activated by different polarities of the actuation voltage.
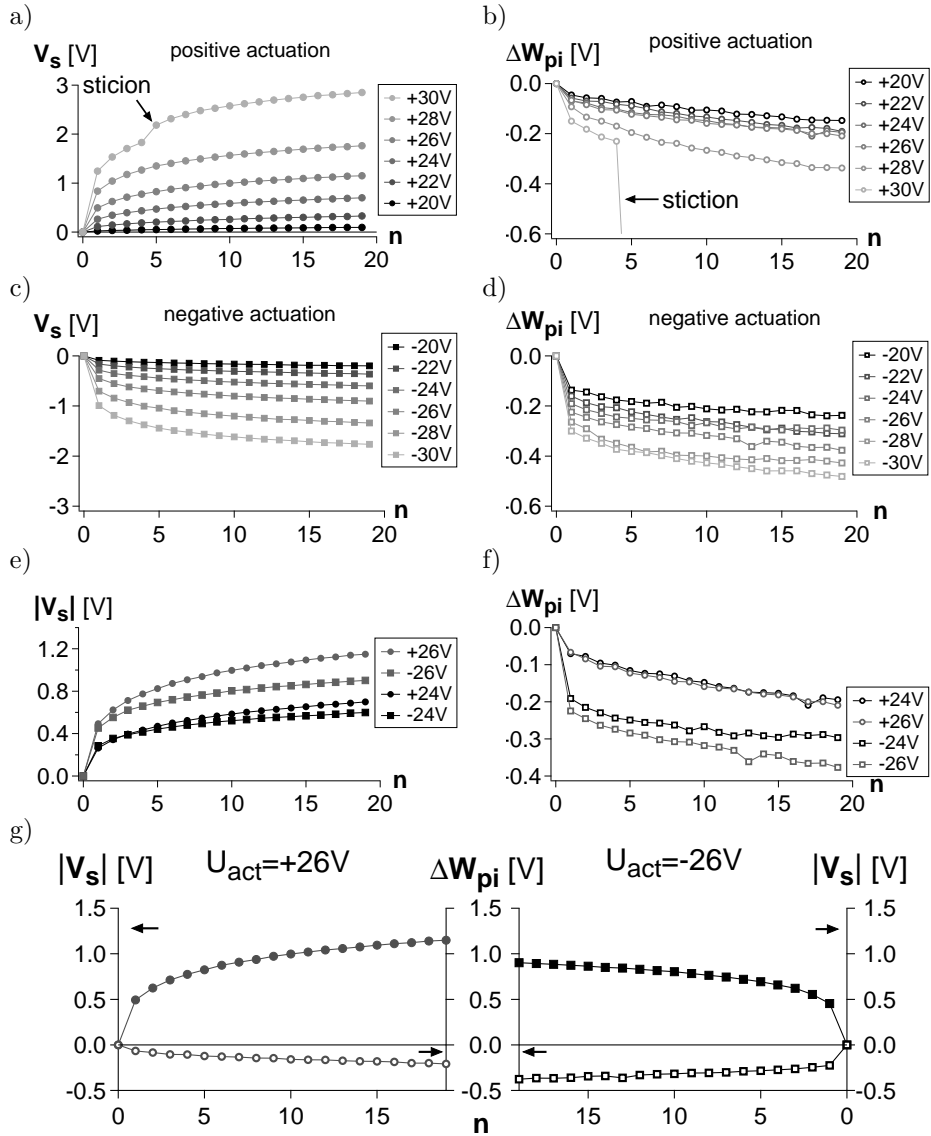
Figure 10.8: The results of "slow" charging observation experiments with idling during stressing technique using positive and negative actuation voltage of various amplitudes. **n** is a number of stressing (1000 cycles) - idling (2min) cycles. Test conditions: 100Hz, 50%d.c., N_2, 1atm, 25°C, light on.
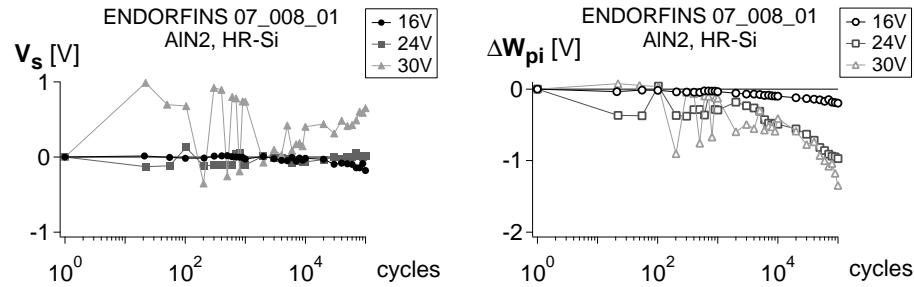
Figure 10.9: The V_s and ΔW_{pi} observed during stressing the ENDORFINS AlN2 devices with bipolar actuation waveforms. Test conditions: $25°C$, N_2, 1atm, light on.

10.6 Bipolar actuation voltage

10.6.1 Introduction

The fact that different polarities of the actuation voltage activate different charging mechanisms may explain the low efficiency of the bipolar actuation biasing scheme. The bipolar actuation voltage was proposed as a remedy for the charge trapping. The portion of charge trapped during a positive stressing period is expected to be released during the consecutive negative stressing period. The total amount of charge should be much lower and the lifetime of the devices should significantly grow. However, an improvement of only about an order of magnitude is observed.

10.6.2 Experiments

A number of devices were stressed with bipolar actuation voltages of various amplitudes. The C-V characteristic was monitored during stressing. The pull-in voltages were extracted and V_s and ΔW_{pi} were calculated. The results are presented in Figure 10.9.

The C-V characteristic of a device stressed with an amplitude lower than the optimal actuation voltage is shifted towards negative voltages. The C-V characteristic of a device stressed with an amplitude higher than the optimal actuation voltage is shifted towards positive voltages. The C-V characteristic of a device stressed with an amplitude of the actuation voltage within the range of the optimal voltages is not shifted indicating no charge trapped. However, the evolution of the pull-in window shows that in all the cases there is charge trapped. The changes of the W_{pi} grow with increasing amplitude of the actuation voltage.

10.6.3 Discussion

The two mechanisms can cancel each other's influence on the shift of the C-V characteristic. However, they both cause narrowing of the C-V characteristic. An explanation of the influence of the two mechanisms on the C-V characteristic and its dependence on the amplitude of the actuation voltage is presented below, and is based on the model proposed by Rottenberg [305].

Two portions of two dielectric materials are placed between two parallel electrodes. It is assumed that the charging properties of the two dielectric materials are different. At a lower actuation voltage ($U_{act} < U_{opt}$) charge is trapped in the dielectric 1 and the dielectric 2 does not charge at all (Figure 10.10a). That causes a shift of the C-V characteristic. In the range of the optimal actuation voltage, both dielectrics trap a similar amount of charge but with opposite sign (Figure 10.10b). The net charges is equal to zero, therefore no shift is observed. However, the charge trapped causes narrowing of the C-V curve. At the actuation voltage higher than the U_{opt}, the dielectric 2 traps more charge than the dielectric 1 (Figure 10.10c). The net charge is not zero, therefore an opposite voltage shift of the C-V curve is observed as well as narrowing.

The effect can be observed in two cases: If both types of charge are trapped in the interposer dielectric, and if one of them is trapped in the interposer dielectric and one in the substrate (see section 9.4.6).

10.7 Impact of the C-V characteristic measurements

10.7.1 Introduction

If both part of the bipolar actuation voltage can cause trapping of charges, then the C-V characteristic measurement can cause unwanted additional charge trapping as well. An experiment to verify that was performed.

10.7.2 Experiment

Two ENDORFINS devices were stressed with a unipolar actuation waveform and the C-V characteristic was measured during stressing. The time between the C-V measurements was either 10^3 or 10^4 cycles. The pull-in voltages were extracted and V_s and ΔW_{pi} were calculated. The results are presented in Figure 10.11.

a) $U_{act} < U_{opt}$
beam
$Q_1=1$ $Q_2=0$
actuation pad

$Q = 1$ $D = 0.5$

$V_s < 0$

$\Delta W_{pi} < 0$

b) $U_{act} = U_{opt}$
beam
$Q_1=2$ $Q_2=-2$
actuation pad

$Q = 0$ $D = 2$

$V_s = 0$

$\Delta W_{pi} << 0$

c) $U_{act} > U_{opt}$
beam
$Q_1=3$ $Q_2=-4$
actuation pad

$Q = -0.5$ $D = 3.5$

$V_s > 0$

$\Delta W_{pi} <<< 0$
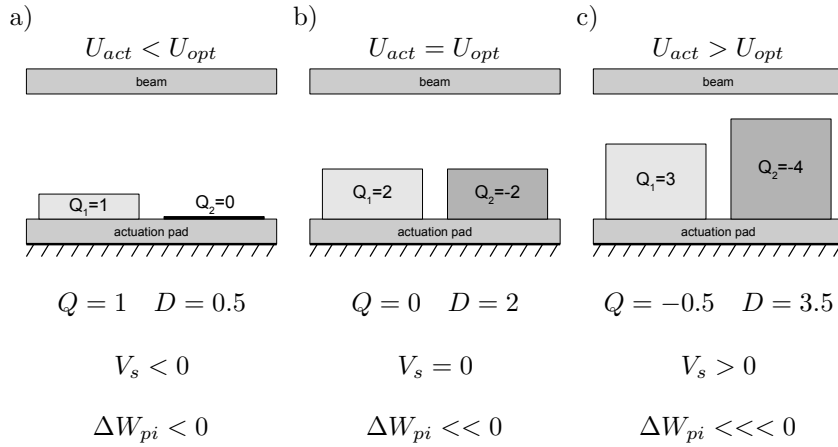
Figure 10.10: One type of charge trapped at lower ($U_{act} < U_{opt}$) voltages causes mainly a shift of the C-V curve a). The amplitude in the range of the optimal value causes trapping of similar amount of both types of charges b). At higher actuation voltages, both mechanisms take place c). Both shift and narrowing are observed.

a)

ENDORFINS 07_144_03
AlN2, HR-Si
$U_{act}=+30V$

V_s [V]

b)

ENDORFINS 07_144_03
AlN2, HR-Si
$U_{act}=+30V$

ΔW_{pi} [V]
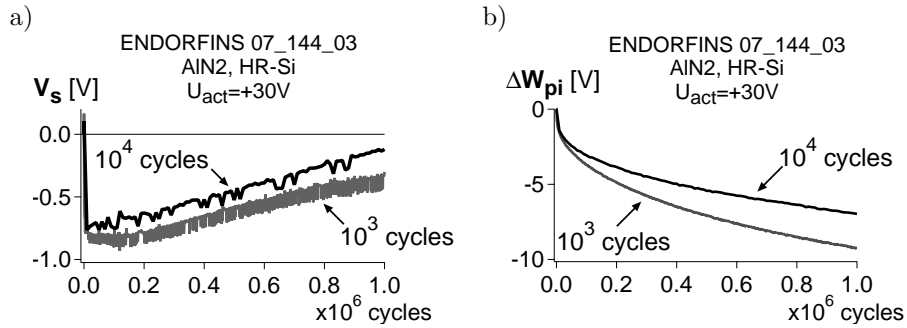
Figure 10.11: The C-V evolution recorded during stressing ENDORFINS devices with a unipolar actuation voltage and C-V characteristic measurements performed every 10^3 or 10^4 cycles. Test conditions: $25°C$, N_2, 1atm, light on.

10.7.3 Conclusions

Figure 10.11 shows an effect of the C-V measurement. So, the C-V characteristic is an invasive method in a sense that the state of the device is modified during probing. However, it is still probably the safest and the simplest method. The device is not destroyed. The C-V characteristic measurement should be performed only when necessary. The amplitude of the actuation voltage should only be a fraction higher than the expected positive and/or negative pull-in voltage. An intelligent C-V measurement can be introduced that stops increasing the actuation voltage as soon as the pull-in is detected.

10.8 Bottom-pad and beam actuation - FEM simulations

It is demonstrated that the charge can be trapped either in the interposer dielectric or in the substrate. Both can influence the C-V characteristic and limit the lifetime of the capacitive RF MEMS devices.

In addition, it was shown that the two charging mechanisms can exhibit different time constants, depending on the amplitude of the actuation voltage. Separation of the "fast" and "slow" ones is possible by modification of the stressing methods. However, an unambiguous identification of the particular mechanisms is still difficult.

The interposer dielectric charging and the substrate charging are additionally separated: in space. The charge is still trapped in the vicinity of the bottom actuation pad and the beam, yet, it can be placed at different positions.

A method to illustrate the distribution of the charge in the switch has been presented by Herfst et al. in [400]. However, the method is destructive. To observe the distribution of the charge in the interposer dielectric, the beam, that usually covers the dielectric layer, needs to be removed. Moreover, the time between end-of-stressing and the charge distribution measurement is finite. The fast charges may have enough time to escape. In that case they will be missed.

It has been already presented that the beam of the switch can be used as a charge sensor. It can sense the surrounding electric field. The readout is hidden in the C-V characteristic modifications.

10.8.1 Bottom-electrode vs. beam actuation

There are two possible ways of actuating the devices:

- the actuation voltage applied to the bottom electrode and the beam grounded,

- the actuation voltage applied to the beam and the bottom electrode grounded.

Considering the parallel-plate model, only the sense of the electric field vector is changed (Figure 10.12a and b). The same effect can be obtained by applying an actuation of the opposite polarity to the bottom electrode.

However, in the case of the ENDORFINS structures, bar-type beam anchored in the ground pads suspended above the signal line, the situation is different (Figure 10.12c and d). The asymmetry due to the shape of the beam and the bottom electrode and the presence of the grounded substrate causes different field distribution for each biasing scheme. Therefore, an extended model of the switch is introduced.

The beam is suspended above the substrate with one actuation and two ground pads. The bottom actuation pad is separated from the ground pads exposing the substrate in the slots. The substrate is represented as a 200nm layer of SiO_2 on a $1\mu m$ aluminum layer. To a first approximation, the HR-Si can be considered conductive. The resistivity of the silicon is much lower than the resistivity of the SiO_2. Therefore, the HR-Si is replaced with a conductive plate.

The actuation voltage applied to the bottom electrode generates an electric field congregated above the bottom electrode (Figure 10.12c). The actuation applied to the beam creates an electric field distributed more uniformly below the whole beam (Figure 10.12d).

Figure 10.13 shows the results of FEM simulations of the field along a line in one slot (the left one) of the structure actuated using the two biasing schemes. The magnitude of the electric field drops very fast aside the bottom actuation pad during the bottom-pad actuation (Figure 10.13a). In the case of the beam-actuation, the field penetrates the slots (Figure 10.13b). The simulated C-V characteristics show that the pull-in voltage is lower when the actuation is applied to the beam (Figure 10.13c). That is due to the fact that the substrate extends the actuation area increasing the electrostatic force. The electrostatic force is generated not only between the beam and the bottom actuation pad. An additional force component is created between the beam and the substrate. Therefore, a lower voltage needs to be applied for the pull-in occurrence. The results are confirmed with results of measurements. The C-V characteristic measured by applying the actuation voltage to the bottom beam is narrower than the bottom-pad actuated curve (Figure 10.13d). That indicates lower positive and negative pull-in voltages.

The changes of the C-V characteristic (shift and narrowing) depend on the influence of the trapped charge on the electric field component generated by the actuation voltage (see section 2.5). The different electric field space distribution obtained
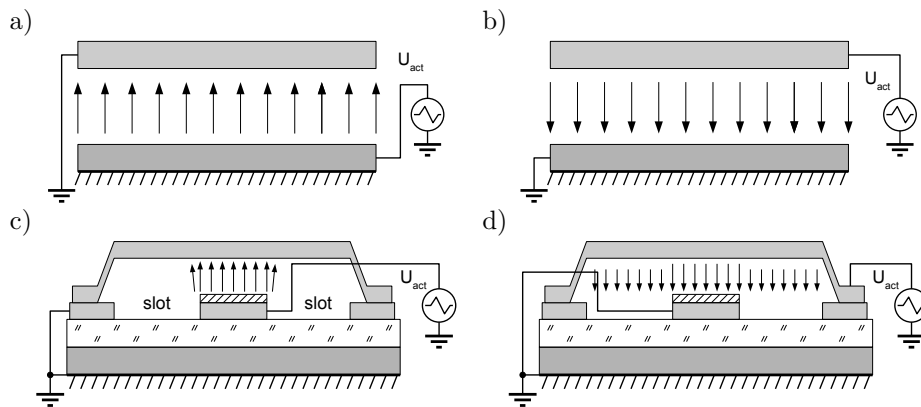
Figure 10.12: The electric field distribution in the parallel-plate model a) and b) and a real structure c) and d) upon actuation applied either to the bottom actuation or the beam.
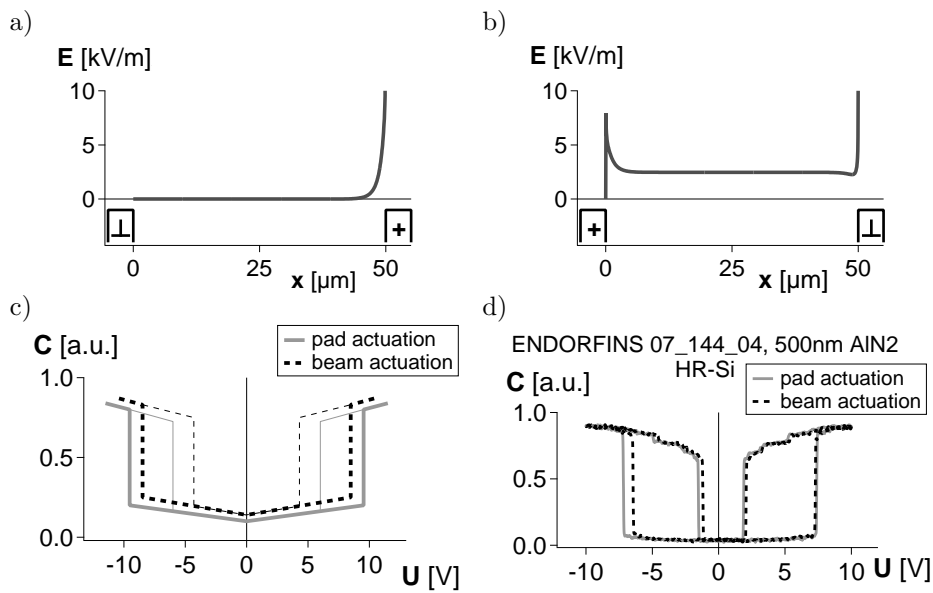
Figure 10.13: The distribution of the electric field in the slots depends on the used biasing scheme a) and b). That results in slightly different C-V characteristics. The results obtained by FEM simulations c) are confirmed by measurements d).

with the two biasing methods can help locating the different charging mechanisms in space.
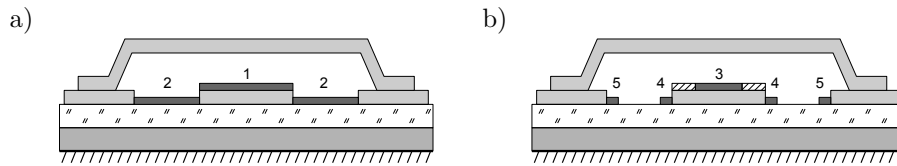
Figure 10.14: The FEM simulations with charge placed in various positions were performed: a) 1. uniformly in the interposer dielectric, 2. uniformly in the substrate (slots), b) 3. non-uniformly in the interposer dielectric, 4. non-uniformly in the substrate, close to the actuation pad and 5. close to the ground pads.

10.8.2   FEM simulation results

A number of FEM simulations using ANSOFT MAXWELL software of bottom-pad and beam actuated cases without and with charge placed in different positions were performed (Figure 10.14). Only one type of charge in one position at a time is considered.

The results are presented in the form of C-V curves, although, only the pull-in voltage was simulated. The pull-out voltage is artificially added to make the graphs easier to read.

No charge trapped

The no charge trapped case has been presented in Figure 10.13. The beam-actuated C-V characteristic is narrower than the bottom-pad-actuated curve. The field between the substrate and the beam creates an additional electrostatic force lowering both pull-in voltages.

Charge uniformly distributed in the interposer dielectric

Figure 10.15a and b show simulated C-V curves of a device with charge uniformly trapped in the interposer dielectric. In both cases mainly a shift of the characteristics is observed. The bottom-pad actuation case is similar to the parallel-plate model case. Most of the electric field is concentrated between the bottom pad and the beam. The charge trapped in the interposer dielectric modifies the electric field component created by the actuation voltage (continuous-line arrows) (Figure 10.15c) resulting in a voltage shift of the C-V characteristic.

In the beam-actuated case, the charge trapped in the interposer dielectric modifies only a part of the electric field generated by the actuation voltage. This case can be compared to the non-uniform charge distribution in the parallel-plate model.

However, due to different beam-bottom pad and beam-substrate distances, the field between the bottom pad and the beam is higher than between the beam and the substrate. Therefore, it is similar the case described by Rottenberg et al. [310] - non-uniformly distributed charge and non-uniformly distributed air gap. Mainly shift with narrowing of the C-V curve is observed.

Charge uniformly distributed in the slots

Figure 10.16a and b show the C-V curves of a device with charge uniformly trapped on the surface of both slots.

The charge trapped in the substrate (slots) does not change the electric field component generated by the actuation voltage. It generates an additional electric field component, thus an electrostatic force, independent on the applied U_{act} (dashed-line arrows). Therefore, mainly narrowing of the C-V characteristic is observed in the bottom-pad actuated case.

The beam-actuated case is different as the electric field generated by the actuation voltage is present in the slots as well as between bottom pad and the beam. The charge in the slots can modify the field component created by the actuation voltage (Figure 10.16d). A shift of the C-V characteristic is observed (Figure 10.16b). The charge modifies only a part of the electric field generated by the actuation voltage. Therefore, the C-V curve is additionally narrowed.

This case is similar to the non-uniform charge distribution case presented by Rottenberg et al. in [310].

Charge non-uniformly distributed in the interposer dielectric

The uniformly distributed charge in either the interposer dielectric or the substrate can be easily recognized using the bottom-pad- and beam-actuated C-V characteristic measurements. It becomes more complicated when the non-uniform charge distribution is considered.

The impact of the non-uniformly distributed charge in the interposer dielectric has been described by Rottenberg [305]. It can cause a shift and narrowing of the C-V curve at the same time (section 2.5). Both, bottom-pad- and beam-actuated, C-V characteristics can be modified in a similar way (Figure 10.17a and b). In both cases, only a part of the actuation voltage generated electric field is modified (Figure 10.17c and d).

a) bottom-pad actuation

b) beam actuation

c) $|V_s| \gg 0 \quad \gg \quad |\Delta W_{pi}/2| \simeq 0$

d) $|V_s| \gg 0 \quad \gg \quad |\Delta W_{pi}/2| > 0$
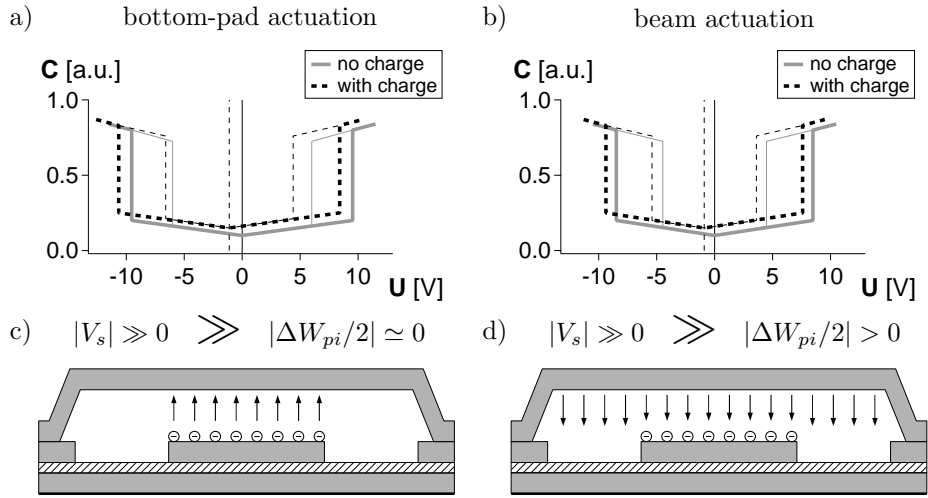
Figure 10.15: Uniform charge distribution in the interposer dielectric causes a voltage shift of the bottom-pad- a) and shift+narrowing of the beam-actuated b) C-V curves.

a) bottom-pad actuation

b) beam actuation

c) $|V_s| \simeq 0 \quad \ll \quad |\Delta W_{pi}/2| > 0$

d) $|V_s| > 0 \quad \gg \quad |\Delta W_{pi}/2| > 0$
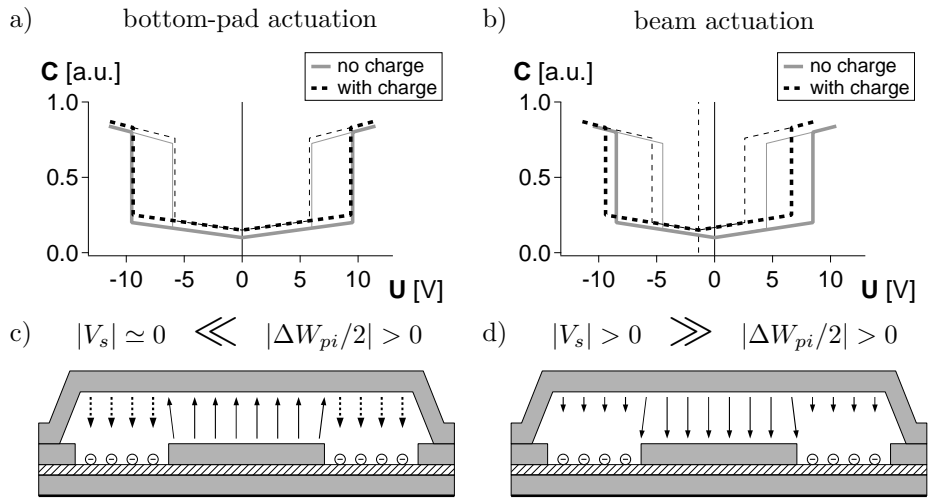
Figure 10.16: Uniform charge distribution in the substrate (slots). During bottom-pad actuation (a and c), mainly small narrowing of the C-V curve is observed. During beam actuation both shift and narrowing are observed.

Charge non-uniformly distributed in the substrate

Two of the possible cases of non-uniform charge distributions in the substrate were simulated: the charge agglomerated close to the bottom actuation pad (Figure 10.18) or close to the ground pads (Figure 10.19).

Charge trapped close to the bottom actuation pad can cause a shift and narrowing of the bottom-pad-actuated C-V curve (Figure 10.18a). The charge creates additional force (dashed-line arrows) that causes narrowing of the C-V characteristic (Figure 10.18c). In the same time the charge may impact the distribution of the field generated by the actuation voltage (continuous-line arrows). Therefore, a shift is observed as well.

The beam-actuated C-V curve is shifted and narrowed due to non-uniform modifications of the actuation-voltage generated electrostatic field (Figure 10.18b and d).

The charge trapped in the slots close to the ground pads causes mainly narrowing of the bottom-pad-actuated C-V characteristic (Figure 10.19a). The charge creates an additional force and does not impact the actuation-voltage generated field (Figure 10.19c).

The beam-actuated C-V characteristic is narrowed as well (Figure 10.19b). That is due to the charge generating a force between the ground pads and the beam (Figure 10.19d).

The beam and the ground pads are electrically connected and on the same potential. Therefore, no electrostatic force between them is expected. However, charge trapped in the vicinity of the two may act as an additional electrode. The charge creates an electric field component that generates an electrostatic force attracting the beam and the ground pad towards each other (dashed-line arrows) (Figure 10.20). The force is independent on the actuation voltage therefore it can cause narrowing of the C-V characteristic.

10.8.3   Voltage shift vs. narrowing of the C-V curve

Charge trapped in the switch can influence the C-V characteristic in several ways. The curve can be either shifted, narrowed or shifted and narrowed at the same time. The shift is attributed to a presence of charge trapped uniformly in the interposer dielectric. Non-uniformly distributed charge can cause the shift+narrowing of the C-V curve. Both narrowing and shift+narrowing can be observed when charge is trapped in the substrate.

Two cases of the shift+narrowing effect on the C-V characteristic can be identified. In one case, the magnitude of one pull-in voltage (e.g. negative) is increased and

a) bottom-pad actuation   b) beam actuation

c) $|V_s| > 0 \quad > \quad |\Delta W_{pi}/2| > 0$ d) $|V_s| > 0 \quad > \quad |\Delta W_{pi}/2| > 0$
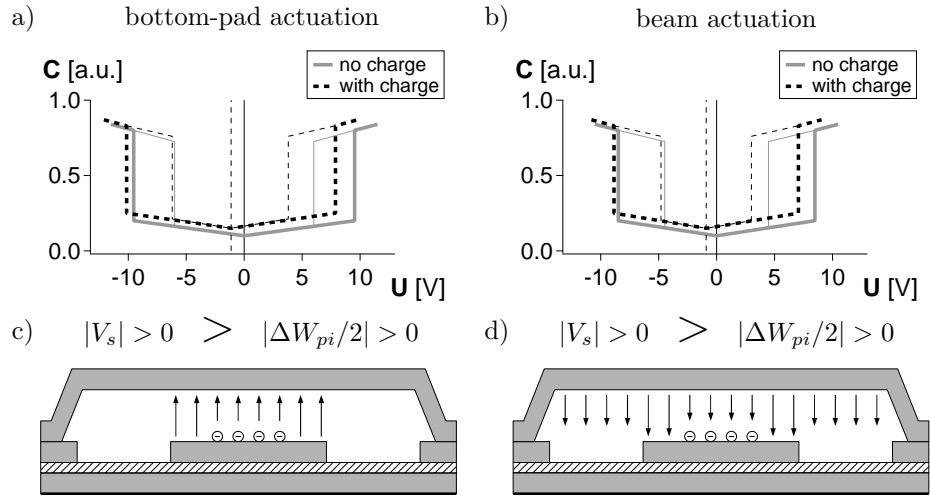
Figure 10.17: Non-uniform charge distribution in the interposer dielectric causes the shift and narrowing of the C-V curve.

a) bottom-pad actuation   b) beam actuation

c) $|V_s| > 0 \quad < \quad |\Delta W_{pi}/2| > 0$ d) $|V_s| > 0 \quad > \quad |\Delta W_{pi}/2| > 0$
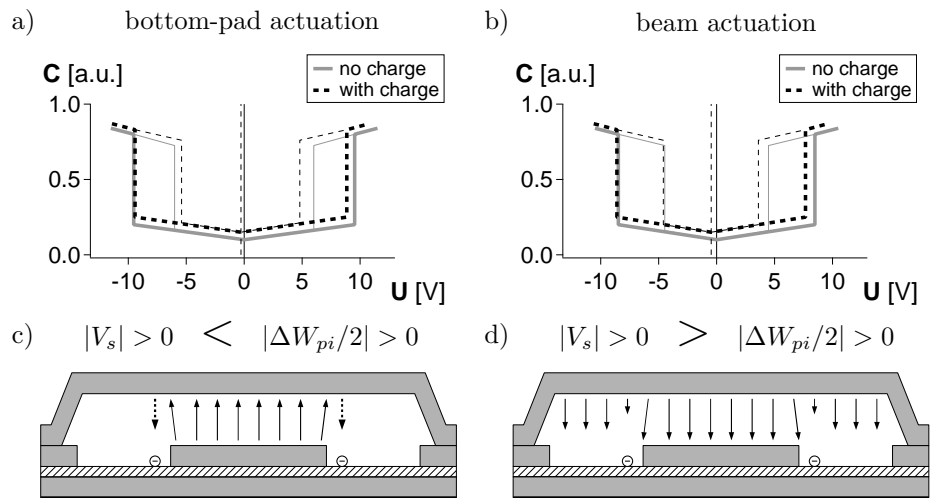
Figure 10.18: Non-uniform charge distribution in the substrate (slots). Charge agglomerated close to the actuation pad causes a shift and narrowing of the bottom-pad- a) and the beam-actuated C-V curves b). In the bottom-pad actuation case, the charge generates an additional force (dashed-line arrows) c).

a)   bottom-pad actuation   b)   beam actuation

c) $|V_s| = 0$ ≪ $|\Delta W_{pi}/2| = 0$ d) $|V_s| = 0$ < $|\Delta W_{pi}/2| = 0$
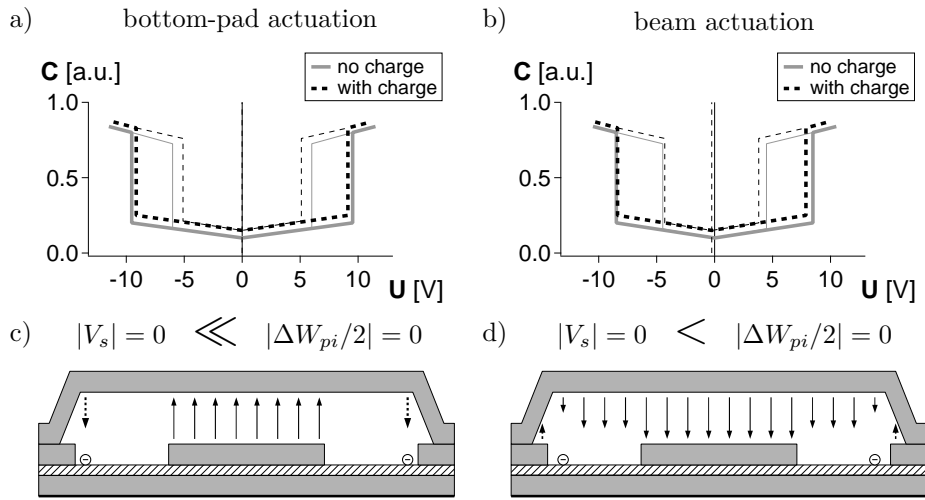
Figure 10.19: Charge trapped close to the ground pads causes mainly narrowing of the both C-V curves.
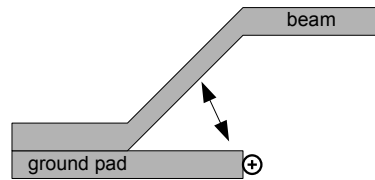
Figure 10.20: The charge trapped close to the ground pad may generate an electrostatic force component attracting the beam to the ground pad. The force does not depend on the polarity of the actuation voltage, therefore it causes narrowing of the C-V beam-actuated C-V characteristic.

the magnitude of the other one (e.g. positive) is decreased (Figure 10.21a). In the other case, the magnitude of the both pull-in voltages is decreased (Figure 10.21b). In both cases, the C-V curve is shifted and narrowed. However, it is clear that there is a difference.

The V_s and the ΔW_{pi} has been, so far, thought as two separate effects on the C-V curve. Yet, the mutual relations between the two can give valuable information about the charge trapped in the switch.

The voltage shift and the pull-in window changes are caused by modifications of the positive and negative pull-in voltages. However, to explain the two shift+narrowing cases the roles are switched: the pull-in voltages change due to factors causing a shift and narrowing of the C-V characteristic.
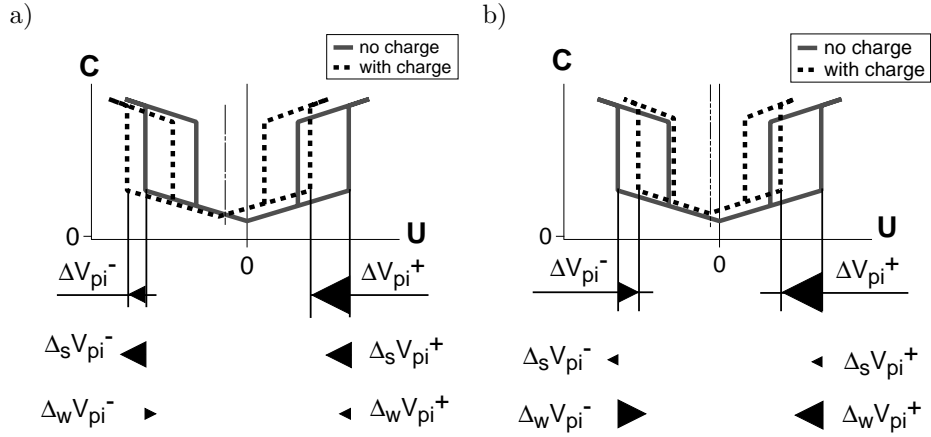
Figure 10.21: The ΔV_{pi}^+ and ΔV_{pi}^- can be split into two components: $\Delta_s V_{pi}$ - change of the V_{pi} due to the factor causing the shift of the C-V characteristic and $\Delta_s V_{pi}$ - change of the V_{pi} due to the factor causing the C-V narrowing.

$$\Delta V_{pi} = \Delta_w V_{pi} + \Delta_s V_{pi} \tag{10.1}$$

$$\Delta_s V_{pi} = V_s \tag{10.2}$$

$$\Delta_w V_{pi} = \frac{\Delta W_{pi}}{2} \tag{10.3}$$

The ΔV_{pi} can be presented as a sum of two components (10.1): the change of the pull-in due to the C-V shift $\Delta_s V_{pi}$ and the change of the pull-in due to the C-V pull-in window modifications $\Delta_w V_{pi}$, i.e. narrowing. Both positive and negative pull-in voltages are shifted with the same magnitude as the center of the C-V curve. Therefore, the $\Delta_s V_{pi}$ is equal to the V_s (10.2). The ΔW_{pi} is a sum of the ΔV_{pi}^+ and ΔV_{pi}^- (see section 2.5.4). Therefore, the $\Delta_w V_{pi}$ is equal $\Delta W_{pi}/2$ (10.3), assuming symmetric changes of the pull-in window.

The relation between the V_s and $\Delta W_{pi}/2$ can be further analyzed.

$|V_s| > |\Delta W_{pi}/2|$ **case**

An example of this case is presented in Figure 10.21a. The magnitude of the positive pull-in voltage is decreased and the negative pull-in becomes more negative.

However, the negative pull-in voltage is increased with a lower value than the positive one is decreased.

The $\Delta_s V_{pi}$ component is higher than the $\Delta_w V_{pi}$. I.e. the C-V characteristic is more shifted than narrowed.

This case, presented in section 2.5.5, is attributed to the non-uniform charge distribution in the interposer dielectric layer. The component of the electric field generated by the actuation voltage is modified. The charge decreases one of the V_{pi} and is not able to shift the other one with the same amplitude.

$|V_s| < |\Delta W_{pi}/2|$ case

An example of this case is presented in Figure 10.21b. The magnitude of both pull-in voltages is decreased with different values. The $\Delta_s V_{pi}$ component is lower than the $\Delta_w V_{pi}$. I.e. the C-V characteristic is more narrowed than shifted.

The C-V characteristic can be narrowed more than shifted when an additional force appears. The force is independent on the actuation voltage. The electric field generating the force cannot be influenced by the actuation voltage. However, the additional electric field may influence the distribution of the field component created by the actuation voltage. Another possibility is a change of the actuation area during stressing. Then, the electrostatic force is higher when the actuation voltage of both polarities is applied. Both pull-in voltages are decreased and mainly a pull-in window change is observed. The change of the actuation voltage can be caused by modifications of the physical dimensions of the device. However, the change of the distribution of the electric field generated by the actuation voltage alongside the beam can give a similar effect.

One of the possible sources of the additional force independent on the actuation voltage is charge trapped in the substrate in the slots between the actuation and ground pads.

10.8.4 Summary

Figure 10.22 shows a summary of the observed effects. The positive and negative pull-in voltages were extracted and V_s and $\Delta W_{pi}/2$ were calculated. The graphs show that the bottom-pad- and beam-actuated C-V characteristics can be used to locate charge trapped in the capacitive RF MEMS switches. Charge trapped in different positions can be identified using a combination of the two types of C-V curves. The method is usefull only when the C-V characteristics are influenced by one type of charge trapped in one position at a time.
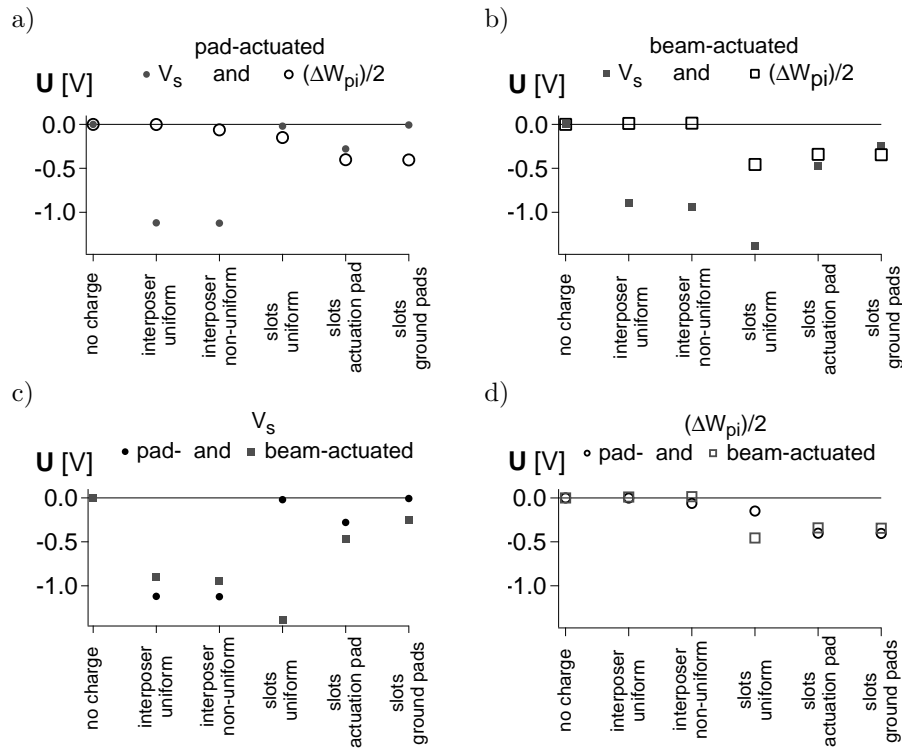
Figure 10.22: The mutual relations between the V_s and $\Delta W_{pi}/2$ of the bottom-pad- and beam-actuated C-V characteristics can give valuable information about the space location of the trapped charge.

10.9 Bottom-pad- and beam-actuated C-V characteristics

10.9.1 Introduction

The bottom-pad- and beam-actuated C-V characteristics can be used to locate the charging mechanisms. However, this can only be done in a reliable way if one of the mechanisms is active at a time. Therefore, the experiments should be performed in such a way that one type of charge is highlighted.

A number of the ENDORFINS 07_144_04 devices fabricated on a HR-Si wafer with 500nm thick layer of the AlN2 dielectric were used fir these experiments. A thicker layer is supposed to limit charge trapping in the interposer dielectric. A low amplitude of the actuation voltage (10V to 16V) is expected to cause less

charging as well. To isolate the "slow" charge the idling-during-stressing technique was used. The devices were first stressed for 1000 cycles and then un-actuated for a period of 20s. The stressing-idling cycle was repeated 100 times. Both types of C-V characteristics, bottom-pad and beam actuated, were measured after every cycle. The pull-in voltages were extracted and the V_s and $\Delta W_{pi}/2$ were calculated. The results are discussed in the following paragraphs.

10.9.2 Results

The results of the experiments point to the interposer dielectric charge trapping. The bottom-pad- and beam-actuated C-V curves are more shifted than narrowed (Figure 10.23). The sign of the voltage shift depends on the polarity of the actuation voltage. The V_s magnitude is proportional to the amplitude of the actuation voltage indicating more charge being trapped with increasing amplitude of the actuation voltage. The ΔW_{pi} does not depend on the amplitude of the actuation voltage. However, different polarities of the actuation voltage cause slightly different changes of the pull-in window. That indicates an U_{act}-polarity dependent distribution of charge.

10.9.3 Summary

The obtained results are different from the anticipated ones. Even though, the test conditions favored the substrate charging, the observed C-V changes point to interposer dielectric charging.

The devices with 500nm AlN2 dielectric layer were expected to trap more charge in the substrate at the used (10V to 16V) amplitudes of the actuation voltage. However, the changes of both types of C-V characteristics point to interposer dielectric charging. The V_s of the bottom-pad- and beam-actuated C-V curves is higher than the $\Delta W_{pi}/2$. According to the proposed model, that can occur when charge is trapped in the interposer dielectric. It is opposed to the previous observations as well (see section 10.2. The failure of the devices stressed with low amplitudes of the actuation voltage ($< U_{opt}$) was attributed to substrate charging.

It is clear that the proposed model of the switch needs further verification.
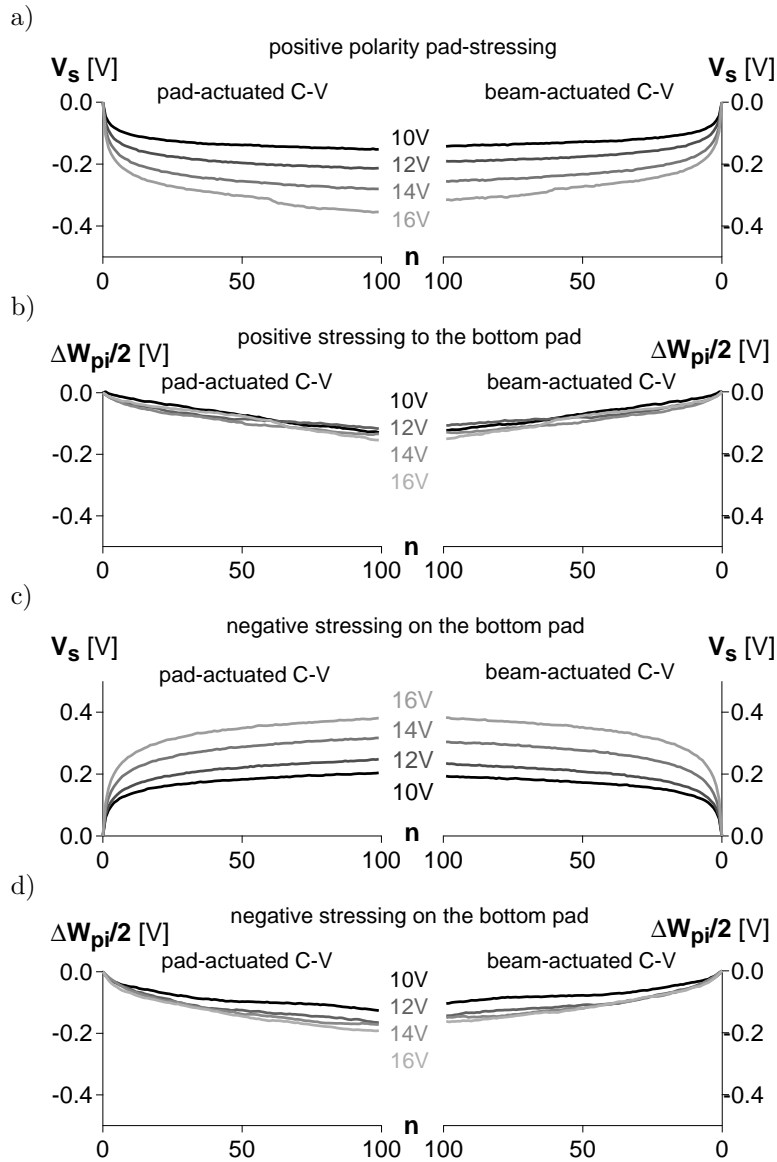
Figure 10.23: The V_s and $\Delta W_{pi}/2$ of the bottom-pad- and beam actuated C-V characteristics recorded during stressing the devices with positive and negative actuation voltages applied to the bottom actuation pad **n** is the number of stressing (1000 cycles) and idling (20sec) cycles. Test conditions: $25^\circ C$, N_2, 1atm, light on.
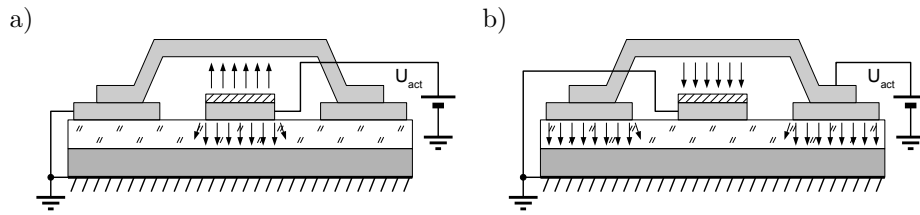
Figure 10.24: Stressing with the actuation voltage applied to either the bottom pad a) or the beam b) allows stressing the two materials, the substrate and interposer dielectric, with electric field components of different senses at a time.

10.10 Bottom-pad and beam stressing

10.10.1 Introduction

The ENDORFINS devices can be actuated in two ways: with the actuation voltage applied to either bottom electrode or to the beam. It is shown in the previous section that the C-V characteristics measured using the two biasing methods allow locating charge trapped in the devices. However, both methods can be used for stressing the devices as well. The effect of this is presented in this section.

10.10.2 Bottom-pad- vs. beam-actuated stressing

Each method causes a different distribution of the electric field between the bottom actuation pad and the beam. In addition, the two types of biasing methods cause stressing of the interposer dielectric and the substrate with different polarities at the same time.

Indeed, a positive actuation applied to the bottom pad causes positive stressing of the interposer dielectric and the substrate (Figure 10.24a). However, a positive actuation applied to the beam causes negative stressing of the interposer dielectric and still positive stressing of the substrate (Figure 10.24b). The substrate is stressed with the same polarity in both cases. A similar situation occurs in the case of the negative actuation voltage. All the combinations are listed in Table 10.1.

10.10.3 Results and discussion

A number of ENDORFINS 07_144_04 500nm AlN2 structures fabricated on a HR-Si substrate were stressed. The actuation voltage was applied to either the bottom pad or the beam. To limit the impact of the "fast" charges the idling-during-

Table 10.1: Positive and negative actuation voltage applied to either the bottom pad or the beam can cause stressing of the interposer dielectric and the substrate of different polarities at a time.

biasing method	U_{act} polarity	interposer dielectric	substrate
pad-actuation	positive	positive	positive
	negative	negative	negative
beam-actuation	positive	negative	positive
	negative	positive	negative

stressing method was used. The devices were stressed for 1000 cycles and then un-actuated for a period of 20s. The stressing-idling cycle was repeated 100 times. The bottom-pad- and beam-actuated C-V characteristics were measured after every stressing-idling cycle. The pull-in voltages were extracted and V_s and ΔW_{pi} were calculated.

Figure 10.25 shows the results of the experiments grouped according to the polarity of the interposer dielectric stressing. Both, bottom-pad- and beam actuated C-V characteristics measured during the bottom-pad and beam positive and negative actuation are modified in a similar way. The V_s is always higher than the $\Delta W_{pi}/2$. That points to the interposer dielectric charging.

The sign of the voltage shift depends on the polarity of the electric field component across the interposer dielectric. However, the charge trapped in the interposer dielectric has been shown to be independent on the polarity of the applied actuation voltage. Therefore, the source of the observed changes of the V_s sign may be in the other dielectric present in the switch - the substrate.

In addition, the evolutions of the V_s and $\Delta W_{pi}/2$ differ during stressing with different actuation methods. That may point to different charge distributions.

10.10.4 Summary

The results of the presented experiment do not bring a clear answer about the location of the charge trapped in the tested devices. There is a discrepancy in the obtained results of the presented experiment. The sign of the voltage shift points to the interposer dielectric charging, even though test conditions favoring the substrate charging were chosen. However, slightly different V_s and ΔW_{pi} observed during the bottom-pad and beam actuation may indicate additional substrate charging.

Once more, the obtained results are different than expected. The mismatch can be attributed to an important factor that is omitted in the presented switch model.

ENDORFINS 07_144_04, 500nm AlN2, HR-Si
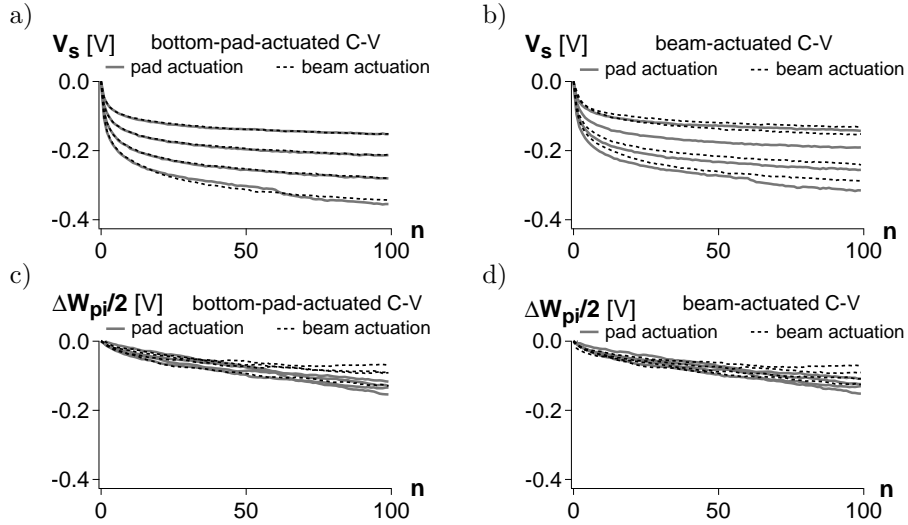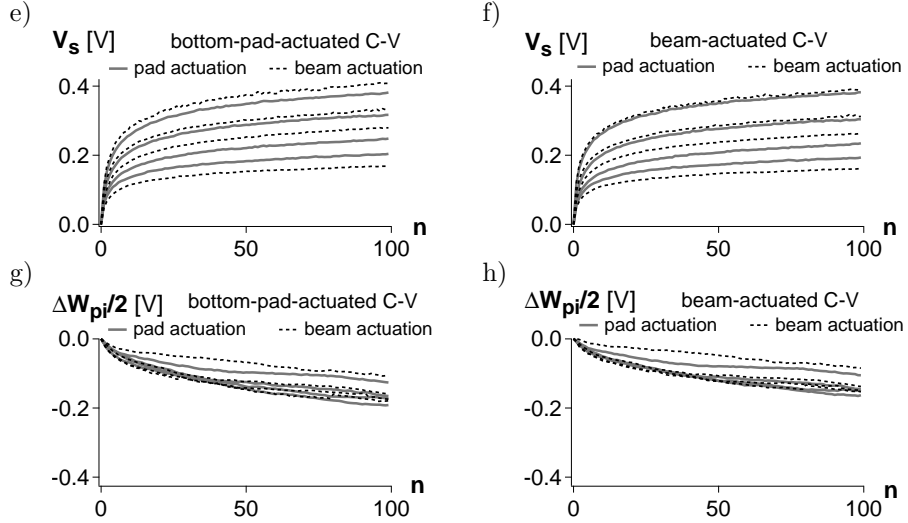
Figure 10.25: The results (V_s and $\Delta W_{pi}/2$) obtained during stressing the ENDORFINS devices with positive and negative actuation voltages of the amplitude from 16V to 20V applied to either the bottom-pad or the beam. **n** is the number of stressing (1000 cycles) and idling (20sec) cycles. Test conditions: $25°C$, N_2, 1atm, light on.

10.11 Dual-alternating actuation method

10.11.1 Introduction

The presented extended model and the method to locate the charge trapped in the switch can give reliable information only when one type of charge is trapped at a time. Therefore, the devices need to be stressed in a way to emphasize one type of charging as much as possible. A thicker dielectric layer, idling-during-stressing, bottom-pad and beam actuated C-V characteristic were not enough. The obtained results were different than expected. Therefore, another method to isolate the mechanisms is needed.

The previous experiments with bottom-pad and beam actuation of the devices required an adaptation of the testing equipment. The introduced modifications allow actuating devices with any combination of the actuation voltages applied to the bottom pad and the beam.

10.11.2 Dual-alternating actuation method

Figure 10.26 shows one of the possible actuation methods. Two unipolar square-shaped waveforms are shifted in phase of $180°$ (Figure 10.26b and c). The first actuation voltage is applied to the bottom pad (U_{pad}) and the second one - to the beam (U_{beam}). The back side of the substrate is grounded. There are three consequent phases "1", "2" and "3" indicated in Figure 10.26:

"1" - a positive actuation voltage is applied across the interposer dielectric, a positive actuation voltage is applied to the substrate on the actuation pad,

"2" - a negative actuation voltage is applied across the interposer dielectric and a positive actuation voltage is applied to the substrate on the ground pads,

"3" - equal to the phase "1".

As a result, the interposer dielectric is stressed with an electric field component of an alternating vector sense. It is similar to the one obtained during the one-source bipolar actuation voltage. The electric field stressing the substrate is a quasi-sum of the voltages. It appears either close to the bottom actuation pad or close to the ground pads. However, it is always of the same polarity. A similar situation takes place when the U_{pad} and U_{beam} components of negative polarity are used. The interposer dielectric is stressed with a bipolar actuation voltage and the substrate with quasi-unipolar negative actuation voltage.

This way of actuating the devices is called the dual-alternating actuation method.

As the interposer dielectric is always stressed with the equivalent of a bipolar actuation voltage, the charging of it is expected to be observed as changes of the C-V characteristic independent on the polarity of the component waveforms. Any difference, especially the sign of the V_s, indicates substrate charging.

10.11.3 Results

A number of ENDORFINS 07_144_04 devices with 500nm thick AlN2 layer fabricated on a HR-Si wafer were tested. The devices were first stressed with the mentioned dual-alternating stressing method of both polarities and with various amplitudes of the component waveforms. Then, the devices were un-actuated and the C-V characteristics (bottom-pad- and beam-actuated) were measured in regular 100s time periods. Therefore, the release of the initially trapped charge was observed.

Groups consisting of 9 devices with one set of parameters were tested. The graphs show averaged values with corresponding 3σ errors.

Figure 10.27 shows the obtained results. The V_s of the two types of C-V curves is higher than the $\Delta W_{pi}/2$ for both polarities. That points to the interposer dielectric charging during stressing the devices with positive and negative component waveforms. However, the sign of the voltage shift depends on the polarity of the component waveforms. While U_{diel} is independent of this (Figure 10.26d). That can be possible only if charge is trapped in the substrate.

10.11.4 Summary

The experiment clearly shows that the mechanism previously identified as the interposer dielectric charging is, in fact, the substrate charging. The interposer dielectric stressed with an alternating sense of the electric field vector should cause a V_s of one sign only. Another possibility would be a random V_s sign. However, the obtained results are consistent. The sign of the voltage shift is always related to the polarity of the used actuation voltage.

It is obvious that an important factor is overlooked in the presented extended model. The experiments presented in the following sections allowed further understanding of the mechanisms governing the physics and reliability of the capacitive RF MEMS switches.
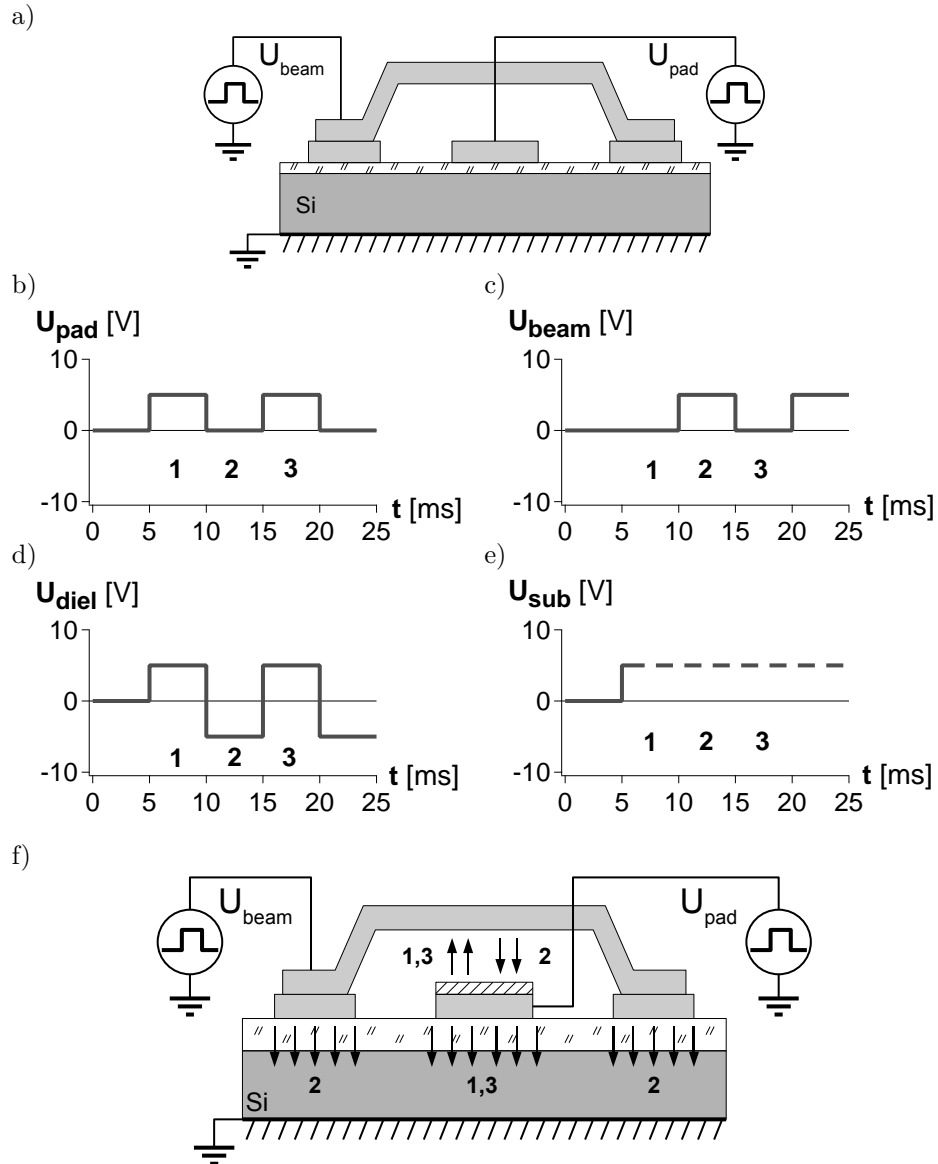
Figure 10.26: The dual-alternating method: Using of two actuation voltages a) U_{pad} b) and U_{beam} c) allow stressing the interposer dielectric with bipolar d) and the substrate with quasi-unipolar e) actuation voltages at the same time.
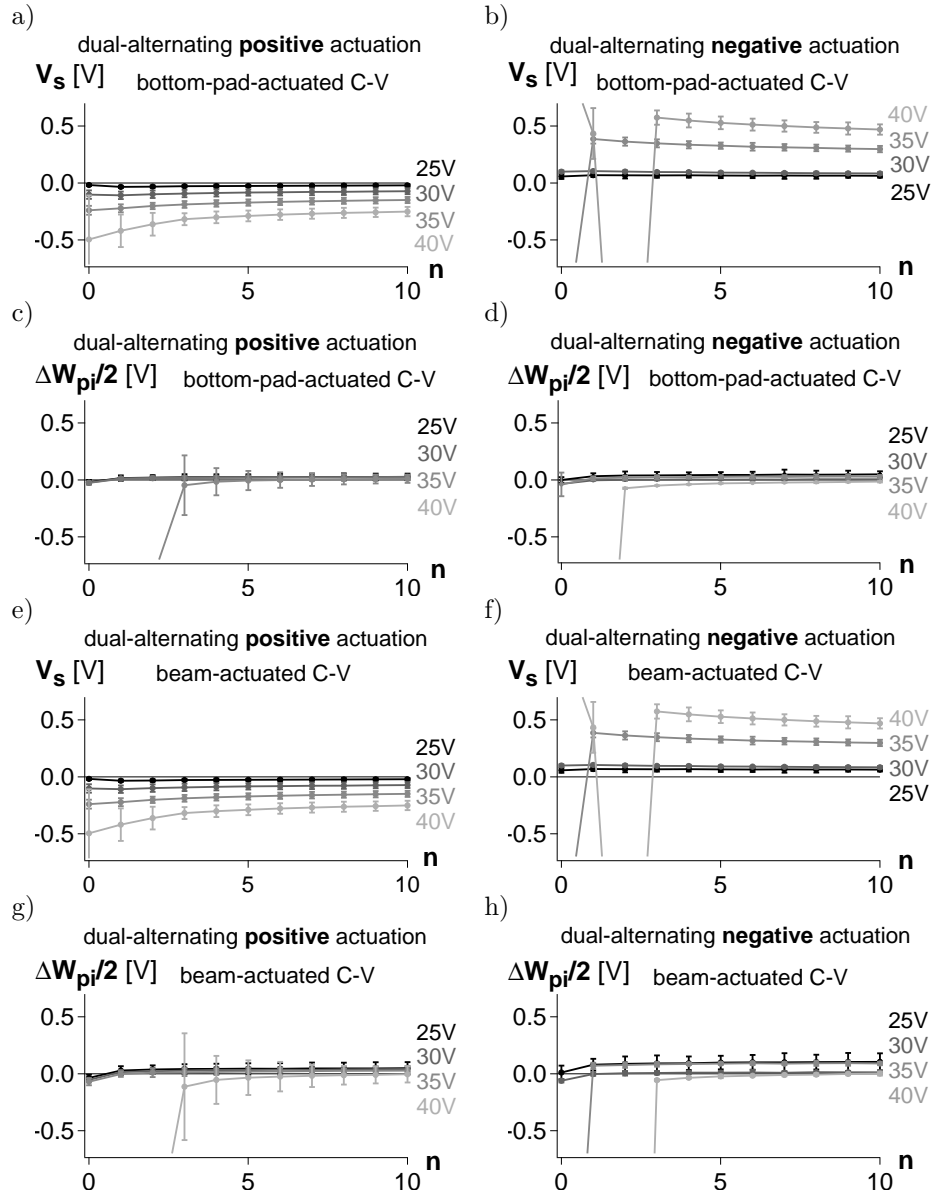
Figure 10.27: The results of experiments performed using the dual-alternating biasing method with positive and negative component waveforms. Test conditions: $25°C$, N_2, 1atm, light on.

10.12   Dual-common actuation method

10.12.1   Introduction

The previous section presented results of experiments where the switches were stressed with a dual-alternating actuation voltage. The method allows stressing the interposer dielectric and the substrate with electric field components of different polarities at the same time. However, the electric field across the interposer dielectric was not zero. There is a possibility to actuate the devices in a way to keep the interposer dielectric electric field component zero. This is discussed in the following.

10.12.2   Dual-common actuation method

If the actuation voltage on the bottom actuation pad and the beam are equal ($U_{pad} = U_{beam}$), and the back side of the silicon wafer is grounded, then there is an electric field present only in the slots (Figure 10.28a). The electric field across the interposer dielectric is equal to zero. The device works in a regime similar to the one used in devices presented by Siegel et al. in [45]. The substrate plays the role of the bottom actuation electrode. The electrostatic force is high enough to actuate the switch with the amplitude of the applied actuation voltage below 50V.

As both actuation voltages are equal, the method is called dual-common actuation.

10.12.3   Dual-common actuation of the switch

An example of the C-V characteristic measured using the dual-common actuation method using triangular waveforms is presented in Figure 10.29a. Figure 10.29b shows the signal recorded during stressing a device with the dual-common actuation method using square-shaped waveforms of 100Hz frequency and 50V amplitude. Both graphs show that it is possible to actuate the ENDORFINS devices using the dual-common actuation method, indicating that the electrostatic force is indeed high enough.

The shape of the C-V characteristic is different than the one obtained during the standard C-V measurements. The pull-in and pull-out transitions are not that sharp and the extraction of the V_{pi} and V_{po} can be loaded with a bigger error.

A number of experiments using the dual-common C-V characteristic measurements were performed. However, due to the uncertainty the results are not reliable. Therefore, the dual-common actuation method was used only for stressing. The
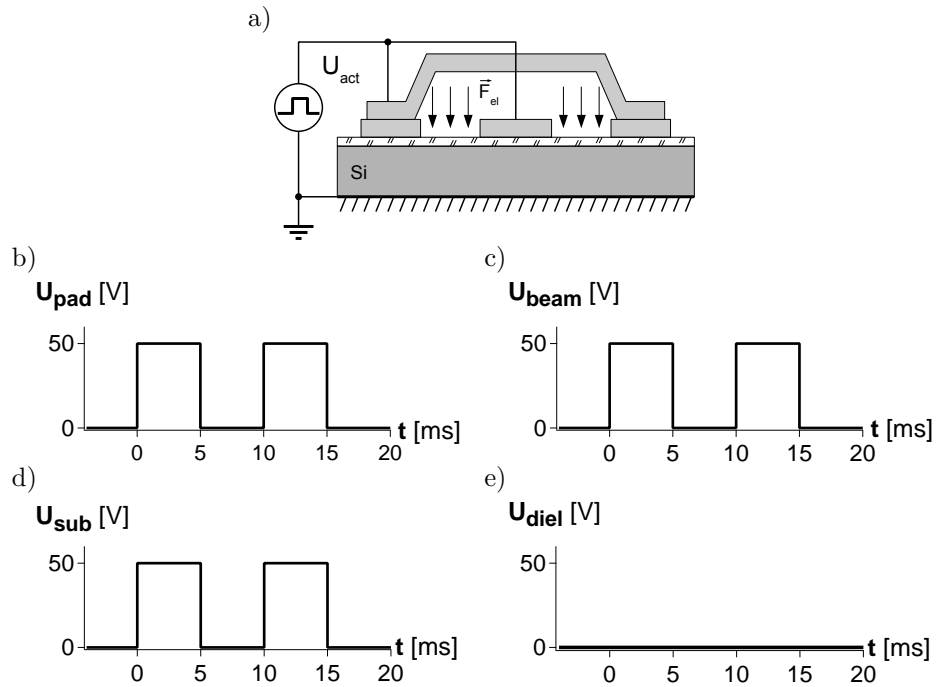
Figure 10.28: Dual-common actuation: Application of the same voltage to the bottom actuation pad and the beam result in electrostatic force only in the slots. The electrostatic field across the interposer dielectric is zero.
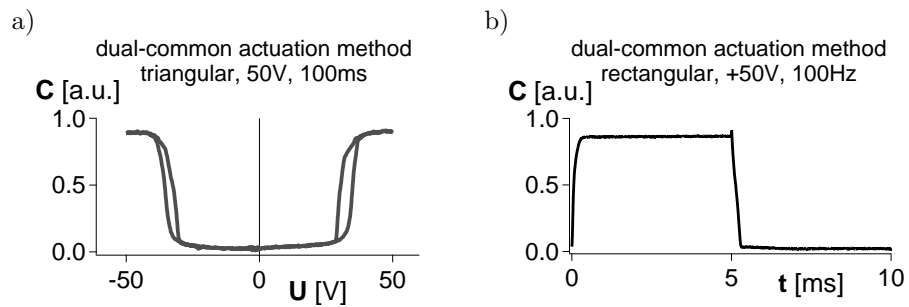
Figure 10.29: The response of the switch on the applied triangular a) and rectangular b) waveforms.

charge detection was done by the regular, bottom-pad- and beam-actuated, C-V characteristic measurements.

10.12.4 Dual-common actuation stressing in N$_2$

A number of experiments using the dual-common actuation method were performed. The procedure was similar to the one used with the dual-alternating actuation method: idling-after-stressing, the stressing time, the time between the C-V measurements after stressing etc.

The results of stressing devices with dual-common positive and negative actuation voltage are presented in Figure 10.30.

The change of the pull-in voltage and pull-in window are significantly lower compared to the dual-alternating stressing results.

10.12.5 Dual-common actuation stressing in air

The C-V characteristic of the devices stressed with the dual-common actuation method in N$_2$ atmosphere did not change during stressing. That may indicate a perfect actuation method that does not cause failure. However, a lifetime experiment to show charging was performed. Two devices were stressed with the dual-common actuation method of positive and negative polarities at this time in ambient air environment. Three types of C-V characteristics before and after stressing were measured: dual-common-, bottom-pad and beam-actuated.

The dual-common-actuated C-V curves show a voltage shift of the sign dependent on the polarity of the actuation voltage (Figure 10.31a and b). This type of C-V characteristic can be shifted only by charge trapped in the substrate. Charge trapped in the interposer dielectric does not change the electric field component generated by the actuation voltage. The component is zero all the time. Therefore, the charge trapped in the interposer dielectric cannot cause a voltage shift. However, the charge can create a constant force independent on the applied actuation. That is mirrored in narrowing of the pull-in window.

The bottom-pad- and beam-actuated C-V characteristics confirms that conclusion. The bottom-pad-actuated C-V curve is more narrowed than shifted (Figure 10.31c and d) and the beam-actuated C-V curve is more shifted than narrowed (Figure 10.31e and f). According to the presented model, this combination can occur only in the case of the substrate charging. As the changes of the C-V characteristics are observed after stressing the devices in a humid environment, it is highly possible that the charge is placed on the surface of the substrate. Both types of charge can be trapped.

ENDORFINS 07_144_04 500nm, AlN2, HR-Si

a)

dual-common **positive** actuation

V_s [V]   bottom-pad-actuated C-V

b)

dual-common **negative** actuation

V_s [V]   bottom-pad-actuated C-V

c)

dual-common **positive** actuation

$\Delta W_{pi}/2$ [V]   bottom-pad-actuated C-V

d)

dual-common **negative** actuation

$\Delta W_{pi}/2$ [V]   bottom-pad-actuated C-V

e)

dual-common **positive** actuation

V_s [V]   beam-actuated C-V

f)

dual-common **negative** actuation

V_s [V]   beam-actuated C-V

g)

dual-common **positive** actuation

$\Delta W_{pi}/2$ [V]   beam-actuated C-V

h)

dual-common **negative** actuation

$\Delta W_{pi}/2$ [V]   beam-actuated C-V

Figure 10.30: The results of stressing ENDORFINS devices with positive and negative dual-common actuation methods. Test conditions: $25°C$, N_2, 1atm, light on.

ENDORFINS 07_144_04, 500nm AlN2, HR-Si
dual-common actuation method

a)

air, dual-common, +50V, 100Hz
dual-common-actuated C-V

b)

air, dual-common, -50V, 100Hz
dual-common-actuated C-V

c)

air, dual-common, +50V, 100Hz
bottom-pad-actuated C-V

d)

air, dual-common, -50V, 100Hz
bottom-pad-actuated C-V

ΔV_{pi}^{-} ▶   ◀ ΔV_{pi}^{+}

ΔV_{pi}^{-} ▶   ◀ ΔV_{pi}^{+}

e)

air, dual-common, +50V, 100Hz
beam-actuated C-V

f)

air, dual-common, -50V, 100Hz
beam-actuated C-V

ΔV_{pi}^{-} ◀   ◀ ΔV_{pi}^{+}

ΔV_{pi}^{-} ▶   ▶ ΔV_{pi}^{+}
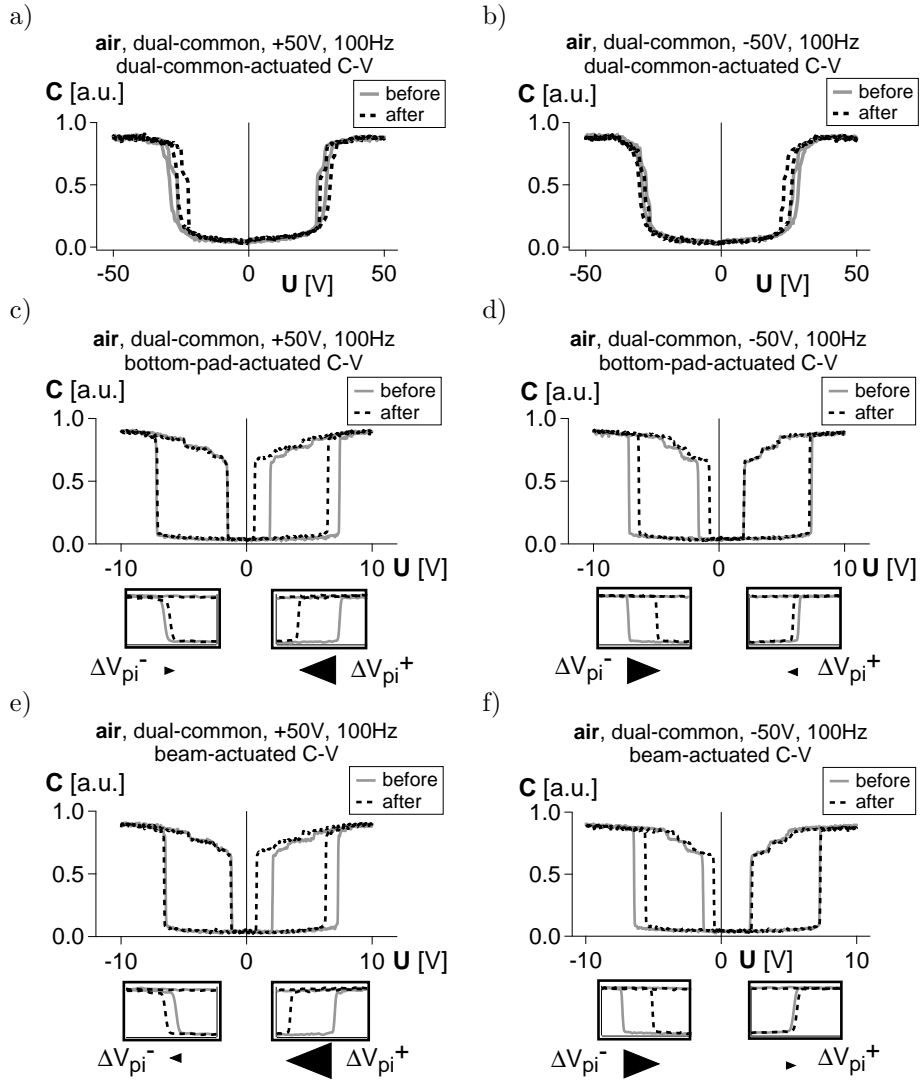
Figure 10.31: Dual-common- a) and b), bottom-pad- c) and d) and beam-actuated
e) and f) C-V characteristics measured before and after stressing devices with
dual-common positive and negative actuation methods in ambient air atmosphere.
Test conditions: $25°C$, light on.

10.12.6 Summary

The dual-common actuation method allows stressing the device with the electric field component across the interposer dielectric equal to zero. Therefore, any observed changes of the C-V characteristic are expected to be due to the charge trapped in the substrate. A number of experiment using the actuation method are presented. The results of the experiments performed in N_2 atmosphere show almost no charging. However, the introduction of humidity does accelerate charging. A voltage shift and narrowing of the C-V characteristics is observed in ambient air.

The observed voltage shift of the dual-common-actuated C-V characteristics can be caused only by charge trapped in the substrate. The results are confirmed with bottom-pad- and beam-actuated C-V curves. The relations between the V_s and the $\Delta W_{pi}/2$ point to substrate charging.

10.13 Summary

A number of methods based mainly on different biasing schemes to isolate and identify different charging mechanisms are presented in this chapter. In the first experiment devices with a thicker interposer dielectric layer were used. A reduction of the lifetime instead of the expected improvement was observed. It is shown that the introduction of the thicker dielectric reduced the interposer dielectric charging and emphasized the other charging mechanism - the substrate charging.

Next, a more detailed study of the "fast" and "slow" charging mechanisms is presented. The "fast" charges cause mainly a shift of the C-V characteristic that saturates relatively fast. The C-V characteristic is influenced in a similar way independently on the polarity of the actuation voltage. The magnitude of the V_s and ΔW_{pi} are very similar. Only the sign of the voltage shift depends on the polarity of the actuation voltage. However, they disappear very fast. They are attributed to charging the capacitance of the switch or to dipolar polarization or space charge migration.

The charging mechanisms of higher time constants, called "slow", can be observed during or after stressing devices with dedicated biasing methods. Idling-during-stressing allows the observation of "slow" trapping and idling-after-stressing - "slow" de-trapping. There are two "slow" charging mechanisms visible. Both occur at different polarities of the actuation voltage. The influence of the C-V characteristic is slightly different: both V_s and ΔW_{pi} are modified differently.

The use of the abovementioned methods allows distinguishing only the mechanisms of different time-constants. Introduction of an extended model of the switch, taking a simplified substrate representation into account, was expected to allow space

location of the charging mechanisms. However, the obtained results were different than expected. The bottom-pad- and beam-actuated C-V characteristics indicate interposer dielectric charging even if the used testing conditions limited or excluded charging of the interposer dielectric. The last experiment, dual-common stressing in air, showed that the method is useful, though, limited. Charge trapped on the surface of the substrate can be detected.

The disagreement of the experimental data with the expectations based on the proposed extended model shows that the model is missing an important factor. The electrical properties of the substrate seem to have a higher than assumed impact on the distribution of the electric field in the switch. That may increase both the charge trapping and the sensitivity of the beam to the charge trapped in the substrate.

The contribution of the substrate to the distribution of the electric field and thus the electrostatic force acting on the beam needs a better understanding. It has been neglected so far. The study on this is presented in the next chapter.

Chapter 11

More about the impact of the substrate

11.1 Introduction

This chapter is focused on a study of an impact of the substrate on the charging sensitivity, thus the reliability, of the MEMS devices.

The impact of different types of substrates has been studied: high-resistivity silicon, glass and quartz. However, the integration of the CMOS and MEMS devices will probably force the use of HR-Si like substrates: a relatively thin layer of dielectric separating the MEMS from a conductive or semi-conductive layer of material. This chapter presents some insights into this aspect.

It has been assumed in the presented model that the high-resistivity silicon below the silicon dioxide layer can be considered conductive. However, the properties of silicon in the Si-SiO$_2$ system has been studied for years. They are known to be far from properties of a metal layer. The silicon, silicon dioxide and metal layers stack bring to mind the well known MOS diode. Charge accumulation, depletion and inversion can occur. The charge trapped in or on top of the silicon dioxide layer may affect the behavior of the silicon layer. On top of that, the silicon is sensitive to light and temperature. All these mentioned factors may affect the distribution of the electric field below the beam of the capacitive switch.

First, the impact of the MOS diode on the characteristic of the ENDORFINS switch is presented. A number of C-V characteristic measurements performed under various conditions are presented.

The sensitivity of the silicon to light may have an impact on the dynamic properties of the MEMS devices. An experiment showing that effect is further presented.

As a result of the research, a decision about substrate modifications was taken. FEM simulation results and experimental data obtained during testing the modified ENDORFINS devices are presented. The results compared with the results of experiments performed on the standard ENDORFINS devices confirm the hypothesis about the substrate charging.

11.2 Impact of the MOS structure

11.2.1 Introduction

The substrate is considered as a source of unwanted RF losses. The choice of the material for RF applications is dictated by the need to reduce the losses. The impact on the actuation of the MEMS beam has been, so far, neglected.

The model of the switch presented in section 10.8 is based on an assumption that the silicon below the silicon dioxide can be considered conductive. Therefore, it was replaced with a layer of metal in the model. However, the properties of silicon in the Si-SiO$_2$ system are well known. They are far from the properties of metal.

The metal bridge of the switch, the bottom actuation pad and the ground pads, together with the silicon dioxide layer and the silicon substrate can create a structure similar to the MOS (metal-oxide-semiconductor) device (Figure 11.1). The presence of this type of structure is mirrored in a C-V characteristic measured at a relatively lower, if compared to the ELT, frequency of the sensing signal.

11.2.2 1MHz C-V characteristics

Figure 11.2a shows a C- V characteristic of an ENDORFINS device on a HR-Si wafer measured at 1MHz frequency of the sensing signal. It is distorted. The curve is not symmetric anymore. The difference between the capacitance at negative and positive voltages are not due to changes of the beam displacement.

Figure 11.2b shows another C-V characteristic measured after removing the beam. The capacitance is measured between the bottom actuation pad and the grounded back side of the wafer (Figure 11.2c). The obtained characteristic is a typical C-V curve of a MOS diode. The drop of the capacitance observed at negative voltage indicates charge depletion. Such a depletion at negative voltages is observed in n-type silicon wafers.
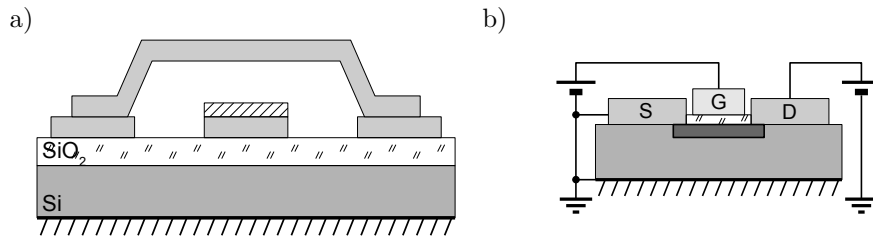
Figure 11.1: The metallization of the switch and the silicon dioxide on the silicon a) create a MOS-like structure b).
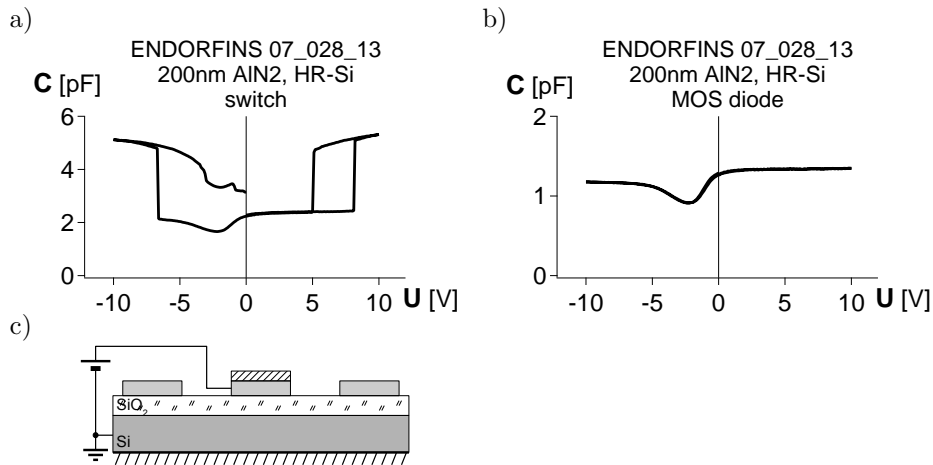
Figure 11.2: The C-V characteristics of the MEMS device a) and the MOS diode b) after the beam removal c)

11.2.3 Influence of light

The presented C-V characteristics (Figure 11.2a and b) were measured with light shining on the structures. However, the C-V characteristic measurement of a MOS device should be performed in the darkness to avoid additional charge generation. Figure 11.3 shows a comparison of the C-V curves of the MEMS and MOS devices performed with the light on and off.

The difference in the shape of the C-V curves is a typical reaction of the MOS device to light. The C-V characteristic of the MEMS switch is affected as well. However, the pull-in and pull-out voltages seem not changed. That may indicate the fact that the MOS structure below the metallization modifies the total capacitance of
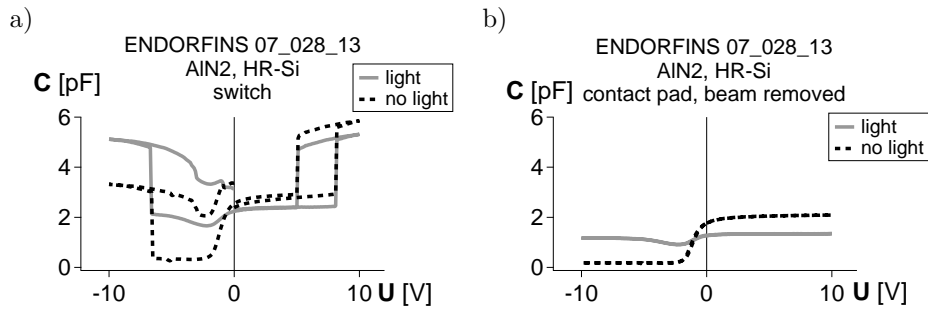
Figure 11.3: A comparison of the C-V characteristics (measured at 1MHz) of the MEMS a) and MOS b) devices measured with the light on and off.

the device especially at low (1MHz) frequency. However, it is possible that the effect occurs only below the metallization and the electric field actuating the beam is not affected.

11.2.4 Summary

The substrate together with the metallization of the switch can create a MOS-like structure below the switch. The C-V characteristic, mainly the capacitance of the switch, is influenced by light in a similar way as the capacitance of a MOS diode. However, the pull-in and pull-out voltage seem to remain unchanged. The MOS structure underneath the MEMS device seems to have no influence on the actuation of the beam. However, the next experiments show that there is some influence occurring under specific testing conditions.

11.3 Impact on the dynamic properties

11.3.1 Introduction

The impact of the MOS structure on the MEMS device may be observed when the properties of the MOS stack are modified. The eventual changes of the switch response can indicate modifications of the electric field caused by the MOS structure.

The previous experiment, the C-V characteristic measurements, did not show a significant impact on the V_{pi} and V_{po} during the standard one-source actuation.

It seems that the highest impact can be observed when the MOS structure affects the field in the slots between the bottom actuation pad and the ground pads.

Therefore, an additional experiment is proposed where the electric field in the slots is dominant. The dual-common actuation method, introduced in section 10.12, causes a generation of the electrostatic force only in the slots. The beam is actuated only by the electric field in the slots. Therefore, any change of the electric field distribution in the slots can have a higher impact on the actuation of the beam than in the case of the standard biasing scheme.

The properties of the MOS structure can be modified by changing the level of light shining on the structure.

11.3.2 Results

The ELT signal recorded during stressing the devices with the positive and negative dual-common actuation method is presented in Figure 11.4.

The ELT signal U_{out} is presented as recorded. It represents the position of the beam. A higher voltage is observed when the capacitance of the switch is low. That occurs when the beam is in the up position. The lower U_{out} points to a higher capacitance - the beam in the down position.

The actuation with the positive voltage is not modified. Both, the ELT and displacement signals, show similar pull-in and pull-out transitions with and without light (Figure 11.4a). However, the ELT signal indicates a lack of actuation during stressing with the negative voltage (Figure 11.4b).

The C-V characteristic of the device presented in the previous section shows a change under different light conditions. The switch is sensitive to light especially when the negative voltage is used. The pull-in and pull-out voltages are not modified, though. It is possible that the ELT signal is sensitive to the changes due to light, even though the beam is still actuated. To verify the effect, the displacement of the beam was monitored with the LDV (Laser Doppler Vibrometer).

The displacement of the beam is modified as well (Figure 11.4d). However, there is a visible difference. The ELT signal indicates a lack of actuation and the recorded displacement points to a change of the t_{on}. The difference may be caused by the presence of the laser light during the displacement measurements. The movement measurements are performed with a laser beam. It cannot be switched off during a measurement. The ELT signal observed during the displacement measurement (Figure 11.4e) confirms the result. In both cases, a change of the pull-in transition is observed.
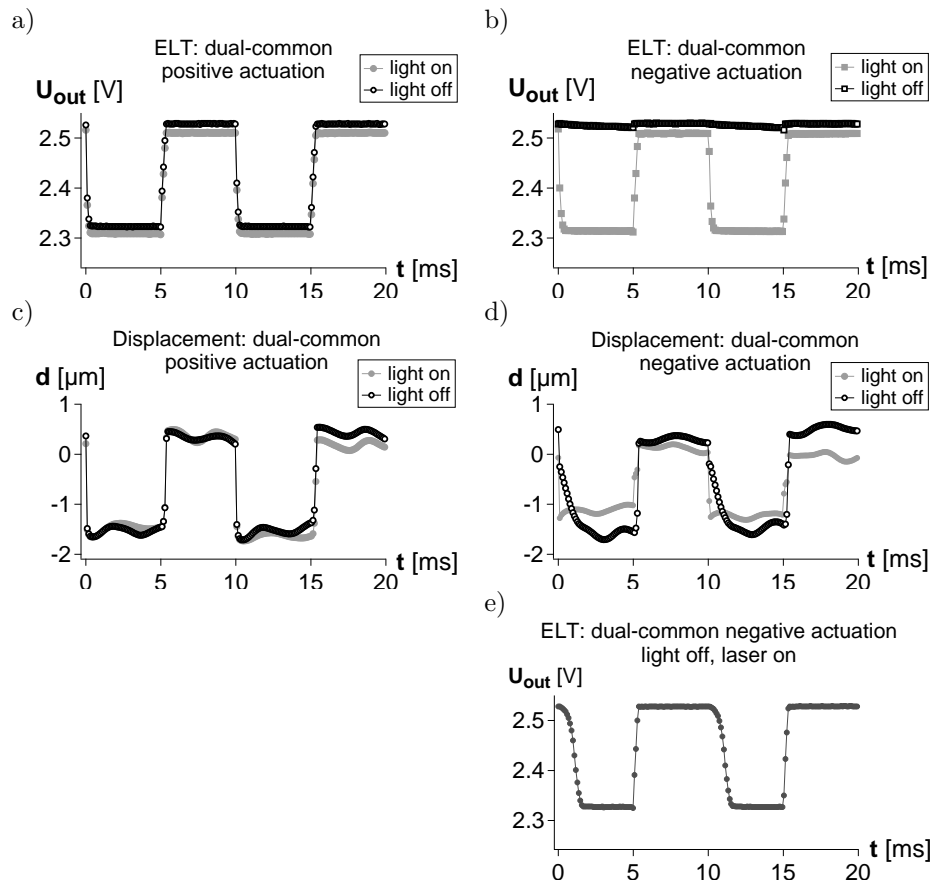
Figure 11.4: The ELT signal (∼500MHz) and beam displacement recorded during actuation of an ENDORFINS switch with positive and negative dual-common actuation method. The response of the device on the applied negative actuation voltage depends on the light.
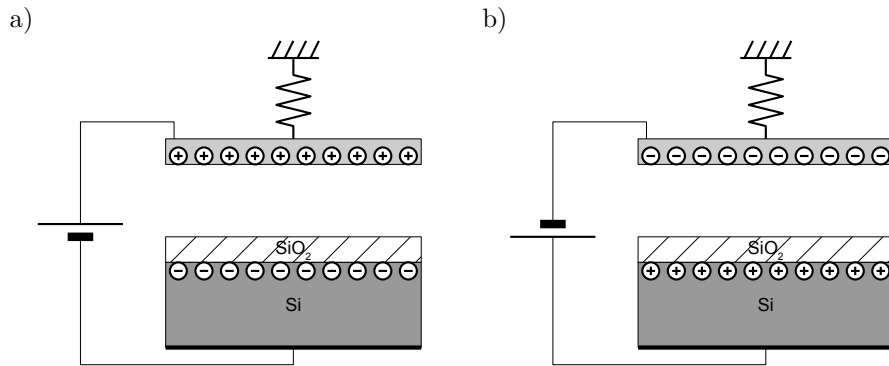
Figure 11.5: The positive voltage applied to the beam attracts the negative charges towards the Si-SiO$_2$ interface a). The negative charges are majority carriers in the n-type silicon. The number of negative charges is high and the additional ones generated with light do not make a big difference. The negative voltage causes attraction of the positive charges towards the Si-SiO$_2$ interface b). The positive charges are minority carriers in the n-type silicon. The number of positive charges is significantly increased with light generation of electron-hole pairs.

11.3.3 Discussion

The actuation of the beam requires agglomeration of opposite types of charge on the bottom electrode and the beam. During the dual-common actuation, the substrate plays the role of the bottom electrode. The actuation can occur when charge is agglomerated close to the Si-SiO$_2$ interface.

Application of the positive dual-common voltage attracts the negative charges towards the Si-SiO$_2$ interface (Figure 11.5a). The negative charges, electrons, are majority carriers in the n-type silicon. As the number of free negative charges at room temperature is already high, the additional negative charges generated by light do not have a big impact.

Application of the negative dual-common voltage attracts the positive charges towards the Si-SiO$_2$ interface (Figure 11.5b). The positive charges, holes, are minority carries in the n-type silicon. The light generation of electron-hole pairs significantly increases the number of positive charges. The amount of positive charge required for actuation can agglomerate much faster. Therefore, an impact of light on the negative actuation is observed.

11.3.4 Summary

The presented impact of light on the dynamic properties of the switch were observed under actuation using the dual-common actuation method. However, a similar effect can be observed in the case of the standard one-source actuation of particular devices. The design of the structure and the type of used material should be adopted to avoid the mentioned problems.

11.4 Slot etching

11.4.1 Introduction

The results of the experiment presented in section 10.2 show that charging of the interposer can be reduced by e.g. increasing its thickness. The thicker dielectric layer reduced one of the observed mechanisms, interposer dielectric charging, emphasizing the other one - substrate charging.

To study charging of the interposer dielectric, substrate charging should be minimized. The reduced impact of the substrate and substrate charging on the C-V characteristic allows highlighting the influence of the interposer dielectric charging. Therefore, a structure with the standard interposer dielectric and a substrate of reduced charging is needed.

The reduced charging of the interposer dielectric is observed as a reduction of the positive V_s component observed during stressing the devices with a positive actuation voltage. The higher amplitude of the negative shift component is attributed to the substrate charging. Therefore, a reduced substrate charging in the case of the standard 200nm AlN2 dielectric is expected to be observed as mainly a positive voltage shift of the C-V characteristic. In addition, a lower change of the pull-in voltage can be measured.

The easiest way of reducing the substrate charging is to remove one of the two causes: the dielectric material or the electric field. The complete removal of the substrate material is not possible as it is a mechanical carrier for the MEMS devices. Replacing it with a conductive material, e.g. metal, is not possible as well. The electric properties of the substrate material should not impede the RF signal passing the switch. Therefore, dielectric or high resistive materials are usually used. On top of that, the actuation pad and the beam must be isolated. Otherwise, the actuation of the beam is not possible.

The electric field, generated by the actuation voltage, is required for the actuation of the switch. It cannot be removed.

One way to reduce the impact of the substrate on the lifetime of the switches is to decrease the sensitivity of the beam to the field generated/modified by the charge trapped in the substrate. That can be probably done by a proper design of the beam shape. E.g. narrower suspension beams cause a lower electrostatic force generated above the substrate.

11.4.2 Slot etching

A possible solution reducing the substrate impact on the lifetime of the capacitive RF MEMS switches has been proposed by the team working on the ENDORFINS project: Ingrid De Wolf, Xavier Rottenberg, Piotr Czarnecki and Philippe Soussan [457]. The idea is discussed in the following.

The silicon oxide present on the high-resistivity silicon wafer is expected to trap most of the charge. The charge trapped in the SiO_2 layer or at the Si-SiO_2 interface layer below the beam can generate an additional force acting on the beam. Therefore, an additional processing step to remove it from the exposed places has been proposed. The silicon oxide is still present below the metallic parts isolating them. Further reduction of the impact of the substrate can be probably achieved by retracting the surface of the substrate away from the beam by removing the silicon. A higher substrate-beam distance is supposed to reduce the electrostatic force generated by the eventual trapped charge (Figure 11.6).

Figure 11.7 shows the results of FEM simulations of the electric field distribution in the slots between the bottom actuation pad and the ground pads. Two cases are compared: the standard with SiO_2 layer and the new with SiO_2 and $2\mu m$ of silicon etched. The electric field generated by the actuation voltage penetrates less into the slots in the etched-slots structure. That can reduce both charging of the substrate and the impact of the trapped charge on the C-V characteristic. The charge trapped close to the actuation pad should cause a lower voltage shift. The charge trapped far from the bottom actuation pad that does not impact the field created by the U_{act} will cause a lower narrowing of the C-V characteristic.

The results of FEM simulations of F_{el}-U curves show both a lower V_s and a lower $\Delta W_{pi}/2$ in the etched-slots structure than in the standard one (Table 11.1).

11.4.3 Experimental results

The proposed ideas were implemented in the processing of additional wafers with the ENDORFINS devices. The silicon oxide and $2\mu m$ of silicon were removed from places not masked by the bottom actuation and ground pad metal layer. The interposer dielectric layer is the standard 200nm AlN2.
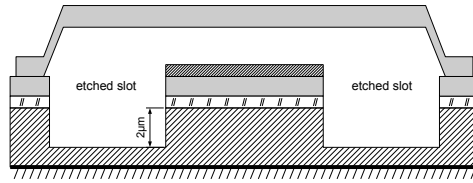
Figure 11.6: Removing of the silicon oxide and $2\mu m$ layer of silicon is expected to reduce the impact of the substrate and substrate charging on the lifetime of the capacitive devices.
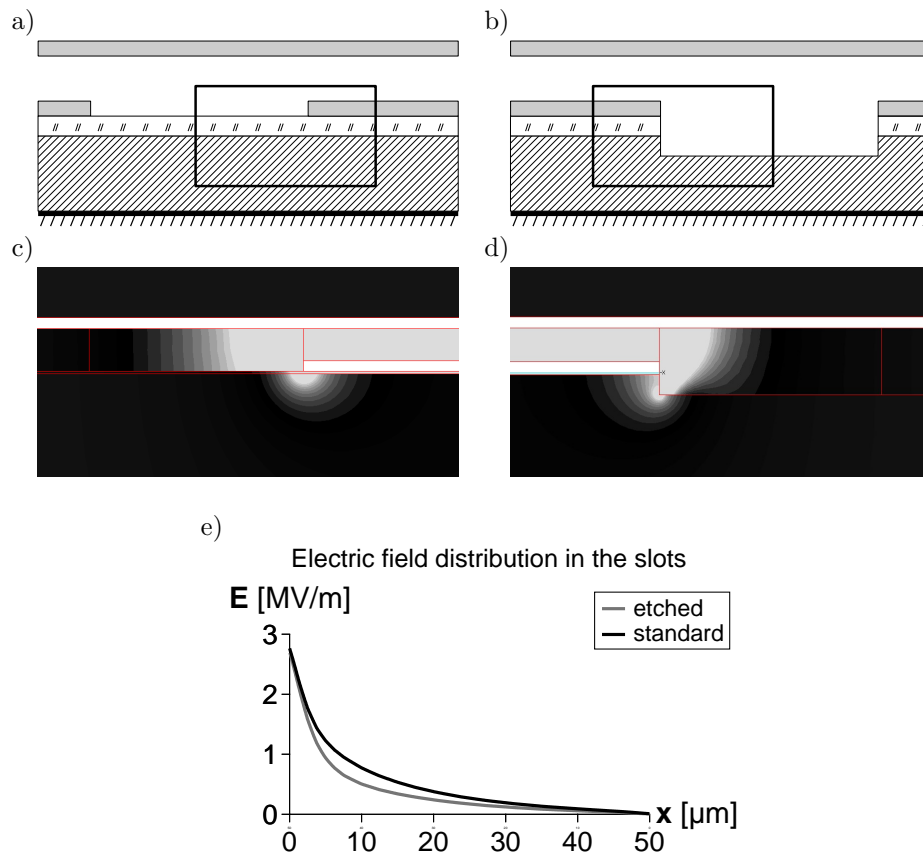
Figure 11.7: The geometry of the test structures used for FEM simulation of the electric field distribution in the standard- a) and etched-slot b) structures close to the beam. The electric field penetrates the etched-slots c-e) less than the standard one d-e). The lower electric field in the slots is expected to reduce both substrate charging and the impact of the charge on the C-V characteristic.

Table 11.1: The results of FEM simulations of structures with standard and etched slots. Charge placed on the surface of the substrate in the slots.

	standard slots		etched slots	
	V_s	$\Delta W_{pi}/2$	V_s	$\Delta W_{pi}/2$
no charge	0.000V	0.000V	0.000	0.000
with charge	-0.226V	0.376V	-0.109V	-0.186V

The new devices were tested using the idling-during-stressing method (see section 10.5.2). The devices were stressed using the one-source actuation voltage applied to the bottom actuation pad. Both polarities, various amplitude and the standard 100Hz frequency and 50% d.c. were used. The devices were stressed for 1000 cycles and un-actuated for 20s to allow the "fast" charges to de-trap. The experiments were performed in N_2, 1bar atmosphere at 25°C. The C-V characteristic was measured before and after every stressing-idling cycle. The positive and negative pull-in voltages were extracted and the voltage shift and pull-in window change were calculated. A comparison of the obtained results with the data obtained during stressing the 500nm AlN2 structures with the standard substrate is presented in Figure 11.8.

In both cases, positive and negative stressing, lower V_s and $\Delta W_{pi}/2$ are observed in spite of the thinner interposer dielectric layer. The positive actuation causes a shift of only one polarity. That points to one dominant mechanism. The sign of the V_s is opposite to the one observed during stressing of the 500nm AlN2 devices.

A comparison of two devices with etched and standard slots with the same thickness of the interposer dielectric would an obvious choice. Unfortunately, only 200nm AlN2 with etched slots and 500nm AlN2 with standard slots devices were available. However, these two types of devices emphasizes the influence of the etched slots.

11.4.4 Discussion and summary

The presented results show that the removal of the SiO2 layer and a part of the silicon substrate can reduce the impact of the substrate on the C-V characteristic of the switches. Both voltage shift and pull-in window narrowing are significantly reduced.

The lower V_s can indicate a reduction of one charging mechanism or a presence of two competing mechanisms. However, the lower $\Delta W_{pi}/2$ points to the presence of one dominant mechanism. Therefore, lower V_s and $\Delta W_{pi}/2$ indicate a significant reduction of one of the mechanisms - probably the substrate charging.

The negative actuation voltage causes a voltage shift of the sign opposite to the
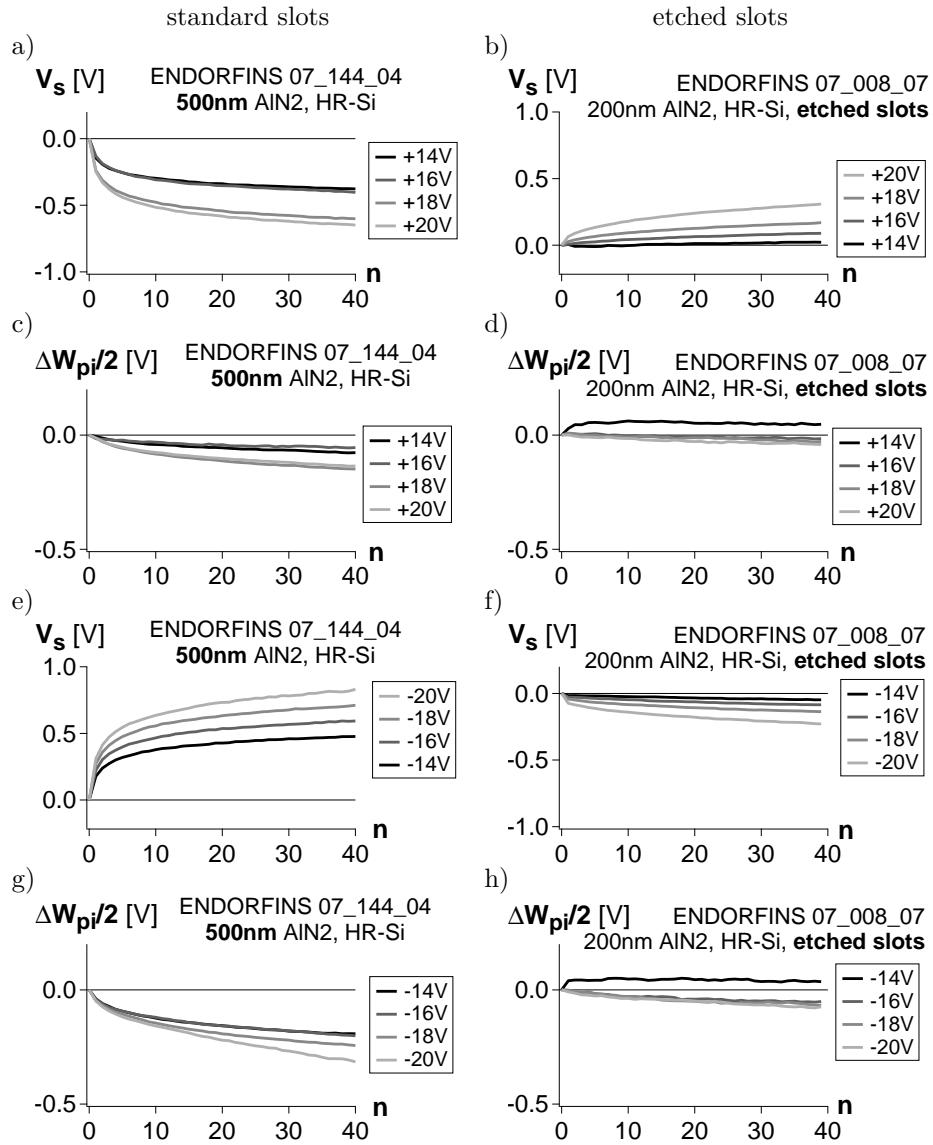
Figure 11.8: The comparison of the results of stressing the standard and etched-slots ENDORFINS structures. A different sign and lower magnitude of the V_s and lower $\Delta W_{pi}/2$ indicate lower charging of the substrate. Test conditions: $25°C$, N_2, 1atm, light on.

one observed during stressing the 500nm AlN2 devices. The origin is not clear. The interposer dielectric is expected to trap only one type of charges independently on the polarity of the actuation voltage. A slightly higher $\Delta W_{pi}/2$ points to either an additional mechanism or substrate charging. It is possible that the slot etching reduced only one charging mechanism and revealed another one. That requires a further study. One of the possibilities would be to test devices fabricated on an n-type silicon wafer with different doping levels.

The sign of the voltage shift during stressing with the positive actuation voltages corresponds to the shift attributed to the interposer dielectric charging. It is the same component that disappeared after introducing the thicker dielectric layer. A very low change of the pull-in window indicates the interposer dielectric charging rather than the substrate.

11.5 Discussion

The results presented in the previous section show lower changes of the V_s and $\Delta W_{pi}/2$ of the slots-etched structures even though the thickness of the interposer dielectric is much lower than in the 500nm AlN2 devices. That points to a reduction of the impact of the charge trapped in the substrate or lower charge trapping in the substrate.

The slots etching reduced significantly the voltage shift recorded during stressing the devices. It has been presented in the previous sections that the charge trapped in the substrate can cause a voltage shift of the C-V characteristic. However, it was accompanied with a large change of the pull-in window. Now, the V_s that was higher than the $\Delta W_{pi}/2$ disappears.

It seems that the substrate can cause a voltage shift that is higher than the narrowing of the C-V characteristic. Therefore, both the substrate charging and the interposer dielectric charging can cause a voltage shift of the C-V curve. Both can be misinterpreted.

The results presented in this chapter show that the electric properties of the substrate have a big impact on the MEMS device fabricated on top. The substrate cannot be considered only as a mechanical carrier. The low RF loss is not the only electrical parameter that needs to be taken into account during a substrate material choice.

The substrate is a part of the device that has a significant impact on its actuation properties.

It has been shown that the electric field distribution in the substrate can be affected by charge trapped or migrating in the substrate. That can result in modifications

of the C-V characteristic of the switch leading to a lifetime drop.

As an example, an experiment showing a change of the dynamic properties of the devices exposed to light is presented. The change of the electrical properties of the substrate may result in changes of the properties of the MEMS devices. These changes can be recognized as a failure in some specific applications.

Based on the presented experiments, a method to reduce the impact of the substrate has been proposed. The removal of a part of the substrate material was expected to improve the lifetime of the devices. The presented experimental data confirmed that the substrate has a big impact on the device.

The results of the experiments performed on the slots-etched devices show considerable changes in the evolution of the C-V characteristic during stressing. A V_s of opposite sign and lower magnitude and lower a $\Delta W_{pi}/2$ point to a reduction of the impact of the substrate.

The lower C-V voltage shift is the most interesting point. The voltage shift has been attributed to the interposer dielectric charging. However, a large voltage shift component disappeared after the substrate modifications. The charge trapped in the substrate may cause a similar effect on the C-V characteristic as the charge trapped in the interposer dielectric. In both cases a voltage shift higher than the narrowing of the pull-in window can be observed. That may lead to a misinterpretation of the obtained results.

11.5.1 Substrate charging and its impact - a possible explanation

Because of their insulating and RF properties, dielectric and semi-conductive materials are chosen for the substrate of MEMS devices. Especially the high-resistivity oxidized silicon is commonly used as a material that provides a high quality surface and is CMOS fab compatible. However, both types of materials allow the electric field to penetrate their volume. The electric field penetrating the substrate can cause charge trapping and be further modified leading to modifications of the C-V characteristic.

A very schematic explanation of the impact of the substrate on the C-V characteristic is presented in Figure 11.9. The left side of each graph corresponds to the negative ("-") and the right side to the positive ("+") polarity of the actuation voltage. The back side of the substrate is grounded. The distribution of the electric field generated by the actuation voltage is represented with field lines. The thickness of the lines symbolizes the magnitude of the field.

With no charge trapped, both polarities of the actuation voltage applied to the bottom actuation pad generate electric field with a similar distribution (Figure 11.9a). It is not important whether the field is uniformly distributed or not. The

electrostatic force is equal and the C-V characteristic is symmetric (Figure 11.9c). The strongest electric field is present close to the bottom actuation pad (thick lines). It may cause local trapping of e.g. negative charges (Figure 11.9b). As a result, the electric field is enhanced (left) or reduced (right). The electrostatic force is different for both polarities. I.e. the positive and negative pull-in voltages are different. The voltage shift of the C-V curve is observed (Figure 11.9f). The trapped charges modify only a part of the field generated by the actuation voltage (Figure 11.9e). Therefore, narrowing of the C-V characteristic may be observed (Figure 11.9g). On top of that, the distribution of the electric field in the vicinity of the trapped charges (thinner lines) can be modified. That can result in additional narrowing of the C-V characteristic.

11.5.2 Underneath the bottom actuation pad

The charge trapped below the bottom actuation pad has been so far considered shielded by the metallic pad. No impact on the electrostatic force generated by the actuation voltage is expected. However, the charge may impact the electric field and/or free charge in the substrate (Figure 11.10). As a result, the field between the beam and the surface of the substrate in the slots can be affected. Therefore, indirectly, it may impact the electrostatic force acting on the beam.

11.5.3 Summary

The substrate and substrate charging may have a big impact on the lifetime of the capacitive RF MEMS switches. It has been shown that the substrate charging may have a similar impact on the C-V characteristic as the interposer dielectric charging. Therefore, both may be mixed-up.

It is clear that a reduction of the substrate impact is required. A complete removal of the substrate is not possible as the MEMS structure needs a mechanical support. The proposed partial removal of the substrate material in the slots is one of the possible solutions. The obtained results show an improvement. The experiments show that minimizing the electric field in the substrate/slots is a good idea. Therefore, a further development is required. A use of a fully metallic and grounded substrate is not possible. The signal line and the ground pads need electrical isolation. Shielding, at least partial, of the substrate material in the slots would be a possibility (Figure 11.11a).

The oxidized high-resistivity silicon (HR-Si) substrates are used because of the acceptable resistivity that defines the RF loss. However, it seems that lower levels of resistivity would be better from the charging point of view. Therefore, a compromise must be found there.
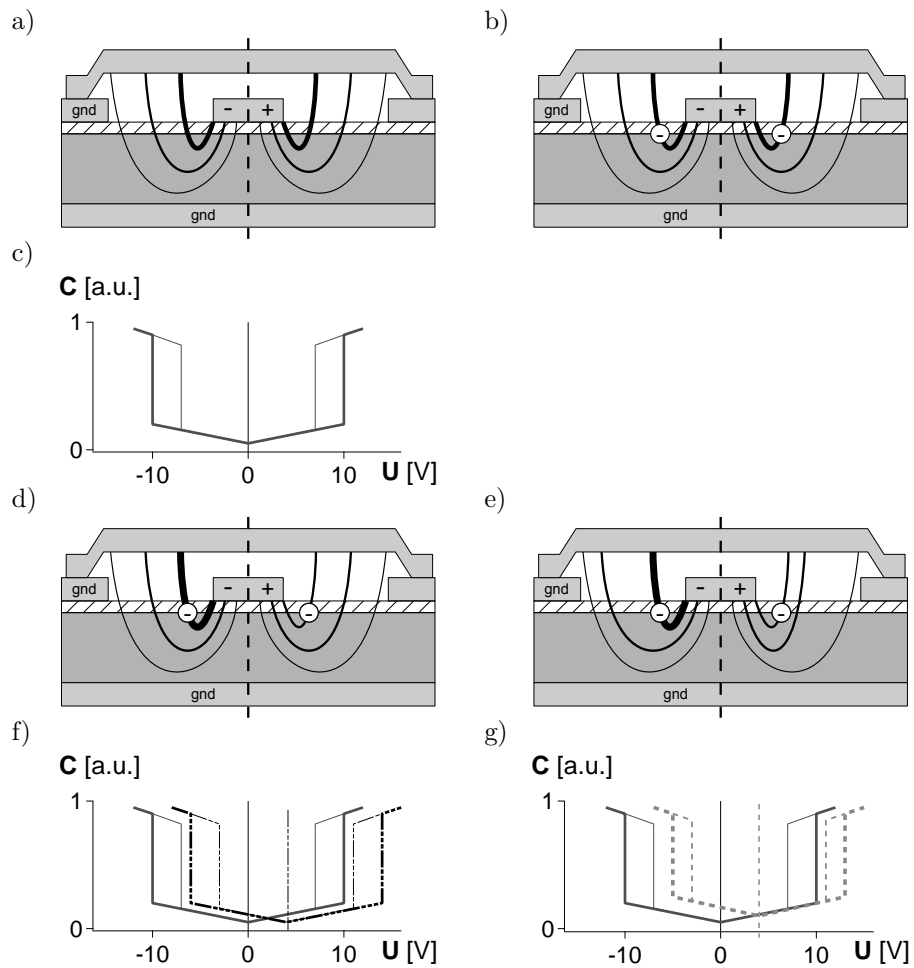
Figure 11.9: The field in the substrate can generate the electrostatic force actuating the beam a and c). The same field can cause local trapping of charges b). The charges can enhance or reduce the strength of the field depending on the polarity of the applied actuation voltage d) causing a voltage shift of the C-V characteristic f). In the same time, the distribution of the electric field in the vicinity of the trapped charges can be distorted d) leading to additional narrowing of the C-V curve g).
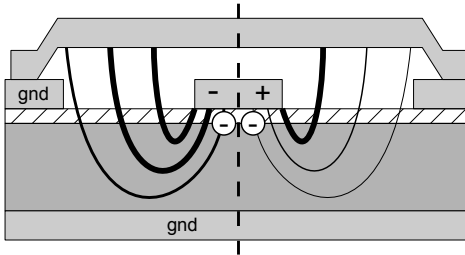
Figure 11.10: Charge trapped in the dielectric below the bottom actuation pad may indirectly impact the electrostatic force actuating the beam.

a) b)
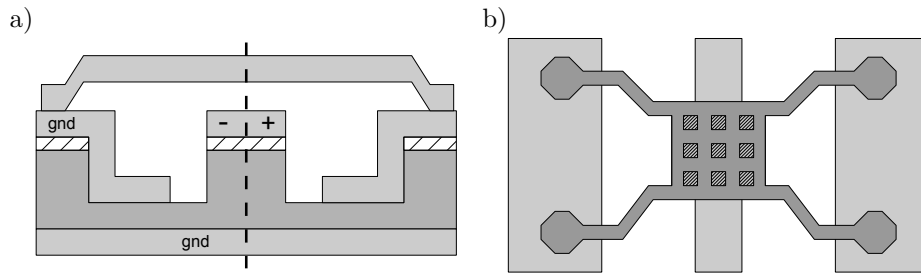
Figure 11.11: Possible ways to reduce the impact of the substrate and substrate charging: shielding the substrate material is the slots a) and thinner suspension beams b).

Another group of possibilities is related to the design of the switch. The structure, the beam especially, can be made less sensitive to the impact of the substrate. A proper design of the shape of the beam may reduce the impact of the field in the substrate. E.g. thinner suspension beams located in a place where the impact of the electric field is lower (Figure 11.11b).

Retracting the beam further from the substrate by increasing the thickness of the signal line and ground pads is another possibility 11.12.
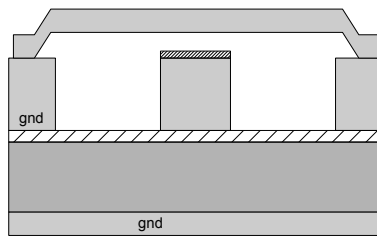
Figure 11.12: Retracting the beam further from the substrate by increasing the thickness of the signal line and ground pads is another possible way of reducing the impact of the substrate on the lifetime of the capacitive RF MEMS switches.

Chapter 12

Summary, conclusions and future work

12.1 Summary

The focus of the work presented in this document was on the physics and reliability of the RF MEMS devices. As a representative the electrostatically driven capacitive RF MEMS switch was chosen. The main goal was a better understanding of the physics of failure. The obtained observations and conclusions were expected to help designers and technologists to develop a reliable capacitive RF MEMS switch.

The by Goldsmith presented electrostatically driven capacitive RF MEMS switch is one of the members of the RF MEMS devices family. The promising properties of the switch caused many research centers to spent effort in development of this type of devices. However, the commercialization of the devices is/was hampered by poor reliability with charging recognized as the main failure mechanism. The first reliability studies pointed to charge trapping in the interposer dielectric governed by the Poole-Frenkel conduction mechanism. A number of reliability models based on the mechanism were proposed. A remedy for the charging problem was presented as well.

Most of the work done during the first phase of this thesis was done in frames of mainly three projects: MEMS2TUNE, MIPA and RETINA. A very limited number of devices were available. The goal of the first experiments was to verify whether the failure mechanism of the available devices was similar to the one described in literature. The obtained results pointed indeed to Poole-Frenkel conduction as a possible failure mechanism. A verification of the by Goldsmith proposed remedy,

bipolar actuation voltages, showed only a slight improvement.

Besides that, an impact of the gas breakdown and/or electron emission on the lifetime of the switches was observed. The relation between the lifetime of the electrostatically driven capacitive RF MEMS switches and ambient gas pressure has never been presented before.

Most of the work presented in the next part was done in the frame of the ESA/ESTEC ENDORFINS project starting with an FMEA study. A number of possible failure mechanisms were listed and the one with the highest priority, charging, was determined. It was chosen for a more detailed study.

An opportunity of designing a set of dedicated test structures was given. Based on the experience gained during the first part, a number of devices were proposed. The design consisted of not fully functional, yet, representative from the charging point of view, electrostatically driven switchable capacitors. The design assured the compatibility with the available and further improved testing equipment (ELT). A number of dedicated test structures to study the impact of the environment were also foreseen. However, the structures could not be used due to processing issues. Still, a relatively large number of identical test structures allowed performing experiments under a large variety of testing conditions.

The first phase of the second part consisted of comparing a number of interposer dielectric candidates. A number of simplified wafers were fabricated and tested. Two best candidates, AlN1 and AlN2, were chosen for further investigation. The following experiments were performed on fully processed test structures.

The lifetime experiments performed using various magnitudes of the actuation voltage amplitude and both, positive and negative, polarities, showed a disagreement with the model based on the Poole-Frenkel conduction mechanism. The unusual behavior pointed to more than one charging mechanism present in the capacitive RF MEMS switches. Substrate charging was identified besides the interposer dielectric charging.

The impact of the substrate was first studied with devices fabricated on two different types of substrate material: AF-45 glass and oxidized high-resistivity silicon. The different sensitivity of both materials to various environmental conditions is presented.

The AF45 glass substrate traps more charge than the HR-Si substrate. Stressing of the devices with an actuation voltage below the V_{pi} revealed a significant difference in charging properties of the two types of substrates. As, in that case, the beam was not in contact with the interposer dielectric, the observed effects are mainly due to substrate charging. The C-V characteristic of the devices fabricated on the glass substrate narrowed significantly. At the same time the change of the C-V curve of the devices fabricated on the HR-Si substrate was minor. The difference

is more visible when the experiments are performed in humid air. Only 4 minutes of stressing an AF45 device is enough to the pull-in occurrence. The HR-Si devices pulled-in after more than 4 hours.

Once the two charging mechanisms were observed, the study of each of them became easier. The focus of the next experiments was on separating and localizing the mechanisms. Since the functionality of the presented in literature technique based on EFM (Electrostatic Force Microscopy) is limited, a number of different testing techniques were introduced. The main advantage of these techniques is that they are non-invasive as they are based on various combinations of stressing and C-V characteristic measurements. Charge observation can be done during or immediately after stressing. There is no problem with dwell time that may cause lost of important information.

Application of the actuation voltage(s) to bottom actuation electrode and/or to the beam allows stressing both dielectrics (substrate and interposer dielectric) with different electric field components simultaneously. Thanks to that an unambiguous identification of the mechanisms was possible. During one of the experiments the interposer dielectric was stressed with an alternating electric field equivalent to a bipolar actuation. In the same time the substrate was exposed to only positive or negative actuation voltage. The obtained results were different than expected, yet, were very consistent. The observed voltage shift and C-V narrowing pointed to charge trapped in the interposer dielectric. However, the fact that the sign of the voltage shift was related to the polarity of the component actuation waveforms indicated that the charge can be trapped only in the substrate. The charge trapped in the interposer dielectric could not depend on the polarity of the component actuation voltages.

Based on the obtained results, an improvement in the switch was proposed. A modification of the substrate allows reducing two factors: Charge trapping in the substrate and the sensitivity of the beam to charge trapped in the substrate. The last presented experiment, consisting of testing devices with a modified HR-Si substrate, showed that the impact of the substrate and substrate charging is higher than anticipated. It definitely cannot be neglected.

In addition, the C-V characteristic of the device can be modified in similar ways by both interposer dielectric and substrate charging. Therefore, both may be confused. The charge trapped in the substrate can be incorrectly recognized as trapped in the interposer dielectric and vice versa.

There is no mathematical reliability model presented. As the charging properties of the switches depend on the design and used materials, a proposition of one universal model is pointless. A very often asked comparison of the obtained results with the models presented in literature is meaningless as well. The used ENDORFINS structures seem to suffer mainly from the substrate charging whereas most of the models describe the impact of the interposer dielectric charging. The models

themselves may need verification as well. They are based on an assumption that the only change of the C-V characteristic can be caused by charge trapped in the interposer dielectric and that the impact is directly proportional to the amount of trapped charge.

12.2   Main achievements

- Improvement of the ELT (Electronic Lifetime Test) setup,

- Observation of gas pressure impact on the lifetime of the capacitive RF MEMS switches.

- Observation of more than one charging mechanism limiting the lifetime.

- Observation of impact of the substrate on the lifetime.

- New testing techniques for non-invasive isolation and localisation of charge trapped in the switches.

- Proposal of modifications reducing sensitivity of the switches on the impact of substrate.

12.3   Conclusions

The presented results show that the interposer dielectric is not the only place to trap charges. The substrate that is also a type of dielectric, can trap charges and impact the reliability of the electrostatically driven capacitive RF MEMS switches. The substrate charging was not considered as a possible failure cause so far.

The impact of a substrate/carrier on the parameters of the devices in the macro world is usually neglected. E.g. the resistance of a PCB substrate is usually high enough to be ignored in most of the electronic circuits. On the other hand, in the semiconductor technology, the substrate (Si, GaAs, etc.) is, in fact, the active part of the device. Therefore, the impact is very well understood.

In MEMS technology, the role of the substrate is considered only as a mechanical carrier. In the case of the parallel plate actuators, the substrate may impact only the fringing field that creates only a small fraction of the electrostatic field. Therefore, it has been considered not important. However, as has been shown in this thesis, it may cause reliability issues.

The capacitive RF MEMS switches are usually presented as two parallel electrodes of the same size. One of the electrodes is mechanically fixed in empty space. The

other electrode is suspended with a spring above the first one. The substrate is not represented at all. Therefore, the only possible place for the observed charge trapping is the interposer dielectric. The theoretical models describing the impact of the charge trapped in that place fit, up to certain extend, measurements results. However, the simple parallel-plate model influences the measurements as well. The impact of the trapped charge is often represented as changes of only one, positive or negative, pull-in voltage. I.e. the pull-in is considered directly proportional to the amount of charge trapped in the interposer dielectric. The by Rottenberg presented influence of the non-uniform charge distribution is not taken into account.

The impact of both, the interposer dielectric and substrate charging, depends on the used materials and the design of the structures. It is possible that one is covered by the other one. E.g. the sign of the voltage shift components generated by the two is the same. That makes the discrimination more difficult or even impossible.

The impact of the substrate charging depends on the design of the switch, mainly the beam, as well. It can be either dominating or invisible in some cases. However, the later is less likely.

The influence of the substrate is visible under certain testing conditions. It has been shown that the impact of the substrate charging on the C-V characteristic may be similar to the influence of the interposer dielectric charging. If one of the mechanisms is dominant, then observation of the second one is more difficult.

12.4   Proposals

The charging (e.g. charge trapping) and its impact on the lifetime of the switch will probably always take place. As long as a dielectric material is placed in an electric field, charging will occur. A use of less sensitive materials is an option. However, it is probably easier to design the devices in a way to minimize the impact of charging on the lifetime. A proper design may minimize the sensitivity of the MEMS movable part to the changes of the electric field in its vicinity.

One suggestion is presented in section 11.5.3. The structure can be made less sensitive to the charge trapped in the substrate by a proper beam design. However, there are more possibilities.

The EOL is of the capacitive RF MEMS switch is observed when one of the pull-out voltage crosses the 0V point. I.e. the charge trapped in the switch generates an electrostatic force high enough to keep the beam in the bottom position even with the external actuation voltage off. If the pull-out voltage is designed much higher, then it is possible that the charge trapped saturates at a level below the critical value. The idea is proved by the results presented by Ekkels et al. [458]. The presented devices exhibit relatively high V_{po}. After the stressing, the pull-out

a)

b)
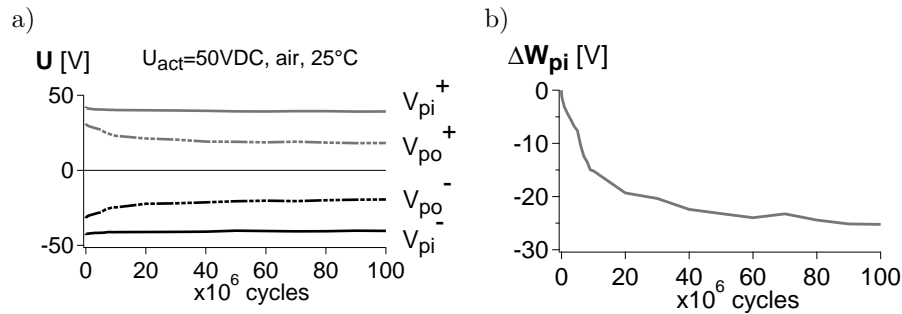
Figure 12.1: The results of stressing a device with a high pull-out voltage. The structure traps charge indicated by the narrowing of the C-V characteristic. The change of the pull-out window is about 30V. Still, the pull-out voltages are higher than 20V. Test conditions: $25°C$, ambient air, light on.

voltage changes more than 10V. Still, it is higher than 20V. Figure 12.1 shows the observed evolution of the C-V characteristic.

A device was stressed with a DC voltage of 50V in ambient air. The stressing was stopped after a time corresponding to the down-time of $2 \cdot 10^8$ cycles. The pull-out voltages seem to saturate. It is possible that they would not change much more even after a much longer stressing period. Even though the charge trapped in the structure is relatively high, the structure survives. I.e. there is enough room for charge to trap.

The pull-out voltage is directly linked to the C_{down} and C_{up}/C_{down} ration. The thickness of the interposer dielectric is one of the factors. It is obvious that by increasing the thickness of the interposer dielectric the charging of the dielectric can be reduced and the pull-out voltage increased. In the same time the C_{down} and C_{up}/C_{down} degrade. Therefore, an optimum should be found.

The proposal of the bipolar actuation voltage as a remedy for the charging problems may work as long as all the charging mechanisms are of the same nature. I.e. all the charging mechanisms should cause trapping of only one type of charge and preferably release the charge e.g. under stressing with the opposite polarity of the actuation voltage.

12.5   Future work

This work covers only a very narrow range of the reliability and charging related issues. There are still a lot of aspects that require verification or further study. One of the examples would be testing devices fabricated on HR-Si substrates of different

types and dielectrics trapping different types of charge. That may help finding materials that can trap and de-trap charge under similar conditions. Therefore, the use of the bipolar or intelligent actuation waveforms improving the lifetime would be possible [459].

The next issue that may have a big impact on the charging properties of the devices is the packaging. The impact of packaging has not been studied in the frame of this work.

It has been shown that the packaging of the MEMS devices is a must. The devices are sensitive to the environment and require protection. However, the package may impact the distribution of the electric field around the switch. Therefore, it may influence the lifetime of the device inside the package. The hermeticity should not be the only factor determining the properties of the package. The packaging, together with the substrate, should create a Faraday cage around the MEMS device.

Bibliography

[1] H.C. Nathanson, W.E. Newell, R.A. Wickstrom, J.R. Davis, Jr., *The Resonant Gate Transistor*, IEEE Transactions on Electron Devices, vol. 14, no. 3, March 1967, pp. 117-133.

[2] C. Goldsmith, J. Randall, S. Eshelman, T.H. Lin, D. Denniston, S. Chen, B. Norvell, *Characteristics of Micromachined Switches at Microwave Frequencies*, IEEE MTT-S International Microwave Symposium Digest, June 1996, San Francisco, CA, USA, vol. 2, pp. 1141-1144.

[3] C. Goldsmith, J. Ehmke, A. Malczewski, B. Pillans, S. Eshelman, Z. Yao, J. Brank, M. Eberly, *Lifetime Characterization of Capacitive RF MEMS Switches*, IEEE MTT-S International Microwave Symposium Digest, May 2001, Phoenix, AZ, USA, vol. 3, pp. 227-230.

[4] G.M. Rebeiz, *RF MEMS Theory, Design, and Technology*, Hoboken, NJ, USA, Wiley, 2003.

[5] Z.J. Lao, S. Chen, S. Eshelman, D. Denniston, C. Goldsmith, *Micromachined Low-Loss Microwave Switches*, Journal of Microelectromechanical Systems, JMEMS, vol. 8. no. 2, June 1999, pp. 129-134.

[6] W. Johler, *RF Performance of Ultra-miniature High Frequency Relays*, IEEE HOLM Conference on Electrical Contacts, Sept. 2003, Washington, DC, USA, pp. 179-189.

[7] P.D. Grant, M.W. Denhoff, *A Comparison Between RF MEMS Switches and Semiconductor Switches*, Proceedings of International Conference on MEMS, NANO and Smart Systems, ICMENS, Aug. 2004, Banff, Alberta, Canada, pp. 515-521.

[8] H.J. De Los Santos, Y.-H. Kao, A. L. Caigoy, E. D. Ditmars, *Microwave and Mechanical Considerations in the Design of MEM Switches for Aerospace Applications*, Proceedings of IEEE Aerospace Conference, Feb. 1997, Aspen, CO, USA, vol. 3, pp. 235-254.

[9] S. Janson, H. Helvaijan, S. Amimoto, G. Smit, D. Mayer, S. Feuerstein, *Microtechnology for Space Systems*, Proceedings of IEEE Aerospace Conference, March 1997, Aspen, CO, USA, vol. 1, pp. 409-418.

[10] S. Cass, *MEMS In Space*, IEEE Spectrum, July 2001, pp. 56-61.

[11] J.J. Yao, C. Chien, R. Mihailovich, V. Panov, J. DeNatale, J. Studer, X. Li, A. Wang, S. Park, *Microelectromechanical system radio frequency switches in a picosatellite mission*, Smart Mater. Struct. vol. 10, no. 6, Dec. 2001, pp. 1196-1203.

[12] J.K. Smith, F.W. Hopwood, K.A. Leahy, *MEM Switch Technology in Radar*, IEEE International Radar Conference, May 2000, Alexandria, VA, USA, pp. 193-198.

[13] D. Saias, P. Robert, S. Boret, C. Billard, G. Bouche, D. Belot, P. Ancey, *An Above IC MEMS RF Switch*, IEEE Journal of Solid-State Circuits, vol. 38, no. 12, Dec. 2003, pp. 2318-2324.

[14] B. Pillans, A. Malczewski, R. Allison, J. Brank, *6-15 GHz RF MEMS Tunable Filters*, IEEE MTT-S International Microwave Symposium Digest, June 2005, Long Beach, CA, USA, pp. 919-922.

[15] J.I. Seeger, B.E. Boser, *Dynamics and Control of Parallel-Plate Actuators Beyond the Electrostatic Instability*, Proceedings of International Conference on Solid-State Sensors and Actuators, TRANSDUCERS, June 1999, Sendai, Japan, pp. 474-477.

[16] O. Bochobza-Degani, D. Elata, Y. Nemirovsky, *A general relation between the ranges of stability of electrostatic actuators under charge or voltage control*, Applied Physics Letters, vol. 82, no. 2, Jan. 2003, pp. 302-304.

[17] J.-B. Lee, C.L. Goldsmith, *Numerical Simulations of Novel Constant-Charge Biasing Method for Capacitive RF MEMS Switch*, Proceedings of NanoTech Conference: Modeling and Simulation of Microsystems, Feb. 2003, San Francisco, CA, USA, pp. 396-399.

[18] J.I. Seeger, B.E. Boser, *Charge Control of Parallel-Plate, Electrostatic Actuators and the Tip-In Instability*, Journal of Microelectromechanical Systems, JMEMS, vol. 12, no. 5, Oct. 2003, pp. 656-671.

[19] P.B. Chu, K.S.J. Pister, *Analysis of Close-loop Control of Parallel-Plate Electrostatic MicroGrippers*, Proceedings of IEEE International Conference on Robotics and Automation, May 1994, San Diego, CA, USA, vol. 1, pp. 820-825.

[20] M.S.-C. Lu, G.K. Fedder, *Position Control of Parallel-Plate Microactuators for Probe-Based Data Storage*, Journal of Microelectromechanical Systems, vol. 13, no. 5, Oct. 2004, pp. 759-769.

[21] B. Borovic, A.Q. Liu, D. Popa, H. Cai, F.L. Lewis, *Open-loop versus closed-loop control of MEMS devices: choices and issues*, J. Micromech. Microeng. vol. 15, no. 10, 2005, pp. 1917-1924.

[22] J.I. Seeger, S.B. Crary, *Stabilization of Electrostatically Actuated Mechanical Devices*, Proceedings of International Conference on Solid-State Sensors and Actuators, TRANSDUCERS, June 1997, Chicago, IL, USA, vol.2, pp. 1133-1136.

[23] E.K. Chan, R.W. Dutton, *Electrostatic Micromechanical Actuator with Extended Range of Travel*, Journal of Microelectromechanical Systems, JMEMS, vol. 9, no. 3, Sept. 2000, pp. 321-328.

[24] R. Nadal-Guardia, A. Dehe, R. Aigner, L.M. Castaner, *Current Drive Methods to Extend the Range of Travel of Electrostatic Microactuators Beyond the Voltage Pull-In Point* JMEMS, vol. 11, no. 3, June 2002, pp. 255-263.

[25] D.M. Pozar, *Microwave Engineering*, Addison-Wesley, Reading, MA, USA, 1993.

[26] A.P. De Silva, C. Vaughan, D. Frear, L. Liu, S.M. Kuo, J. Foerstner, J. Drye, J. Abrokwah, H. Hughes, C. Amrine, C. Butler, S. Markgraf, H. Denton, S. Springer, *Motorola MEMS Switch Technology for High Frequency Applications*, Proceedings of Microelectromechanical Systems Conference, Aug. 2001, Berkeley, CA, USA, pp. 22-24.

[27] X. Rottenberg, H. Jansen, B. Nauwelaers, P. Fiorini, W. De Raedt, H.A.C. Tilmans, *Boosted RF-MEMS capacitive shunt switches*, Proceedings of Workshop on Semiconductor Sensor and Actuator, SeSens, Veldhoven, Nov. 2003, The Netherlands, pp. 667-671.

[28] C. Siegel, V. Ziegler, B. Schonlinner, U. Prechtel, H. Schumacher, *Simplified RF-MEMS Switches Using Implanted Conductors and Thermal Oxide*, Proceedings of European Microwave Conference, Sept. 2006, Manchester, UK, pp. 1735-1738.

[29] M. Driesen, F. Ceyssens, J. De Coster, R. Puers, *Nickel-plated thermal actuator with electrostatic latch*, Proceedings of EUROSENSORS XXII Conference, Sept. 2008, Dresden, Germany, pp. 904-907.

[30] S. Chen, K. Suzuki, T. Marumoto, Y. Ara, R. Iwata, *Design of Micromachined RF Switch*, Proceedings of European Microwave Conference, Oct. 1999, Munich, Germany, vol. 2, pp. 49-52.

[31] J.H. Schaffner, R.Y. Loo, C. Quan, R.C. Allison, B.M. Pierce, S.W. Livingston, A.E. Schmitz, T.-Y. Hsu, D.F. Sievenpiper, F.A. Dolezal, G.L. Tangonan, *Microwave Components with MEMS Switches*, Proceedings of European Microwave Conference, Oct. 2000, Paris, France, pp. 1-4.

[32] Y. Cai, L.P.B. Katehi, *Wide Band Series Switch Fabricated Using Metal As Sacrificial layer*, Proceedings of European Microwave Conference, Oct, 2000, Paris, France, pp. 1-3.

[33] A. Margomenos, D. Peroulis, K.J. Herrick, L.P.B. Katehi, *Silicon Micromachined Packages for RF MEMS Switches*, Proceedings of European Microwave Conference, Oct. 2001, London, England, pp. 1-4.

[34] A. Jourdain, S. Brebels, W. De Raedt, H.A.C. Tilmans, *Influence of 0-level packaging on the microwave performance of RF-MEMS devices*, Proceedings of European Microwave Conference, Sept. 2001, London, UK, pp. 403-406, 419.

[35] B. Yassini, A. Zybura, S. Choi, M. Yu, *DC-to-20 GHz Metal-to-Metal Contact Flip Chip Assembly Shunt MEMS Switch*, Proceedings of European Microwave Conference, Oct, 2002, Milan, Italy, pp. 1-3.

[36] X. Rottenberg, H. Jansen, P. Fiorini, W. De Raedt, H.A.C. Tilmans, *Novel RF-MEMS capacitive switching structures*, Proceedings of European Microwave Conference, Sept. 2002, Milano, Italy, pp. 809-812.

[37] D. Girbau, A. Lazaro, L Pradell, *RF MEMS Switches Based on the Buckle-beam Thermal Actuator*, European Microwave Conference, Oct. 2003, Munich, Germany, pp. 651-654.

[38] X. Rottenberg, J. Geerlings, R.P. Mertens, B. Nauwelaers, W. De Raedt, H.A.C. Tilmans, *MEMS near-DC to RF capacitive series switches*, Proceedings of European Microwave Conference, OCt. 2003, Munich, Germany, pp. 975-978.

[39] E. Beyne, W. De Raedt, G. Carchon, S. Brebels, H.A.C. Tilmans, *RF systems in a package*, Proceedings of European Microwave Conference, Oct. 2004, Amsterdam, The Netherlands.

[40] R.P. Mertens, W. De Raedt, G. Carchon, H.A.C. Tilmans, M. Germain, *Microwave applications of advanced semiconductor technologies*, Proceedings of European Microwave Conference, Oct. 2004, Amsterdam, The Netherlands, pp. 147-152.

[41] G. Wang, D. Thompson, E.M. Tentzeris, J. Papapolymerou, *Low Cost RF MEMS Switches Using LCP Substrate*, Proceedings of European Microwave Conference, Oct. 2004, Amsterdam, The Netherlands, vol. 3, pp. 1441-1444.

[42] T. Ketterl, T. Weller, *SPDT RF MEMS Switch Using A Single Bias Voltage And Based On Dual Series And Shunt Capacitive MEMS Switches*, Proceedings of European Microwave Conference, Oct. 2005, Paris, France, vol. 3.

[43] S.G. Tan, W.P. McErlean, J.-S. Hong, Z. Cui, L. Wang, R.B. Greed, D.C. Voyce, *Electromechanical Modelling of High Power RF-MEMS Switches with Ohmic Contact*, Proceedings of European Microwave Conference, Oct. 2005, Paris, France, vol. 3.

[44] F. Coccetto, B. Ducarouge, E. Scheid, D. Dubuc, K. Grenier, R. Plana, *Thermal Analysis of RF-MEMS Switches for Power Handling Front-end*, Proceedings of European Microwave Conference, Oct. 2005, Paris, France, vol. 3.

[45] C. Siegel, V. Ziegler, U. Prechtel, B. SChonlinner, H. Schumacher, *Very low complexity RF-MEMS technology for wide range tunable microwave filters*, Proceedings of European Microwave Conference, Oct. 2005, Paris, France, vol. 3.

[46] A. Fukuda, H. Okazaki, S. Narahashi, *A Novel Compact Reconfigurable Quad-band Power Amplifier Employing RF-MEMS Switches*, Proceedings of European Microwave Conference, Sept. 2006, Manchester, UK, pp. 344-347.

[47] V. Olivier, C. Schaffauser, C. Drevon, J.L. Cazaux, O. Lafond, M. Himdi, G. Carchon, H.A.C. Tilmans, T. Buck, J. Schoebel, *Use of RF MEMS and micromachined parts to realize highly integrated V band active feed for satellite antennas*, Proceedings of European Microwave Conference, Sept. 2006, Manchester, UK, pp. 807-810.

[48] T. Vaha-Heikkila, M. Ylonen, *CMOS Compatible Switched MEMS Capacitors Up to 220GHz Applications*, Proceedings of European Microwave Conference, Sept. 2006, Manchester, UK, pp. 1060-1063.

[49] M. Paillard, G. Puyatier, Th.G.S.M. Rijks, A. Jourdain, P.G. Steeneken, J.T.M. van Beek, J. De Coster, C. Drevon, H.A.C. Tilmans, J.L. Cazaux, *MEMS-based MCM VCO for space applications*, Proceedings of European Microwave Conference, Sept. 2006, Manchester, UK, pp. 1068-1071.

[50] B. Lacroix, A. Pothier, A. Crunteanu, C. Cibert, F. Dumas-Bouchiat, *CMOS Compatible Fast Switching RF MEMS Varactors*, Proceedings of European Microwave Conference, Sept. 2006, Manchester, UK, pp. 1072-1075.

[51] J. Bouchaud, B. Knoblich, H. Wicht, *Will RF MEMS live up their promise?*, Proceedings of European Microwave Conference, Sept. 2006, Manchester, UK, pp. 1076-1079.

[52] J. McKillop, T. Fowler, D. Goins, R. Nelson, *Design, Performance and Qualifiaction of a Commercially Avaiable MEMS Switch*, Proceedings of European Microwave Conference, Sept. 2006, Manchester, UK, pp. 1399-1401.

[53] X. Rottenberg, P. Soussan, S. Stoukatch, P. Czarnecki, B. Nauwelaers, G. Carchon, I. De Wolf, W. De Raedt, H.A.C. Tilmans, *RF-MEMS technology platform for agile mobile and satellite communications*, Proceedings of European Microwave Conference, Sept. 2006, Manchester, UK, pp. 1723-1726.

[54] D. Girbau, L. Pradell, A. Lazaro, A. Nebot, *In-Plane Electrostatically-Actuated RF MEMS Switch Suspended on a Low-Resistivity Substrate*, Proceedings of European Microwave Conference, Sept. 2006, Manchester, UK, pp. 1731-1734.

[55] P. Arcioni, L. Perregrini, G. Conciauro, *A Novel Low Reflection-Loss MEMS Reconfigurable Patch Antenna*, Proceedings of European Microwave Conference, Oct. 2007, Munich, Germany, pp. 1015-1018.

[56] J. Bouchaud, B. Knoblich, H. Tilmans, F. Coccetti, A. El Fatatry, *RF MEMS Roadmap*, Proceedings of European Microwave Conference, Oct. 2007, Munich, Germany, pp. 1141-1144.

[57] C. Siegel, V. Ziegler, U. Prechtel, B. Schnonlinner, H. Schumacher, *A Ka-band RF-MEMS phase shifter approach based on a novel dual-state microstrip line*, Proceedings of European Microwave Conference, Oct. 2007, Munich, Germany, pp. 1221-1224.

[58] A. Stehle, C. Siegel, V. Ziegler, B. Schonlinner, U. Prechtel, S. Thilmont, H. Seidel, U. Schmid, *Low Complexity RF-MEMS Switch Optimized for Operation up to 120C*, Proceedings of European Microwave Conference, Oct. 2007, Munich, Germany, pp. 1229-1232.

[59] H.A.C. Tilmans, K. Baert, A. Verbist, R. Puers, *CMOS foundry-based micromachining*, J. Micromech. Microeng., vol. 6, 1996, pp. 122-127.

[60] I. Schiele, B. Hillerich, *Comparison of lateral and vertical switches for application as microrelays*, J. Micromech. Microeng. vol. 9, 1999, pp. 146-150.

[61] J.J. Yao, *RF MEMS from a device perspective*, J. Micromech. Microeng. vol. 10, no. 4, 2000, pp. R9-R38.

[62] L. Miao, Z. Zhengping, H. Xiaodong, Z. Xuefeng, L. Haifeng, G. Ronghui, *Adaptive contact for improving the behavior of silicon MEMS switches*, J. Micromech. Microeng., vol. 12, no. 5, Sept. 2002, pp. 696-701.

[63] W.M. van Spengen, R. Puers, I. De Wolf, *A physical model to predict stiction in MEMS*, J. Micromech. Microeng., vol. 12, no. 5, 2002, pp. 702-713.

[64] M. Hill, C. O'Mahony, R. Duane, A. Mathewson, *Performance and reliability of post-CMOS metal/oxide MEMS for RF application* J. Micromech. Microeng., vol. 13, no. 4, July 2003, pp. 131-138.

[65] R.A. Coutu, Jr, P.E. Kladitis, K.D. Leedy, R.L. Crane, *Selecting metal alloy electric contact materials for MEMS switches*, J. Micromech. Microeng., vol. 14, no. 8, Aug. 2004, pp. 1157-1164.

[66] X. Rottenberg, S. Brebels, B. Nauwelaers, W. De Raedt, H.A.C. Tilmans, *RF-Power: driver for electrostatic RF-MEMS devices*, J. Micromech. Microeng., vol. 14, no. 9, 2004, pp. 43-48.

[67] J. De Coster, H.A.C. Tilmans, J.T.M. van Beek, Th.G.S.M. Rijks, R. Puers, *The influence of mechanical shock on the operation of electrostatically driven RF-MEMS switches*, J. Micromech. Microeng., vol. 14, no. 9, Sept. 2004, pp. 49-54.

[68] A.Q. Liu, M. Tang, A. Agarwal, A. Alphones, *Low-loss lateral micromachined switches for high frequency applications*, J. Micromech. Microeng. vol. 15, no. 1, Jan. 2005, pp. 157-167.

[69] P.G. Steeneken, Th.G.S.M. Rijks, J.T.M. van Beek, M.J.E. Ulenaers, J. De Coster, R. Puers, *Dynamics and squeeze film gas damping of a capacitive RF MEMS switch*, J. Micromech. Microeng. vol. 15, no. 1, Jan. 2005, pp. 176-184.

[70] L. Kogut, *The influence of surface topography on the electromechanical characteristics of parallel-plate MEMS capacitors*, J. Micromech. Microeng., vol. 15, no. 5. May 2005, pp. 1068-1075.

[71] A. Jourdain, P. De Moor, K. Baert, I. De Wolf, H.A.C. Tilmans, *Mechanical and electrical characterization of BCB as a bond and seal material for cavities housing (RF-) MEMS devices*, J. Micromech. Microeng. vol. 15, no. 7, June 2005, pp. 89-96.

[72] X. Rottenberg, R.P. Mertens, B. Nauwelaers, W. De Raedt, H.A.C. Tilmans, *Filter-through device: a distributed RF-MEMS capacitive series switch*, J. Micromech. Microeng., vol. 15, no. 7, 2005, pp. 97-102.

[73] J.-M. Kim, S. Lee, J.-M.Kim, C.-W. Baek, Y. Kwon, Y.-K. Kim, *A mechanically reliable digital-type single crystalline silicon (SCS) RF MEMS variable capacitor*, J. Micromech. Microeng., vol. 15, no. 10, Oct. 2005, pp. 1854-1863.

[74] H.-C. Lee, J.-H. Park, J.-Y. Park, H.-J. Nam, J.-U. Bu, *Design, fabrication and RF performances of two different types of piezoelectrically actuated Ohmic MEMS switches*, J. Micromech. Microeng., vol. 15, no. 11, Nov. 2005, pp. 2098-2104.

[75] Th.G.S.M. Rijks, P.G. Steeneken, J.T.M. van Beek, M.J.E. Ulenaers, A. Jourdain, H.A.C. Tilmans, J. De Coster, R. Puers, *Microelectromechanical tunable capacitors for reconfigurable RF architectures*, J. Micromech. Microeng., vol. 16, no. 3, March 2006, pp. 601-611.

[76] E. Hamad, A. Omar, *An improved two-dimensional coupled electrostatic-mechanical model for RF MEMS switches*, J. Micromech. Microeng, vol. 16, no.7, 2006, pp. 1424-1429.

[77] J.-H. Park, H.-C. Lee, Y.-H. Park, Y.-D. Kim, C.-H. Ji, J. Bu, H.-J. Nam, *A fully wafer-level packaged RF MEMS switch with low actuation voltage using a piezoelectric actuator*, J. Micromech. Microeng., vol. 16, no. 11. Nov. 2006, pp. 2281-2286.

[78] X. Rottenberg, S. Brebels, P. Ekkels, P. Czarnecki, P. Nolmans, R.P. Mertens, B. Nauwelaers, R. Puers, I. De Wolf, W. De Raedt, H.A.C. Tilmans, *An electrostatic fringing-field actuator (EFFA)L applications towards a low-complexity thin-film RF-MEMS technology*, J. Micromech. Microeng., vol. 17, no. 7, 2007, pp. 204-210.

[79] O. Rezvanian, M.A. Zikry, C. Brown, J. Krim, *Surface roughness, asperity contact and gold RF MEMS switch behavior*, J. Micromech. Microeng., vol. 17, no. 10, Oct. 2007, pp. 2006-2015.

[80] A.B. Yu, A.Q. Liu, J. Oberhammer, Q.X. Zhang, H.M. Hosseini, *Characterization and optimization of dry releasing for the fabrication of RF MEMS capacitive switches*, J. Micromech. Microeng. vol. 17, no. 10, Oct. 2007, pp. 2024-2030.

[81] G. Klaasse, R. Puers, H.A.C. Tilmans, *Stress release structures for actuator beams with a stress gradient*, J. Micromech. Microeng., vol. 17, no. 10, Oct. 2007, pp. 2093-2101.

[82] A.M. Elshurafa, E.I. El-Masry, *The effects of non-uniform nanoscale deflections on capacitance on RF MEMS parallel-plate variable capacitors*, J. Micromech. Microeng., vol. 18, no. 4, April 2008.

[83] M. Esashi, *Wafer level packaging of MEMS*, J. Micromech. Microeng., vol. 18, no. 7, July 2008.

[84] C.T.-C. Nguyen, *Microelectromechanical Devices for Wireless Communications*, Proceedings of IEEE International Workshop on Micro Electro Mechanical Systems, MEMS, Jan. 1998, Heidelberg, Germany, pp. 1-7.

[85] H.A.C. Tilmans, E. Fullin, H. Ziad, M.D.J. Van de Peer, J. Kesters, E. Van Geffen, J. Bergqvist, M. Pantus, E. Beyne, K. Baert, F. Naso, *A fully-packaged electromagnetic microrelay*, Proceedings of IEEE International Conference on Micro Electro Mechanical Systems, MEMS, Jan. 1999, Orlando, FL, USA, pp. 25-30.

[86] J.Y. Park, G.H. Kim, K.W. Chung, J.U. Bu, *Electroplated RF MEMS Capacitive Switches*, Proceedings of IEEE International Conference on Micro Electromechanical Systems, MEMS, Jan. 2000, Miyazaki, Japan, pp. 639-644.

[87] V. Milanovic, M. Maharabiz, A. Singh, B. Warneke, Z. Ningning, H.K. Chan, K.S.J. Pister, *Microrelays for Batch Transfer Integration in RF Systems*, Proceedings of IEEE International Conference on Micro Electro Mechanical Systems, MEMS, Jan. 2000, Miyazaki, Japan, pp. 787-792.

[88] A. Jourdain, P. De Moor, S. Pamidighantam, H.A.C. Tilmans, *Investigation of the hermeticity of BCB-sealed cavities for housing (RF-)MEMS devices*, Proceedings of IEEE International Conference on Micro Electro Mechanical Systems, MEMS, Jan. 2002, Las Vegas, NV, USA, pp. 677-680.

[89] Y.-K. Park, H.-W. Park, D.-J. Lee, J.-H. Park, I.-S. Song, C.-W. Kim, C.-M. Song, Y.-H. Lee, C.-J. Kim, B.-K. Ju, *A Novel Low-Loss Wafer-Level Packaging of the RF-MEMS Devices*, Proceedings of IEEE International Conference on Micro Electro Mechanical Systems, MEMS, Jan. 2002, Las Vegas, NV, USA, pp. 681-684.

[90] Y.J. Ko, J.Y. Park, H.T. Kim, J.U. Bu, *Integrated Five-bit RF MEMS Phase Shifter for Satellite Broadcasting/Communication Systems*, Proceedings of IEEE International Conference on Micro Electro Mechanical Systems, MEMS, Jan. 2003, Kyoto, Japan, pp. 144-148.

[91] S. Frederico, C. Hibert, R. Fritschi, Ph. Fluckiger, Ph. Renaud, A.M. Ionescu, *Silicon Sacrificial Layer Dry Etching (SSLDE) for free-standing RF MEMS architectures*, Proceedings of IEEE International Conference on Micro Electro Mechanical Systems, MEMS, Jan. 2003, Kyoto, Japan, pp. 570-573.

[92] X. Rottenberg, S. Brebels, B. Nauwelaers, R.P. Mertens, W. De Raedt, H.A.C. Tilmans, *Modelling of the RF Self-Actuation of Electrostatic RF-MEMS Devices*, Proceedings of IEEE International Conference on Micro Electro Mechanical Systems, MEMS, Jan. 2004, Maastricht, The Netherlands, pp. 245-248.

[93] M. Innocent, P. Wambacq, H.A.C. Tilmans, W. Sansen, H. De Man, *Measurement of the nonlinear behavior of a MEMS variable capacitor*, Proceedings on IEEE International Conference of Micro Electro Mechanical Systems, MEMS, Jan. 2004, Maastricht, The Netherlands, pp. 773-776.

[94] N. Nishijima, J.-J. Hung, G.M. Rebeiz, *Parallel-Contact Metal-Contact RF-MEMS Switches for High Power Applications*, Proceedings of IEEE International Conference on Micro Electro Mechanical Systems, MEMS, Jan. 2004, Maastricht, The Netherlands, pp. 781-784.

[95] C.V. Jahnes, J. Cotte, J.L. Lund, H. Deliggianni, A. Chinthakindi, L.P. Buchwalter, P. Fryer, J.A. Tornello, N. Hoivik, J.H. Magerlein, D. Seeger, *Simultaneous Fabrication of RF MEMS Switches and Resonators using Copper-based CMOS Interconnect Manufacturing Methods*, Proceedings of IEEE International Conference on Micro Electro Mechanical Systems, MEMS, Jan. 2004, Maastricht, The Netherlands, pp. 789-792.

[96] L. Que, K. Udeshi, J. Park, Y.B. Gianchandi, *A Bi-Stable Electro-Thermal RF Switch for High Power Applications*, Proceedings of IEEE International Conference on Micro Electro Mechanical Systems, MEMS, Jan. 2004, Maastricht, The Netherlands, pp.797-800.

[97] A. Jourdain, K. Vaesen, J. Scheer, W. Weekamp, J. van Beek, H.A.C. Tilmans, *From zero- to second-level packaging of RF-MEMS devices*, Proceedings of IEEE International Conference on Micro Electro Mechanical Systems, MEMS, Jan. 2005, Miami, FL, USA, pp. 36-39.

[98] X. Rottenberg, K. Vaesen, S. Brebels, B. Nauwelaers, R.P. Mertens, W. De Raedt, H.A.C. Tilmans, *MEMS Capacitive Series Switches: Optimal Test Vehicles for the RF Self-Biasing Phenomenon*, Proceedings of IEEE International Conference on Micro Electro Mechanical Systems, MEMS, Jan. 2005, Miami, FL, USA, pp. 147-150.

[99] Y. Shi, S.-G. Kim, *A Lateral, Self-cleaning, Direct Contact MEMS Switch*, Proceedings of IEEE International Conference on Micro Electro Mechanical Systems, MEMS, Jan. 2005, Miami, FL, USA, pp. 195-198.

[100] R.W. Moseley, E.M. Yeatman, A.S. Holmes, R.R.A. Syms, A.P. Finlay, P. Boniface, *Laterally Actuated, Low Voltage, 3-Port RF MEMS Switch*, Proceedings of IEEE International Conference on Micro Electro Mechanical Systems, MEMS, Jan. 2006, Instabul, Turkey, pp. 878-881.

[101] S. Pranonsatit, G. Hong, A.S. Holmes, S. Lucyszyn, *Rotary RF MEMS Switch based of the Wobble Motor Principle*, Proceedings of IEEE International Conference on Micro Electro Mechanical Systems, MEMS, Jan. 2006, Instabul, Turkey, pp. 886-889.

[102] J.-H. Park, Y.-D. Kim, Y.-H. Park. H-C. Lee, H. Kwon, H.-J. Nam, J.-U. Bu, *Tunable Planar Inverted-F Antenna Using RF MEMS Switch for the Reduction of Human Hand Effect*, Proceedings of IEEE International Conference on Micro Electro Mechanical Systems, MEMS, Jan. 2007, Kobe, Japan, pp. 162-166.

[103] B. Pillans, F. Morris, P. Chahal, G. Frazier, J.-B. Lee, *Schottky Barrier Contact-Based RF MEMS Switch*, Proceedings of IEEE International Conference on Micro Electro Mechanical Systems, MEMS, Jan. 2007, Kobe, Japan, pp. 167-170.

[104] X. Rottenberg, P. Nolmans, P. Ekkels, P. Czarnecki, R.P. Mertens, B. Nauwelaers, I. De Wolf, W. De Raedt, H.A.C. Tilmans, *Electrostatic fringing-field actuator (EFFA): application towards a low-complexity RF-MEMS technology*, Proceedings of IEEE International Conference on Micro Electro Mechanical Systems, MEMS, Jan. 2007, Kobe, Japan, pp. 203-206.

[105] P. Ekkels, X. Rottenberg, R. Puers, H.A.C. Tilmans, *Surface micromachined platinum structures with a high thermal stability*, Proceedings of IEEE International Conference on Micro Electro Mechanical Systems, MEMS, Jan. 2007, Kobe, Japan, pp. 325-328.

[106] S. Kang, H.C. Kim, K. Chun, *Single Pole Four Throw RF MEMS Switch With Double Stop Comb Drive*, Proceedings of IEEE International Conference on Micro Electro Mechanical Systems, MEMS, Jan. 2008, Tucson, AZ, USA, pp. 1036-1039.

[107] J.Y. Park, G.H. Kim, K.W. Chung, J.U. Bu, *Monolithically integrated micromachined RF MEMS capacitive switches*, Sensors and Actuators A, vol. 89, no. 1-2, March 2001, pp. 88-94.

[108] Z. Feng, H. Zhang, K.C. Gupta, W. Zhang, V.M. Bright, Y.C. Lee, *MEMS-based series and shunt variable capacitors for microwave and milimeter-wave frequencies*, Sensors and Actuators A, vol. 91, no. 3, July 2001, pp. 256-265.

[109] J.-M. Huang, A.Q. Liu, C. Lu, J. Ahn, *Mechanical characterization of micromachined capacitive switches: design consideration and experimental verification*, Sensors and Actuators A, vol. 108, no. 1-3, Nov. 2003, pp. 36-48.

[110] J.-M. Sallese, P. Fazan, *Switch and RF ferroelectric MEMS: a new concept*, Sensors and Actuators A, vol. 109, no. 3, Jan. 2004, pp. 186-194.

[111] H. Nieminen, J. Hyyrylainen, T. Veijola, T. Ryhanen, V. Ermolov, *Transient capacitance measurement of MEM capacitor*, Sensors and Actuators A, vol. 117, no. 2, Jan. 2005, pp. 267-272.

[112] A.B. Yu, A.Q. Liu, Q.X. Zhang, A. Alphones, L. Zhu, A.P. Shacklock, *Improvement of isolation for MEMS capacitive switch via membrane planarization*, Sensors and Actuators A, vol. 119, no. 1, March 2005, pp. 206-213.

[113] M. Tang, A.B. Yu, A.Q. Liu, A. Agarwal, S. Aditya, Z.S. Liu, *High isolation X-band MEMS capacitive switches*, Sensors and Actuators A, vol. 120, no. 1, April 2005, pp. 241-248.

[114] M. Tang, A.-Q. Liu, A. Agarwal, Z.-S. Liu, C. Lu, *A single-pole double-throw (SPDT) circuit using lateral metal-contact micromachined switches*, Sensors and Actuators A, vol. 121, no. 1, May 2005, pp. 187-196.

[115] K. Rangra, B. Margesin, L. Lorenzelli, F. Giacomozzi, C. Collini, M. Zen, G. Soncini, L. del Tin, R. Gaddi, *Symmetric toggle switch - a new type of rf MEMS switch for telecommunication applications: Design and fabrication*, Sensors and Actuators A, vol. 123-124, Sept. 2005, pp. 505-514.

[116] G. Cusmai, M. Mazziani, P. Rossi, C. Combi, B. Vigna, F. Svelto, *A simple lumped electrical model for an RF MEMS switch considering lossy substrate effects*, Sensors and Actuators A, vol. 123-124, Sept. 2005, pp. 525-521.

[117] J. De Coster, H.A.C. Tilmans, J.M.J. den Toonder, J.T.M. van Beek, Th.G.S.M. Rijks, P.G. Steeneken, R. Puers, *Empirical and theoretical characterisation of electrostatically driven MEMS structures with stress gradients*, Sensors and Actuators A, vol. 123-124, Sept. 2005, pp. 555-562.

[118] A.B. Yu, A.Q. Liu, Q.X. Zhang, A. Alphones, H.M. Hosseini, *Micromachined DC contact capacitive switch on low-resistivity silicon substrate*, Sensors and Actuators A, vol. 127, no. 1, Feb. 2006, pp. 24-30.

[119] M. Ylonen, T. Vaha-Keikkila, K. Kattelus, *Amorphous metal alloy based MEMS for RF applications*, Sensors and Actuators A, vol. 132, no. 1. Nov. 2006, pp. 283-288.

[120] T. Seki, Y. Uno, K. Narise, T. Masuda, K. Inoue, S. Sato, F. Sato, K. Imanaka, S. Sugiyama, *Development of a large-force low-loss metal-contact RF MEMS switch*, Sensors and Actuators A, vol. 132, no. 2, Nov. 2006, pp. 683-688.

[121] J.-M. Sallese, D. Bouvet, *Principles of space-charge based bi-stable MEMS: The junction-MEMS*, Sensors and Actuators A, vol. 133, no. 1, Jan. 2007, pp. 173-179.

[122] H. Sumali, J.E. Massad, D.A. Czaplewski, C.W. Dyck, *Waveform design for pulse-and-hold electrostatic actuation in MEMS*, Sensors and Actuators A, vol. 134, no. 1, Feb. 2007, pp. 213-220.

[123] C.F. Herrmann, F.W. DelRio, D.C. Miller, S.M. George, V.M. Bright, J.L. Ebel, R.E. Strawse, R. Cortez, K.D. Leedy, *Alternative dielectric films for RF MEMS capacitive switches deposited using atomic layer deposited Al2O3/ZnO alloys*, Sensors and Actuators A, vol. 135, no. 1, March 2007, pp. 262-272.

[124] Y.-T. Song, H.-Y. Lee, M. Esashi, *A corrugated bridge of low residual stress for RF-MEMS switch*, Sensors and Actuators A, vol. 135, no. 2, April 2007, pp. 818-826.

[125] H.-C. Lee, J.-H. Park, Y.-H. Park, *Development of shunt type ohmic RF MEMS switches actuated by piezoelectric cantilever*, Sensors and Actuators A, vol. 136, no. 1, May 2007, pp. 282-290.

[126] Y. Zhang, J. Lu, K. Onodera, R. Maeda, *Development of hafnium oxynitride dielectrics for radio-frequency-microelectromechanical system capacitive switches*, Sensors and Actuators A, vol. 139, no. 1-2, Sept. 2007, pp. 337-342.

[127] J. Tian, S. Sosin, J. Iannacci, R. Gaddi, M. Bartek, *RF-MEMS wafer-level packaging using through-wafer interconnect*, Sensors and Actuators A, vol. 142, no. 1, March 2008, pp. 442-451.

[128] S.C. Saha, H. Sagberg, E. Poppe, G.U. Jensen, T.A. Fjedly, T. Saether, *Tuning of resist slope with hard-baking parameters and release methods for extra hard photoresist for RF MEMS switches*, Sensors and Actuators A, vol. 143, no. 2, May 2008, pp. 452-461.

[129] M. Shavezipur, K. Ponnambalam, A. Khajepour, S.M. Hashemi, *Fabrication uncertainties and yield optimization in MEMS tunable capacitors*, Sensors and Actuators A, vol. 147, no. 2, Oct. 2008, pp. 613-622.

[130] S. Seok, N. Rolland, P.-A. Rolland, *A novel packaging method using wafer-level BCB polymer bonding and glass wet-etching for RF applications*, Sensors and Actuators A, vol. 147, no. 2, Oct. 2008, pp. 677-682.

[131] C. Goldsmith, T.-H. Lin, B. Powers, W.-R. Wu, B. Norvell, *Micromechanical Membrane Switches for Microwave Applications*, IEEE MTT-S International Microwave Symposium Digest, May 1995, Orlando, FL, USA, vol. 1, pp. 91-94.

[132] S.P. Pacheco, L.P.B. Katehi, C.T.-C. Nguyen, *Design of Low Actuation Voltage RF MEMS Switch*, IEEE MTT-S International Microwave Symposium Digest, June 2000, Boston, MA, USA, vol. 1, pp. 165-168.

[133] D. Peroulis, S. Pacheco, K. Sarabandi, L.P.B. Katehi, *MEMS Devices for High Isolation Switching and Tunable Filtering*, IEEE MTT-S International Microwave Symposium Digest, June 2000, Boston, MA, USA, vol. 2, pp. 1217-1220.

[134] Y.A. Wang, Q. Kang, B. Liu, A.M. Ferendeci, M. Mah, *Interlayer MEMS RF Switch for 3D MMICs*, IEEE MTT-S International Microwave Symposium Digest, June 2000, Boston, MA, USA, vol. 2, pp. 1245-1248.

[135] D. Mercier, P. Blondy, D. Cros, P. Guillon, *An Electromechanical Model for MEMS Switches*, IEEE MTT-S International Microwave Symposium Digest, May 2001, Phoenix, AZ, USA, vol. 3, pp. 2123-2126.

[136] B. Schauwecker, K.M. Strohm, W. Simon, J. Mehner, J.-F. Luy, *Toggle-Switch - A new type of RF MEMS switch for power applications*, IEEE MTT-S International Microwave Symposium Digest, June 2002, Seattle, WA, USA, vol. 1, pp. 219-222.

[137] D. Peroulis, K. Sarabandi, L.P.B. Katehi, *Low Contact Resistance Series MEMS Switches*, IEEE MTT-S International Microwave Symposium Digest, June 2002, Seattle, WA, USA, vol. 1, pp. 223-226.

[138] C.H. Chang, J.Y. Qian, B.A. Cetiner, Q. Xu, M. Bachman, H.K. Kim, Y. Ra, F. De Flaviis, G.P. Li, *RF MEMS Capacitive Switches Fabricated with HDICP CVD SiNx*, IEEE MTT-S International Microwave Symposium Digest, June 2002, Seattle, WA, USA, vol. 1, pp. 231-234.

[139] B. Pillans, J. Kleber, C. Goldsmith, M. Eberly, *RF Power Handling of Capacitive RF MEMS Devices*, IEEE MTT-S International Microwave Symposium Digest, June 2002, Seattle, WA, USA, vol. 1, pp. 329-332.

[140] H.-T. Kim, J.-H. Park, Y.-K. Kim, Y. Kwon, *V-Band Low-Loss and Low-Voltage Distributed MEMS Digital Phase Shifter Using Metal-Air-Metal Capacitors*, IEEE MTT-S International Microwave Symposium Digest, June 2002, Seattle, WA, USA, vol. 1, pp. 341-344.

[141] T. Veijola, T. Tinttunen, H. Nieminen, V. Ermolov, T. Ryhanen, *Gas Damping Model for a RF MEM Switch and its Dynamic Characteristics*, IEEE MTT-S International Microwave Symposium Digest, June 2002, Seattle, WA, USA, vol. 2, pp. 329-332.

[142] J.B. Rizk, G.M. Rebeiz, *Digital-Type RF MEMS Switched Capacitors*, IEEE MTT-S International Microwave Symposium Digest, June 2002, Seattle, WA, USA, vol. 2, pp. 1217-1220.

[143] D. Balaraman, S.K. Bhattacharya, F. Ayazi, J. Papapolymerou, *Low-Cost Low Actuation Voltage Copper RF MEMS Switches*, IEEE MTT-S International Microwave Symposium Digest, June 2002, Seattle, WA, USA, vol. 2, pp. 1225-1228.

[144] Y.J. Ko, J.Y. Park, J.U. Bu, *Integrated RF MEMS Phase Shifters with Constant Phase Shift*, IEEE MTT-S International Microwave Symposium Digest, June 2003, Philadelphia, PA, USA, vol. 3, pp. 1489-1492.

[145] G. Wang, S. Barstow, A. Jeyakumar, J. Papapolymerou, C. Henderson, *Low Cost RF MEMS Switches Using Photodefinable Mixed Oxide Dielectrics*, IEEE MTT-S International Microwave Symposium Digest, June 2003, Philadelphia, PA, USA, vol. 3, pp. 1633-1636.

[146] S. Majumder, J. Lampen, R. Morrison, J. Maciel, *A Packaged, High-Lifetime Ohmic MEMS RF Switch*, IEEE MTT-S International Microwave Symposium Digest, June 2003, Philadelphia, PA, USA, vol. 3, pp. 1935-1938.

[147] P. Blondy, A. Crunteanu, C. Champeaux, A. Catherinot, P. Tristant, O. Vendier, J.L. Cazaux, L. Marchand, *Dielecric Less Capacitive MEMS Switches*, IEEE MTT-S International Microwave Symposium Digest, June 2004, Fort Worth, TX, USA, vol. 2, pp. 573-576.

[148] R.G. Polcawich, D. Judy, J.S. Pulskamp, S. Trolier-McKinstry, M. Dubey, *Advances in Piezoelectrically Actuated RF MEMS Switches and Phase Shifters*, IEEE MMT-S International Microwave Symposium Digest, June 2007, Honolulu, HI, USA, pp. 2083-2086.

[149] J. De Coster, H.A.C. Tilmans, J.T.M. van Beek, Th.G.S.M. Rijks, P.G. Steeneken, *Operation of RF MEMS switches and relays in shock environment*, Proceedings of Workshop on MEMS for MilimeterWave Communications, MEMSWAVE, June 2004, Uppsala, Sweden, pp. F6-F9.

[150] L. Petit, P. Panaia, C. Luxey, G. Jacquemod, R. Staraj, L. Dussopt, J.-M. Laheurte, *MEMS-Switched Reconfigurable antennas*, Proceedings of International Conference on RF MEMS and RF Microsystems, MEMSWAVE, June 2005, Lausanne, Switzerland, pp. 31-34.

[151] D. Girbau, N. Otegi, A. Lazaro, L. Pradell, *Origin and effects of intermodulation on RF MEMS capacitors*, Proceedings of International Conference on RF MEMS and RF Microsystems, MEMSWAVE, June 2005, Lausanne, Switzerland, pp. 45-48.

[152] C. Palego, A. Pothier, P. Blondy, *High-power MEMS Varactors*, Proceedings of International Conference on RF MEMS and RF Microsystems, MEMSWAVE, June 2005, Lausanne, Switzerland, pp. 67-70.

[153] G. Klaasse, R. Puers, H.A.C. Tilmans, *Stress and stress gradient compensation technique for MEM actuators*, Proceedings of Workshop on MEMS for MilimeterWave Communications, MEMSWAVE, June 2005, Lausanne, Switzerland, pp. 157-160.

[154] P. Farinelli, A. Ocera, B. Margesin, F. Giacomozzi, R. Sorrentino, *High Performance RF-MEMS cantilever switch*, Proceeding of International Conference of RF MEMS and RF Microsystems, MEMSWAVE, June 2006, Orvieto, Italy, pp. 88-91.

[155] A. Ferrari, S. Catoni, R. Marcelli, G. Bartolucci, *Analog and Digital RF MEMS Variable Capacitors*, Proceeding of International Conference of RF MEMS and RF Microsystems, MEMSWAVE, June 2006, Orvieto, Italy, pp. 92-95.

[156] G.J. Papaioannou, F. Giacomozzi, E. Papandreou, B. Margesin, *Alpha Particle Radiation Effects in RF-MEMS switches*, Proceeding of International Conference of RF MEMS and RF Microsystems, MEMSWAVE, June 2006, Orvieto, Italy, pp. 99-102.

[157] H.I. Atasoy, K. Topalli, M. Unlu, I. Istanbulluoglu, E.U. Temocin, O. Bayaraktar, S. Demir, O.A. Civi, S. Koc, T Akin, *Metal-to-Metal and Capacitive Contact RF MEMS Shunt Switch Structures*, Proceeding of International Conference of RF MEMS and RF Microsystems, MEMSWAVE, June 2006, Orvieto, Italy, pp. 154-156.

[158] T. Vaha-Heikkila, M. Ylonen, *Highly Reliable Wideband Switched MEMS Capacitors*, Proceeding of International Conference of RF MEMS and RF Microsystems, MEMSWAVE, June 2006, Orvieto, Italy, pp. 172-174.

[159] M. Sterner, N. Roxhed, G. Stemme, J. Oberhammer, *Deep-reactive-ion-etched 3D transmission lines with integrated mechanically multi-stable SPST and SPDT RF MEMS switches*, Proceeding of International Symposium of RF MEMS and RF Microsystems, MEMSWAVE, June 2007, Barcelona, Spain, pp. 21-24.

[160] A. Stehle, V. Ziegler, B. Schonlinner, U. Prechtel, H. Seidel, U. Schmid, *RF MEMS Switch for W-Band Applications*, Proceeding of International Symposium of RF MEMS and RF Microsystems, MEMSWAVE, June 2007, Barcelona, Spain, pp. 25-28.

[161] M. El Khatib, A. Pothier, A. Crunteanu, O. Vendier, J.L. Cazaux, P. Blondy, *An Improved Reliability Switching Network Design based on DC Contact MEMS Switches dedicated to Switching Matrix Applications*, Proceeding of International Symposium of RF MEMS and RF Microsystems, MEMSWAVE, June 2007, Barcelona, Spain, pp. 35-37.

[162] S. Hebib, H. Aubert, O. Pascal, N.J.G. Fonseca, L. Ries, J.-M.E. Lopes, *Pyramidal Circularly Polarized Antenna with RF-MEMS Switches for Frequency Flexibility*, Proceeding of International Symposium of RF MEMS and RF Microsystems, MEMSWAVE, June 2007, Barcelona, Spain, pp. 59-61.

[163] G. Lissorgues, F. Flourens, A. Phommahaxay, F. Marty, L. Rousseau, C. Papon, P. Nicole, T. Dousset, *A Dual-Gap Tunable RF-MEMS Capacitor for Reflect Array Applications*, Proceeding of International Symposium of RF MEMS and RF Microsystems, MEMSWAVE, June 2007, Barcelona, Spain, pp. 71-74.

[164] A.K. Skriverik, J. Perruisseau-Carrier, *MEMS Reconfigurable Antennas*, Proceeding of International Symposium of RF MEMS and RF Microsystems, MEMSWAVE, June 2007, Barcelona, Spain, pp. 105-108.

[165] T. Prodromakis, C. Papavassiliou, K. Michelakis, *A Ka-Band True-Delay-Line Phase Shifter using Capacitive MEMS Switches*, Proceeding of International Symposium of RF MEMS and RF Microsystems, MEMSWAVE, June 2008, Heraklion, Grecee.

[166] M. Fernandez-Bolanos, P. Dainesi, A.M. Ionescu, *High-Isolation Shunt-Series MEMS Switch for a Wide Frequency Range (6-40GHz)*, Proceeding of International Symposium of RF MEMS and RF Microsystems, MEMSWAVE, June 2008, Heraklion, Grecee.

[167] K.M. Hiltmann, B. Schmidt, H. Sandmaier, W. Land, *Development of Micromachined Switches with Increased Reliability*, Proceedings of International Conference on Solid-State Sensors and Actuators, TRANSDUCERS, June 1997, Chicago, IL, USA, vol.2, pp. 1157-1160

[168] T. Veijola, T. Mattila, *Compact Squeezed-Film Damping Model for Perforated Surface*, Proceedings of International Solid-State Sensors, Actuators and Microsystems Conference, TRANSDUCERS, June 2001, Munich, Germany, pp. 1506-1509.

[169] T. Seki, S. Sato, T. Masuda, I. Kimura, K. Imanaka, *Low-Loss RF MEMS Metal-to-metal Contact Switch with CSP Structure*, Proceedings of International Conference on Solid State Sensors, Actuators and Microsystems, TRANSDUCERS, Boston, MA, USA, June 2003, vol. 1, pp. 340-341.

[170] R.L. Borwick III, P.A. Stupar, J. DeNatale, *A Hybrid Approach To Low-Voltage MEMS Switches*, Proceedings of International Conference on Solid-State Sensors, Actuators and Microsystems, TRANSDUCERS, June 2003, Boston, MA, USA, vol. 1, pp. 859-862.

[171] P. Ericsson, M. Hedstrom, A. Olsson, A Scholes, J. Svennebrink, C. Vieider, B. Wenk, *MEMS Switches and Other RF Components Fabricated Using CMOS Postprocess Compatible Surface Micromachining*, Proceedings of International Conference on Solid State Sensors, Actuators and Microsystems, TRANSDUCERS, June 2003, Boston, MA, USA, vol. 1, pp. 895-898.

[172] J.-M. Kim, S. Lee, J.-H. Park, C.-W. Baek, Y. Kwon, Y.-K. Kim, *A 5-17 GHz Wideband Reflection-Type Phase Shifter Using Digitally Operated Capacitive MEMS Switches*, Proceedings of International Conference on Solid State Sensors, Actuators and Microsystems, TRANSDUCERS, June 2003, Boston, MA, USA, vol. 1, pp. 907-910.

[173] Ph. Robert, D. Saias, C. Billard, S. Boret, N. Sillon, C. Maeder-Pachurka, P.L. Charvet, G. Bouche, P. Ancey, P. Berruyer, *Integrated RF-MEMS Switch Based on a Combination of Thermal and Electrostatic Actuation*, Proceedings of International Conference on Solid State Sensors, Actuators and Microsystems, TRANSDUCERS, Boston, MA, USA, June 2003, vol. 2, pp. 1714-1717.

[174] K. Suzuki, Y. Neav, *Silicon MEMS Micro-Switch with Charge-Induced Retention*, Proceedings of International Conference on Solid State Sensors, Actuators and Microsystems, TRANSDUCERS, June 2003, Boston, MA, USA, vol. 2, pp. 1718-1721.

[175] G.M. Rebeiz, *RF MEMS Switches: Status of the Technology*, Proceedings of International Conference on Solid State Sensors, Actuators and Microsystems, TRANSDUCERS, June 2003, Boston, MA, USA, vol. 2, pp. 1726-1729.

[176] A. Jourdain, X. Rottenberg, G. Carchon, H.A.C. Tilmans, *Optimization of 0-level Packaging for RF-MEMS Devices*, Proceedings of International Conference on Solid State Sensors, Actuators and Microsystems, TRANSDUCERS, June 2003, Boston, MA, USA, vol. 2, pp. 1915-1918.

[177] J.J. Yao, M.F. Chang, *A Surface Micromachined Miniature Switch for Telecommunications Applications with Signal Frequencies from DC up to 4 GHz*, Proceedings of International Conference on Solid-State Sensors, Actuators and Microsystems, TRANSDUCERS, June 2005, Stockholm, Sweden, vol. 2, pp. 384-387.

[178] K. Segueni, A.-S. Rollier, L. Le Garrec, R. Robin, S. Touati, A. Kanciurzewski, L. Buchaillot, O. Millet, *A Totally Free Flexible Membrane: A Design For Low Electrostatic Actuation MEMS*, Proceedings of International Conference on Solid-State Sensors, Actuators and Microsystems, TRANSDUCERS, June 2007, Lyon, France, pp. 461-464.

[179] X. Rottenberg, P. Ekkels, S. Brebels, T. Webers, P. Czarnecki, R.P. Mertens, B. Nauwelaers, R. Puers, L. Marchand, I. De Wolf, W. De Raedt, H.A.C. Tilmans, *Novel EFFA-based thin-film RF-MEMS technology*, Proceedings of International Conference on Solid-state Sensors, Actuators and Microsystems, TRANSDUCERS, June 2007, Lyon, France, pp. 145-148.

[180] H.A.C. Tilmans, *MEMS components for wireless communications*, Proceedings of Eurosensors, Sept. 2002, Prague, Chech Republic, pp. 1-34.

[181] J. De Coster, H.A.C. Tilmans, J.T.M. van Beek, Th.G.S.M. Rijks, P.G. Steeneken, R. Puers, *A general and simplified method for rapid evolution of electrostatic switches with varying geometries*, Technical Digest of Eurosensors, Sept. 2004, Rome, Italy, pp. 502-503.

[182] H.A.C. Tilmans, *RF-MEMS: an enabling technology for reconfigurable wireless communication systems*, Proceedings of Eurosensors, Sept. 2006, Goteborg, Sweden, pp. 330-331.

[183] P. Zavracky, S. Majumder, N.E. McGruer, *Micromechanical Switches Fabricated Using Nickel Surface Micromachining*, Journal of Microelectromechanical Systems, JMEMS, vol. 6, no. 1, Mar 1997, pp. 3-9.

[184] J.-H. Park, H.-T. Kim, W. Choi, Y. Kwon, U.-K. Kim, *V-Band Reflection-Type Phase Shifters Using Micromachined CPW Coupler and RF Switches*, Journal of Microelectromechanical Systems, JMEMS, vol. 11, no. 6, Dec. 2002, pp. 808-814.

[185] R. Chan, R. Lesnick, D. Becher, M. Feng, *Low-Actuation Voltage RF MEMS Shunt Switch With Cold Switching Lifetime of Seven Billion Cycles*, Journal of Microelectromechanical Systems, JMEMS, vol. 12, no. 5, Oct. 2003, pp. 713-719.

[186] H.D. Nguyen, D. Hah, P.R. Patterson, R. Chao, W. Piyawattanametha, E.K. Lau, M.C. Wu, *Angular Vertical Comb-Driven Tunable Capacitor With High-Tuning Capabilities*, Journal of Microelectromechanical SyStems, JMEMS, vol. 13, no. 3, June 2004, pp. 406-413.

[187] Y. Wang, Z. Li, D.T. McCornick, N.C. Tien, *A Low-Voltage Lateral MEMS Switch With High RF Performance*, Journal of Microelectromechanical Systems, JMEMS, vol. 13, no. 6, Dec. 2004, pp. 902-911.

[188] W.-B. Zheng, Q.-A. Huang, X.-P. Liao, F.-X. Li, *RF MEMS Membrane Switches on GaAs Substrates for X-Band Applications*, Journal of Microelectromechanical Systems, JMEMS, vol. 14, no. 3, June 2005, pp. 464-471.

[189] D.A. Czaplewski, C.W. Dyck, H. Sumali, J.E. Massad, J.D. Kuppers, I. Reines, W.D. Cowan, C.P. Tigges, *A Soft-Landing Waveform for Actuation of a Single-Pole Single-Throw Ohmic RF MEMS Switch*, Journal of Microelectromechanical Systems, JMEMS, vol. 15, no. 6, Dec. 2006, pp. 1586-1594.

[190] S. Pranonsatit, A.S. Holmes, I.D. Robertson, S. Lucyszyn, *Single-Pole Eight-Throw RF MEMS Rotary Switch*, Journal of Microelectromechanical Systems, JMEMS, vol. 15, no. 6, Dec. 2006, pp. 1735-1744.

[191] K.D. Leedy, R.E. Strawser, R. Cortex, J.L. Ebel, *Thin-Film Encapsulated RF MEMS Switches*, Journal of Microelectromechanical Systems, JMEMS, vol. 16, no. 2, April 2007, pp. 304-309.

[192] D. Girbau, L. Pradell, A. Lazaro, A. Nebot, *Electrothermally Actuated RF MEMS Switches Suspended on a Low-Resistivity Substrate*, Journal of Microelectromechanical Systems, JMEMS, vol. 16, no. 5, Oct. 2007, pp. 1061-1070.

[193] E.R. Brown, *RF-MEMS Switches for Reconfigurable Integrated Circuits*, IEEE Transactions on Microwave Theory and Techniques, vol. 46, no. 11, Nov. 1998, pp. 1868-1880.

[194] N.S. Barker, G.M. Rebeiz, *Distributed MEMS True-Time Delay Phase Shifters and Wide-Band Switches*, IEEE Transactions on Microwave Theory and Techniques, vol. 46, no. 11, Nov. 1998, pp. 1881-1890.

[195] A. Dec, K. Suyama, *Micromachined electro-mechanically tunable capacitors and their applications to RF IC's*, IEEE Transactions on Microwave Theory and Techniques, vol. 46, no. 12, December 1998, pp. 2587-2596.

[196] J.B. Muldavin, G.M. Rebeiz, *High-Isolation CPW MEMS Shunt Switches - Part 1: Modeling*, IEEE Transactions on Microwave Theory and Techniques, vol. 48, no. 6, June 2000, pp. 1045-1052.

[197] J.B. Muldavin, G.M. Rebeiz, *High-Isolation CPW MEMS Shunt Switches - Part 2: Design*, IEEE Transactions on Microwave Theory and Techniques, vol. 48, no. 6, June 2000, pp. 1052-1056.

[198] D. Hah, E. Yoon, S. Hong, *A Low-Voltage Actuated Micromachined Microwave Switch Using Torsion Springs and Leverage*, IEEE Transactions of Microwave Theory and Techniques, vol. 48, no. 12, Dec. 2000, pp. 2540-2545.

[199] L. Dussopt, G.M. Rebeiz, *Intermodulation Distortions and Power Handling in RF MEMS Switches, Varactors, and Tunable Filters*, IEEE Transactions on Microwave Theory and Techniques, vol. 51, no. 4, Aprlil 2003, pp. 1247-1256.

[200] B. Schoenlinner, A. Abbaspour-Tamijani, L.C. Kempel, G.M. Rebeiz, *Switchable Low-Loss RF MEMS Ka-Band Frequency-Selective Surface*, IEEE Transactions on Microwave Theory and Techniques, vol. 51, no. 11, Nov. 2004, pp. 2474-2481.

[201] B. Lacroix, A. Pothier, A. Crunteanu, C. Cibert, F. Dumas-Bouchiat, C. Champeaux, A. Catherinot, P. Blondy, *Sub-Microsecond RF MEMS Switched Capacitors*, IEEE Transactions on Microwave Theory and Techniques, vol. 55, no. 6, June 2007, pp. 1314-1321.

[202] J. Muldavin, C.O. Bozler, S. Rabe. P.W. Wyatt, C.L. Keast, *Wafer-Scale Packaged RF Microelectromechanical Switches*, IEEE Transactions on Microwave Theory and Techniques, vol. 56, no. 2, Feb. 2008, pp. 522-529.

[203] H.A.C. Tilmans, W. De Raedt, E. Beyne, *MEMS for wireless communications: "From RF-MEMS components to RF-MEMS-SiP"*, Journal of Micromechanics and Microengineering, JMM, vol. 13, no. 4, June 2003, pp. 139-163.

[204] X. Rottenberg, S. Brebels, W. De Raedt, B. Nauwelaers, H.A.C. Tilmans, *RF-power, driver for electrostatic RF-MEMS devices*, Proceedings of MicroMechanics Europe Workshop, MME, Nov. 2003, Delft, The Netherlands, pp. 65-68.

[205] X. Rottenberg, R.P. Mertens, B. Nauwelaers, W. De Raedt, H.A.C. Tilmans, *Switched filter-through RF-MEMS device used as an improved series capacitive switching device*, Proceedings on MicroMechanics Europe Workshop, MME, Sept. 2004, Leuven, Belgium, pp. 241-244.

[206] A. Jourdain, P. De Moor, H.A.C. Tilmans, *Mechanical and electrical characterization of BCB as a bond and seal material for cavities housing (RF-)MEMS devices*, Proceedings of MicroMechanics Europe Workshop, MME, Sept. 2004, Leuven, Belgium, pp. 167-170.

[207] J. De Coster, H.A.C. Tilmans, J.T.M. van Beek, Th.G.S.M. Rijks, P.G. Steeneken, R. Puers, *Parametric modeling of an RF MEMS switch subjected to mechanical shock*, Proceedings of MicroMechanics Europe Workshop, MME, Sept. 2004, Leuven, Belgium, pp. 253-256.

[208] P. Ekkels, R. Puers, H.A.C. Tilmans, *Platinum membrane and polyimide sacrificial layer technology for RF-MEMS*, Proceedings of MicroMechanics Europe Workshop, MME, Sept. 2005, Goteborg, Sweden, pp. 84-87.

[209] J. De Coster, H.A.C. Tilmans, P.G. Steeneken, R. Puers, *The influence of gas damping on the harmonic and transient response of MEMS devices*, Proceedings of MicroMechanics Europe Workshop, MME, Sept. 2005, Goteborg, Sweden, pp. 300-303.

[210] W.H. Weedon, W.J. Payne, G.M. Rebeiz, *MEMS-Switched Reconfigurable Antennas*, Proceedings of IEEE Antennas and Propagation Society International Symposium, July 2001, vol. 3, pp. 654-657.

[211] J.H. Schaffner, D.F. Sievenpiper, R.Y. Loo, J.J. Lee, S.W. Livingston, *A Wideband Beam Switching Antenna Using RF MEMS Switches*, Proceedings of IEEE Antennas and Propagation Society International Symposium, July 2001, vol. 3, pp. 658-661.

[212] D. Anagnostou, M.T. Chryssomallis, J.C. Lyke, C.G. Christodoulou, *Re-configurable Sierpinski Gasket Antenna using RF-MEMS Switches*, Proceedings of IEEE Antennas and Propagation Society International Symposium, June 2003, Columbus, OH, USA, vol. 1, 375-378.

[213] R. Ramadoss, S. Lee, V.M. Bright, Y.C. Lee, K.C. Gupta, *RF MEMS Capacitive Switches for Integration with Printed Circuits Antennas*, Proceedings of IEEE Antennas and Propagation Society International Symposium, June 2003, Columbus, OH, USA, vol. 1, 395-398.

[214] M.C. Scardelletti, C.A. Zorman, D.R. Oldham, *RF MEMS Switches with SiC Microbridges for Improved Reliability*, Proceedings of IEEE Antennas and Propagation Society International Symposium, July 2008, San Diego, CA, USA, pp. 1-4.

[215] R.E. Mihailovich, M. Kim, J.B. Kacker, E.A. Sovero, J. Studer, J.A. Higgins, J.F. DeNatale, *MEM Relay for Reconfigurable RF Circuits*, IEEE Microwave and Wireless Components Letters, vol. 11, no. 2, Feb. 2001, pp. 53-55.

[216] M. Kim, J.B. Hacker, R.E. Mihailovich, J.F. DeNatale, *A Dc-to-40 GHz Four-Bit RF MEMS True-Time Delay Network*, IEEE Microwave and Wireless Components Letters, vol. 11, no. 2, Feb. 2001, pp. 56-58.

[217] J.B. Muldavin, G.M. Rebeiz, *Inline Capacitive and DC-Contact MEMS Shunt Switches*, IEEE Microwave and Wireless Components Letters, vol. 11, no. 8, Aug. 2001, pp. 334-336.

[218] G.-L. Tan, G.M. Rebeiz, *A DC-Contact MEMS Shunt Switch*, IEEE Microwave and Wireless Components Letters, vol. 12, no. 6, June 2002, pp. 212-214.

[219] H.-C. Lee, J.-Y. Park, J.-U. Bu, *Piezoelectrically Actuated RF MEMS DC Contact Switches With Low Voltage Operation*, IEEE Microwave and Wireless Components Letters, vol. 15, no. 4, April 2005, pp. 202-204.

[220] M. Tang, A. Agarwal, J. Li, Q.X. Zhang, P. Win, J.M. Huang, A.Q. Liu, *An Approach of Lateral RF MEMS Switch for High Performance*, Proceedings of Symposium on Design, Test, Integration and Packaging of MEMS/MOEMS, May 2003, Cannes, France, pp. 99-102.

[221] L. Lorenzelli, K. Rangra, C. Collini, F. Giacomozzi, B. Margesin, F. Pianegiani, *On-wafer electro-mechanical characterization of silicon MEMS switches*, Proceedings of Symposium on Design, Test, Integration and Packaging of MEMS/MOEMS, May 2003, Cannes, France, pp. 281-285

[222] T. Veijola, *Analytic Model for Perforated Squeezed-Film Dampers*, Proceedings of Symposium on Design, Test, Integration and Packaging of MEMS/MOEMS, April 2006, Lago Maggiore, Italy.

[223] A. Jourdain, H. Ziad, P. De Moor, H.A.C. Tilmans, *Wafer-scale 0-level packaging of (RF-)MEMS devices using BCB*, Proceedings of Symposium on Design, Test, Integration and Packaging of MEMS/MOEMS, May 2003, Cannes, France, pp. 239-244.

[224] R. Ramesham, R. Ghaffarian, *Challenges in Interconnection and Packaging of Micromechanical Systems (MEMS)*, Proceedings of Electronic Components and Technology Conference, May 2000, Las Vegas, NV, USA, pp. 666-675.

[225] L.-T. Hwang, L. Li, J. Drye, S.-M. Kuo, *Performance Evaluation of RF MEMS Packages*, Proceedings of IEEE Electronic Components and Technology Conference, May 2002, San Diego, CA, USA, pp. 1032-1036.

[226] W. Kim, Q. Wang, J. Hwang, M. Lee, K. Jung, S. Ham, C. Moon, K. Baek, B. Ha, I. Song, *A Low Temperature, Hermetic Wafer Level Packaging Method for RF MEMS Switch*, Proceedings of Electronic Components and Technology Conference, May 2005, Orlando, FL, USA, vol. 2, pp. 1103-1108.

[227] G. Carchon, A. Jourdain, O. Vendier, J. Schoebel, H.A.C. Tilmans, *Integration of 0/1-Level Packaged RF-MEMS Devices on MCM-D at Milimeter-Wave Frequencies*, Proceedings of Electronic Components and Technology Conference, May 2005, Orlando, FL, USA, pp. 1664-1669.

[228] H.A.C. Tilmans, W. De Raedt, H. Jansen, S. Pamidighantam, *RF-MEMS devices for space telecommunication*, 3rd Round Table on Micro/Nano-Technologies for Space, May 2000, Noordwijk, The Netherlands.

[229] H.A.C. Tilmans, X. Rottenberg, P. Soussan, P. Nolmans, P. Ekkels, P. Czarnecki, R. Modlinski, S. Stoukatch, A. Jourdain, B. Nauwelaers, K. Vaesen, G. Carchon, I. De Wolf, W. De Raedt, *Generic RF-MEMS technology platform for mobile and satellite communications*, 5th ESA-ESTEC Micro-Nano Technology Round Table, Oct. 2005, Noordwijk, The Netherlands.

[230] X. Rottenberg, O. DiMonaco, P. Fiorini, W. De Raedt, H.A.C. Tilmans, *RF-MEMS switching devices for space telecom application*, Proceedings of ESA-ESTEC Microwave Technology and Techniques Workshop, Oct. 2002, Noordwijk, The Netherlands, pp. 219-226.

[231] G. Carchon, X. Rottenberg, G. Posada, A. Jourdain, H.A.C. Tilmans, W. De Raedt, *MCM-D and RF-MEMS for Integrated Millimetre Wave Functions*, Proceedings of ESA Workshop on Millimetre Wave Technology and Applications: Circuits, Systems and Measurement Techniques, Esposo, Finland, pp. 485-490.

[232] L.X. Zhang, Y.-P. Zhao, *Electromechanical model of RF MEMS switches*, Microsystem Technologies, vol. 9, no. 6-7, Sept. 2003, pp. 420-426.

[233] C.-L. Dai, J.-H. Chen, *Low voltage actuated RF micromechanical switches fabricated using CMOS-MEMS technique*, Microsystem Technologies, vol. 12, no. 12, Oct. 2006, pp. 1143-1151.

[234] X.-L. Yuan, Q.-A. Huang, Z.-P. Liao, *Analysis of electromagnetic interference of a capacitive RF MEMS switch during switching*, Microsystem Technologies, Vol. 14, no. 3, March 2008, pp. 349-360.

[235] D.T. Haluzan, D.M. Klymyshyn, M. Borner, S. Achenbach, G. Wells, T. Mappes, J. Mohr, *Stiction issues and actuation of RF LIGA-MEMS variable capacitors*, Microsystem Technologies, vol. 14, no. 9-11, Oct. 2008, pp. 1709-1714.

[236] H.S. Newman, *RF MEMS Switches and Applications (INVITED)*, Proceedings of International Reliability Physics Symposium, April 2002, Dallas, TX, USA, pp. 111-115.

[237] P.J. van der Wel, J. Stulemeijer, J.A. Bielen, F.G.A. Theunis, A. den Dekker, M.A.J. van Gils, R.J. Havens, *Hermeticity testing of capacitive RF MEMS switches*, Proceedings of International Reliability Physics Symposium, April 2008, Phoenix, AZ, USA, pp. 691-692.

[238] J. Tsaur, K. Onodera, T. Kobayashi, M. Ichiki, R. Maeda, T. Suga, *Wideband and high reliability RF-MEMS switches using PZT/HfO2 multi-layers high k dielectrics*, Proceedings of International Reliability Physics Symposium, April 2004, Phoenix, AZ, USA, pp. 259-264.

[239] H.A.C. Tilmans, H. Ziad, H. Janses, O. Di Monaco, A. Jourdain, W. De Raedt, X. Rottenberg, E. De Backer, A. Decaussemaeker, K. Baert, *Wafer-level packaged RF-MEMS switches fabricated in a CMOS fab*, International Electron Devices Meeting, IEDM Technical Digest, December 2001, Washington, DC, USA, pp. 41.4.1-41.4.4.

[240] Y. Oya, A. Okubora, W.M. van Spengen, P. Soussan, S. Stoukatch, X. Rottenberg, P. Ratchev, H.A.C. Tilmans, W. De Raedt, E. Beyne, P. De Moor, I. De Wolf, K. Baert, *A reliable and compact polymer-based package for capacitive RF-MEMS switches*, International Electron Device Meeting Technical Digest, Dec. 2004, Washington, DC, USA, pp. 31-34.

[241] G.M. Rebeiz, J.B. Muldavin, *RF MEMS Switches and Switch Circuits*, IEEE Microwave Magazine, December 2001, pp. 59-71.

[242] H.J. De Los Santos, G. Fischer, H.A.C. Tilmans, J.T.M. van Beek, *RF MEMS for Ubiquitous Wireless Connectivity: Part 1 - Fabrication*, IEEE Microwave Magazine, December 2004, vol. 5, no. 4, pp. 36-49.

[243] H.J. De Los Santos, G. Fischer, H.A.C. Tilmans, J.T.M. van Beek, *RF MEMS for Ubiquitous Wireless Connectivity: Part 2 - Applications*, IEEE Microwave Magazine, December 2004, vol. 5, no. 4, pp. 50-65.

[244] A. Margomenos, D. Peroulis, J.P. Becker, L.P.B. Katehi, *Silicon Micromachined Interconnects for On-wafer Packaging of MEMS Devices*, Topical Meeting on Silicon Monolithic Integrated Circuits in RF Systems, Digest of Paper, Sept. 2001, Ann Arbor, MI, USA, pp. 33-36.

[245] K.M. Strohm, B. Schauwecker, D. Pilz, W. Simon, J.-F. Luy, *RF-MEMS Switching Concepts for High Power Applications*, Topical Meeting on Silicon Monolithic Integrated Circuits in RF Systems, Digest of Paper, Sept. 2001, Ann Arbor, MI, USA, pp. 42-46.

[246] P. Blondy, D. Cros, P. Guillon, P. Rey, P. Charvet, B. Diem, C. Zanchi, J.B. Quoirin, *Low Voltage High Isolation MEMS Switches*, Topical Meeting on Silicon Monolithic Integrated Circuits in RF Systems, Digest of Paper, Sept. 2001, Ann Arbor, MI, USA, pp. 47-49.

[247] W.D. van Driel, D.G. Yang, C.A. Yuan, M. van Kleef, G.Q. Zhang, *Mechanical reliability challenges for MEMS packages: Capping*, Microelectronics Reliability (ESREF), vol. 47, no. 9-11. Sept.-Nov. 2007, pp. 1823-1826.

[248] D.M. Tanner, T.B. Parson, A.D. Corwin, J.A. Walraven, J.W. Wittwer, B.L. Boyce, S.R. Winzer, *Science-based MEMS reliability methodology*, Microelectronics Reliability (ESREF), vol. 47, no. 9-11. Sept.-Nov. 2007, pp. 1806-1811.

[249] J. De Coster, H.A.C. Tilmans, K. Hameyer, R. Puers, *Mechanical Design of RF MEMS Capacitive Switches*, Proceedings of Workshop on Semiconductor Sensor and Actuator, Nov. 2002, Veldhoven, The Netherlands, pp. 608-611.

[250] G. Klaasse, R. Puers, H.A.C. Tilmans, *Piezoelectric versus electrostatic actuation for a capacitive RF-MEMS switch*, Proceedings of Workshop on Semiconductor Sensor and Actuator, Nov. 2002, Veldhoven, The Netherlands, pp. 631-634.

[251] T. Tinttunen, T. Veijola, H. Nieminen, V. Ermolov, T. Ryhanen, *Static Equivalent Circuit Model for a Capacitive MEMS RF Switch*, Proceedings of International Conference on Modeling and Simulations of Microsystems, April 2002, San Juan, PR, USA, pp. 166-169.

[252] M. Innocent, P. Wambacq, S. Donnay, H.A.C. Tilmans, M. Engels, H. De Man, W. Sansen, emphAnalysis of the nonlinear behavior of a MEMS variable capacitor, Proceedings of International Conference on Modeling and Simulations of Microsystems, April 2002, San Juan, PR, USA, pp. 234-237.

[253] M.N. Mollah, N.C. Karmakar, *RF-MEMS switches: Paradigms of Microwave Switching*, Proceedings of Asia-Pacific Microwave Conference, Dec. 2001, Taipei, Taiwan, vol. 3, pp. 1024-1027.

[254] S. Lucyszyn, S. Pranonsatit, J.Y. Choi, R.W. Moseley, E.M. Yeatman, A.S. Holmes, *Novel RF MEMS Switches*, Proceedings of Asia-Pacific Microwave Conference, Dec. 2007, Bangkok, Thailand, pp. 1-4.

[255] K. Lee, R. Liu, B.C. Kim, *Double beam RF MEMS switches for wireless applications*, Electronics Letters, vol. 39, no. 6, March 2003, pp. 532-533.

[256] B. Schauwecker, K.M. Strohm, T. Mack, W. Simon, J.-F. Luy, *Serial combination of ohmic and capacitive RF MEMS switches for large broadband applications*, Electronics Letters, vol. 40, no. 1, Jan. 2004, pp. 44-46.

[257] J.N. Randall, C. Goldsmith, D. Denniston, T.-H. Lin, *Fabrication of micromechanical switches for routing radio frequency signals*, J. Vac. Sci. Technol. B, vol. 14, no. 6, Nov. 1996, pp. 3692-3696.

[258] C.T.-C. Nguyen, L.P.B. Katehi, G.M. Rebeiz, *Micromachined devices for wireless communications*, Proceedings of the IEEE, vol. 86, no. 8, Aug. 1998, pp. 1756-1768.

[259] B. Pillans, S. Eshelman, A. Malczewski, J. Ehmke, C. Goldsmith, *Ka-band RF MEMS Phase Shifters for Phased Array Applications*, Proceedings of IEEE Radio Frequency Integrated Circuits (RFIC) Symposium, June 2000, Boston, MA, USA, pp. 195-199.

[260] A. Kaiser, *The potential of MEMS components for re-configurable RF interfaces in mobile communication terminals*, Proceedings of European Solid-State Circuits Conference, Sept. 2001, Villach, Austria, pp. 25-28.

[261] S. Lee, C. Kim, S. Jung, I.-S. Song, Y.C. Cho, *MEMS for IT applications*, Proceedings of International Symposium on Micromechatronics and Human Science, 9-12 Sept. 2001, Nagoya, Japan, pp. 17-23.

[262] C. Wang, R. Ramadoss, S. Lee, K.C. Gupta, V.M. Bright, Y.C. Lee, *Flexible Circuit-based RF MEMS Switches*, Proceedings of ASME International Mechanical Engineering Congress and Exposition, Nov. 2001, New York, NY, USA, pp. 1-6.

[263] G. Prophet, *MEMS flex their tiny muscles*, Electronic Design News, Feb. 2002, pp. 63-72.

[264] D. Anagostou, C.G. Christodoulou, J.C. Lyke, *Re-configurable Array Antennas for Wideband Applications*, IEEE Aerospace Conference Proceedings, March 2002, Big Sky, MT, USA, vol. 2, pp. 2-885-2-861.

[265] G. Hong-ming, L. Miao, Z. Xue-feng, L. Chun-guang, G. Bao-xin, *Transient Response Characterization of Ohmic Contact RF MEMS Switches*, Proceedings of International Conference on Microwave and Millimeter Wave Technology, Beijing, China, Aug. 2002, pp. 271-274.

[266] B.A. Warneke, K.S.J. Pister, *MEMS for Distributed Wireless Sensor Networks*, Proceedings of International Conference on Electronics, Circuits and Systems, Sept. 2002, Dubrovnik, Croatia, vol. 1, pp. 291-294.

[267] A. Margomenos, L.P.B. Katehi, *DC to 40 GHz On-wafer Package for RF MEMS Switches*, Proceedings of IEEE Conference on Electrical Performance of Electronic Packaging, Oct. 2002, Monterey, CA, USA, pp. 91-94.

[268] R. Fritschi, A.M. Ionescu, C. Dehollain, M.J. Declercq, C. Hibert, P. Fluckiger, P. Renaud, *A Novel RF MEMS Technological Platform*, Proceeding of IEEE Conference of the Industrial Electronics Society, Nov. 2002, Sevilla, Spain, vol. 4, pp. 3052-3056.

[269] S. Majumder, J. Lampen, R. Morrison, J. Maciel, *MEMS Switches*, IEEE Instrumentation and Measurement Magazine, March 2003, pp. 12-15.

[270] H.-P. Chang, J. Qian, B.A. Cetiner, F. De Flaviis, M. Bachman, G.P. Li, *RF MEMS Switches Fabricated on Microwave Laminate Printed Circuit Boards*, IEEE Electron Device Letters, vol. 24, no. 4, April 2003, pp. 227-229.

[271] Y. Zhu, H.D. Espinosa, *Electromechanical Modeling and Simulation of RF MEMS Switches*, Proceedings of International Symposium on MEMS and Nanotechnology, June 2003, Charlotte, NC, USA, pp. 8-11.

[272] K.-K. Lee, B.C. Kim, *RF MEMS Switch for Wireless LAN applications*, Proceedings of IEEE International Conference on MEMS, NANO and Smart Systems, July 2003, Banff, Alberta, Canada, pp. 100-102.

[273] A.P. De Silva, H.G. Hughes, *The Package Integration of RF-MEMS Switch and Control IC for Wireless Applications*,IEEE Transactions on Advanced Packaging, vol. 26, no. 3, August 2003, pp. 255-260.

[274] C.-P. Chang, *MEMS for Telecommunications: Devices and Reliability*, Proceedings of IEEE Custom Integrated Circuits Conference, Sept. 2003, San Jose, CA, USA, pp. 199-206.

[275] J.T. Aberle, S.-H. Oh, D.T. Auckland, S.D. Rogers, *Reconfigurable Antennas for Portable Wireless Devices*, IEEE Antennas and Propagation Magazine, vol. 45, no. 6, Dec. 2003, pp. 148-154.

[276] B. Robertson, F.D. Ho, T. Hudson, *Modeling and Fabrication of RF MEMS Switches*, Communications and Computing 2004, pp. 127-133.

[277] J. Oberhammer, G. Stemme, *Low-Voltage High-Isolation DC-to-RF MEMS Switch Based on an S-shaped Film Actuator*, IEEE Transactions on Electron Devices, vol. 51, no. 5, Jan. 2004, pp. 149-155.

[278] J. DeNatale, *Reconfigurable RF Circuits Based on Integrated MEMS Switches*, IEEE International Solid-State Circuits Conference, Digest of Technical Papers, Feb. 2004, San Francisco, CA, USA, vol. 1, pp. 310-311.

[279] B. Ducarouge, D. Dubuc, F. Fluorens, S. Melle, E. Ongareau, K. Grenier, A. Boukabache, V. Conedera, P. Pons, E. Perret, H. Aubert, R. Plana, *Power Capabilities of RF MEMS*, Proceedings of International Conference on Microelectronics, May 2004, Nis, Serbia and Montenegro, vol. 1, pp. 65-70.

[280] Z.D. Milosavljevic, *RF MEMS Swtiches*, IEEE Microwave Review, June 2004, pp. 2-8.

[281] L. Kogut, A. Lumbantobing, K. Komvopoulos, *In situ Monitoring on Native Oxide Film Behavior at MEMS Contact Interfaces Through Basic Electrical Measurements*, Technical Digest, Solid-State Sensor, Actuator and Microsystems Workshop, Hilton Head Island, SC, June 2004, pp. 310-315.

[282] G. Wang, T. Polley, A. Hunt, J. Papapolymerou, *A High Performance Tunable RF MEMS Switch Using Barium Strontium Titanite (BST) Dielectrics for Reconfigurable Antennas and Phased Arrays*, IEEE Antennas and Wireless Propagation Letters, vol. 15, no. 4, April 2005, pp. 217-220.

[283] T. Veijola, *Compact Model for a Cantilever Beam MEM Contact Switch*, Proceedings of European Conference on Circuit Theory and Design, Aug. 2005, Cork, Ireland, vol. 1, pp. I/47-I/50.

[284] N.V. Lakamraju, S.M. Phillips, *Bi-stable RF MEMS switch with low actuation voltage*, Proceedings of International Symposium on Microelectronics, Sept. 2005, Philadelphia, PA, USA.

[285] S. Pranonsatit, S. Lucyszyn, *RF-MEMS Activities in Europe*, Proceedings of Microwave Workshops and Exhibition Digest, Yokohama, Japan, Nov. 2005, pp. 111-122.

[286] D.-S. Lee, S.-W. Jung, N.-K. Cho, W-H. Kim, W-K. Seong, H.-D. Park, *PZT Actuated Seesaw SPDT RF MEMS Switch*, Journal of Physics: Conferece Series, vol. 34, 2006, pp. 304-309.

[287] C. Siegel, V. Ziegler, C. von Wachter, B. Schonlinner, U. Prechtel, H. Schumacher, *Switching speed analysis of low complexity RF-MEMS switches*, Proceedings of German Microwave Conference, March 2006, Karlsruhe, Germany.

[288] D. Vasilache, M. Dragoman, G. Conantinidis, Y. Psychias, F. Vladoianu, T. Kostopoulos, C. Tibeica, L Bary, A. Cismaru, D. Neculoiu, C. Buiculescu, I. Petrini, R. Plana, A. Muller, *60GHz Band RF MEMS Switch*, Proceedings of International Semiconductor Conference, Sept. 2006, Sinaia, Romania, pp. 119-122.

[289] I. Gill, F. Martin, X. Rottenberg, W. De Raedt, *Tunable stop-band filter at Q-band on RF-MEMS metamaterials*, Electronics Letters, vol. 43, no. 21, 2007, pp. 1153-1154.

[290] A. Lazaro, D. Girbau, L. Pradell, A. Nebot, *Non linear actuation model for lateral electrostatically-actuated DC-contact RF MEMS series switches*, Proceedings of Spanish Conference on Electron Devices, Jan. 2007, Madrid, Spain, pp. 181-184.

[291] M. Lamhamdi, P. Pons, L. Boudou, J. Gustavino, Y. Segui, R. Plana, *Correlation between Chemical and Electrical Properties of SiNx Deposited by PECVD. Impact on RF MEMS devices*, Proceedings of International Conference on Solid Dielectrics, July 2007, Winchester, UK, pp. 643-646.

[292] T.D. Hudson, *Development of Piezoelectric RF MEMS Switch and Phase Shifter*, Proceedings of University/Government/Industry/ Micro/Nano Symposium, July 2008, Louisville, KY, USA, pp. 112-115.

[293] F. Jay, J.A. Goetz, *IEEE Standard Dictionary of Electrical and Electronics Terms*, New York, NY, USA, Wiley, 1984.

[294] R.J.Ross, C. Boit, D. Staab, *Micorelectronics Failure Analysis: Desk Reference*, Materials Park, Ohio, USA, ASM International, 2001.

[295] I. De Wolf, *Reliability of MEMS*, Proceedings of International Conference on Thermal, Mechanical and Multiphysics Simulation and Experiments in Micro-Electronics and Micro-Systems, EuroSime, April 2006, Como, Italy. pp. 716-721.

[296] MIL-STD-721C.

[297] MIL-STD-1629A.

[298] M. Krasich, *Can Failure Modes and Effects Analysis Assure a Reliable Product?*, Proceedings of Annual Reliability and Maintainability Symposium, Jan. 2007, Orlando, FL, USA, pp. 277-281.

[299] N. Somsuk, P. Pongpanich, *The Application of FMEA in Defect Reduction for the Spindle Motor Assembly Process for Hard Disk Drives*, Proceedings of IEEE International Conference on Management of Innovation and Technology, Sept. 2008, Bangkok, Thailand, pp. 704-709.

[300] S. Prasad, *Improving Manufacturing Reliability in IC Package Assembly Using FMEA Technique*, Proceedings of IEEE/CHMT International Electronic Manufacturing Technology Symposium, Oct. 1990, Washington, DC, USA, pp. 356-360.

[301] J. Wibbeler, G. Pfeifer, M. Hietschold, *Parasitic charging of dielectric surface in capacitive microelectromechanical systems (MEMS)*, Sensors and Actuators A: Physical, vol. 71, no. 1-2, November 1998, pp. 74-80.

[302] J.R. Reid, *Simulation and Measurement of Dielectirc Charging in Electrostatically Actuated Capacitive Microwave Switches*, Proceedings of Modeling Simulation of Microsystems, April 2002, San Juan, PR, USA, pp. 250-253.

[303] R. Reid, R.T. Webster, *Measurements of charging in capacitive microelectromechanical switches*, Electronic Letters, vol. 38, no. 24, Nov. 2002, pp. 1544-1545.

[304] O. Bochobza-Degani, E. Socher, Y. Nemirovsky, *On the effect of residual charges on the pull-in parameters of electrostatic actuators*, Sensors and Actuators A: Physical, vol. 97-98, April 2002, pp. 563-568.

[305] X. Rottenberg, B. Nauwelaers, W. De Raedt, H.A.C. Tilmans, *Distributed dielectric charging and its impact on RF MEMS devices*, Proceedings of European Microwave Conference, Oct. 2004, Amsterdam, The Netherlands, pp. 77-80.

[306] W.M. van Spengen, R. Puers, R. Mertens, I. De Wolf, *A comprehensive model to predict the charging and reliability of capacitive RF MEMS switches*, J. Micromech. Microeng., vol. 14, no. 4, April 2004, pp. 514-521.

[307] R.W. Herfst, P.G. Steeneken, H.G.A. Huizing, J. Schmitz, *Center-Shift Method for the Characterization of Dielectric Charging in RF MEMS*, IEEE Transaction on Semicondcutor Manufacturing, vol. 21, no. 2, May 2008, pp. 148-153.

[308] J.R. Reid, R.T. Webster, L.A. Starman, *Noncontact Measurements of Charge Induced Voltage Shift in Capacitive MEM-Switches*, IEEE Microwave and Wireless Components Letters, vol. 13, no. 9, Sept. 2003, pp. 367-369.

[309] X. Rottenberg, B. Nauwelaers, W. De Raedt, H.A.C. Tilmans, *Novel 2D+ model for the impact of the dielectric charge distribution on the electrostatic actuation of RF MEMS devices*, Proceedings of Workshop on MEMS for MilimeterWave Communications, MEMSWAVE, June 2004, Uppsala, Sweden, B11-B14.

[310] X. Rottenberg, I. De Wolf, B.J.K.C. Nauwelaers, W. De Raedt, H.A.C. Tilmans, *Analytical Model of the DC Actuation of Electrostatic MEMS Devices With Distributed Dielectric Charging and Nonplanar Electrodes*, Journal of Microelectromechanical Systems, vol. 16, no. 5, Oct. 2007, pp. 1243-1253.

[311] R.W. Herfst, P.G. Steeneken, J. Schmitz, *Identifying Degradation Mechanisms in RF MEMS Capacitive Switches*, Proceedings of IEEE International Conference on Micro Electro Mechanical Systems, MEMS, Jan. 2008, Tucson, AZ, USA, pp. 168-171.

[312] Z. Olszewski, R. Duane, C. O'Mahony, *A study of capacitive-voltage curve narrowing effect in capacitive microelectromechanical switches*, Applied Physics Letters 93, No. 8, Sept. 2008, pp. 094101-1 - 094101-3.

[313] W.M. van Spengen, R. Puers, R.P. Mertens, I. De Wolf, *Experimental characterization of stiction due to charging in RF MEMS*, International Electron Devices Meeting Technical Digest, Dec. 2002, San Francisco, CA, USA, pp. 901-904.

[314] J.D. Kraus, D.A. Fleisch, *Electromagnetics with Applications*, Fifth Edition, WCB/McGraw-Hill, 1999.

[315] Arthur R. von Hippel, *Dielectric Materials and Applications*, New edition, Artech House, Boston, MA, USA, 1995.

[316] E.B. Harris, R.W. Gregor, D.C. Dennis, T.T. Lai, S. Sen, Y.F. Yan, T. Esry, M. Pita, *Charging damage in metal-oxide-metal capacitors*, Proceedings of International Symposium on Plasma Process-Induced Damage, June 1998, Honolulu, HI, USA, pp. 15-17.

[317] B.-Y. Tsui, S.-S. Lin, C.-S. Tsai, C.C. Hsia, *Plasma Damage during Dielectric Etch in High Density Plasma Etcher*, Proceedings of International Symposium on Plasma Process-Induced Damage, May 1999, Monterey, CA, USA, pp. 84-87.

[318] W.M. van Spengen, R. Puers, R. Mertens, I. De Wolf, *A comprehensive model to predict the charging and reliability of capacitive RF MEMS switches*, J. Micromech. Microeng., vol. 14, no. 4, April 2004, pp. 514-521.

[319] S. Melle, D. De Conto, D. Dubuc, K. Grenier, O. Vendier, J.-L. Muraro, J.-L. Cazaux, R. Plana, *Reliability Modeling of Capacitive RF MEMS*, IEEE Transactions of Microwave Theory and Techniques, vol. 53, no. 11, Nov. 2005, pp. 3482-3488.

[320] S. Melle, D. De Conto, L. Mazenq, D. Dubuc, G. Krenier, L. Bary, O. Vendier, J.L. Muraro, J.L. Cazaux, R. Plana, *Modeling of the dielectric charging kinetic for capacitive RF-MEMS*, IEEE MTT-S International Microwave Symposium Digest, June 2005, Long Beach, USA, pp. 757-760.

[321] G. Papaioannou, M.-N. Exarchos, V. Theonas, G. Wang, J. Papapolymerou, *Temperatures Study of the Dielectric Polarization Effects of Capacitive RF MEMS Switches*, IEEE Transactions on Microwave Theory and Techniques, vol. 53, no. 11, Nov. 2005, pp. 3457-3473.

[322] G.J. Papaioannou, M. Exarchos, V. Theonas, G. Wang, J. Papapolymerou, *On the Dielectric Polarization Effects in Capacitive RF-MEMS Switches*, IEEE MTT-S International Microwave Symposium Digest, June 2005, Long Beach, USA, pp. 761-764.

[323] G.J. Papaioannou, G. Wang, D. Bessas, J. Papapolymerou, *Contactless Dielectric Charging Mechanisms in RF-MEMS Capacitive Switches*, Proceedings of European Microwave Conference, Sept. 2006, Manchester, UK, pp. 1739-1742.

[324] G.J. Papaioannou, T. Lisec, *Dielectric charging process in AlN RF-MEMS capacitive switches*, Proceedings of European Microwave Conference, Oct. 2007, Munich, Germany, pp. 1338-1341.

[325] G. Papioannou, R. Marcelli, G. Bartolucci, S. Catoni, G. De Angelis, A. Lucibello, E. Proietti, B. Margesin, F. Giacomozzi, F. Deborgies, *Charging Effects and related Equivalent Circuits for Ohmic Series and Shunt Capacitive RF MEMS Switches*, Proceeding of International Symposium of RF MEMS and RF Microsystems, MEMSWAVE, June 2008, Heraklion, Greece.

[326] D. Mardivirin, A. Pothier, A. Crunteanu, P. Blondy, *Charging Effect in RF MEMS Switches with Dielectric Less Actuators*, Proceeding of International Symposium of RF MEMS and RF Microsystems, MEMSWAVE, June 2008, Heraklion, Grecee.

[327] D. Mardivirin, A. Pothier, A. Crunteanu, B. Vialle, P. Blondy, *Charging in Dielectricless Capacitive RF-MEMS Switches*, IEEE Transactions on Microwave Theory and Techniques, vol. 57, no. 1, Jan. 2009, pp. 231-236.

[328] X. Yuan, J.C.M. Hwang, D. Forehand, C.L. Goldsmith, *Modeling and Characterization of Dielectric-Charging Effects in RF MEMS Capacitive Switches*, IEEE MTT-S International Microwave Symposium Digest, June 2005, Long Beach, USA, pp. 753-756.

[329] X. Yuan, Z. Peng, J.C.M. Hwang, D. Forehand, C.L. Goldsmith, *Temperature Acceleration of Dielectric Charging in RF MEMS Capacitive Switches*, IEEE MTT-S International Microwave Symposium Digest, June 2006, San Francisco, CA, USA, pp. 47-50.

[330] X. Yuan, Z. Peng, J.C.M. Hwang, D. Forehand, C.L. Goldsmith, *Acceleration of Dielectric Charging in RF MEMS Capacitive Switches*, IEEE Transactions on Device and Materials Reliability, vol. 6, no. 4, Dec. 2006, pp. 556-563.

[331] Z. Peng, X. Yuan, J.C.M. Hwang, D. Forehand, C.L. Goldsmith, *Top vs. Bottom Charging of the Dielectric in RF MEMS Capacitive Switches*, Proceedings of Asia-Pacific Microwave Conference, Dec. 2006, Yokohama, Japan, pp. 1535-1539.

[332] Z. Peng, X. Yuan, J.C.M. Hwang, D.I. Forehand, C.L. Goldsmith, *Dielectric Charging of RF MEMS Capacitive Switches under Bipolar Control-Voltage Waveforms*, IEEE MMT-S International Microwave Symposium Digest, June 2007, Honolulu, HI, USA, pp. 1817-1820.

[333] Z. Peng, X. Yuan, J.C.M. Hwang, D.I. Forehand, C.L. Goldsmith, *Superposition Model for Dielectric Charging of RF MEMS Capacitive Switches Under Bipolar Control-Voltage Waveforms*, IEEE Transactions on Microwave Theory and Techniques, vol. 55, no. 12, Dec. 2007, pp. 2911-2918.

[334] R.W. Herfst, P.G. Steeneken, J. Schmitz, *Time and voltage dependence of dielectric charging in RF MEMS capacitive switches*, Proceedings of International Reliability Physics Symposium, April 2007, Phoenix, AZ, USA, pp. 417-421.

[335] C. Cabuz, E.I. Cabuz, T.R. Ohnstein, J. Neuis, R. Maboudian, *Factors enhancing the reliability of touch-mode electrostatic actuators*, Sensors and Actuators A, vol. 79, no. 3, 2000, pp. 245-250.

[336] I. De Wolf, P. Czarnecki, A. Jourdain, R. Modlinski, H.A.C. Tilmans, R. Puers, J.T.M. van Beek, W.M. van Spengen, *The Influence of the Package Environment on the Functioning and Reliability of Capacitive RF-MEMS Switches*, Microwave Journal, vol. 48, no. 12, Dec. 2005, pp. 102-116.

[337] Z. Olszewski, R. Duane, C. O'Mahony, *Effect of environment humidity on the C-V characteristics of RF-MEMS capacitive switch*, Proceeding of International Symposium of RF MEMS and RF Microsystems, MEMSWAVE, June 2008, Heraklion, Greece.

[338] P. Blondy, A. Crunteanu, A. Pothier, P. Tristant, A. Catherinot, C. Champeaux, *Effects of Atmosphere on the Reliability of RF-MEMS Capacitive Switches*, Proceedings of European Microwave Conference, Oct. 2007, Munich, Germany, pp. 1346-1348.

[339] S. Lucyszyn et al., *Advanced RFMEMS, Chapter 5: Reliability*, Cambridge University Press, to be published in 2010.

[340] E.K. Chan, K. Garikipati, R.W. Dutton, *Characterization of Contact Electromechanics Through Capacitance-Voltage Measurements and Simulations*, JMEMS, vol. 8, no. 2, June 1999, pp. 208-217.

[341] S. Melle, F. Flourens, D. Dubuc, K. Grenier, P. Pons, J.L. Muraro, Y. Segui, R. Plana, *Investigation of Dielectric Degradation of Microwave Capacitive Microswitches*, Proceedings of IEEE International Conference on Micro Electro Mechanical Systems, MEMS, Jan. 2004, Maastricht, The Netherlands, pp.141-144.

[342] W.M. van Spengen, *MEMS reliability: Stiction, charging, and RF MEMS*, Ph.D. thesis, K.U. Leuven, Leuven, Belgium, May 2004.

[343] X. Yuan, S. Cherepko, J. Hwang, C.L. Goldsmith, C. Nordquist, C. Dyck, *Initial Observation and Analysis of Dielectric-Charging Effects on RF MEMS Capacitive Switches*, IEEE MTT-S International Microwave Symposium Digest, June 2004, Fort Worth, TX, USA, vol. 3, pp. 1943-1946.

[344] C. O'Mahony, R. Duane, M. Hill, A. Mathewson, *Low-voltage micromechanical test structures for measurement of residual charge in dielectrics*, Electronic Letters, vol. 41, no. 7, March 2005, pp. 409-411.

[345] M. Exarchos, V. Theonas, P. Pons, G.J. Papaioannou, S. Melle, D. Dubuc, F. Cocetti, R. Plana, *Investigation of charging mechanisms in Metal-Insulator-Metal structrues*, Microelectronics Reliability (ESREF), vol. 45, no. 9-11, Sept.-Nov. 2005, pp. 1782-1785.

[346] S. Melle, D. De Conto, L. Mazenq, D. Dubuc, B. Poussard, C. Bordas, K. Grenier, L. Bary, O. Vendier, J.L. Muraro, J.L. Cazaux, R. Plana, *Failure Predictive Model of Capacitive RF-MEMS*, Microelectronics Reliability (ESREF), vol. 45, no. 9-11, Sept.-Nov. 2005, pp. 1770-1775.

[347] Q.-H. Duong, L. Buchaillot, D. Collard, P. Schmitt, X. Lafontan, P. Pons, F. FLourens, F. Pressecq, *Thermal and electrostatic reliability characterization in RF MEMS switches*, Microelectronics Reliability (ESREF), vol. 45, np. 9-11, Sept.-Nov. 2005, pp. 1790-1793.

[348] R.W. Herfst, H.G.A. Huizing, P.G. Steeneken, J. Schmitz, *Characterization of dielectric charging in RF MEMS capacitive switches*, Proceedings of IEEE International Conference on Microelectronic Test Structures, March 2006, Austin, TX, USA, pp. 133-136.

[349] M. Lamhamdi. J. Gustavino, L. Boudou, Y. Segui, P. Pons, L. Bouscayrol, R. Plana, *Charging-Effects in RF Capacitive Switches Influence of insulating layers composition*, Microelectronics Reliability (ESREF), vol. 46, no. 9-11, Sept.-Nov. 2006, pp. 1700-1704.

[350] E. Papandreou, M. Lamhamdi, C.M. Skoulikidou, P. Pons, G. Papaioannou, R. Plana, *Structure dependent charging process in RF MEMS capacitive switches*, Microelectronics Reliability (ESREF), vol. 47, no. 9-11. Sept.-Nov. 2007, pp. 1812-1817.

[351] C. Palego, A. Pothier, A. Crunteanu, P. Blondy, *High power reliability aspects in RF MEMS varactor design*, Microelectronics Reliability (ESREF), vol. 46, no. 9-11, Sept.-Nov. 2006, pp. 1705-1710.

[352] J. Ruan, N. Nolhier, M. Bafleur, L. Bary, F. Coccetti, T. Lisec, R. Plana, *Electrostatic discharge failure analysis of capacitive RF MEMS switches*, Microelectronics Reliability (ESREF), vol. 47, no. 9-11. Sept.-Nov. 2007, pp. 1818-1822.

[353] S. Sangameswaran, J. De Coster, D. Linten, M. Scholz, S. Thijs, L. Haspeslagh, A. Witvrouw, C. Van Hoof, G. Groeseneken, I. De Wolf, *ESD issues in MEMS: a case study in micromirrors*, Proceedings EOS/ESD Symposium, Sept. 2008, Tucson, AZ, USA.

[354] Z. Hou, Z. Liu, G. Hu, L. Liu, Z. Li, *Study on the Reliability of Capacitive Shunt RF MEMS Switch*, Proceeding of International Conference on Electronics Packaging Technology, Aug. 2006, Shanghai, China, pp. 1-4.

[355] M.P. de Boer, J.A. Knapp, T.M. Mayer, T.A. Michalske, *The role of interfacial properties on MEMS performance and reliability*, Invited paper for SPIE/EOS Conference on Microsystems Metrology and Inspection, June 1999, Munich, Germany.

[356] W.M. van Spengen, I. De Wolf, R. Puers, *An auto-adhesion model for MEMS surface taking into account the effect of surface roughness*, Proceedings of Material and Device Characterization in Micromachining, Sept. 2000, Santa Clara, CA, USA, pp. 104-112.

[357] L.L. Mercado, S.-M. Kuo, T.-Y. Tom Lee, L. Liu, *A Mechanical Approach to Overcome RF MEMS Switch Stiction Problem*, Proceedings of Electronic Components and Technology Conference, May 2003, New Orleans, LA, USA pp. 377-384.

[358] W.M. van Spengen, R. Puers, I. De Wolf, *The prediction of stiction failures in MEMS*, IEEE Transactions on Device and Materials Reliability, vol. 3, no. 4, Dec. 2003, pp. 167-172.

[359] R. Modlinski, A. Witvrouw, P. Ratchev, A. Jourdain, V. Simons, H.A.C. Tilmans, J.M.J. den Toonder, R. Puers, I. De Wolf, *Creep as a reliability problem in MEMS*, Microelectronics Reliability, vol. 44, no. 9-11, 2004, pp. 1733-1738.

[360] A. Witvrouw, H.A.C. Tilmans, I. De Wolf, *Materials issues in the processing, the operation and the reliability of MEMS*, Microelectronics Reliability, vol. 76, no. 1-4, 2004, pp. 245-257.

[361] D. Becher, R. Chan, M. Hattendorf, M. Feng, *Reliability Study of Low-Voltage RF MEMS Switches*, The International Conference on Compound Semiconductor Manufacturing Technology Digest, April 2002.

[362] J. Kuchenbecker, L. Bary, X. Lafontan, F. Flourens, A. Takacs, P. Pons, K. Grenier, D. Dubuc, H. Aubert, F. Pressecq, R. Plana, *Microwave and Physical Behavior of Micro-Machined Structures on Membrane for Space Applications*, Proceedings of International Semiconductor Conference, Sept. 2003, Sinaia, Romania, vol. 1, pp. 105-108.

[363] Y. Zhu, H.D. Espinosa, *Reliability of Capacitive RF MEMS Switches at High and Low Temperatures*, International Journal of RF and Microwave Computer-Aided Engineering, vol. 14, pp. 317-328, 2004.

[364] Y. Zhu, H.D. Espinosa, *Effect of temperatures on capacitive RF MEMS switch performance - a coupled-field analysis*, J. Micromech. Microeng. vol. 14, no. 8, 2004, pp. 1270-1279.

[365] B. Schauwecker, J. Mehner, K.M. Strohm, H. Haspeklo, J.-F. Luy, *Investigations of rf shunt airbridge switches among different environmental conditions*, Sensors and Actuators A, vol. 114, no. 1. 2004, pp. 49-58.

[366] V.T. Srikar, S.D. Senturia, *The Reliability of Microelectromechanical Systes (MEMS) in Shock Environments*, Journal of Microelectromechanical Systems, JMEMS, vol. 11, no. 3, June 2002, pp. 206-214.

[367] M.K. Chengalva, R.A. Webster, D.G. Packard, *Simplified Highly-Accelerated Life Testing on Component for Product-level Vibration Reliability Enhancement*, Proceedings of Intersociety Conference on Thermal and Thermomechanical Phenomena in Electronic Systems, June 2004, Las Vegas, NV, USA, vol. 2, pp. 231-237.

[368] L.D. Edmonds G.M. Swift, C.I. Lee, *Radiation Response of a MEMS Accelerometer: An Electrostatic Force*, IEEE Transactions on Nuclear Science, vol. 45, no. 6, Dec. 1998, pp. 2779-2788.

[369] A. Crunteanu, A. Pothier, P. Blondy, F. Dumas-Bouchiat, C. Champeaux, A. Catherinot, P. Tristant, O. Vendier, C. Drevon, J.L. Cazaux, L. Marchand, *Gamma radiation effects on RF MEMS capacitive switches*, Microelectronics Reliability (ESREF), vol. 46, no. 9-11, Sept.-Nov. 2006, pp. 1741-1746.

[370] J. Kuchenbecker, L. Bary, X. Lafontan, F. Flourens, A. Takacs, P. Pons, K. Grenier, D. Dubuc, H. Aubert, F. Pressecq, R. Plana, *Microwave and Physical Behavior of Micro-Machined Structures on Membrane for Space Applications*, Proceedings of International Semiconductor Conference, Sept. 2003, Sinaia, Romania, vol. 1, pp. 105-108.

[371] Y. Zhu, H.D. Espinosa, *Reliability of Capacitive RF MEMS Switches at High and Low Temperatures*, International Journal of RF and Microwave Computer-Aided Engineering, vol. 14, 2004, pp. 317-328.

[372] Y. Zhu, H.D. Espinosa, *Effect of temperatures on capacitive RF MEMS switch performance - a coupled-field analysis*, J. Micromech. Microeng. vol. 14, no. 8, 2004, pp. 1270-1279.

[373] B. Schauwecker, J. Mehner, K.M. Strohm, H. Haspeklo, J.-F. Luy, *Investigations of rf shunt airbridge switches among different environmental conditions*, Sensors and Actuators A, vol. 114, no. 1., 2004, pp. 49-58.

[374] B. Stark, *MEMS Reliability Assurance Guidelines For Space Applications*, JPL Publication 99-1, Jet Propulsion Laboratory, NASA, Pasadena, California, USA, Jan. 1999.

[375] K.F. Man, *MEMS reliability for space applications by elimination of potential failure modes through testing and analysis*, Proc. SPIE Vol. 3880, MEMS Reliability for Critical and Space Applications, Aug. 1999, pp. 120-129.

[376] J. DeNatale, R. Mihailovich, J. Waldrop, *Techniques for Reliability Analysis of MEMS RF Switch*, Proceedings of International Reliability Physics Symposium, IRPS, April 2002, Dallas, TX, USA, pp. 116-117.

[377] I. De Wolf, W.M. van Spengen, R. Modlinski, A. Jourdain, A. Witvrouw, P. Fiorini, H.A.C. Tilmans, *Reliability and failure analysis of RF MEMS switches*, Proceedings of International Symposium for Testing and Failure Analysis, Nov. 2002, Phoenix, AZ, USA, pp. 275-281.

[378] I. De Wolf, *MEMS reliability*, Microelectronics Reliability, vol. 43, no. 7, 2003, pp. 1047-1048.

[379] J. DeNatale, R. Mihailovich, *RF MEMS Reliability*, Proceedings of International Conference on Solid-State Sensors, Actuators and Microsystems, TRANSDUCERS, June 2003, Boston, MA, USA, vol. 1, pp. 943-946.

[380] C.-P. Chang, *MEMS for Telecommuunications: Devices and Reliability*, Proceedings of Custom Integrated Circuits Conference, Sept. 2003, San Jose, CA, USA, pp. 199-206.

[381] B. Wunderle, B. Michel, *Progress in reliability research in the micro and nano region*, Microelectronics Reliability (ESREF), vol. 46, no. 9-11, Sept.-Nov. 2006, pp. 1685-1694.

[382] E. Weissmann, Ch. Petrescu, D. Tarina, *An apparatus with electrostatically driven vibrating condenser for contact potential measurements*, Journal of Physics E: Scientific Instruments, vol. 1, no. 4, April 1968, pp. 426-428.

[383] S. Danyluk, *A UHV guarded Kelvin probe*, Journal of Physics E: Scientific Instruments, vol. 5, no. 5, May 1972, pp. 478-480.

[384] A. Noblet, H. Ridelaire, G. Sylin, *Measurement of surface potentials*, Journal of Physics E: Scientific Instruments, vol. 17, no. 3, March 1984, pp. 234-239.

[385] K. Germanova, Ch. Hardalov, V. Strashilov, B. Georgiev, *An improved apparatus for surface photovoltage studies with bimorphous piezoelectric Kelvin probe*, Journal of Physics E: Scientific Instruments, vol. 20, no. 3, March 1987, pp. 273-276.

[386] U. Klein, W. Vollmann, P.J. Abatti, *Contact Potential Differences Measurement: Short History and Experimental Setup for Classroom Demonstration*, IEEE Transactions on Education, vol. 46, no. 3, Aug. 2003, pp. 338-344.

[387] G. Binnig, H. Rohrer, Ch. Gerber, E. Weibel, *7x7 Reconstruction on Si(111) Resolved in Real Space*, Physical Review Letters, vol. 50, no. 2, Jan. 1982, pp. 120-123.

[388] G. Binnig, C.F. Quate, *Atomic Force Microscope*, Physical Review Letters, vol. 56, no. 9, March 1986, pp. 930-933.

[389] Y. Martin, D.W. Abraham, H.K. Wickramasinghe, *High-resolution capacitance measurement and potentiometry by force microscopy*, Applied Physics Letters, vol. 52, no. 13, March 1988, pp. 1103-1105.

[390] M. Nonnenmacher, M.P. OŠBoyle, H.K. Wickramsinghe, *Kelvin probe force microscopy*, Applied Physics Letters, vol. 58, no. 25, June 1991, pp. 2921-2923.

[391] P. Girard, *Electrostatic force microscopy: principles and some applications to semiconductors*, Nanotechnology, vol. 14, no. 4, Dec. 2001, pp. 485-490.

[392] D. Bonnell, *Scanning Probe Microscopy and Spectroscopy: Theory, Techniques, and Applications*, Second Edition, 2001, A.J. Wiley & Sons, USA.

[393] www.kelvininfo.com

[394] www.ntmdt.com

[395] N.A. Surplice, R.J. DŠArcy, *A critique of the Kelvin method of measuring work functions*, Journal of Physics E: Scientific Instruments, vol. 3, no. 7, July 1970, pp. 477-482.

[396] C.J. Kang, G.H. Buh, S. Lee, C.K. Kim, K.M. Mang, C. Im, Y. Kuk, *Charge trap dynamics in a SiO_2 layer on Si by scanning capacitance microscopy*, Applied Physics Letters, vol. 74, no. 13, March 1999, pp. 1815-1817.

[397] W. McNeil, J.F. Conley, Jr., H. Walker, *2-D Imaging of Trapped Charge in SiO_2 using Scanning Kelvin Probe Microscopy*, Proceeding of IEEE International SOI Conference, Oct. 2000, Wakefield, MA, USA, pp. 38-39.

[398] G.Lubarsky, R. Shikler, N. Ashkenasy, Y. Rosenwaks, *Quantitative evaluation of local charge trapping in dielectric stacked gate structures using Kelvin probe force microscopy*, Journal of Vacuum Science and Technology B, vol. 20, no. 5, Sep/Oct. 2002, pp. 1914-1917.

[399] C.Y. Ng, T.P. Chen, H.W. Lau, Y. Liu, M.S. Tse, O.K. Tan, V.S.W. Lim, *Visualizing charge transport in silicon nanocrystals embedded in SiO_2 films with electrostatic force microscopy*, Applied Physics Letters, vol. 85, no. 14, Oct. 2004, pp. 2941-2943.

[400] R.W. Herfst, P.G. Steeneken, J. Schmitz, A.J.G. Mank, M. van Gils, *Kelvin probe study of laterally inhomogeneous dielectric charging and charge diffusion in RF MEMS capacitive switches*, Proceedings of IEEE International Reliability Physics Symposium, April 2008, Phoenix, AZ, USA, pp. 492-495.

[401] P.M. Bridger, Z.Z. Bandic, E.C. Piquette, T.C. McGill, *Measurement of induced surface charges, contact potential, and surface states in GaN by electric force microscopy*, Applied Physics Letters, vol. 74, no. 23, June 1999, pp. 3522-3524.

[402] B.J. Rodriguez, W.-C. Yang, R.J. Nemanich, A. Gruverman, *Scanning probe investigation of surface charge and surface potential of GaN-based heterosctructures*, Applied Physics Letters, vol. 86, no. 11, 2005.

[403] J.W. Hong, D.S. Kahng, J.C. Shin, H.J. Kim, Z.G. Khim, *Detection and control of ferroelectric domains by an electrostatic force microscope*, Journal of Vacuum Science and Technology B, vol.16, no. 6, Nov/Dec. 1998, pp. 2942-2946.

[404] X. Liu, K. Kitamura, K. Terabe, *Surface potential imaging of nanoscale $LiNbO_3$ domains investigated by electrostatic force microscopy*, Applied Physics Letters, vol. 89, no. 13, 2006.

[405] S. Hong, J. Woo, H. Shin, E. Kim, K-H. Kim, J.U. Jeon, Y.E. Pak, K. No, *Effect of metal-insulator-semiconductor structure derived space charge field on the tip vibration signal in electrostatic force microscopy*, Journal of Vacuum Science and Technology B, vol. 18, no. 6, Nov/Dec. 2000, pp. 2688-2691.

[406] B. Martin, H. Kliem, *Space Charge Measurements with the Scanning Kelvin Probe*, IEEE Transactions on Dielectrics and Electrical Insulation, vol. 15, no. 2, April 2008, pp. 560-567.

[407] H.A. Engelhardt, P. Feulner, H. Pfnur, D. Menzel, *An accurate and versatile vibrating capacitor for surface and adsorption studies*, Journal of Physics E: Scientific Instruments, vol. 10, no. 11, Nov. 1977, pp. 1133-1136.

[408] J. Mizsei, *Vibrating capacitor: applications in the research of semiconductor gas sensors*, Proceedings of IEEE Sensors, Oct. 2004, Vienna, Austria, vol. 2, pp. 947-950.

[409] J.M.R. Weaver, D.W. Abraham, *High resolution atomic force microscopy potentiometry*, Journal of Vacuum Science and Technology B, vol. 9, no. 3, May/June 1991, pp. 1559-1561.

[410] C.-S. Jiang, H.R. Moutinho, J.F. Geisz, D.J. Friedman, M.M. Al-Jassim, *Direct measurement of electrical potentials in $GaInP_2$ solar cells*, Applied Physics Letters, vol. 81, no. 14, Sept. 2002, pp. 2569-2571.

[411] A.K. Henning, T. Hochwitz, J. Slinkman, J. Never, S. Hoffman, P. Kaszuba, C. Daghlian, *Two-dimensional surface dopant profiling in silicon using scanning Kelvin probe microscopy*, Journal of Applied Physics, vol. 77, no. 5, March 1995.

[412] T. Hochwitz, A.K. Henning, C. Levey, c. Daghlian, J. Slinkman, J. Never, P. Kaszuba, R. Gluck, R. Wells, J. Pekarik, R. Finch, *Imaging integrated circuit dopant profiles with the force-based scanning Kelvin probe microscope*, Journal of Vacuum Science and Technology B, vol. 14, no. 1, Jan/Feb 1996, pp. 440-446.

[413] M.D.H. Lay, C.I. Pakes, J.C. McCallum, *Kelvin-probe Force Microscopy Defect Study of Ion Implanted Thermal Oxide Thin Films on Silicon*, Proceedings of Conference on Optoelectronic and Microelectronic Materials and Devices, Dec. 2004, Brisbane, Qld, Australia, pp. 405-408.

[414] C. Schonenberger, S.F. Alvarado, *Observation of Single Charge Carriers by Force Microscopy*, Physical Review Letters, vol. 65, no. 25, Dec. 1990, pp. 3162-3165.

[415] M. Tanimoto, O. Vatel, *Kelvin probe force microscopy for characterization of semiconductor devices and processes*, Journal of Vacuum Science and Technology B, vol. 14, no. 2. Mar/Apr. 1996, pp. 1547-1551.

[416] R.S. Ferguson, K. Fobelets, L.F. Cohen, *Kelvin probe force microscopy of beveled semiconductors*, Journal of Vacuum Science and Technology B, vol. 20, no. 5, Sep/Oct. 2002, pp. 2133-2136.

[417] T. Gotszalk, P. Czarnecki, P. Grabiec, K. Domanski, M. Zaborowski, I. W. Rangelow, *Microfabricated cantilever with metallic tip for electrostatic and capacitance microscopy and its application to investigation of semiconductor devices*, Journal of Vacuum Science and Technology B, vol. 22, no. 2, Mar/Apr. 2004,

[418] R.A. Lodge, B. Bhushan, *Surface potential measurement of human hair using Kelvin probe microscopy*, Journal of Vacuum Science and Technology A, vol. 25, no. 4, Jul/Aug. 2007, pp. 893-902.

[419] J.T.M. van Beek, M.H.W.M. van Delden, A. van Dijken, P. van Eerd, M. van Grootel, A.B.M. Jansman, A.L.A.M. Kemmeren, Th.G.S.M. Rijks, P.G. Steeneken, J. den Toonder, M. Ulenaers, A. den Dekker, P. Lok, N. Pulsford, F. van Straten, L. van Teeffelen, J. de Coster, R. Puers, *High-Q integrated RF passives and micromechanical capacitors on silicon*, Proceedings of Bipolar/BiCMOS Circuits and Technology Meeting, September 2003, Toulouse, France, pp. 147-150.

[420] J.T.M. van Beek, P.G. Steeneken, G.J.A.M. Verheijden, J.W. Weekamp, A. den Dekker, M. Giesen, A.J.M. de Graauw, J.J. Koning, F. Theunis, P. van der Wel, B. van Velzen, P. Wessels, *MEMS for wireless communication: application, technology, opportunities and issues*, Proceedings of International Conference on RF MEMS and RF Microsystems, June 2006, Orvieto, Italy, pp. 135-140.

[421] T. Buck, M. Reimann, M. Ulm, R. Mueller-Fiedler, J. Seidel, E. Kasper, C. Schoellhorn, S. Haak, *Monolithic integration of RF-MEMS and semiconductor devices for the K-Band*, Proceedings of SPIE, vol. 4981, Bellingham, WA, 2003, pp. 131-138.

[422] M. Ulm, J. Schoebel, M. Reimann, T. Buck, J. Dechow, R. Mueller-Fiedler, H.P. Trah, E. Kasper, *Millimeter Wave Microelectromechanical (MEMS) Switches for Automotive Surround Sensing Systems*, Topical Meeting on Silicon Monolithic Integrated Circuits in RF Systems Digest of Papers, April 2003, Grainau, Germany, pp. 142-149.

[423] M. Ulm, T. Walter, R. Mueller-Fiedler, K. Voigtlaender, E. Kasper, *K-Band Capacitive MEMS - Switches*, Topical Meeting on Silicon Monolithic Integrated Circuits in RF Systems Digest of Papers, April 2000, Garmisch, Germany, pp. 119-122.

[424] J. Schoebel, T. Buck, M. Reimann, M. Ulm, M. Schneider, *W-Band RF-MEMS Subsystems for Smart Antennas in Automotive Radar Sensors*, Proceedings of European Microwave Conference, Oct. 2004, Amsterdam, The Netherlands. vol. 3, pp. 1305-1308.

[425] P. Ekkels, *Metal surface micromachining technologies for implementation in RF-MEMS switching devices*, PhD dissertation, Katholieke Universiteit Leuven, March 2010.

[426] J.C. Wyant, *White Light Interferometry*, Proc. SPIE, 4737, 2002, pp. 98-107.

[427] www.veeco.com

[428] www.polytec.com

[429] www.agilent.com

[430] J.S. Schultz, S.L. Firebaugh, H.K. Charles, Jr, R.L. Edwards, A.C. Keeney, S.F. Wilderson, *Dielectric Charge Measurement in Capacitive Microwave Shunt Switches*, Proceedings of IEEE Instrumentation and Measurement Technology Conference IMTC, May 2005, Ottawa, Canada, vol. 2, pp. 1345-1349.

[431] A. Ziaei, T. Dean, Y. Mancuso, *Lifetime characterization of capacitive power RF MEMS switches*, Proceedings of IEEE European Microwave Conference, Oct. 2005, Paris, France, vol. 3.

[432] C. Goldsmith, D. Forehand, X.B. Yuan, J. Hwang, *Tailoring Capacitive Switch Technology for Reliable Operation*, Proceedings of Government Microcircuit Applications and Critical Technology Conference, Mar. 2006, San Diego, CA, USA, pp. 1-4.

[433] W.M. van Spengen, R. Puers, R.P. Mertens, I. De Wolf, *A low frequency electrical test set-up for the reliability assessment of capacitive RF MEMS switches*, J. Micromech. Microeng, vol. 13, no. 13, May 2003, pp. 604-612.

[434] P.A. Flinn, D.S. Gardner, W.D. Nix, *Measurement and Interpretation of Stress in Aluminum-Based Metallization as a Function of Thermal History*, IEEE Transactions on Electron Devices, vol. ED-34., No. 3, March 1987, pp. 689-699.

[435] R. Modlinski, P. Ratchev, A. Witvrouw, R. Puers, I. De Wolf, *Creep-resistant aluminum alloys for use in MEMS*, Journal of Micrimechanics and Microengineering, vol. 15, no. 7, July 2005, pp. 165-170.

[436] H. Nieminen, V. Ermolov, S. Silanto, K. Nybergh, T. Ryhanen, *Design of a Temperature-Stable RF MEM Capacitor*, Journal of Microelectromechanical Systems, vol. 13, no. 5, Oct. 2004, pp. 705-714.

[437] D.R. Lide, *Handbook of Chemistry and Physics, 79th edition*, CRC Press, LLC, 1998, USA.

[438] M. Abdel-Salam, P. Weiss, B. Lieske, *Discharges in Air from Point Electrodes in the Presence of Dielectric Plates: Experimental results*, IEEE Transactions on Electrical Insulation, April 1992, vol. 27, no. 2, pp. 309-319.

[439] A. Kaluzny, *The electric strength of the air polluted by industrial dust*, IEEE Conference on Electrical Insulation and Dielectric Phenomena, Oct. 1990, Pocono Manor, PA, USA, pp. 569-574.

[440] F. Massines, N. Gherardi, N. Naude, P. Segur, *Glow and Townsend dielectric barrier discharge in various atmosphere*, Plasma Physics and Controlled Fusion, Dec. 2005, vol. 47, no. 12B, pp. 577-588.

[441] R. Kacprzyk, *Wybrane zagadnienia badan ladunku i jego zaniku w dielektrykach stalych*, Monograph, Oficyna Wydawnicza Politechniki Wroclawskiej, Wroclaw 2004.

[442] D.L. Myers, B.D. Arnold, *Electret Media For HVAC Filtration Applications*, International Nonwovens Journal, vol. 12, no. 4, Winter 2003, pp. 43-54.

[443] M. Goel, *Electret sensors, filters and MEMS devices: New challenges in material research* Current Science, Aug. 2003, vol. 85, no. 4, pp. 443-453.

[444] P. Guenther, *Mechanism of Charge Storage in Electron-beam or Corona-charged Silicon-dioxide Electrets*, IEEE Transactions on Electrical Insulation, Feb. 1991, vol. 26, no. 1, pp. 42-48.

[445] X. Huang, X. Xie, *Theoretical Analysis of Mechanism of Charge Storage in Silicon Dioxide Wafer Electrets*, Proceeding of IEEE International Symposium on Electrets, Sept. 1996, Shanghai, P.R. of China, pp. 46-48.

[446] M. Abdel-Salam, H. Singer, A. Ahmed, *Effect of the dielectric barrier on discharges in non-uniform electric fields*, Journal of Physics D: Applied Physics, April 2001, vol. 34, no. 8, pp. 1219-1234.

[447] M. Abdel-Salam, H. Singer, A. Ahmed, *On the static behaviour of dielectric barrier discharges in uniform electric fields*, Journal of Physics D: Applied Physics, April 2001, vol. 34, no. 8, pp. 1974-1981.

[448] R.S. Dhariwal, J-M. Torres, M.P.Y. Desmulliez, *Electric field breakdown at micrometer separations in air and nitrogen at atmospheric pressure*, IEE Proceedings - Science, Measurement and Technology, vol. 147, no. 5, Sep. 2000, pp. 261-265.

[449] J-M. Torres, R.S. Dhariwal, *Electric field breakdown at micrometre separations*, Nanotechnology, vol. 10, no. 1, March 1999, pp. 102-107.

[450] J-M. Torres, R.S. Dhariwal, *Electric field breakdown at micrometer separations in air and vacuum*, Microsystem Technologies, Nov. 1999, vol. 6, no. 1, pp. 6-10.

[451] C-H. Chen, J.A. Yeh, P-J. Wang, *Electrical breakdown phenomena for devices with micron separations*, J. Micromech. Microeng, vol. 16, no. 7, May 2006, pp. 1366-1373.

[452] F. Paschen *Ueber die zum Funkenuebergang in Luft, Wasserstoff und Kohlensaeure bei verschiedenen Drucken erforderliche Potentialdifferenz*, Annalen der Physik 273 (5), 1889, pp. 69Ű75.

[453] R.B. Abernethy, *The New Weibull Handbook*, 5th Edition, Dec. 2006, 536 Oyster Road, North Palm Beach, Florida 33408-4328, USA.

[454] www.schott.com

[455] W. Shockley, W.W. Hooper, H.J. Queisser, W. Schroen, *Mobile Electric Charges on Insulating Oxides with Application to Oxide Covered Silicon p-n Junctions*, Surface Science, vol. 2, 1964, pp. 277-287

[456] X.G. Zhang, *Electrochemistry of silicon and its oxide*, Kluwer Academic, New York, USA, 2001.

[457] I. De Wolf, X. Rottenberg, P. Czarnecki, P. Soussan, *Method for reducing substrate charging*, EP2107038A2, App. no. 09156532.5, Oct. 2009.

[458] P. Ekkels, X. Rottenberg, P. Czarnecki, R. Puers and H.A.C. Tilmans, *Simple and Robust Air Gap-based MEMS Switch Technology for RF-applications*, Proceeding of 22nd International IEEE Conference on Micro Electro Mechanical Systems - MEMS, Jan. 2009, Sorrento, Italy, pp. 856-859.

[459] H. Yamazaki, T. Ikehashi, T. Ohguro, E. Ogawa, K. Kojima, K. Ishimaru, H. Ishiuchi, *An intelligent bipolar actuation method with high stiction immunity for RF MEMS capacitive switches and variable capacitors*, Sensors and Actuators A, A, vol. 139, no. 1-2, Sept. 2007, pp. 233-236.

List of publications

Journal papers

1. I. De Wolf, <u>P. Czarnecki</u>, A. Jourdain, R. Modlinski, H. Tilmans, R. Puers, J.T.M. van Beek and M. van Spengen, *The influence of the package environment on the functionality and reliability of capacitive RF-MEMS switches*, Microwave Journal, vol. 48, no. 12, 2005, pp. 102-116.

2. X. Rottenberg, S. Brebels, P. Ekkels, <u>P. Czarnecki</u>, P. Nolmans, R. Mertens, B. Nauwelaers, R. Puers, I. De Wolf, W. De Raedt and H.A.C. Tilmans, *An electrostatic fringing-field actuator (EFFA): application towards a low-complexity thin-film RF-MEMS technology*, Journal of Micromechanics and Microengineering, vol. 17, no. 7, July 2007, pp. 204-210.

3. <u>P. Czarnecki</u>, X. Rottenberg, P. Soussan, P. Ekkels, P. Muller, P. Nolmans, W. De Raedt, H.A.C. Tilmans, R. Puers, L. Marchand and I. De Wolf, *Effect of charging on the reliability of capacitive RF MEMS switches*, Sensors and Actuators A, vol. 154, no. 2, pp. 261-268.

4. V. Cherman, <u>P. Czarnecki</u>, I. De Wolf, T. Yamada, N. Setter, B. Malic, M. Vukadinovic and M. Kosec, *Reliability study of tunable ferroelectric capacitors*, Journal of Applied Physics, vol. 104, no. 6, 2008, pp. 064104.

5. P. Ekkels, X. Rottenberg, <u>P. Czarnecki</u>, H. Philipsen, R. Mertens, R. Puers and H.A.C. Tilmans, *Air gap-based MEMS switch technology using nickel surface micromachining*, Sensors and Actuators A: Physical, accepted for publishing.

Conferences, symposiums and workshops

1. M. van Spengen. <u>P. Czarnecki</u>, R. Puers, J.T.M. van Beek and I. De Wolf, *The influence of the package environment on the functioning and reliability of RF-MEMS switches*, Proceedings of the 43rd Annual IEEE International Reliability Physics Symposium, April 2005, San Jose, CA, USA, pp. 337-341.

2. <u>P. Czarnecki</u>, X. Rottenberg, R. Puers and I. De Wolf, *Impact of biasing scheme and environment conditions on the lifetime or RF-MEMS capacitive switches*, Proceedings of MEMSWAVE Workshop, June 2005, Lausanne, Switzerland, pp. 133-136.

3. I. De Wolf, <u>P. Czarnecki</u>, A. Jourdain, S. Kalicinski, R. Modlinski, P. Muller, X. Rottenberg, P. Soussan, H.A.C. Tilmans, *Failure mechanisms and reliability issues of RF-MEMS switches*, 5th ESA Round Table on Micro/Nano Technologies for Space, Oct. 2005, Noordwijk, The Netherlands.

4. H.A.C. Tilmans, X. Rottenberg, P. Soussan, P. Nolmans, P. Ekkels, <u>P. Czarnecki</u>, R. Modlinski, S. Stoukatch, A. Jourdain, B. Nauwelaers, K. Vaesen, G. Carchon, I. De Wolf and W. De Raedt, *Generic RF-MEMS technology platform for mobile and satellite communications*, 5th ESA-ESTEC Round Table on Micro/Nano Technologies for Space, Oct. 2005, Noordwijk, The Netherlands

5. X. Rottenberg, <u>P. Czarnecki</u>, G. Klasse, P. Nolmans, R. Mertens, B. Nauwelaers, I. De Wolf, W. De Raedt and H.A.C. Tilmans, *Out-of-plane electrostatic interdigitated actuator*, Proceedings of 17th Workshop on Micromachining, Micromechanics and Microsystems - MME, Sept. 2006, Southampton, UK, pp. 165-168.

6. A. Mehta, M. Gromova, <u>P. Czarnecki</u>, K. Baert, A. Witvrouw, *Optimisation of PECVD poly-SiGe layers for MEMS post-processing on top of CMOS*, Proceedings of 13th International Conference on Solid State Sensors, Actuators and Microsystems - TRANSDUCERS, June 2005, Seoul, Korea, pp. 1326-1329.

7. <u>P. Czarnecki</u>, X. Rottenberg, R. Puers and I. De Wolf, *Effect of gas pressure on the lifetime of capacitive RF MEMS switches*, Proceedings of the IEEE 19th International Conference on Microelectromechanical Systems - MEMS, Jan. 2006, Istanbul, Turkey, pp. 890-893.

8. X. Rottenberg, P. Soussan, S. Stoukatch, <u>P. Czarnecki</u>, B. Nauwelaers, G. Carchon, I. De Wolf, W. De Raedt and H.A.C. Tilmans, *RF-MEMS technology platform for agile mobile and satellite communications*, Proceedings of the European Microwave Conference - EuMC, Sept. 2006, Manchester, UK, pp. 1723-1726.

9. X. Rottenberg, P. Nolmans, P. Ekkels, <u>P. Czarnecki</u>, R. Mertens, B. Nauwelaers, I. De Wolf, W. De Raedt and H.A.C. Tilmans, *Electrostatic fringing-field actuator (EFFA): application towards a low-complexity RF-MEMS technology*, Technical Digest of the 20th IEEE International Conference on Mico Electro Mechanical Systems - MEMS, Jan. 2007, Kobe, Japan, pp. 203-206.

10. X. Rottenberg, P. Ekkels, S. Brebels, T. Webers, <u>P. Czarnecki</u>, R. Mertens, B. Nauwelaers, R. Puers, L. Marchand, I. De Wolf, W. De Raedt and H.A.C. Tilmans, *Novel EFFA-based thin-film RF-MEMS technology*, Proceedings of the 14th International Conference on Solid-State Sensors, Actuators and Microsystems, Transducers & Eurosensors, June 2007, Lyon, France, pp. 145-148.

11. <u>P. Czarnecki</u>, X. Rottenberg, P. Soussan, P. Nolmans, P. Ekkels, P. Muller, H.A.C. Tilmans, W. De Raedt, R. Puers, L. Marchand and I. De Wolf, *Experimental evidence of non-uniform dielectric charging in capacitive RF-MEMS switches*, Proceedings of the 18th Workshop on MicroMechanics Europe - MME, Sept. 2007, Guimaraes, Portugal, pp. 227-230.

12. X. Rottenberg, P. Ekkels, S. Brebels, <u>P. Czarnecki</u>, B. Nauwelaers, P. Soussan, P. Nolmans, L. Marchand, J. Guijarro, I. De Wolf, H.A.C. Tilmans and W. De Raedt, *RF-MEMS technology, components and circuits*, 6th ESA Round Table on Micro & Nano Technologies for Space Applications, Oct. 2007, Noordwijk, The Netherlands.

13. <u>P. Czarnecki</u>, P. Soussan, X. Rottenberg, P. Muller, P. Nolmans, P. Ekkels, W. De Raedt, H.A.C. Tilmans, R. Puers, O. Vendier, L. Marchand and I. De Wolf, *ENDORFINS: Enabling deployment of RF MEMS technology in space telecommunication*, 6th ESA Round Table on Micro & Nano Technologies for Space Applications, Oct. 2007, Noordwijk, The Netherlands.

14. <u>P. Czarnecki</u>, X. Rottenberg, P. Soussan, P. Ekkels, P. Muller, P. Nolmans, W. De Raedt, H.A.C. Tilmans, R. Puers, L. Marchand and I. De Wolf,

Influence of the substrate on the lifetime of capacitive RF MEMS switches, Proceedings of the 21st IEEE International Conference on Micro Electro Mechanical Systems - MEMS, Jan. 2008, Tucson, AZ, USA, pp. 172-175.

15. X. Rottenberg, P. Czarnecki, H.A.C. Tilmans, W. De Raedt and I. De Wolf, *Multi-physics simulation and reliability analysis for RF-MEMS devices*, Proceedings of the EuroSimE: Thermal, Mechanical and Multiphysics Simulation and Experiments in Micro-Electronics and Micro-Systems, April 2008, Freiburg, Germany.

16. P. Czarnecki, X. Rottenberg, P. Soussan, P. Nolmans, P. Ekkels, P. Muller, H.A.C. Tilmans, W. De Raedt, R. Puers, L. Marchand and I. De Wolf, *New insights into charging in capacitive RF MEMS switches*, Proceedings of the IEEE International Reliability Physics Symposium - IRPS, April 2008, Phoenix, AZ, USA, pp. 496-505.

17. P. Ekkels, X. Rottenberg, P. Czarnecki, R. Puers and H.A.C. Tilmans, *Simple and robust air gap-based MEMS switch technology for RF-application*, Proceedings of the 22nd IEEE International Conference on Micro Electro Mechanical Systems - MEMS, Jan. 2009, Orvieto, Italy, pp. 856-859.

18. I. De Wolf, J. De Coster, V. Cherman, P. Czarnecki, S. Kalicinski, O. Varela Pedreira, S. Sangameswaran, K. Vanstreels, *New methods and instrumentation for functional, yield and reliability testing of MEMS on device, chip and wafer level*, Proceedings of the SPIE Europe Microtechnologies for the New Millenium, vol. 7362, May, 2009, Dresden, Germany, p. 73620N.

Book chapters

1. P. Czarnecki, X. Rottenberg, R. Puers and I. De Wolf, *Impact of biasing scheme and environment conditions on the lifetime of RF-MEMS*, MEMS Technologies for RF and Milimeter Wave Circuits, chapter in book, Ed. Academiei Romane, Bucuresti, Romania, 2006, pp. 157-162.

Curriculum vitae

Piotr Czarnecki was born in Szczecin, Poland in September 1977.

He received his M.Sc. degree in Microsystems Technology from Wroclaw University of Technology in 2002 with a thesis entitled: Electron emission study from emitters fabricated using thin-film technology (Badanie emisji elektronowej z emiterow wykonanych technika cienkowarstwowa).

In 2004 he joined reliability group at Interuniversity Micro-Electronics Center (IMEC) in Leuven, Belgium, where he started working on his Ph.D. thesis under supervision of Prof. Robert Puers from K.U. Leuven.

Since August 2009 he has been working in the Reliability and Modeling group at IMEC. His work is focused on reliability of RF MEMS devices, in particular capacitive RF MEMS switches.

KATHOLIEKE UNIVERSITEIT
LEUVEN

ASSOCIATIE K.U.LEUVEN